FABRICATION AND CHARACTERIZATION OF WAVEGUIDES ON RBTIOPO4 CRYSTALS FOR PHOTONIC APPLICATIONS

Jaume Cugat Mulet

Dipòsit Legal: T.1024-2013

UNIVERSITAT ROVIRA I VIRGILI
FABRICATION AND CHARACTERIZATION OF WAVEGUIDES ON RBTIOPO4 CRYSTALS FOR PHOTONIC APPLICATIONS
Jaume Cugat Mulet
Dipòsit Legal: T.1024-2013

Fabrication and characterization of waveguides on $RbTiOPO_4$ crystals for photonic applications

Jaume Cugat Mulet

This thesis contains results based on the growth of (Yb,Nb): $RbTiOPO_4$ / $RbTiOPO_4$ (001) epitaxial layers and consequent planar waveguide fabrication and characterization. The results of fabrication and characterization of rib waveguides over this planar waveguides using several techniques are also presented. The fabrication and characterization of channel waveguides by diffusion over $RbTiOPO_4$ (001) substrates is also studied.

Jaume Cugat Mulet · Fabrication and characterization of waveguides on $RbTiOPO_4$ crystals for photonic applications

UNIVERSITAT ROVIRA I VIRGILI

Fabrication and characterization of waveguides on $RbTiOPO_4$ crystals for photonic applications

Jaume Cugat Mulet

Doctoral Thesis

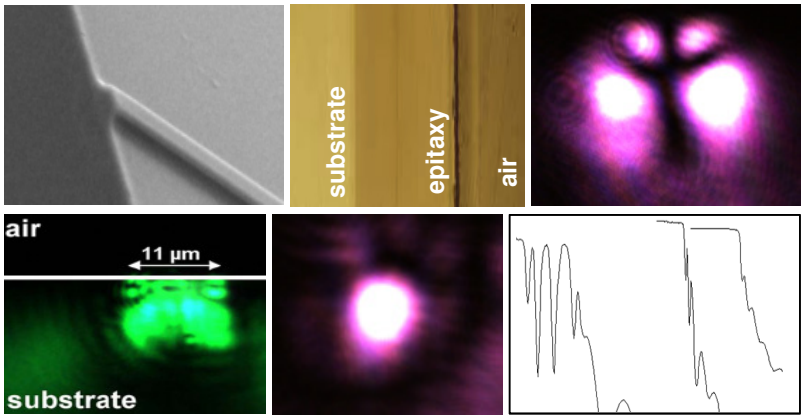

Supervised by:
Dr. Rosa Maria Solé
Prof. Dr. Magdalena Aguiló

Tarragona, 2013

Fabrication and characterization of waveguides on $RbTiOPO_4$ crystals for photonic applications

Doctoral Thesis

Jaume Cugat Mulet

Doctoral Thesis

Supervised by:

Dr. Rosa Maria Solé Cartañá

Prof. Dr. Magdalena Aguiló Díaz

Departament de Química Física i Inorgànica

Física i Cristal·lografia de Materials i Nanomaterials (FiCMA - FiCNA)

UNIVERSITAT ROVIRA I VIRGILI

Tarragona

2013

Fabrication and characterization of waveguides on $RbTiOPO_4$ crystals for photonic applications

Jaumet Cugat Mulet

Física i Cristal·lografia de Materials i Nanomaterials (FiCMA - FiCNA)

Departament de Química Física i Inorgànica

Universitat Rovira i Virgili

C/Marcel·lí Domingo, s/n

E-43007, Tarragona, Spain

UNIVERSITAT ROVIRA I VIRGILI

DEPARTAMENT DE QUÍMICA FÍSICA I INORGÀNICA

Campus Sescelades
Marcel·lí Domingo, s/n
43007 Tarragona
Tel. +34 977 55 81 37
Fax +34 977 55 95 63
www.quimica.urv.es

Prof. Dr. Magdalena Aguiló Díaz, Catedràtica de Cristal·lografia i Mineralogia, i Dr. Rosa Maria Solé Cartañà, Professora Titular de Física Aplicada del Departament de Química Física i Inorgànica de la Universitat Rovira i Virgili,

FAIG CONSTAR:

Que aquest treball, titulat "Fabrication and characterization of waveguides on $RbTiOPO_4$ crystals for photonic applications", que presenta Jaume Cugat Mulet per l'obtenció del títol de Doctor, ha estat realitzat sota la nostra direcció al Departament de Química Física i Inorgànica d'aquesta universitat.

Tarragona, 24 d'abril de 2013

Fabrication and characterization of waveguides on $RbTiOPO_4$ crystals for photonic applications

Jaume Cugat Mulet

Abstract

$RbTiOPO_4$ is a bifunctional nonlinear optical crystal. It can be doped with Yb^{3+} ions up to concentrations able to get laser emission around 1 μm, as well as to obtain Second Harmonic Generation. These characteristics make it interesting for photonic applications. In fact, this field of research is looking for a multifunctional material able to be the base for optical chips.

The aim of this doctoral thesis is to investigate the possibilities of (Yb,Nb):RTP/RTP (001) epitaxial layers as substrates for photonic applications. The thesis focuses on the fabrication of epitaxies, planar and channel waveguides, as well as the consequent characterization. Different methods have been used for channel waveguides fabrication, in order to investigate the versatility of (Yb,Nb):RTP/RTP (001) in front of the common used techniques in this field.

The manuscript is divided in four chapters. Chapter 1 describes an overview of the nonlinear optical crystals and the use of them for waveguide applications, as well as an introduction to the (Yb,Nb):$RbTiOPO_4$. Chapter 2 gives the relevant information about the experimental techniques used in this work. Chapter 3 describes the fabrication of epitaxies, planar and channel waveguides. Chapter 4 shows the results of characterization of the waveguides obtained. Finally, the conclusions are presented with the main results.

Keywords: Crystal growth, Yb^{3+} rare earth, Rubidium Titanyl Phosphate, Planar waveguides, Second Harmonic Generation, Waveguide laser, Channel waveguide, Rib waveguide.

UNIVERSITAT ROVIRA I VIRGILI
FABRICATION AND CHARACTERIZATION OF WAVEGUIDES ON RBTIOPO4 CRYSTALS FOR PHOTONIC APPLICATIONS
Jaume Cugat Mulet
Dipòsit Legal: T.1024-2013

Preface

The Ph.D investigation reported in this thesis was carried out at the group of *Física i Cristal·lografia de Materials i Nanomaterials (FiCMA-FiCNA)* at the *Department de Química Física i Inorgànica* of the *Universitat Rovira i Virgili, Tarragona, Spain* and was supervised by Dr. Rosa Maria Solé and Prof. Dr. Magdalena Aguiló.

Within the development of this thesis, we have collaborated actively with the following groups: *Optoelectronics Research Centre* (ORC) led by D.P. Shepherd, at the *University of Southampton,* UK; the *Instituto de Óptica* leaded by J. Solís, at the *Consejo Superior de Investigaciones Científicas*, Madrid, Spain, and *Departamento de Física de Materiales C-IV,* leaded by G. Lifante at the *Universidad Autónoma de Madrid,* Spain.

This work was partially financed by Ministerio de Educación, Cultura i Deporte, with MAT 2008-06729-C02-02, MAT 2011-29255-C02-02, TEC 2010-21574-C02-02 and the Fellowship to J. Cugat, BES-2009-024190 and by Generalitat de Catalunya: Universitat i Recerca under project 2009 SGR 235.

UNIVERSITAT ROVIRA I VIRGILI
FABRICATION AND CHARACTERIZATION OF WAVEGUIDES ON RBTIOPO4 CRYSTALS FOR PHOTONIC APPLICATIONS
Jaume Cugat Mulet
Dipòsit Legal: T.1024-2013

Acknowledgements

First, I would like to thank my advisors, Professor Magdalena Aguiló and Dra. Rosa Solé, as well as to the header of FiCMA group, Professor Francesc Díaz, for giving me the opportunity to perform my Ph.D. Thesis in this group. I also want to thank the other members of FiCMA group, for their collaboration during all the years of my stay in this group. I would like to thank Dr. Jaume Massons and Dra. Josefina Gavaldà. I would like to thank Dra. Cinta Pujol, Dr. Josep Joan Carvajal and Dr. Xavier Mateos, for their guidance and scientific discussions. I would like to thank members outside of FiCMA, Professor Ginés Lifante, for his help in many points of this thesis, as well as Professor Javier Solis and Alex Ruiz de la Cruz, for give me the opportunity to stay some days working with them in *Processing Laser Group* in Madrid. I also want to thank some members of *Optoelectronics Research Centre* in Southampton, Professor J.S. Wilkinson, Professor D.P. Shepherd and A. Choudhary. I like to thank the technicians of FiCMA group, they make possible the day to day work in the laboratory, Agustí Montero, Nicole Bakker and Laura Escorihuela. I would like to thank all of my colleagues Montserrat Galceran, Western Bolaños, Martha Segura, Venkatesan Jambunathan, Raj kumar, William Barrera, Muhammad Usman Qadri, Maria Mendez, Oleksandr Bilousov, Ali Butt, Carla Berrospe, Oleksandr Savchuk, Mina Moeini, Josué Mena y Marc Medina, they make me feel like at home. I would like to thank the technicians of *Unitat de Microscòpia* of SRCiT, for their friendly treatment, as well as the lessons in Clean Room, Lukas Vojkuvka, Rita Marimon, Núria Argany, Mariana Stefanova and Mercè Moncusí.

I would like to thank my whole family and friends from Campredó, as well as my new family from Amposta. Especially to Andrea, Dafne, Rosa, and of course to my parents, Joan Cugat and Maria Rosa Mulet for their unconditional support.

UNIVERSITAT ROVIRA I VIRGILI
FABRICATION AND CHARACTERIZATION OF WAVEGUIDES ON RBTIOPO4 CRYSTALS FOR PHOTONIC APPLICATIONS
Jaume Cugat Mulet
Dipòsit Legal: T.1024-2013

a Francisca, Rosa, Andrea i Dafne.

molt especialment als meus pares, Joan i Mari, pel seu suport incondicional i tot el que m'han ensenyat

List of publications

This doctoral thesis is partially based on the work contained in the following papers, referred by roman numerals in the text:

Paper I

J. Cugat, R.M. Solé, J.J. Carvajal, M. C. Pujol, X. Mateos, F. Díaz, M. Aguiló,
Crystal growth and characterization of $RbTi_{1-x-y}Yb_xOPO_4/RbTiOPO_4$ (001) non-linear optical layers
CrystlEngComm, **13**, 2015 (2011).

Paper II

J. Cugat, R. Solé, M.C. Pujol, J.J. Carvajal, X. Mateos, F. Díaz, M. Aguiló,
Waveguiding demonstration on $Yb:Nb:RbTiOPO_4/RbTiOPO_4$ (001) epitaxies grown by LPE
Optical Materials, **32**, 1648 (2010).

Paper III

J. Cugat, R.M. Solé, J.J. Carvajal, M. C. Pujol, X. Mateos, M. Aguiló, F. Díaz,
Green light waveguide demonstration on $Yb:Nb:RbTiOPO_4/RbTiOPO_4$ epitaxial layers
Physics Procedia, **8**, 136 (2010).

Paper IV

J. Cugat, R. Solé, J.J. Carvajal, X. Mateos, M.C. Pujol, J. Massons, F. Díaz, M. Aguiló,
Efficient Type II phase-matching second-harmonic generation in $Ba:Yb:Nb:RbTiOPO_4/RbTiOPO_4$ waveguides
Optics Letters, **36**(10), 1881 (2011).

Paper V

J. Cugat, R.M. Solé, M.C. Pujol, J.J. Carvajal, X. Mateos, F. Díaz, M. Aguiló,
Efficient second harmonic generation green light in RTP planar waveguide
Physics Status Solidi C, **8**(9), 2946 (2010).

Paper VI

J. Cugat , A. Ruiz de la Cruz, R. Solé , A. Ferrer, J.J. Carvajal, X. Mateos, J. Massons , J. Solís, G. Lifante, F. Díaz, M. Aguiló,
fs-laser microstructuring of ribs on active (Yb,Nb):RTP/RTP planar waveguides
Journal of Lightwave Technology, **31**(3), 385 (2013).

Paper VII

J. Cugat, A. Choudhary, R. Solé, J.J. Carvajal, J. Massons, D.P. Shepherd, F. Díaz, M. Aguiló,
Ar^+ ion milling rib waveguides on nonlinear optical (Yb,Nb):RTP/RTP epitaxial layers
Applied Materials & Interfaces, (to be submitted).

Paper VIII

A. Choudhary, J. Cugat, K. Pradeesh, R. Solé, F. Díaz, M. Aguiló, H.M.H. Chong, D.P. Shepherd,
Single-mode rib waveguides in $(Yb, Nb):RbTiOPO_4$ by reactive ion etching

Journal of Physics D: Applied Physics, **46**, 145108 (2013).

Paper IX

J. Cugat, R. Solé, J.J. Carvajal, X. Mateos, J. Massons, G. Lifante, F. Díaz, M. Aguiló,
Channel waveguides on $RbTiOPO_4$ by Cs^+ ion exchange
Optics Letters, **38**(3), 323 (2013).

Related publications

RP1
A. Choudhary, H.M.H. Chong, K. Pradeesh, G.S. Murungan, J.S. Wilkinson, D.P. Shepherd, J. Cugat, R. Solé, F. Díaz, M. Aguiló.
Waveguide lasers in (Yb,Nb):$RbTiOPO_4$
Proceedings of *ECIO 2012*, April **2012**, Sitges, Spain.

Table of Contents

Chapter 1

Introduction

1.1. Nonlinear optics

The nonlinear optical materials, among other applications, are used for frequency conversion of light by Second Harmonic Generation. For that, this nonlinear optical process will be overviewed in this section. Due to $RbTiOPO_4$ (RTP) is a nonlinear optical crystal, and it has been used as a base of the present work, an extended bibliographic study of nonlinear optical crystals, as well as, RTP is presented. In this section, the state of the research about self frequency doubling materials is also summarized. Finally, the research made in the field of doping crystals of the $KTiOPO_4$ family, which includes RTP, with laser active ions is explained.

If an electromagnetic wave passes through a dielectric material produces a polarization of the material, i.e., a distortion of the electron cloud around the atoms and molecules and consequently a displacement of the valence electrons from their stationary orbits. The polarization can be developed in terms of power series:

$$P = \varepsilon_0 \chi^{(1)} E + \varepsilon_0 (\chi^{(2)} E^2 + \chi^{(3)} E^3 + ...) = P^L + P^{NL} \qquad 1.1$$

where ε_0 is the permittivity of the vacuum, E is the electric field associated to the electromagnetic wave, and $\chi^{(2)}$ and $\chi^{(3)}$ are the second and third order nonlinear optical

susceptibilities and are tensors of third and fourth rank, respectively. P^L corresponds to the linear part of the polarization and P^{NL} to the nonlinear part.

In the ordinary reality, the strength of the electric field is relatively small, and the induced polarization is proportional to the electric field, thus the material response can be solely described by P^L. However, if the light is intense enough, like a high power laser, the relative displacement of the electron cloud from its nucleus is nonlinear with the electric field, and P^{NL} has to be taken into account [1].

According to the expression 1.1 the generated polarization for second order nonlinear processes is given by $P^{(2)} = \varepsilon_0 \chi^{(2)} E^2$, where $\chi^{(2)}$ is a 3x3x3 tensor [2]. However, due to intrinsic permutation symmetries, as well as Kleinman's symmetry, the $\chi^{(2)}$ tensor can be remplaced by a 3x6 matrix [2], called nonlinear *d* matrix, where $2d_{il}=\chi^{(2)}_{ijk}$. This simplifies further calculations and the polarization for second order processes, for instance in the case of SHG process is given by [2]:

$$\begin{pmatrix} P_x(2\omega) \\ P_y(2\omega) \\ P_z(2\omega) \end{pmatrix} = 2\varepsilon_o \begin{pmatrix} d_{11} & d_{12} & d_{13} & d_{14} & d_{15} & d_{16} \\ d_{21} & d_{22} & d_{23} & d_{24} & d_{25} & d_{26} \\ d_{31} & d_{32} & d_{33} & d_{34} & d_{35} & d_{36} \end{pmatrix} \begin{pmatrix} E_x(\omega)^2 \\ E_y(\omega)^2 \\ E_z(\omega)^2 \\ 2E_y(\omega)E_z(\omega) \\ 2E_x(\omega)E_z(\omega) \\ 2E_x(\omega)E_y(\omega) \end{pmatrix} \qquad 1.2$$

For most crystals, the *d* matrix can be simplified due to spatial symmetries of the material, resulting that some elements take the same values as other elements and others are zero. For example, in the KTP family of crystals, the d_{il} matrix is [1]:

$$d = \begin{pmatrix} 0 & 0 & 0 & 0 & d_{15} & 0 \\ 0 & 0 & 0 & d_{24} & 0 & 0 \\ d_{31} & d_{32} & d_{33} & 0 & 0 & 0 \end{pmatrix} \qquad 1.3$$

For understanding the interaction of the electromagnetic waves in a nonlinear optical material, a set of coupled wave equations should be derived. The natural beginnings are the Maxwell's equations and assuming that the interactions take place in a nonlinear optical, dielectric material, the following equation can be obtained [3]:

$$\nabla^2 \vec{E} = \mu_0 \varepsilon_0 \frac{\partial^2 \vec{E}}{\partial t^2} + \mu_0 \frac{\partial^2 \vec{P}^L}{\partial t^2} + \frac{\partial^2 \vec{P}^{NL}}{\partial t^2} \qquad 1.4$$

where μ_0 is the permeability of vacuum and ε_0 the permittivity of vacuum. This differential equation describes the relationship between the electric field in a nonlinear optical material and the polarization, which acts as a source of electromagnetic waves at new frequencies. We assume that the electric field consists of monochromatic fields and hence write:

$$\vec{E} = \frac{1}{2}\sum_m \left[\vec{A}'_m e^{-i\omega_m t} + c.c.\right] \qquad 1.5$$

where A_m is the amplitude of the mth field and ω_m the frequency of such a field. The complex conjugate, c.c., is added, to obtain real values for the electric field and the polarization.

Using the slowly varying envelope approximation (SVEA) [3], writing the field amplitudes as $A'(\vec{r}) = A(z)e^{ikz}$, and introducing 1.5 to equation 1.4, we reach to the next first-order differential equation:

$$2ik\ \frac{dA}{dz}e^{ikz} = -\omega^2 \mu_0 P^{(NL)} \qquad 1.6$$

where k is the wave vector.

By solving this first-order differential equation [3], and taking into account the Second Harmonic Generation process (see figure 1.1), where two identical photons from a single pump beam adds their frequency and leads to a single photon with twice the frequency ($\omega_1 = \omega_2 = \omega$ and $\omega_3 = 2\omega$), we obtain the expression of the amplitude of both fields:

$$\begin{aligned} \frac{dA_{2\omega}}{dz} &= i\frac{2\omega}{n_{2\omega}c} d_{eff} A_\omega^2 e^{-i\Delta kz} \\ \frac{dA_\omega}{dz} &= i\frac{\omega}{n_\omega c} d_{eff} A_{2\omega} A_\omega^* e^{-i\Delta kz} \end{aligned} \qquad 1.7$$

where $\Delta k = k_{2\omega} - 2k_\omega$, d_{eff} is the effective value of d and the material is assumed to be loss-less [3].

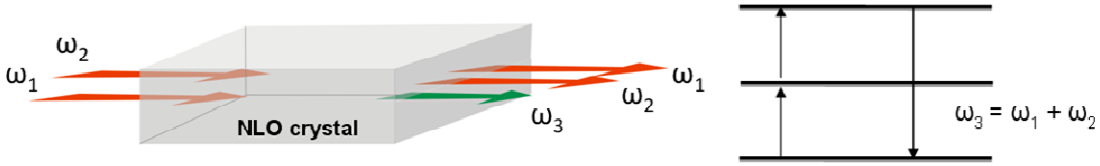

Figure 1.1. Scheme of the SHG process.

This set of equations can be solved analytically taking into account that the pump is not depleted, $E_\omega(x) \cong E_\omega(0)$. The intensities of both waves are:

$$I_\omega = \frac{1}{2}\varepsilon_0 c n_\omega E_\omega^2$$

$$I_{2\omega} = \frac{1}{2}\varepsilon_0 c n_{2\omega} E_{2\omega}^2 \qquad 1.8$$

By integrating the first equation of (1.7) over the crystal length L and taking into account (1.5) and (1.8), the intensity of the wave generated by the SHG process is obtained [3]:

$$I_{2\omega} = \frac{2\mu_0 \omega^2 d_{eff}^2 L^2 I_\omega^2}{n_\omega^2 n_{2\omega} c}\ sinc^2\left(\frac{\Delta kL}{2}\right) \qquad 1.9$$

Here d_{eff} can be obtained from the matrix 1.3, $\sin c(x) = \frac{\sin(x)}{x}$, I_ω is the pump intensity at the frequency ω, n_ω and $n_{2\omega}$ are the refractive indices for pumping and the second harmonic signals, respectively. From this equation, we can see that the intensity of the second harmonic generation decrease if the process is not phasematched, that is to say, $\Delta k \neq 0$. However , if $\Delta k = 0$ the intensity increase as a function of the crystal length squared and the nonlinear coefficient squared.

1.2. Nonlinear optical crystals

Since the development of the laser, a drawback of most laser materials has been the limited ability to generate radiation in a wide spectral region. For some purposes, an energetic beam at a wavelength where no laser material operates would be needed.

Although there are appropriate laser sources for other applications, however, the emitted power is restricted by the thermal properties of the laser crystal. A solution to both problems is given by nonlinear optics. Nonlinear optical crystals can, therefore, be employed for the generation of beams at wavelength not available with conventional laser materials and also to obtain high power radiation for some wavelengths where is difficult to obtain by other means [4].

Nonlinear optical crystals have several applications in nonlinear optical devices: sum frequency generation (SFG), difference frequency generation (DFG), optical rectification (OR), or optical parametric oscillation (OPO). Finally, as has been mentioned above, the most important process in terms of the scope of this thesis is the Second Harmonic Generation (SHG), that is a particular case of SFG. For instance a huge number of inorganic crystals have been used to achieve SHG of Nd^{3+} solid state lasers around 1 μm, such as KH_2PO_4 (KDP) [5], $NH_4H_2PO_4$ (ADP) [6], CsH_2AsO_4 (CDA) [7], β-BaB_2O_4 (BBO) [8], LiB_3O_5 (LBO) [9], $KTiOPO_4$ (KTP)[10], $KNbO_3$ [11] and $LiIO_3$ [12].

Among all of these inorganic crystals, $KTiOPO_4$ (KTP) possess very large nonlinearity [13], and large angular and temperature bandwidths for SHG at a wavelength of 1.06 μm, which makes it of special interest. Trough the time, KTP has been established as a unique inorganic material because its exceptional properties for several nonlinear optical applications [14,15]. Particularly KTP has been used as a frequency doubler of lasers emitting in the IR spectral range [16,17], but this application can be extended as well to RTP.

1.3. Self-frequency doubling crystals

Many nonlinear optical crystals can be used for Self Frequency Doubling (SFD) near to 1 μm. The SFD process is produced in a nonlinear optical material able to be a host of active ions and therefore emission and frequency doubling can be made in the same crystal. For instance, the infrared laser emission of Yb^{3+} and Nd^{3+} as active ions can be converted in visible light by using the second harmonic generation properties of the host.

Initially, Nd^{3+} was the lanthanide active ion most used for self-frequency doubling lasers operating at 1 μm and producing green light. But nowadays there is an increasing interest in replacing Nd^{3+} by Yb^{3+}. Doping of crystals with Yb^{3+} as active ion has some

advantages like no exited state absorption, no concentration quenching and no up-conversion, all of them due to its simple level scheme which is constituted by the ground level ($^2F_{7/2}$) and the excited one ($^2F_{5/2}$).

In 1969 the first SFD laser was obtained, it was a pulsed $LiNbO_3$:Tm laser [18]. In the continuous regime, the first SFD laser was discovered in 1986 and it was based on Nd:MgO:$LiNbO_3$ [19]. From that moment, Nd:MgO:$LiNbO_3$ has been widely used for SFD [20-22] among other crystals such as Nd:$GdCaO(BO_3)_3$ [23-26] and Nd:$YCa_4O(BO_3)_3$ [27,28] , using Nd^{3+} as active ion. Taking Yb^{3+} as active element, some SFD laser materials used until now are Yb:MgO:$LiNbO_3$ [29], Yb:$Ca_4GdO(BO_3)_3$ [30,31] and Yb:$YAl_3(BO_3)_4$ [32-36]. All the above references correspond to Birefringent Phase Matching process, of great interest for the present study.

CW laser operation in Yb^{3+} doped Yb:$GdAl_3(BO_3)_4$ [37], Yb:$KGd(PO_3)_4$ [38] and (Yb,Nb):RTP [39] have been recently achieved and these material are candidates for self-frequency conversion lasers.

Rare earth-doped waveguides have already been used for SFD lasers. In fact, a SFD waveguide laser was first fabricated and demonstrated using a Ti:Er:$LiNbO_3$ waveguide [40]. In the same year, a similar demonstration was made using a Nd:$LiNbO_3$ waveguide [41].

1.4. RE^{3+} doped crystals of the $KTiOPO_4$ family

Due to the above mentioned properties of the crystals of the KTP family, KTP and its isostructural crystals have been used for several nonlinear optical applications [42]. Great efforts have been made to dope KTP with RE^{3+} (or Ln^{3+}) ions to obtain a SFD laser in the visible spectral range. In the literature several techniques for crystal growth of Ln-doped KTP are shown. One of them, which is used in this work is the Top Seeded Solution Growth – Slow Cooling technique (TSSG-SC) [43-45]. The incorporation of Ln^{3+} ions into the KTP lattice using this technique has limitations. The concentrations of RE^{3+} in KTP crystals obtained by the TSSG-SC technique were as low as $5x10^{17}$ – $6x10^{18}$ ions/cm^3 [46-48], and are far from the threshold needed to obtain efficient fluorescence. The Ln^{3+} distribution coefficient in RTP is generally higher than in KTP but not enough high to obtain efficient fluorescence. This can be solved by codoping RTP with Ln^{3+} and Nb^{5+} [46].

Other techniques have been used to introduce RE^{3+} ions into KTP such as, electron beam evaporation [47], ion implantation [48] and pulsed laser deposition [49].

Recently, in FICMA's laboratory, great results have been achieved in the enhancement of RE^{3+} concentration in $RbTi_{1-x}Nb_xOPO_4$ single crystals grown by the TSSG-SC technique. Concentrations up to ~ $2x10^{20}$ and $0.65x10^{20}$ ions/cm^3 were achieved for Yb^{3+} and Er^{3+} doping, respectively [50,51]. Finally, X. Mateos et al. have obtained laser emission at 1064 nm using a Yb:Nb:RTP crystal [39].

1.5. Integrated Optics (IO's)

The term "integrated photonics" refers to the fabrication and integration of several photonic components on a common planar substrate. These components include beam splitters, gratings, couplers, polarisers, interferometers, sources and detectors, among others.

The science that studies the light is called optics. It describes and studies the generation, as well as, the propagation of the light and its interaction with the matter. Optics is an old science, but in the last century it has suffered a spectacular renaissance. The first and more important development in modern optics, without any doubt, was the invention of the laser by T.H. Maiman in 1960 [52]. The development of semiconductor optical devices and the introduction of new fabrication techniques for obtaining optical fibbers with very low propagation losses have been important. As a result of these new developments and associated with other technologies, such as electronics, new disciplines such as electro-optics, opto-electronics, etc. have been generated.

Due to the combination of electronics and optics, new devices, more complex than lasers, semiconductor detectors, light modulators, etc have appeared. Then a new scientific discipline has arise to explain these new devices, which are not completely described for optics neither electronics. This scientific branch of applied physics is called *photonics*. If electronics can be considered as the discipline that describes the flow of electrons, the term of photonics deals with the control of photons.

We can consider integrated photonics to be constituted by the combining of waveguide technology (guided optics) with other disciplines, such as acustooptics, electrooptics or nonlinear optics among others, which is of great importance in this thesis.

In integrated photonics, the basic optical elements for generation, focusing, splitting, junction, etc. of light should be integrated in a single *optical chip*. Thus, the main goal purposed by integrated photonics is therefore the miniaturization of optical systems. This is possible thanks to the small wavelength of the light, which permits the fabrication of circuits and compact photonic devices with sizes of the order of microns.

1.5.1. Optical Dielectric waveguides

As has been mentioned above, the basic element in integrated photonics technology is the optical waveguide. Optical waveguides are structures that confine and guide optical waves by total internal reflection at interfaces between dielectric materials. They are classified into planar waveguides and channel waveguides. In the channel waveguides, the light is confined in two dimensions, while in planar waveguides, the light confinement takes place in only one dimension. Figure 1.2 shows a scheme of a planar waveguide (Figure 1.2.a) and a channel waveguide (Figure 1.2.b).

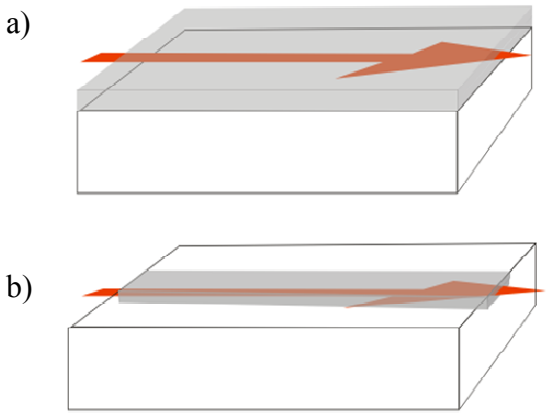

Figure 1.2. Schematic illustration of optical waveguides. a) Planar waveguide and b) channel waveguide

The main requirement for obtaining guided light inside a waveguide is that the refractive index of the thin film must be larger than the refractive indices of the substrate and cladding (see Figure 1.3).

As an example, in a hypothetical planar film of glass with refractive index n, surrounded by air, the rays inside the film that propagates with an internal angle θ grater than the critical angle $\theta_c = \sin^{-1}(1/n)$ will suffer total reflection at the interfaces, and will remain trapped inside the film, that is to say, the film surrounded by air acts as an optical waveguide.

Taking into account the refractive index distribution, the waveguides can be classified in *step-index waveguides* and *graded index waveguides*.

The step-index waveguides, either planar or channel waveguides, are formed by a region of material with uniform refractive index, which is higher than the refractive indices of the substrate and the cladding. On the other hand, in graded index waveguides the refractive index is depth dependent. Obviously, the region where the light is travelling, that is to say, the waveguide part, has higher refractive index than the substrate and the cladding (usually air). Figure 1.3 shows schemes of these two kinds of waveguides with their refractive index profiles.

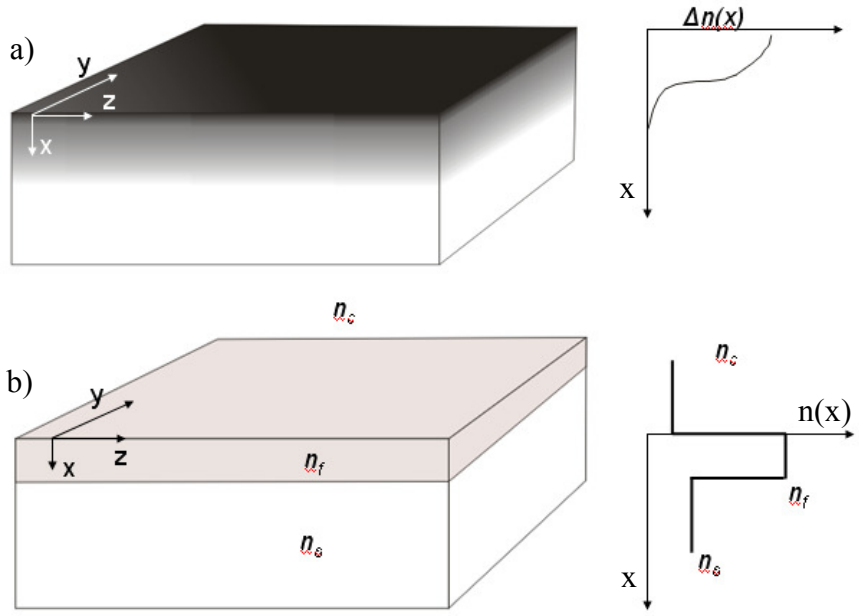

Figure 1.3. Scheme of refractive index distribution for the two main kinds of waveguides. a) Graded index waveguide and b) step-index waveguide.

There are many techniques for the fabrication of planar and channel waveguides. These techniques can be also ordered taking into account the kind of waveguide fabricated: step index waveguides or graded index waveguides. So, the main known techniques used to produce planar waveguides in step index regime are Liquid Phase Epitaxy (LPE) [53], Pulsed Laser Deposition (PLD) [54], sputtering or deposition [55] and Molecular Beam Epitaxy (MBE) [56]. On the other hand, the techniques used to fabricate graded index waveguides are suitable for PWGs fabrication, as well as channel waveguides. These techniques are proton-exchange [57], ion-exchange [58], metal-diffusion [59] and ion-implantation [60].

There is another important structure for integrated photonics: the rib waveguides. In fact, rib waveguides consists of a stripe not completely etched on a surface which is a PWG, as is shown in Figure 1.4

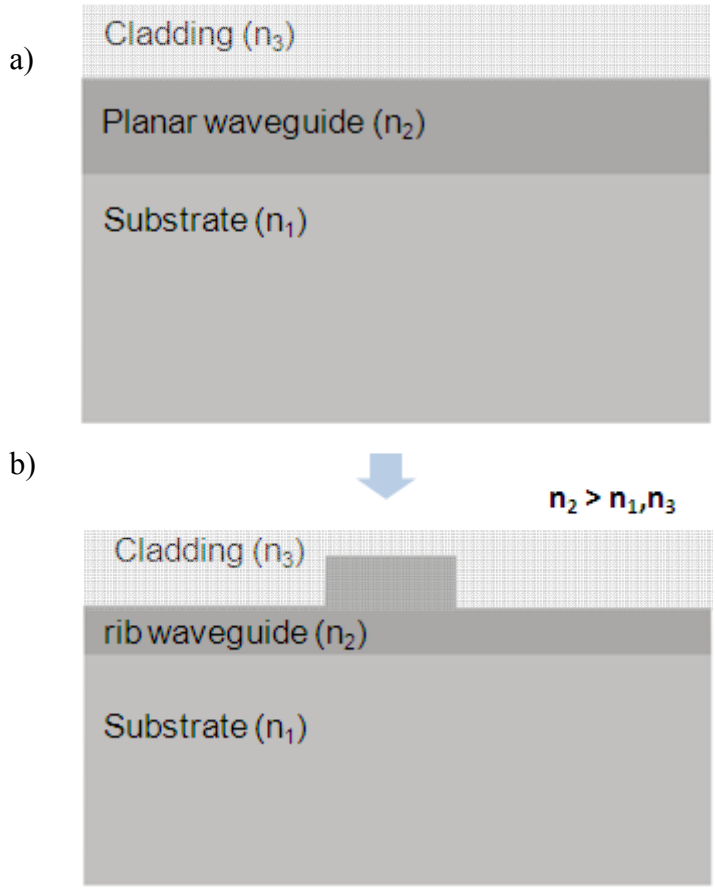

Figure 1.4. Scheme of a) planar waveguide and b) rib waveguide.

The rib structure confines the light in two dimensions like a channel waveguide, but has the advantage that can be obtained easily from a PWG fabricated previously.

The principal surface structuring techniques to produce rib waveguides are: Reactive Ion Etching (RIE) [61], ion milling [62] and laser ablation [63].

1.5.2. Waveguide lasers

Among the active components for optical chips, such as optical amplifiers, laser oscillators and frequency converters, one of the most important is the waveguide laser. Up to now the most common procedure to obtain laser action from a waveguide is to use active impurities such as rare earths embedded in the waveguide structure. This procedure has been used in this work. The first demonstration in this field was a planar waveguide laser and was reported in 1961 [64].

Waveguide lasers have several advantages in front of bulk lasers [65]. The main of them is that they have lower thresholds and there is the possibility of combining the waveguide laser as a photon source and other devices obtaining integrated photonic chips.

1.5.3. Nonlinear optical materials for SHG waveguides

In the late eighties and in the nineties, there was a strong need for implementation of waveguides in optoelectronics. In fact, compact short-wavelength coherent light sources were needed for developing high-density optical disk memory systems. As blue diode lasers were not available, then, waveguides SHG devices combined with near-infrared semiconductor lasers were considered as the best approach. Therefore, waveguides SHG devices with phase matching by periodic structures, for instance quasi-phase matching (QPM), were extensively studied. Thus, nonlinear optical waveguides have gained a lot of interest from the earliest research in integrated optics. The first experiment was demonstrated in 1970, and consisted in a ZnS thin-film waveguide on a ZnO substrate, used to produce SHG of a pulsed Nd:YAG laser light with Cerenkov-radiation type phase matching. Then, a lot of materials were proved for SHG using several phase matching schemes. Materials, such as amorphous thin films [66], ferroelectric crystals [67], III-V semiconductors [68], organic crystals [69], and poled polymers [70] were used for SHG radiation.

Most of the research related with nonlinear optical waveguides has been made on inorganic ferroelectric crystals such as $LiNbO_3$, and $LiTaO_3$. Other ferroelectric crystals, not so much extensively studied, are $KTiOPO_4$ and $KNbO_3$. Table 1.1 shows the main ferroelectric crystals studied for SHG waveguides. Details of the fabrication technique, waveguide type and phase matching process are summarized in the table.

RTP is demonstrated to be a nonlinear optical material suitable for SHG waveguides for the first time to our knowledge.

Table 1.1. Ferroelectric crystals studied for SHG waveguides.

waveguide	Waveguide fabrication	Waveguide type	Phase matching	Pumping wavelength (nm)	references
$LiNbO_3$	Ti-diffusion	channel	Temperature tuning	1060	[71]
	Ti-diffusion	planar	Mode dispersion	1080	[72]
	ptoton-exchange	planar	Mode dispersion	-	[73]
	proton-exchange	channel	Cerenkov	840	[74,75]
	Ti-diffusion	planar	QPM	several	[76-82]
$MgO:LiNbO_3$	Ti-diffusion	Planar	Mode dispersion	-	[83]
$Mg:LiNbO_3$	Proton-exchange	planar	Cerenkov	1060	[84]
$LiTaO_3$	Annealed proton-exchange	several	QPM	~ 800	[85-90]
$KNbO_3$	He-implantation	planar	Birefringence	868	[91]
	Ion-implantation	channel	Cerenkov	~ 800	[92]
$KTiOPO_4$	Rb-exchange	Segmented	balanced	1060	[93]
	Ion-exchange	planar	birrefringence	~ 800-1100	[94]
	Rb,Ba-exchange	segmented	balanced	760-960	[95]
	He-implantation	planar	birefringence	1070	[96]
	Ion-exchange	channel	Periodic grating	~ 800	[97]
$Sc:KTiOPO_4$	Ion-exchange	segmented	balanced	-	[98]

1.6. (Yb, Nb):$RbTiOPO_4$ / $RbTiOPO_4$ (001) waveguides as a promising material for IO's

Active materials such as ferroelectric materials can be used to produce modulators and switches based on the classic electro-optic effect.

The integration of passive and active optical devices, in a multicomponent circuit is known as an *integrated optic circuit* (IOC).

Integrated optic devices interface efficiently with optical fibres, and can reduce the cost in complex circuits by eliminating the need for separate, individual packaging of each circuit element. They also offer smaller size and weight, lower power consumption, improved reliability, and often larger electrical modulation bandwidth compared to their bulk-optic counterparts.

In this work we present (Yb, Nb):RTP/RTP (001) as a promising material for integrated photonics applications, as well as a platform for IOC. It is clear that an ideal material for IOC must be as multifunctional as possible.

As it has been mentioned previously, $RbTiOPO_4$ is a nonlinear optical crystal that can be used for frequency doubling of the radiation emitted by Nd and Yb lasers, which is close to 1 μm [99]. This crystal is specially useful for non-critical type II Second harmonic generation (SHG) for fundamental radiation near to 1 μm. Moreover, RTP can be doped with active ions with the possibility to obtain a self-frequency doubling (SFD) material, which would be useful for compact and efficient laser sources in the visible range. Its large linear electro-optical coefficients and low dielectric constants give chances for various electro-optical applications, such as modulators and *Q* switches [58].

In addition, recently electric-field poling of RTP at room temperature was demonstrated [100]. Initial studies indicate that the effective nonlinearity in periodic poling of RTP crystals (PPRTP) is comparable to that of periodic poling of KTP (PPKTP) crystals. Moreover, flux-grown RTP crystals present a much lower ionic conductivity than flux-grown KTP crystals, which contributes to do the RTP electric-field poling and monitoring procedures easier and more predictable than in KTP crystals.

It is well known that $LiNbO_3$ is a promising material for integrated photonics due to its excellent properties [101], but it has a disadvantage in front of KTP, its higher damage threshold [102]. RTP could be an interesting alternative for phase-matched interactions, because its damage threshold is ~ 2 times larger than the one of KTP [103,104], while it has similar nonlinear optical coefficients [105].

KTP could be a possible candidate to host RE^{3+} active ions arising as a promising self-frequency doubling (SFD) material. But, unfortunately the RE^{3+} distribution coefficients obtained were very low (typically about 10^{-3}) [45]. RTP has higher Yb^{3+} distribution coefficient than KTP but it is still too low for laser operation. On the other hand, the co-doping of RTP with Yb^{3+} and Nb^{5+} increase the concentration of Yb^{3+} in the crystal enough to obtain laser radiation [39]. Recently, laser operation has been demonstrated in a (Yb, Nb):RTP bulk crystal [39].

The Yb^{3+} has a clear absorption band between 800 and 1000 nm which is associated to the $^2F_{7/2} \rightarrow {}^2F_{5/2}$ transition. The absorption is characterized by three main peaks centred at 902, 955 and 972 nm for the three polarizations [106]. Otherwise, the corresponding emission spectra at low temperature, which extends from 955 to 1095 nm, show four

main lines, corresponding to transitions from the lowest excited sublevel $^2F_{5/2}$ (0') to the four ground state sublevels $^2F_{5/2}$ (3) $^2F_{5/2}$(2) $^2F_{5/2}$(1) and $^2F_{5/2}$(0) [107].

If we take into account the possibility of doping RTP with Yb^{3+}, which is a laser active ion, as well as, the fact that RTP could double the Yb^{3+} laser emission, and also the other characteristics mentioned above, RTP becomes a very interesting and promising material for integrated photonics applications. In fact, for all of this is interesting to check the possibilities of (Yb, Nb):RTP to fabricate waveguides. The epitaxial layers that we propose in this work, are grown in ***a* – *b*** plane, or in (001) plane (perpendicular to ***c*** crystallographic direction). This is due to the birefringence characteristics of the RTP crystals. In fact, the (001) plane contains the non-critical phase matching (PM) type II SHG directions for the range of 985 to 1118 nm, and the Yb^{3+} laser emission at 1064 nm is in this range.

1.7. Doctoral thesis aims

As it has been mentioned in the above section, (Yb, Nb):RTP is a potential material for IO's. So, the objective of this thesis can be decomposed in smaller objectives:

► Investigate the best growth conditions and composition, for the fabrication of epitaxial layers of (Yb,Nb):RTP/RTP (001), (Ba,Yb,Nb):RTP/RTP (001), (Yb,Nb):RTP/K:RTP (001) and (Ba,Yb,Nb):RTP/K:RTP (001) by LPE with good optical quality.

► Investigate the best conditions (mainly composition) in order to obtain high refractive index contrast between the substrate and the epitaxial layer, suitable for fabricating planar waveguides.

► Fabrication of rib waveguides on the planar ones obtained previously by femtosecond laser ablation, Ar^+ ion milling and reactive ion etching techniques.

► Fabrication of planar and channel waveguides by Cs^+ diffusion.

► Demonstration of type II SHG inside the planar and channel waveguides obtained.

In fact, taking into account all of the above smaller objectives, a complete objective arise: study and investigation of RTP as a multifunctional material for integrated photonics

The structure of this manuscript is the following: in chapter 1 there is an introduction with a bibliographical study of the previous research related to the materials used in this PhD thesis. The experimental techniques used in this work are described in chapter 2. The techniques used to grow the crystals and films, Top Seeded Solution Growth and Liquid Phase Epitaxy respectively, are detailed. Microstructuring techniques of the planar waveguides are also explained, since they are an important part of the work. In the same chapter 2, a set of techniques for characterizing the samples are explained, such as microscopy techniques, X-Ray diffraction, Electron Probe Micro Analysis, etc. Finally, there is an explanation of the set up used to prove experimentally that the waveguides obtained successfully work. Finally, the method used to determine the optical losses in the waveguides is also explained.

The main chapter of this thesis is the third one (chapter 3), which corresponds to the waveguide fabrication chapter. Mostly, it explains the results of (Yb, Nb):RTP films grown over RTP substrates, the rib fabrication over the planar waveguides obtained, as well as, the channel waveguides obtained by Cs^+ ion exchange on RTP substrate.

After that, chapter 4 is related to the characterization of the waveguides obtained. In this chapter, the propagation modes in the waveguides, the SHG process, some laser results etc. of the planar and channel waveguides are studied.

Finally, the conclusions give an overview of the main results obtained and the accomplishment of the objectives described above.

Chapter 2

Experimental Techniques

2.1. Crystal growth and processing of materials

This work studies doped RTP waveguides grown on RTP substrates. RTP melts incongruently below its melting point at a temperature of 1343 K [108]. Consequently, we grow these crystals from high temperature solutions (HTS), using self-flux and WO_3 solutions. The technique we used to obtain single crystals is top seeded solution growth (TSSG) and epitaxial films of doped RTP on substrates of the same family are also grown from HTS. Finally, the same solutions are also used to obtain small crystals by spontaneous nucleation on a Pt wire. In fact, these small crystals are analyzed using electron probe microanalysis to determine the dopant concentration. The powder obtained from these crystals is also used for X-ray diffraction to calculate the unit cell parameters of the crystals.

2.1.1. Top seeded solution growth

In this study, single crystals are grown from high temperature solutions using the top seeded solution growth-slow cooling (TSSG-SC) technique [109].

The set up used in this work for RTP single-crystal growth is basically a vertical tubular furnace connected to a temperature control unit consisting of a temperature controller and a thyristor (see figure 2.1). The axial thermal gradient of the furnace and solution was determined before the crystal growth began so that the crucible with the solution could be placed inside the furnace in a position with a suitable thermal gradient. So, the solution surface should be colder than the bottom of the solution. This can be ensured and the suitable thermal gradient obtained by adjusting the position of the crucible in the right thermal zone of the furnace.

The experimental procedure followed in this work for bulk single-crystal growth by TSSG is the consequence of previous work carried out by the Physics and Crystallography of Materials and Nanomaterials laboratory, FiCMA-FiCNA, in Tarragona [106,107].

The first step in bulk single-crystal growth is to prepare and homogenize the solution. Then, the saturation temperature of the solution is determined. At the beginning of this process a sharp seed is slowly introduced into the furnace and the temperature of the solution is maintained slightly above the expected T_s. The seed must be maintained above the solution surface for at least 1 h to obtain a seed temperature close to that of the solution surface. Then it is placed in contact with the surface of the solution. The growth or dissolution rates of the seed are measured at several temperatures close to saturation (T_s) to determine the T_s at which neither growth nor dissolution of the seed is observed. With the growth equipment used, these measurements are made at an accuracy of up to 10 μm with a micrometer fixed to the mechanical structure of the furnace that allows the rod to travel vertically and which supports the crystal seed (see figure 2.1).

Once the saturation temperature has been determined, the seed is pulled for a few μm without losing contact with the solution surface. The seed is pulled to minimize the probability of defects at the beginning of crystal growth. Then, the supersaturation of the solution, which is the driving force behind the crystal growth, is induced by slowly decreasing the temperature of the solution. In our case, typical cooling rates of 0.1 K/h up to 5 K below T_s, and 0.05 K/h up to 30 K below T_s are applied. The first rate is applied not only to prevent contact being lost between the seed and the solution but also to create a faster supersaturation in the first stage of the crystal growth. The second rate

is slower to prevent fast crystal growth and consequently an increase in the probability that inclusions will form in the crystals.

The final part is the extraction process, which begins when the cooling ramp has finished, and the crystal has the desired size. The crystal is slowly pulled from the solution at a rate of 1 mm every 5 minutes until it is no longer in contact with the solution. After this, a typical cooling ramp of 25 K/h is applied until room temperature.

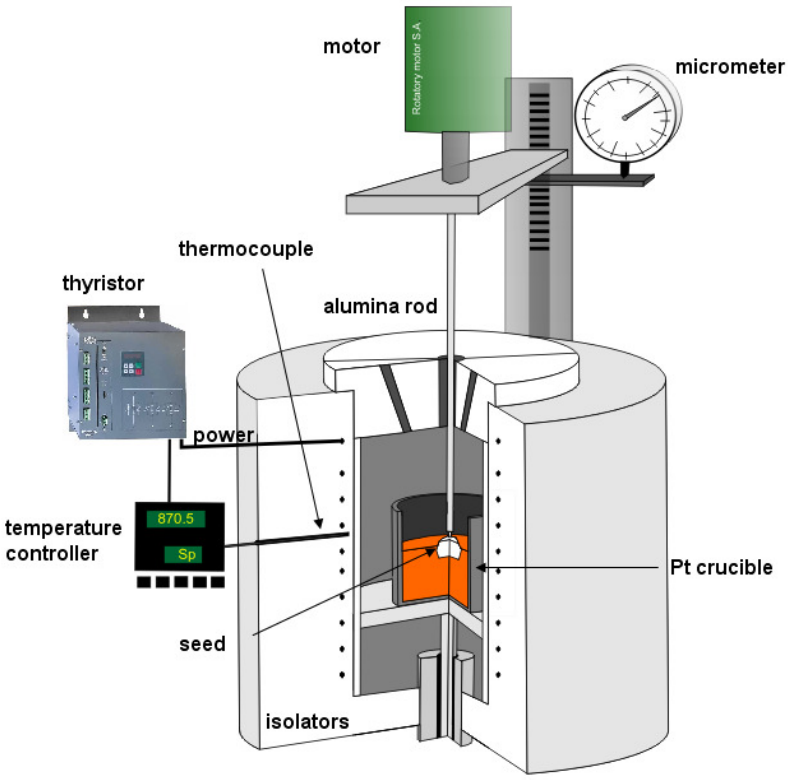

Figure 2.1. Schematic view of the set up furnace used for RTP crystal growth

2.1.2. Liquid phase epitaxy

An epitaxial layer is a crystalline film grown on a substrate. There are three principal methods for obtaining epitaxial layers on substrates: vapor phase epitaxy (VPE), solid phase epitaxy (SPE) and liquid phase epitaxy (LPE), which is the technique used here. The LPE method consists of growing an epitaxy from a liquid phase on a polished substrate or a natural face. The film usually has the same crystalline properties as the substrate, except in those cases in which the grown film and the substrate are from different crystalline families but, in this case, the substrate/layer mismatch is usually large enough and the probability that defects will appear at the interface is higher.

The epitaxy growth procedure by LPE is similar to crystal growth by TSSG. But for growth to be homogeneous throughout the dipped substrate, a practically zero thermal gradient is needed. So, the furnace used for LPE has better isolation than the one used in TSSG experiments. The saturation temperature, and the growth and dissolution rate at temperatures slightly below and above the saturation temperature must be determined. Then a polished substrate is slowly introduced into the furnace, to prevent cracks due to thermal stress. This substrate is dipped several mm into the solution and maintained at 1 K above the T_s for 5 minutes so that the external part of the surface dissolves slightly.

The epitaxial growth starts by supersaturating the solution. Taking into account the growth rates at T slightly below the T_s measured previously, this supersaturation is generated inside the solution by decreasing the temperature a few degrees (from 2 to 7 K) below the T_s. The growth time usually ranges from 1 to 6 hours.

Before the substrate is introduced into the furnace, it is cleaned carefully. The cleaning process consists of dipping and rotating the substrate in three different liquids for five minutes: the first one is a solution of HNO_3/H_2O with ½ ratio in volume, followed by distilled water and, finally, ethanol.

2.1.3. Sample cutting and polishing

Once the single crystals have been obtained, they must be cut into plates so that they can be used as substrates. The top of the crystals is not flat and polished. In fact, the stairs of growth are present and inclusions and defects are usually at the interface between seed and crystal. So, before cutting, the crystal must be fixed to a sample holder with wax so that the top can be polished. This is done using by a Logitech PM5 polishing machine. First, the top of the crystal is lapped with alumina powder of 9 μm, and then polished smooth with 1 μm alumina powder.

Once the tops of the crystals, which are perpendicular to the seed, have been planed and polished, they are cut into plates perpendicular to the ***c*** crystallographic direction using a Minitom Struers diamond disk saw. The disk is 0.12 mm thick.

The last step is to polish the plates to obtain substrates suitable for epitaxial growth. They are polished down to a high optical quality, and the rms of the surface is below 50 nm. The polishing process is done first with alumina powders of 9 μm, 3 μm, 1 μm and 0.3 μm in diameter and finally with a polishing suspension SF1 from the Logitech company.

Before the planar waveguides (PWGs) of (Yb,Nb):RTP obtained by LPE are optically characterised, the epitaxial layer that has grown on one of the substrate faces is removed and the epitaxial layer on the other face is carefully polished down to the suitable thickness. In all cases the PWGs are rectangles with sides parallel to the ***a*** and ***b*** crystallographic directions.

After both end-faces of interest have been identified, they are carefully polished to laser quality by sandwiching the sample between two flint glass blocks at the substrate and epitaxial layer sides in order to minimize the edge bend effect. Taking into account the hardness of KTP (~ 5 Mohs), flint glass was used for end-face polishing because it is as hard as KTP (~ 5.5 Mohs).

2.1.4. Microstructuring of epitaxial layers and substrates

The (Yb,Nb):RTP planar waveguides obtained are microstructured by three different techniques: fs-laser ablation, Ar^+ ion milling and reactive ion etching. A fourth technique called Cs^+ ion-exchange was used for microstructuring the RTP substrates.

2.1.4.1. *fs-laser ablation*

The first technique used to fabricate rib waveguides on the (Yb,Nb):RTP planar waveguides used here is fs-laser ablation. The fabrication was done in collaboration with the Instituto de Óptica in the Centro Superior de Investigaciones Científicas (Madrid), with Dr. A. Ruiz de la Cruz and Prof. J. Solis.

The set up that we use to fabricate the channels is shown in figure 2.2. We use a pulsed fs-laser amplification system (Tsunami and Spitfire from Spectra-Physics), working at a repetition rate 1KHz and a pulse duration of $\tau_p \approx 120\,fs$. The output pulse energy is E = 1 mJ and the central wavelength λ = 799 nm. We also use a spatial light modulator (SLM, Hamamatsu X8267) to control the beam wavefront before focusing on the surface of the sample. This allows us to design the intensity profile of the focused beam. An image relaying system with magnification M=0.4 (f1=50 cm and f2=20 cm) transfers the beam at the SLM surface to the back-focal position of the focusing microscope objective (Mitutoyo M Plan Apo NIR 20X NA=0.4). The sample is placed on a 3-axis motorized stage, which moves at a speed of v=100 μm/s.

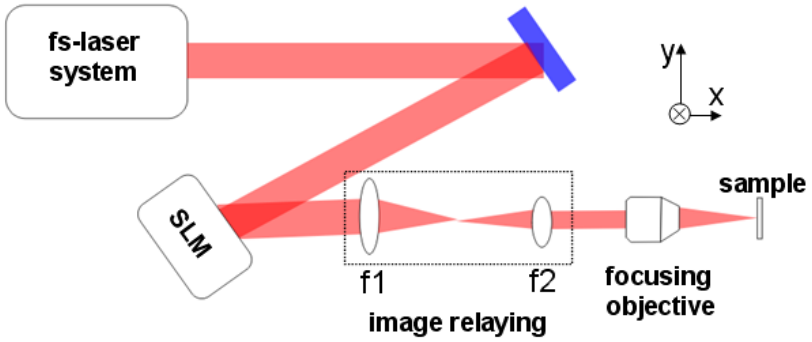

Figure 2.2. Scheme of fs-laser ablation

To improve the quality of the micromachined channels, we use the approximation scanning method [110]. It consists of performing several irradiation scans, each one slightly displaced from the previous one in the direction perpendicular to the channels. This produces steeper channel walls than when a single irradiation scan is used. It also helps to minimize the redeposition of debris in the walls of the channel and reduce the surface roughness.

Our approach uses an SLM to multiplex the irradiation beam at the material surface, creating seven spots. The spots are arranged diagonally, such that each spot rewrites the channel written by the previous one, but with a slight lateral displacement just us the approximation scanning does. Thus, a multiplexed beam requires only a single scan to inscribe a channel in the sample, whereas a non-multiplexed beam requires several scans. In order to multiplex the beam, the wavefront of the irradiation beam is modified by the SLM, so that at the focal point on the surface of the sample we obtain a predesigned intensity distribution. For this purpose, a phasemap must be created. This is done using a weighted Gerchberg-Saxton algorithm, which helps to equalize the peak intensities of the multiplexed spots in the designed intensity distribution [110].

2.1.4.2. *Ar^+ ion milling technique*

The second technique used to fabricate surface rib waveguides on (Yb,Nb):RTP planar waveguides is Ar^+ ion milling. The ribs are transferred to the (Yb,Nb):RTP planar waveguides by standard photolithography and Ar^+ ion milling. The fabrication is performed in the clean room at the Optoelectronics Research Centre in the University of Southampton in collaboration with the PhD. student A. Choudhary, Prof. J.S. Wilkinson and Prof. D.P. Shepherd.

The procedure used to structure the surface planar waveguides has several steps: a) inclusion of the sample in resin to prevent the edge bead effect during the deposition of the photoresist (PR), b) deposition of the PR in two stages by spin coating, c) mask pattern transfer to the PR by standard UV photolithography and finally d) rib pattern transfer from the PR to the sample by Ar^+ ion milling.

a) During the spin coating process the film thickness at the edges of the substrates increases considerably. The difference in coating thickness between the edge and the center of the substrate is known as the edge bead effect. In our case this effect was due to the relatively small area of the planar waveguides (~ 7 x 10 mm^2). We overcome this effect by surrounding the surface of the sample with a transparent resin. A commercial Unipond Power Epoxy resin of two components is used. This resin was chosen because it is heat resistant up to 150 K, which is necessary for the soft and hard bakes after the spin coating process. At the beginning of the procedure the two components of the resin are mixed on a glass slide (slide 1), which also serves as a sample holder for the spin coating process. The planar waveguide is stuck with tape on a second glass slide (slide 2) and then the sample is sandwiched by the set (slide 1 + resin + sample + tape + slide 2). In order to ensure that the resin around the substrate is flat, additional pressure is applied by placing an iron block on top of the sandwich. After 6 hours, the resin is completely cured and (slide 2 + tape) can be removed leaving the substrate stuck to slide 1 and surrounded by the resin.

b) A Rohm & Haas S1828 photoresist is deposited over the sample by spin coating. This process is performed in two stages in order to obtain ~ 8 μm of resist thickness. Figures 2.3 and 2.4 show the steps of both stages. Once the first PR layer has been deposited, the sample is softbaked at 363 K for 30 minutes. After the softbake, the second stage is carried out. Then, a second softbake is performed at 363 K for 50 minutes.

c) In this step the sample is carefully aligned with the channels of the dark field mask. This is done by taking into account the direction along which the channels would be made. The dark field mask that we use had channels with widths ranging from 1 μm to *10* μm, at an interval of 0.2 μm and with 100 μm spacing between each waveguide.

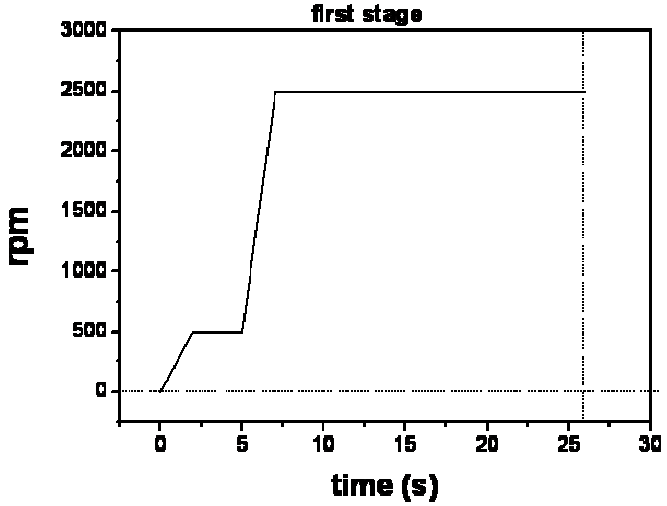

Figure 2.3. First stage of the spin coating process

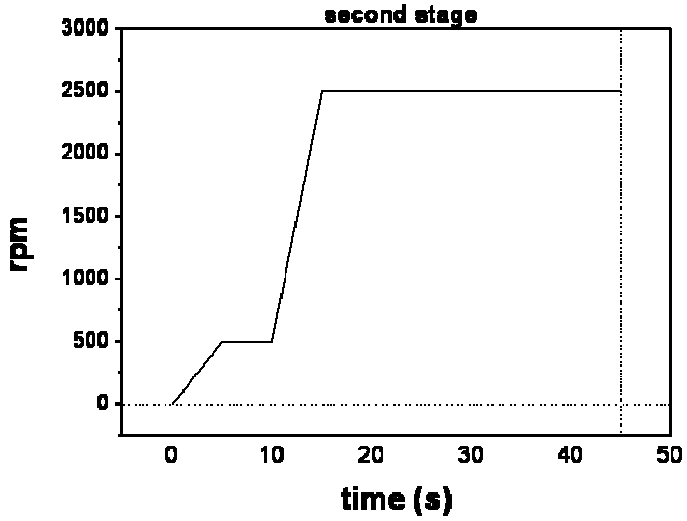

Figure 2.4. Second stage of the spin coating process

d) Finally, the channel pattern is transferred to a planar waveguide using an Ar^+ ion milling in an Oxford Plasma Technology Ionfab 300 plus system. This system uses an accelerated beam of Ar^+ ions at 500 V and a beam current of 100 mA. The sample was mounted on a cooled plate (288.5 K) held at 45º, and which rotated at 5 rpm for the duration of the etching (typically 6 h).

2.1.4.3. *Reactive ion etching*

In the semiconductor industry, reactive ion etching is commonly used for etching materials. It is a combination of chemical and physical etching. The masked substrate to be etched is placed on a plate located inside a vacuum chamber filled with the chemical

reactants. An RF field is applied between the plate which acts as electrode and the chamber (which acts as the ground) and this results in the formation of a plasma. This creates an electrical field in the chamber and the substrate becomes negatively charged. The positive ions in the plasma are attracted towards the substrate and they collide with it, dissociate bonds and thus etch the material (see figure 2.5). This has been used to fabricate waveguides in Ti:sapphire [111] and Yb:KYW [112]. The advantages of RIE over physical processes like ion beam milling are that it is more selective and gives nearly perpendicular side walls.

Inductively-coupled plasma reactive ion etching (ICP-RIE) has been widely used to fabricate waveguides in sapphire. This has the advantage of having a separate RF generator for creating the plasma which results in a high plasma density. The walls obtained using this technique are smooth and vertical and it is possible to obtain deeper channels than when other methods are used [113-116].

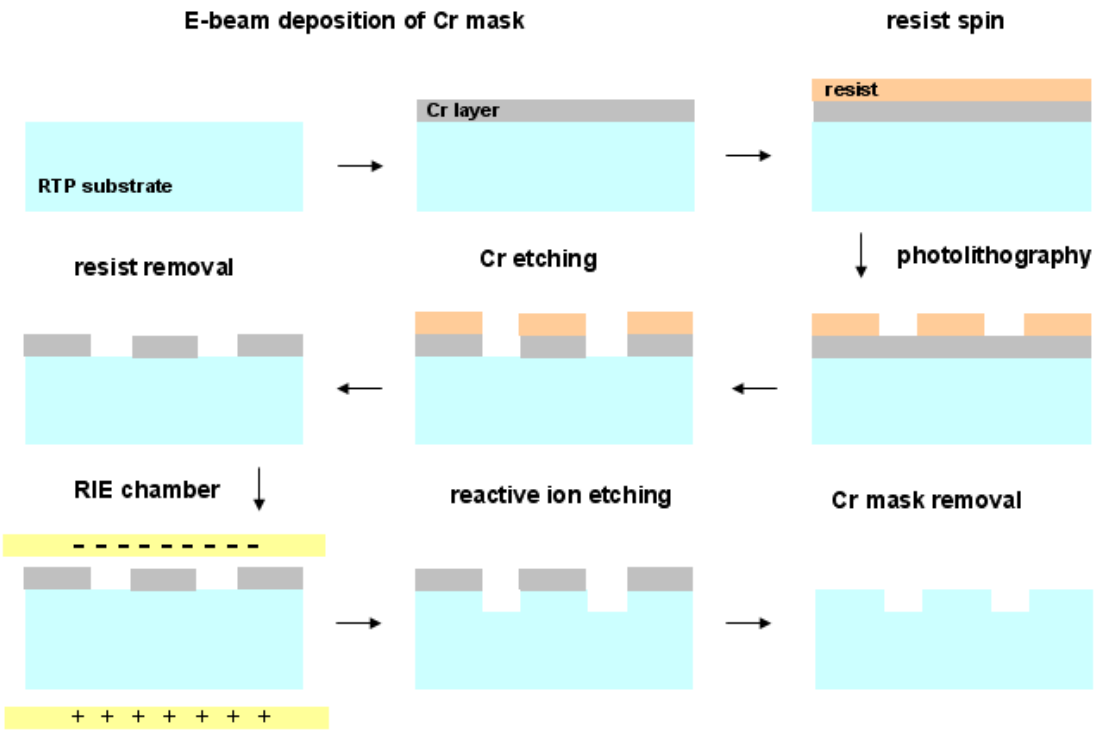

Figure 2.5. Reactive ion etching scheme

In this study, the RIE experiments are carried out in the Optoelectronics Research Centre in the University of Southampton in collaboration with the PhD. Student A. Choudhary, Prof. J.S. Wilkinson and Prof. D.P. Shepherd. The equipment used is an OPT Plasmalab 80 plus RIE system (Oxford Instruments) with an RF frequency of

13.56 MHz. The layer deposited on the RTP substrate in the e-beam deposition step (figure 2.5) is Cr. In the resist spin step we use a S1813 positive resist. The hard-masked RTP substrates are then etched in an RIE chamber with SF_6 and Ar gases where the pattern of the Cr is transferred onto the RTP substrate.

2.1.4.4. *Cs^+ ion-exchange*

In this study the RTP substrate is microstructured by Cs^+ ion exchange with a Ti mask on the substrate surface. Cs:RTP channel waveguides are fabricated by Cs^+ diffusion into RTP substrates from $CsNO_3$ melt (687 K). In general, the structuring process can be summarized in the following procedure: a) dark field mask fabrication by laser photolithography, b) transfer of the channel pattern to the (Ti-film)-substrate system, and finally d) the Cs^+ ion exchange process.

The RTP substrates used in this study are plates 1.5 mm thick perpendicular to the ***c*** direction and with a surface area of at least 1 cm^2.

a) The dark field mask is fabricated on a glass (50 x 50 x 2 mm^3) by the etching technique. The glass is carefully cleaned in an ultrasonic bath with acetone and isopropanol, and is finally washed with distilled water. After cleaning, 100 nm of Ti is RF-sputtered at 200 W on the glass. Then a layer (~ 1 μm) of photoresist AZ 1505® from the Microchemicals company is spin coated on the (Ti-fim)-glass system, and a soft bake (hot plate for 1 min) is applied. The designed pattern is transferred to the resist layer by exposure to UV light using a Heidelberg Instruments DWL 66 fs laser for lithography. After the exposed part has been developed, an etching solution is used to transfer the channel pattern designed to the Ti film. This solution is a mixture of H_2O_2 and NH_4OH with a molar proportion of 2:1.

b) A metal channel pattern must be on the substrate if selective ion diffusion is to come about. This metal film must remain attached to the surface of the substrate during the diffusion process, because otherwise the channels obtained will be of low quality. In our case the Ti-film complies with this condition.

The Ti-film pattern on the RTP plate is transferred by conventional photolithography. The procedure is the same as for dark field mask fabrication, except the UV exposure step, which is performed using the dark field mask fabricated. That is: 1) sputtering of a Ti-film on the polished substrate, 2) spin coating of resist on the (Ti-film)-system, 3) conventional photolithography using the dark field mask fabricated for transferring the

channel pattern from the mask to the resist-(Ti-film)-substrate system, and finally 4) transfer of the channel pattern from the resist to the (Ti-film)-substrate system.

In step 2, the resist-(Ti-film)-substrate system is stuck with tape on the glass mask to obtain a sandwich formed by a mask-resist-(Ti-mask)-substrate system. Then in step 3, the system is exposed to UV for 0.8 seconds using an MG 1410 mask aligner.

c) Cs^+ ion exchange is carried out in a $CsNO_3$ melt at 698 K. A Pt crucible is filled with 25 g of $CsNO_3$ and maintained at 698 K for 1 h. Then the sample with the Ti mask is submerged 6 mm below the melt surface. The substrate is maintained in the melt for the desired time (usually 2 h) with a rotation of 40 rpm.

2.2. Characterization techniques

2.2.1. Electron probe micro analysis (EPMA)

In this study, electron probe microanalysis (EPMA) is used to determine the chemical composition of the crystals and the dopant concentrations in these crystals. The equipment used is a Cameca SX-50 microprobe analyzer available at the Servei de Recursos Científico-Tècnics of the University of Barcelona.

Electron probe microanalysis is a nondestructive technique which uses a focused electron beam to produce characteristic X-rays from the samples. The electron beam generated has an intensity in the range 30-100 nA, depending on the concentration of the element to be determined. The acceleration voltage applied is 20 kV. A wavelength-dispersive spectrometer (WDS) is used to detect and characterize the X-rays produced by the samples. The spectrometer crystals used are: lithium fluoride 200 (LIF) ($2d$ = 4.028 Å), pentaerythritol 002 (PET) ($2d$ = 8.742 Å), thallium acid phthalate 1011 (TAP) ($2d$ = 25.75 Å), and PC1 (W/Si multilayered with $2d$ = 60 Å). The wavelengths covered by these spectrometer crystals range from 1 to 24 Å.

2.2.2. X-Ray diffraction

X-rays have been a driving force for crystallography. Thanks to X-rays, atomic positions, and the distance between adjacent lattice planes in crystals can be measured and crystalline structures determined.

The first scientist to observe X-ray diffraction in a crystal was W.L. Bragg. The scattered radiation from the crystals showed that they act as individual atoms

periodically aligned on planes. That is to say, these planes act as reflecting mirrors and the waves reflected by these lattice planes interfere constructively only if $\lambda = 2d_{hkl}\sin\theta$, where λ is the wavelength of the radiation used, d_{hkl} is the spacing distance between two consecutive lattice planes, and θ is the incident angle of the X-ray beam [117]. This equation is known as Bragg's Law.

In this study the X-ray powder diffraction method has been used. X-ray powder diffraction is a non-destructive tool for identifying crystalline phases and analyzing mixtures. A set of patterns compiled by the Joint Committee for Powder Diffraction Standards (JCPDS) is compared with the patterns we recorded. The FULLPROF program [118,119], which is based on the Rietveld method, makes it possible to obtain precise cell-parameters.

The X-ray diffraction patterns discussed here are obtained with an Siemens EM-10110BU model D5000 X-ray diffractometer by using the k_α line of copper available at the Servei de Recursos Cientifics i Tècnics of the Universitat Rovira i Virgili. This equipment works with the Bragg-Bretano parafocusing geometry and θ - θ configuration. To obtain the pattern of reflections from all the possible planes of the sample, the θ angle of the X-ray source and the detector is varied.

2.2.3. Determination of refractive indices and dark mode spectra using a prism-film coupler

In 1970 P.K. Tien and Ulrich [120] made an important contribution to the understanding of the guiding properties of thin films: the theory behind the light-wave coupler. This coupler makes it possible to measure thin film parameters such as refractive indices, film thickness and propagation modes of the light waves accurately, simply and quickly. The equipment used in this study is a Prism-Film Coupler with a laser source, a rotator stage table and a prism. A PC acquires the information from the detector, displays and analyzes the mode patterns and, after some calculations, gives the results.

A pneumatically-operated coupling head brings the plate of refractive index n_{bulk} and a prism of refractive index n_{prism} into close contact The roughness of both surfaces (prism and sample) produces an air gap that is typically less than 100 – 200 nm.

This gap is crossed by the evanescent waves produced by a laser beam directed onto the prism base and which is totally reflected. Then the rotary table starts to rotate the

coupling head and the detector records the intensity reflected at the base of the prism. When the angle of incidence θ is less than the critical angle θ_c, the detector records an abrupt drop in intensity (see figure 2.6) and the refractive index of the bulk can be determined by $\theta_c = \sin^{-1}\frac{n_{bulk}}{n_{prism}}$.

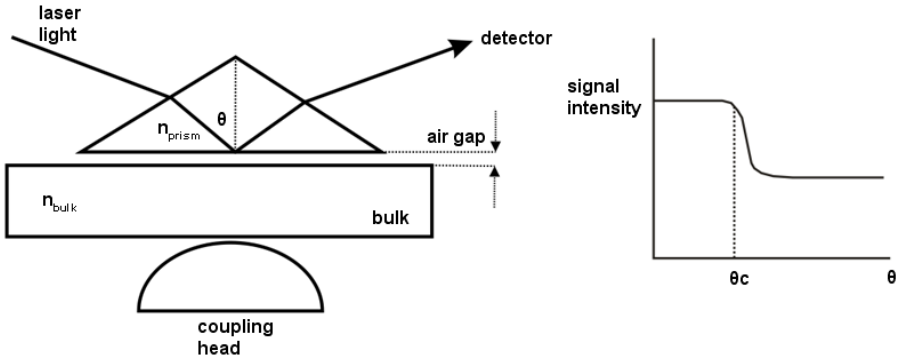

Figure 2.6. Experimental arrangement of prism-sample coupler and drop in the detector intensity. Picture reproduced from the user's manual provided by Metricon.

When a planar waveguide is coupled on the prism instead of a bulk plate, the *dark mode spectrum* can be obtained. As can be seen in figure 2.7, the outcoupled light is imaged on a screen, showing dark lines. The guided modes are excited when the phase velocity of the light wave in the prism matches that of a guided mode in the waveguide:

$$\left(\frac{2\pi}{\lambda}\right) = n_{prism}(\sin\theta)\beta_m$$

where λ is the free-space wavelength and β_m is the propagation constant of a particular mode of order m in the film.

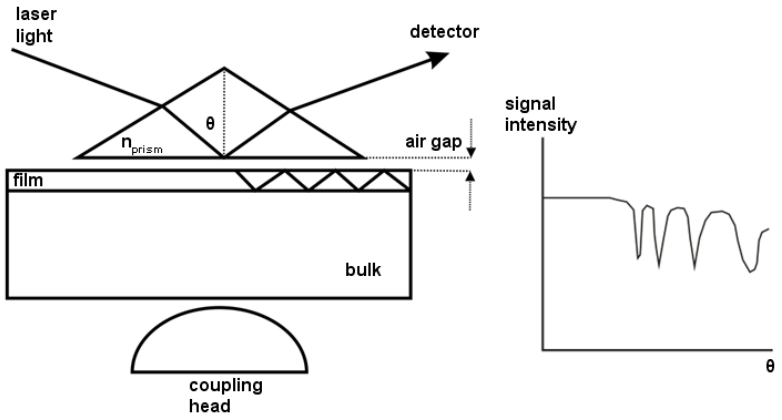

Figure 2.7. Experimental arrangement of the prism-film coupler and *dark mode spectrum*. Picture reproduced from the user's manual provided by Metricon.

2.2.4. Microscopy techniques

Reflection optical microscopy is the first technique that we use to get an immediate view of the epitaxies, before and after polishing. The confocal microscope is also widely used to provide profiles of the as-grown epitaxial layers after polishing and a preview of the morphology of the epitaxy surface. In some cases, a more accurate view of the morphologies on the as-grown surfaces is obtained by Atomic Force Microscopy (AFM). The microstructures machined on the surface of the planar waveguides, as well, as the polished end-faces with rib shapes are visualized with Environmental Scanning Electron Microscopy (ESEM) and confocal microscopy.

2.2.4.1. Reflection and transmission optical microscopy

Reflection optical microscopy is based on the simultaneous normal incidence of visible light on the sample surface and normal visualization through the objective. The reflected unobscured image, which is highly illuminated, is provided by a specific configuration of the incident and reflected light paths. The high contrast enhances the observation of details on the sample surface. Also important for saving time is that this technique requires no sample preparation. In this study we use an Olympus BH-2 microscope. The same microscope makes transmission possible; in this case the lamp is below the sample holder. This holder has a hole that allows light to pass through the sample. The images obtained, then, are by transmission instead of reflection.

2.2.4.2. Environmental scanning electron microscopy (ESEM)

Environmental scanning electron microscopy (ESEM) is one of the most commonly used techniques in several research fields today, mainly because it can focus on a wide range of specimen surfaces as a result of its large depth of field. It can also be used to observe fine details, because of its high resolution. The electron beam usually consists of a tungsten or LaB_6 filament. However, a field emission gun (FEG) is becoming increasingly necessary to obtain high-resolution images of nanostructures. The accelerating voltage is usually between 1 and 30 kV and lower voltages increase the brightness. This technique can provide magnifications between 20 and 300,000. The surface of the sample is scanned with an electron beam with a fine focal spot size, obtained by condenser lenses. This spot size determines the resolution of the image, which is obtained by scanning. Several types of signals are produced when the focused

electron beam impinges on the sample surface and they can be used to create an ESEM image. In comparison with SEM, ESEM has some advantages. ESEM, unlike SEM, has the advantage that samples do not need to be covered with a conducting media such as gold to make observations. Thus, non-conductive samples can be directly observed, without any coating.

An ESEM contains gas at low pressure in the sample chamber. Here the primary electrons travel across the gas phase and interact with the surface of the sample, which releases secondary electrons that interact with the phase gas to produce additional secondary electrons. The primary electrons interact with the gas molecules to produce ions and additional electrons. Thus, the phase gas functions as an amplifier of the electron signal from the sample.

In this study, a FEI QUANTA 600 environmental scanning electron microscope from the Serveis de Recursos Científics i Tècnics of the Universitat Rovira i Virgili is used to obtain images.

2.2.4.3. Confocal imaging profilometry

Confocal microscopy uses a LED beam to provide the excitation light, usually in the blue region (λ = 470 nm). Unlike fluorescence microscopy, it illuminates only one point of the sample: the focal point of the lens. Thus, the detector receives fluorescence from only one point of the sample. Conventional fluorescence microscopy illuminates the entire sample and produces considerable background haze. Logically, in confocal microscopy only one point of the sample is observed at a time. The detector is attached to a computer, which builds up the image, pixel by pixel, by scanning the volume of the sample layer by layer. To restrict the illumination, a pinhole is added to the point where the focal point of the objective lens of the microscope forms the image. The pinhole is conjugated to the focal point of the lens, and is thus a confocal pinhole. In this study a Sensofar PLμ 2300 optical imaging profiler was used. Figure 2.8 gives a schematic view of the confocal microscopy technique.

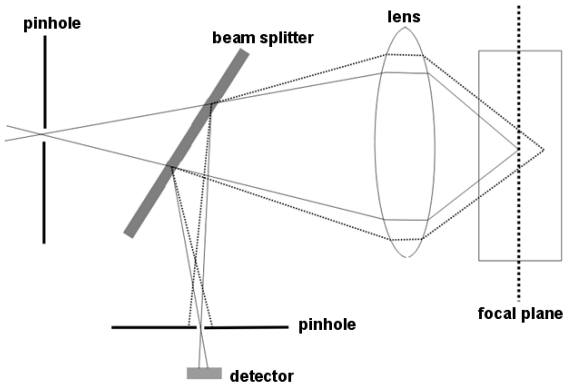

Figure 2.8. Confocal microscopy scheme

2.2.4.4. μ - Raman microscopy

The structure of a material can be obtained from Raman scattering, which gives information about the vibrational energy levels of the molecules. In addition, Raman scattering is non-contact and non-destructive. By merging Raman scattering and infrared absorption, we can describe the characterization of the vibrational, rotational, and other low-frequency modes of the molecules, such as the lattice vibrations of crystals.

Because the energies of the incident and scattered photons are different, Raman scattering is an inelastic scattering of monochromatic light that shifts the energy of the scattered photons down or up for the Stokes and anti-Stokes lines, respectively. This shift is related to the vibrational energy spacing in the ground electronic state of the molecules, since the positions of the Stokes and anti-Stokes lines are a direct measurement of the vibrational energy of the molecule. Only molecules that are at the first vibrational level of the excited state lead to anti-Stokes lines, and at room temperature very few molecules are at this level. The most intense Stokes line is measured in Raman scattering.

By combining Raman scattering and a conventional optical microscope, Raman microstructural investigations can be carried out on the micrometer scale.

The experimental set up used consists of a Renishaw Invia spectrometer with excitation in the visible range by a cw argon laser (λ = 514 nm). Behind a monochromator, the light is detected by a two dimensional CCD camera. A pre-monochromator eliminates the plasma discharge lines of the argon laser. A high resolution microscope (Leica) is

used to locate the laser spot in the sample. In this study, the laser power incident on the sample is about 3.9 mW. We chose a backward scattering scheme to increase the signal-to-noise ratio. This equipment is available at the Servei de Recursos Científico-Tècnics of the Universitat Rovira i Virgili.

2.2.5. Waveguide set up

The most important part of characterizing a waveguide is the optical study. In this paper, a waveguide set up (see figure 2.9) is used to study the properties of the light traveling through the waveguides. In general, the set up consists of three precision 3-axis mobile stages. One of them holds a tilt stage with the waveguide. The other two hold the input and output microscope objectives. The input microscope objective was used to couple the laser sources to the waveguide (NA = 0.28, focal length = 20 mm, working distance = 33.5 mm). The output signal from the waveguide is outcoupled with a 50x microscope objective lens (NA = 0.42, focal length = 4 mm, working distance = 17 mm). In all the experiments, the wavelength is measured with a laser spectrum analyzer (Wavescan, APE instruments, Berlin) at a spectral resolution of 0.1 nm. The powers are measured with an Ophir power meter (measurement range from 60 μW to 3 W) with an accuracy of 1 μW.

The near field patterns of the waveguides are recorded with a CCD camera using the set up mentioned above. In this study the laser sources used are a 632 nm He-Ne laser and a Ti:Shappire laser (~ 700 – 1000 nm).

In this study, the second harmonic generation (SHG) experiments are performed using a waveguide set up, but in this case the OPO laser is used as a source. In order to accomplish type II SHG, a half-plate is placed before the input microscope objective. By applying this polarizer we can excite both polarization modes – TE and TM – simultaneously.

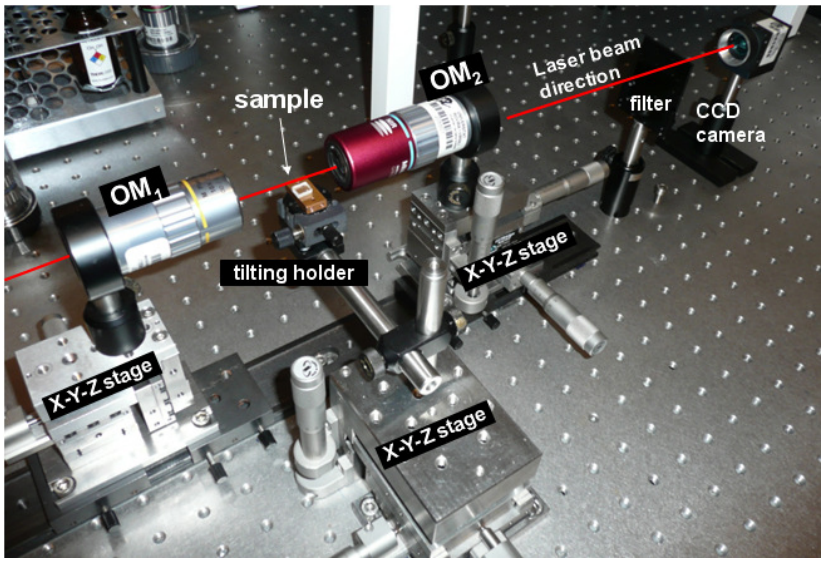

Figure 2.9. Waveguide set up and CCD camera

2.2.6. Determination of the optical losses in waveguides

In this study, the optical losses are measured by two different methods, depending on whether the type of waveguide investigated is planar, rib or channel. These optical losses are measured by coupling a 632 nm radiation from a He-Ne laser and a 972 nm radiation from a Ti:sapphire laser inside the waveguides. The end-coupling process is performed using the waveguide set up described above.

2.2.6.1. Planar waveguides

In planar waveguides, the scattered light from the waveguide is collected in different positions [121], and recorded in the chip of a CCD camera. This device can measure the distribution of the scattered light along the propagation direction.

If we assume that the intensity $I_{sc}(z)$ of the scattered light detected is proportional to the intensity $I(z)$ of the light that is traveling through the waveguide ($I(z) = S \cdot I_{sc}(z)$), and this proportionality factor (S) is independent of the distance along the waveguide z, we can consider an attenuation factor α. This factor gives us information about the quality of the waveguide confinement. This coefficient can be determined by fitting the measured intensities to the expression $I(z) = I(0) \cdot \exp(\alpha z)$, where $I(0)$ is the intensity at the waveguide entrance, z is the distance along the waveguide, α is the attenuation coefficient and $I(z)$ is the intensity along the waveguide.

2.2.6.2. Rib and channel waveguides

In this kind of waveguide, optical losses are measured by the **single pass transmission method**. This method has been chosen because the shape of the surface rib waveguides disturbs the scattered light emitted by the rib or channels. This means that the intensity recorded with the CCD camera will not really be that of the guided light scattered. The method compares the outcoupled power (P_{out}) with the incident power (P_{in}) measured before coupling the light in the waveguide. So the total waveguide losses, L_T (dB), can be determined by $L_T = -10\log\frac{P_{out}}{P_{in}}$. Note that some corrections must be made to P_{out} and P_{in}. In fact, power losses are subtracted due to the reflectance of both waveguide faces. In fact, power losses are subtracted due to the reflectance of both waveguide faces. In particular, for (Yb,Nb): RTP crystals the reflectance of both faces is around 9 %. The launch efficiency must also be taken into account. The launch efficiency is the % of light that does not go within the rib and channel waveguides due to the mismatch between the focus of the microscope objective and the area of the channel or rib. Finally, the transmittance losses of the output microscope objective are also taken into account.

Chapter 3

Waveguide fabrication on $RbTiOPO_4$ (001)

The $RbTiOPO_4$ (RTP) crystals crystallize in the orthorhombic system with $Pna2_1$ space group, and cell parameters a = 12.974(2) Å, b = 6.494(3) Å, and c = 10.564(6) Å [122]. The atoms in $RbTiOPO_4$ are in general positions and for each different atom exists two non-equivalent positions. The $RbTiOPO_4$ structure (as for KTP's structural family) consists of a extended helical network of distorted TiO_6 octahedra linked by slightly distorted PO_4 tetrahedra, and a mobile framework of Rb atoms [122].

In the literature, we found that the morphology of the crystals of the KTP family was first studied by Voronkova and Yanovskii [123] and Pavlova *et al.* [124]. The RTP crystal habit is made up of {100}, {201}, {20-1}, {011}, {01-1} and {110} forms, see figure 3.1.

RTP crystals grew with the same forms as KTP crystals. However, in the case of RTP crystals, the {201} and {011} forms develop sharp morphologies, whereas the morphologies developed by {011} and {110} forms are less sharp.

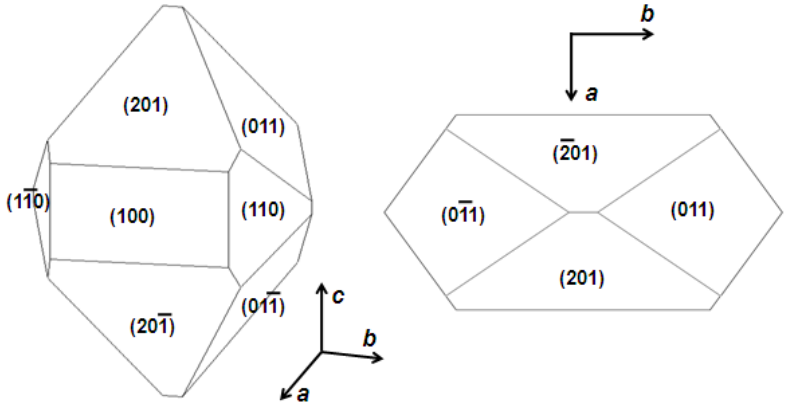

Figure 3.1. Morphologies of RTP single crystals.

The $RbTiOPO_4$ crystals melt incogruently [125]. So, crystals cannot be grown from the melt. Instead, a high-temperature solution is used to grow RTP in this work.

RTP crystal seeds were used in the growth experiments, with the ***c*** crystallographic direction normal to the surface of the solution.

In this chapter we summarize how the planar, rib and channel waveguides were fabricated. The growth of single crystals of $RbTiOP_4$ (RTP) and K:$RbTiOPO_4$ (K:RTP) to be cut for substrates is explained in the first part of the chapter. Then, the fabrication of planar waveguides (PWGs) of (Yb,Nb):RTP and (Ba,Yb,Nb):RTP on RTP and K:RTP substrates is described. Finally, the microstructuring processes of the PWGs obtained, and the channel and planar waveguide fabrication by Cs^+ ion exchange on RTP substrates are explained.

3.1. Bulk single crystal growth for substrates

3.1.1. $RbTiOPO_4$ bulk single crystals

$RbTiOPO_4$ (RTP) single crystals were grown to be cut into plates for substrates. These crystals were grown from fluxes containing WO_3 by the top-seeded solution growth technique and slow-cooling of the solution (TSSG-SC). The solution composition was Rb_2O - P_2O_5 - TiO_2 - WO_3 = 44.24 – 18.96 – 16.8 – 20 (mol %). This composition was chosen on the basis of the primary crystallization region of RTP in the Rb_2O-P_2O_5-TiO_2-WO_3 system with 20 mol % of WO_3 [126].

The addition of WO_3 to the solution is interesting because it decreases the solution viscosity, as has been proved in solutions used to grow crystals of the same family

[127]. It was decided that the solution should contain 20 mol % of WO_3 because the crystallization region of RTP in solutions with 30 mol % of WO_3 is already rather narrow [126] and this increases the probability of losing the RTP phase by decreasing the temperature during crystal growth, which makes it more likely that a neighbouring phase will be obtained. Figure 3.2 shows the RTP primary crystallization region in the Rb_2O-P_2O_5-TiO_2-WO_3 system with 20 mol % WO_3 and the point inside this crystallization region represents the solution composition used for crystal growth. As can be seen, the point is chosen close to the lower boundary of the RTP primary crystallization region, since the solution viscosity increases when the P_2O_5 concentration increases.

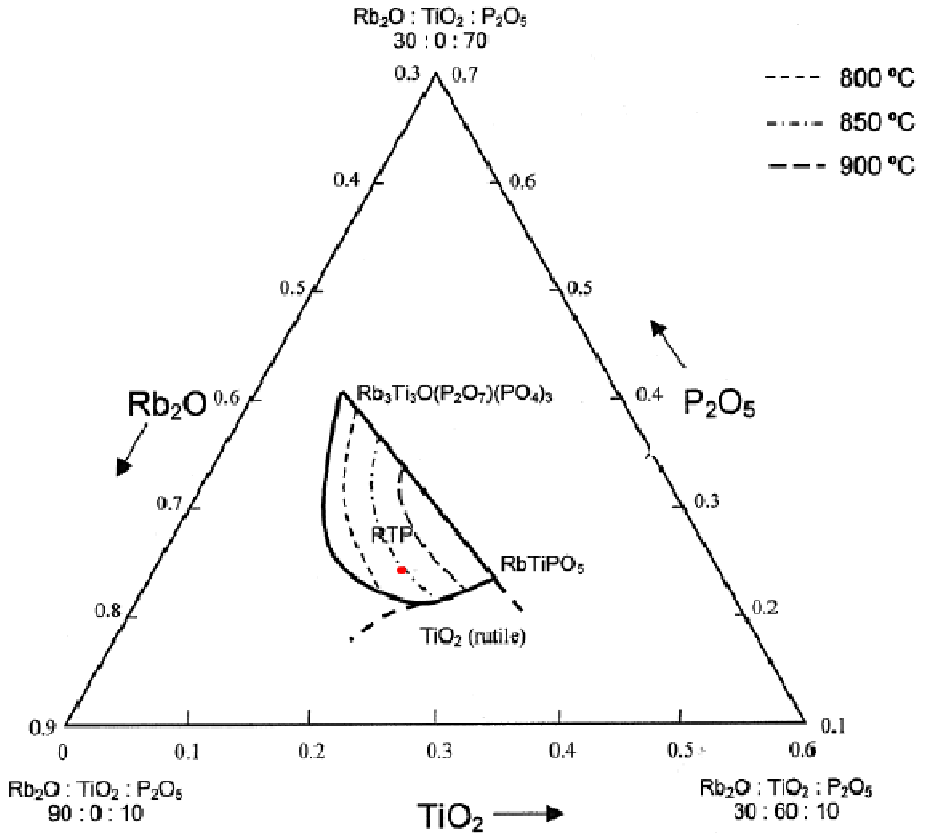

Figure 3.2. Primary crystallization region and saturation temperature isotherms of RTP in the Rb_2O–P_2O_5–TiO_2–WO_3 system with 20 mol % WO_3. The composition used in this work is marked (red point)

The solution was prepared by mixing the desired amounts of Rb_2CO_3, $NH_4H_2PO_4$, TiO_2 and WO_3, used as initial reagents. In these experiments, a cylindrical Pt crucible of 125 cm^3, filled with about 170 g of solution was used. The axial thermal gradient in the solution was 1.5 $K \cdot cm^{-1}$ for the first centimeter and 0.8 $K \cdot cm^{-1}$ for the next 1.5 cm. The bottom was hotter than the surface of the solution. The radial gradient was 1.8 $K \cdot cm^{-1}$,

and the crucible wall was hotter than the centre of the solution surface. The solution temperature was kept at about 75 K above the expected saturation temperature (T_s) for about 5 h to homogenize the solution. Subsequently, the saturation temperature was accurately determined by repeated seeding. The supersaturation of the solution, needed for crystal growth, was obtained by slowly decreasing the temperature of the solution at a rate of 0.1 K/h for several K. The velocity of rotation was constant in all the experiments and fixed at 64 rpm. The crystals obtained were generally colorless, transparent and free of inclusions and cracks. As can be seen in Table 3.1 different conditions were used. For instance, a cooling interval of 20 K without pulling produced crystals with dimensions in the ranges 14.0-14.9, 15.1-26.0 and 11.1-15.9 mm along ***a,*** ***b*** and ***c*** directions, respectively and weights in the range 5.71-7.99 g. On the other hand,

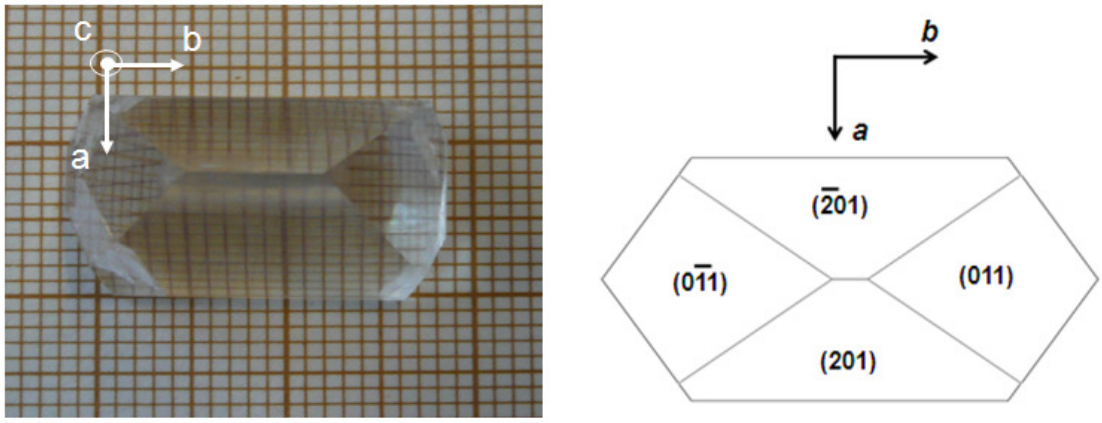

Figure 3.3: RTP bulk crystal and morphological scheme with the indices of the faces obtained

an experiment with a cooling interval of 30 K and total pulling of 6.5 mm (pulling rate 1 mm/day), produced a crystal with dimensions 19.2 × 21.1 × 21.9 (***a*** × ***b*** × ***c***) mm^3 and a weight of 13.94 g. As an example, figure 3.3 shows an image of a crystal obtained in this work and a scheme of its morphology. To obtain substrates, the crystals were cut in plates perpendicular to the ***c*** crystallographic direction and polished to optical quality so that the roughness of the surfaces was lower than 10 nm and curvature 8-20 m. In fact, all the PWGs fabricated in this study were grown on the (001) plane, since this plane is suitable for obtaining type II SHG phase matching for a wide range of wavelengths and makes it possible to obtain type II SHG for the Yb^{3+} emission. The dimensions of the plates obtained were in the range 4.2-10.3, 12.0-19.3 and 1.5 mm along the ***a***, ***b*** and ***c*** crystallographic directions, respectively.

Table 3.1. Growth conditions, dimensions and weight of some crystals grown for substrates

Experiment number	Cooling interval (K)	Total pulling (mm)	Crystal dimensions a×b×c (mm)	Crystal weight (g)
1	20	0	14.0x26.0x11.1	7.99
2	20	0	14.9x15.1x15.9	5.71
3	27	4	17.3x18.7x20.4	9.37
4	28	5.5	17.9x20.0x21.5	12.32
5	30	6.5	19.2x21.1x21.9	13.94

3.1.2. K doped $RbTiOPO_4$ bulk crystals

In an attempt to obtain planar waveguides that guide the light in at least two polarizations, and taking into account that the KTP refractive indices [58] are lower than those of RTP (reported in papers I and II), $Rb_{1-x}K_xTiOPO_4$ single crystals were grown for substrates.

Before the bulk single crystals were grown, small crystals were grown to be analyzed by X-ray powder diffraction and EPMA. The solution composition used was (Rb_2O+K_2O)–P_2O_5–TiO_2–WO_3 = 43.90–23.60–22.50–10.00 (mol %), with 1, 5 and 10 mol % of Rb_2O substituted by K_2O.

Among other solutions, this solution composition was selected because it contains WO_3, which decreases the viscosity of the solution and makes the crystal growth process easier. We have chosen a solution composition located at the centre of the primary crystallization region of RTP in a system containing 10 mol% WO_3, because when Rb_2O is substituted by K_2O, the boundaries of the K:RTP crystallization region can be slightly different to the boundaries of the RTP crystallization region. To maintain the RTP orthorhombic phase during the crystal growth, a solution composition should be used that is quite a distance from the boundaries.

The small crystals were obtained from 40 g of solution, contained in a 25 cm^3 platinum crucible. After the solution had been homogenized, its temperature decreased by 10 K every 30 min until small single crystals had appeared on a Pt rod immersed in the solution. Once the crystals had appeared on the Pt rod, the solution temperature was

maintained constant for 24 h so that the crystals could grow. Then the crystals were removed from the solution for analysis.

The composition of these crystals was measured by EPMA. From these results we calculated the coefficient of distribution of K^+ in the RTP phase for each K^+ substitution, according to $K_K = \frac{\{[K^+]/([K^+]+[Rb^+])\}_{crystal}}{\{[K^+]/([K^+]+[Rb^+])\}_{solution}}$, where $[K^+]$ and $[Rb^+]$ are the K^+ and Rb^+ concentration in atomic % respectively

Table 3.2 shows the stoichiometric composition of the crystals obtained and the distribution coefficient of K^+ in RTP for 5 and 10 mol % of Rb_2O substituted by K_2O in the solution. These values show that with 10 mol % substitution of Rb_2O by K_2O in the solution, the distribution coefficient is near to 1, while for lower substitutions the distribution coefficient is lower.

Table 3.2. Composition of the crystals grown at different K^+ substitution

Sample	**$[K_2O]/([K_2O]+[Rb_2O])$ (mol %) in the solution**	**Crystal composition**	**Distibution coefficient of K**
K:RTP 5	5	$Rb_{0.975}K_{0.025}TiOPO_4$	0.5
K:RTP 10	10	$Rb_{0.901}K_{0.099}Ti\ OPO_4$	0.99

These small crystals were used to calculate the unit cell parameters for different levels of substitution of Rb by K in the crystals. Table 3.3 summarizes these results and shows that the unit cell volume gradually decreases, which is logical since the K^+ ionic radius is smaller than that of Rb^+.

Table 3.3. Unit cell parameters of $Rb_{1-x}K_xTiOPO_4$

Sample	**$[K_2O]/([K_2O]+[Rb_2O])$ (mol %) in the solution**	**a (Å)**	**b (Å)**	**c (Å)**	**volume ($Å^3$)**
RTP	0	12.9650	6.5007	10.5576	889.81
K:RTP 1	1	12.9608	6.5002	10.5577	889.46
K:RTP 5	5	12.9573	6.4975	10.5554	888.66
K:RTP 10	10	12.9501	6.4885	10.5619	887.48

The lattice mismatches between the (Yb,Nb):RTP epitaxial layer to be grown and the K:RTP substrate were calculated from the unit cell parameters that had in turn been calculated using the X-ray power diffraction results reported in table 4 of paper I. The formula used to calculate the epitaxial layer / substrate lattice mismatch was:

$f_{(hkl)} = 100 \times (S_{(hkl)}(layer) - S_{(hkl)}(substrate)) / S_{(hkl)}(substrate)$, where $S_{(hkl)}$(layer) and $S_{(hkl)}$(substrate) are the areas obtained from the *(hkl)* periodicity vectors of the layer and the substrate, respectively. Table 3.4 reports the lattice mismatches calculated for the (001) face.

Table 3.4. Lattice mismatch between the (Yb,Nb):RTP layers and the K:RTP substrates

Epitaxial layer/substrate	**Epitaxial layer/substrate lattice mismatch (001)**
$RbTi_{0.975}Yb_{0.014}Nb_{0.011}OPO_4/Rb_{0.901}K_{0.099}\ TiOPO_4$	0.612
$RbTi_{0.971}Yb_{00.015}Nb_{0.014}OPO_4/\ Rb_{0.901}K_{0.099}\ TiOPO_4$	0.743

Despite this high lattice mismatch, the epitaxial layers were grown as is described in section 3.2.1.3.

Bulk single crystals of K:RTP were grown from a solution with the same basic composition that was used to obtain small crystals, but a $[K_2O]/([K_2O]+[Rb_2O])$ ratio of 10 mol % was used. For these growth experiments, a 25 cm^3 Pt crucible was filled with 80 g of solution. The axial thermal gradient in the solution was 1.4 K/cm. After accurately determining the saturation temperature of the solution, a cooling rate of 0.1 K/h was applied for 20 K. Throughout the experiments, the crystal was rotated at 64 rpm. Table 3.4 summarizes the experiments carried out and the dimensions and weight of the crystals obtained.

Table 3.5. Dimensions and weight of the K:RTP crystals

Experiment number	**Crystal dimensions $a \times b \times c$ (mm^3)**	**Crystal weight (g)**
1	9.0 x 10.9 x 7.6	1.37
2	7.9 x 13.5 x 10.4	1.51
3	9.1 x 14.2 x 10.7	2.21
4	10.3 x 14.2 x 9.7	2.09

These crystals were free of inclusions and cracks, which makes them useful for producing substrates for epitaxial growth experiments. As an example, figure 3.4 shows an as-grown crystal just after it has been removed from the furnace.

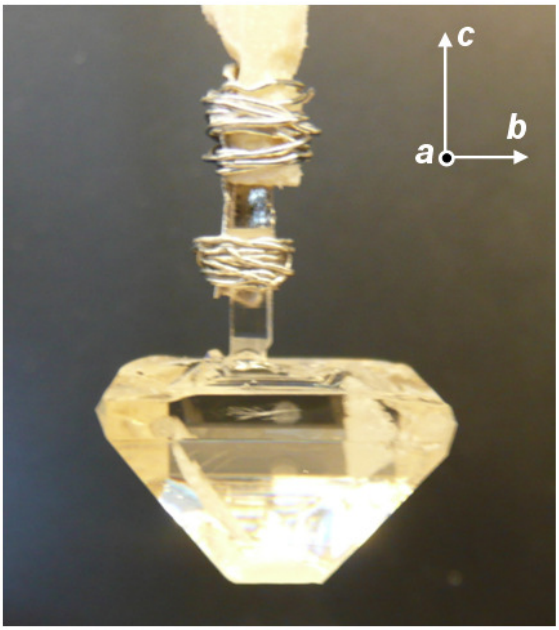

Figure 3.4. As-grown K:RTP crystal

3.2. Fabrication of planar waveguides (PWGs) by LPE

As has been explained in the introduction, waveguides are the basic element of integrated photonics. There are several possible geometries for waveguides, but planar guides are logically the easiest to fabricate. So, in this section, the fabrication of two types of PWGs will be described: the first is (Yb,Nb):RTP/RTP step index PWGs grown by LPE, and the second is gradient index PWGs fabricated by Cs^+ ion exchange.

The objective of this section was to obtain RTP waveguides doped with Nb^{5+} and Yb^{3+} on RTP substrates (see Papers I, II and III). The first stage was to grow (Yb,Nb):RTP (001) layers on RTP substrates to obtain PWGs. As will be shown in the characterization chapter, these waveguides can only support TM modes. Because type II SHG can only be obtained if TM and TE modes are excited simultaneously, other strategies were applied to increase the refractive index contrast (Δn) in x or y direction (in TE polarization). These strategies maintained the LPE method to fabricate PWGs. Thus, layers of (Yb,Nb):RTP codoped with Ba^{2+} were grown on RTP substrates since

the Ba^{2+} ion increases [128]. A second way of increasing Δn in TE polarization was to obtain (Yb, Nb):RTP and (Ba, Yb, Nb):RTP epitaxial layers on RTP doped with K substrates. This strategy was applied because the refractive indices of are lower than those of RTP, which makes the (Yb,Nb):RTP/K:RTP system able to guide the light.

3.2.1. (Yb,Nb):$RbTiOPO_4$ PWGs on $RbTiOPO_4$ (001) substrates

If epitaxial layers are to be used as planar waveguides, they need to be transparent and free of defects; but they also need other characteristics. The refractive index contrast must be high (with $n_{layer} > n_{substrate}$), so that the light confinement is strong. In addition, if the Yb^{3+} concentration in the PWGs is high enough for lasing experiments, this would be of great importance, because the Yb^{3+} emission could be frequency doubled in the same crystal (self-doubling process). Hereby, (Yb,Nb):RTP/RTP epitaxial layers were grown using several basic solution compositions and also several TiO_2 substitutions for Nb_2O_5 and Yb_2O_3, as is reported in Papers I and II, in order to obtain epitaxial layers with both characteristics. Table 3.6 shows the different ratios of oxides that we used in this section.

Table 3.6. Basic solution compositions for (Yb,Nb):RTP epitaxial growth on RTP substrates

	Rb_2O	P_2O_5	$TiO_2 + Nb_2O_5 + Yb_2O_3$	WO_3
1	40.80	27.20	32.0	0.00
2	43.90	23.60	22.50	10.00
3	43.82	22.58	13.60	20.00

Composition 1 in table 3.6 was chosen because ref [42] showed that with this composition the critical Yb_2O_3 concentration in the solution which allows the RTP phase to crystallise and the distribution coefficient of Yb^{3+} in RTP are higher than when solutions with lower TiO_2 concentrations and higher P_2O_5/Rb_2O ratios are used. In addition, this solution does not contain foreign ions such as W^{6+}, which can become impurities in the grown layer and can limit some uses. Composition 2 contains WO_3, although in a low proportion (10 mol %) and, as has been mentioned above, helps to decrease the viscosity of the solution and improve the growth conditions. This composition has been chosen near the centre of the RTP crystallization region in

solutions containing 10 mol % of WO_3 [126], because the dopant elements can displace the boundaries of the crystallization region, as was reported by J.J. Carvajal *et al* [126]. Composition 3 contains higher WO_3 concentration, which enables defect-free crystals to grow faster and very few W^{6+} impurities are incorporated. A (Yb, Nb):RTP single crystal grown using this composition has been used to demonstrate Yb^{3+} laser operation [39].

Table 3.7. Conditions of epitaxial growth. Solution composition, size of the substrates, ΔT = Ts - Tg (Ts= saturation temperature, Tg = growth temperature) and growth time.

Experiment number	**Solution composition Rb_2O–P_2O_5–TiO_2–Yb_2O_3–Nb_2O_5–WO_3 (mol%)**	**Substrate dimensions a × b × c (mm)**	**ΔT = Ts – Tg (K)**	**Growth time (h)**
1	40.8–27.2–30.08–1.92–0–0	6.7 × 16.9 × 1.0	2	3
2	40.8–27.2–30.08–1.92–0–0	6.5 × 12.0 × 1.0	2	6
3	40.8–27.2–30.08–1.92–0–0	6.9 × 19.3 × 1.0	2	0.30-1-2.30-4-15
4	40.8–27.2–30.4–0.64–0.96–0	4.2 × 18.5 × 1.0	2	16
5	40.8–27.2–29.76–1.92–0.32–0	6.5 × 18.5 × 1.0	2	5
6	40.8–27.2–29.76–1.92–0.32–0	9.6 × 13.6 × 1.0	2	5
7	40.8–27.2–29.44–1.92–0.64–0	10.3 × 18.2 × 1.0	2	6
8	40.8–27.2–29.44–1.92–0.64–0	6.2 × 16.1 × 1.0	2	6
9	43.9–23.6–20.70–1.35–0.45–10	10.24 × 18.14 × 1.0	9	7
10	43.9–23.6–20.70–1.35–0.45–10	10.15 × 12.58 × 1.0	10	6
11	43.82–22.58–12.92–0.27–0.41–20	8.6 × 16.2 × 1.0	7	3

Table 3.7 summarizes several experiments performed using these three basic solution compositions. The levels of TiO_2 substitution for Yb_2O_5 and Nb_2O_5 in the solution, ranged from 2 to 6 mol % for Yb_2O_3 and from 0 to 3 mol % for Nb_2O_5. The sizes of the planar substrates for epitaxial growth experiments are also shown in the same table. They range from 4.2 to 10.3 mm in the ***a*** direction, from 12.0 to 19.3 mm in the ***b*** direction and were 1.0 mm in all cases in the ***c*** direction. The same table also shows $\Delta T=T_s-T_g$ (T_s= saturation temperature, T_g= growth temperature), which is related to the

supersaturation of the solution. In general, ΔT was 2 K, except in the experiments with WO_3 solutions, where ΔT ranged from 7 to 10 K. Finally, the growth time in each experiment ranged from 3 to 7 h, except in experiment number 3, in which growth times varied from 30 minutes to 16 h so that the correlation between layer and growth time could be studied.

Table 3.8 shows the composition of the epitaxial layers obtained from solutions with different concentrations of Yb_2O_3 and Nb_2O_5. The distribution coefficients of these doping ions in RTP are also shown. The epitaxial layer with the highest Yb^{3+} concentration has a stoichiometric composition of $RbTi_{0.958}Yb_{0.016}Nb_{0.026}OPO_4$, which corresponds to 6 mol % TiO_2 substituted by Yb_2O_3 and 2 mol % of TiO_2 substituted by Nb_2O_5 in the solution. The PWGs obtained from this solution were used for microstructuration.

Table 3.8. Composition of the epitaxial layers grown from different solution composition and distribution coefficients of the doping ions.

Exp. num.	$\frac{[Yb_2O_3]}{[TiO_2]+[Yb_2O_3]+[Nb_2O_3]} \times 100$ $(mol\%)$	$\frac{[Nb_2O_5]}{[TiO_2]+[Yb_2O_3]+[Nb_2O_3]} \times 100$ $(mol\%)$	**Epilayer stoichiometry**	K_{Yb}	K_{Nb}
1	6	0	$RbTi_{0.995}Yb_{0.005}OPO_4$	0.04	-
6	6	1	$RbTi_{0.975}Yb_{0.014}Nb_{0.011}OPO_4$	0.125	0.590
8	6	2	$RbTi_{0.971}Yb_{0.015}Nb_{0.014}OPO_4$	0.135	0.378
9	6	2	$RbTi_{0.958}Yb_{0.016}Nb_{0.026}OPO_4$	0.140	0.658
11	2	3	$RbTi_{0.983}Yb_{0.004}Nb_{0.013}OPO_4$	0.106	0.226

The lattice mismatch between the substrate and the epitaxial layer is related to the stress in the substrate/epitaxy interface. This value can be obtained from the unit cell parameters of the substrate and the layer, according to the expression given above. Table 3.9 shows the unit cell parameters of several crystals with different levels of Ti^{4+} substituted by Yb^{3+} and Nb^{5+} and table 3.10 summarizes the calculated lattice mismatches in the (001) plane, which are lower than those we obtained for other materials [129].

Table 3.9. Unit cell parameters of $RbTi_{1-x-y}Yb_xNb_yOPO_4$.

Exp. num.	Stoichiometric formula	*a* (Å)	*b* (Å)	*c* (Å)
Substrate	$RbTiOPO_4$	12.9650(5)	6.5007(3)	10.5576(4)
1	$RbTi_{0.995}Yb_{0.005}OPO_4$	12.9664(6)	6.5012(3)	10.5611(5)
6	$RbTi_{0.975}Yb_{0.014}Nb_{0.011}OPO_4$	12.9831(8)	6.5116(4)	10.5711(6)
8	$RbTi_{0.971}Yb_{0.015}Nb_{0.014}OPO_4$	12.9933(2)	6.5150(6)	10.5852(8)

Table 3.10. Lattice mismatch between $RbTi_{1-x-y}Nb_yYb_xOPO_4$ and RTP (001) substrate. The unit cell parameters of the substrate used in these calculations correspond to RTP grown from a solution containing 20% WO_3.

Epitaxial layer	Substrate/epilayer lattice mismatch (001)
$RbTi_{0.995}Yb_{0.005}OPO_4$	0.05
$RbTi_{0.975}Yb_{0.014}Nb_{0.011}OPO_4$	0.342
$RbTi_{0.971}Yb_{0.015}Nb_{0.014}OPO_4$	0.473

We observed the as-grown epitaxial layers obtained with a confocal microscope to study the growth morphologies. The film thickness and the profiles of the epitaxial samples were also obtained with the confocal microscope. As an example, figure 3.5 shows a profile of an as-grown epitaxial layer before polishing. As can be seen in this figure, on the μm scale, the film is smooth and almost plane. Studying these profiles, we noticed that the surfaces of the epilayers grown from self-flux solutions were generally smoother than those grown from WO_3 –containing solutions.

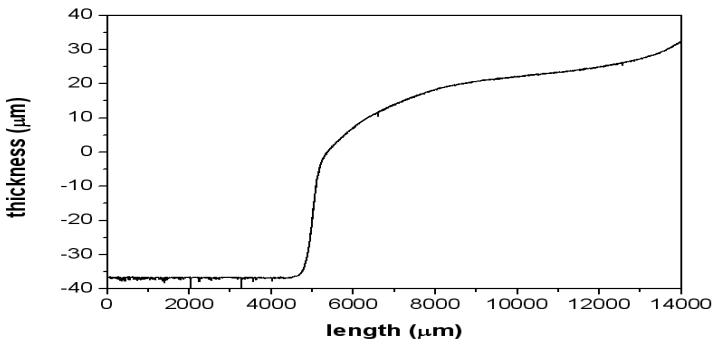

Figure 3.5. As-grown epitaxial layer profile

The surface morphologies of the as-grown epitaxial layers were studied carefully with the confocal microscope. In some cases, a sequence of parallel macrosteps, which may be related to some screw dislocation, appeared, mostly in the WO_3-containing solutions (see figure 3.6). This may be due to a higher growth rate in WO_3-containing solutions as a consequence of the higher supersaturation of the solutions and lower viscosity.

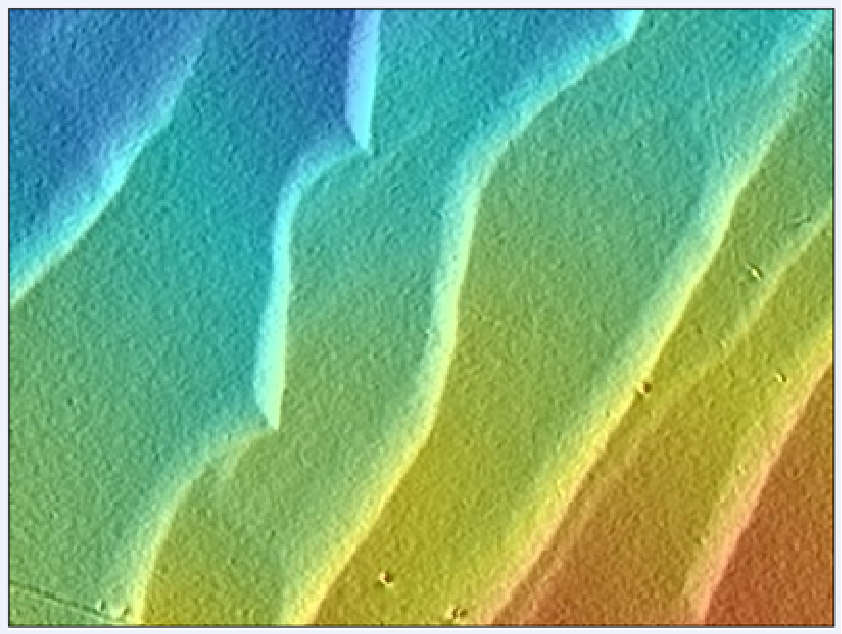

Figure 3.6. 3D image of a sequence of parallel macrosteps located on an as-grown epitaxial layer

The homogeneity of the Nb^{5+} and Yb^{3+} doping elements through the epitaxy was studied. A polished 10 μm (Yb,Nb):RTP epilayer on a RTP substrate was analysed by EPMA. The results are summarized in figure 3.7, which shows the Yb^{3+} and Nb^{5+} concentrations in the epitaxial layer. As can be seen, the concentrations of the doping ions were homogeneous throughout the epitaxy.

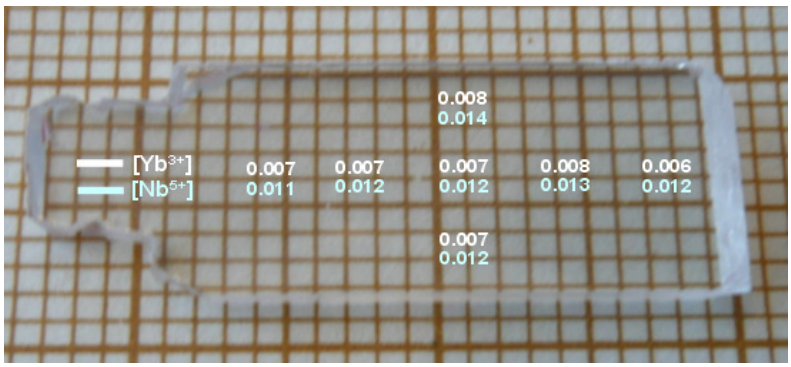

Figure 3.7. (Yb,Nb):RTP/RTP (001) epitaxial layer with the concentration of Yb^{3+} and Nb^{5+} distributed on the sample

Finally, after the complete process of crystal growth and surface characterization, the epilayers were polished so that the PWGs could be fabricated. As will be discussed in the chapter on PWG characterization, the epitaxial layers were polished to 5 or 10 μm depending on the case, since PWGs of these thicknesses support several modes in TM polarization. Moreover, as the simulation reveals, the PWGs with these dimensions are suitable for microstructuring.

3.2.2. (Ba,Yb, Nb):$RbTiOPO_4$ PWGs on $RbTiOPO_4$ (001) substrates

As has been mentioned above and will be demonstrated in Chapter 4, the planar waveguides obtained using TiO_2 substitutions by Nb_2O_5 and Yb_2O_3, (basically the epitaxial layers discussed in the 3.2.1 section), guide the light only in TM polarization. In order to obtain type II SHG in waveguide regime, light needs to be guided in TM and TE polarizations. For this reason we decided to dope the RTP epitaxial layers with Ba^{2+} as well as Yb^{3+} and Nb^{5+}, since the Ba^{2+} ions increase the refractive indices [128].

In order to know if RTP was successfully doped with Ba^{2+} ions, we measured the concentration of the doping ions in RTP by EPMA, using small crystals grown from different solution compositions.

We grew small crystals with solution compositions of (Rb_2O+BaO)-P_2O_5-TiO_2-WO_3=43.9–23.6–22.5–10 (mol %), in which the $BaO/(Rb_2O+BaO)$ ratios were 2, 4, 6, 8 and 10 mol %. In all cases the Ba:RTP orthorhombic phase was maintained.

Table 3.11. Stoichiometric composition of RTP doped with several concentrations of Ba^{2+} and distribution coefficient of Ba^{2+} in RTP

$\frac{[BaO]}{[BaO]+[Rb_2O]}$ (mol %)	**Stoichiometric composition**	**Distribution coefficient**
2	$Rb_{0.991}Ba_{0.009}TiOPO_4$	0.89
8	$Rb_{0.990}Ba_{0.010}TiOPO_4$	0.24
10	$Rb_{0.989}Ba_{0.011}TiOPO_4$	0.21

Table 3.11 shows the stoichiometric concentration of Ba^{2+} in RTP for compositions containing 2, 8 and 10 mol % of BaO substituting Rb_2O in solution. These values show that after 2 mol % of BaO substitution, the distribution coefficient decreases

considerably and the crystal composition hardly changes. For this reason we grew epitaxial layers from solutions with 2 mol % of Rb_2O substituted by BaO.

We also carried out X-Ray diffraction measurements to calculate the unit cell parameters of Ba:RTP. Since the concentration of Ba^{2+} in RTP was almost the same in all the substitutions studied (see table 3.11), we performed the X-Ray diffraction measurements using the crystals obtained from a solution with 2 mol % of Rb_2O substituted by BaO and the unit cell parameters obtained were: **a** = 12.9587 Å, **b** = 6.4998 Å and **c** = 10.5557 Å.

Taking into account that 2 mol % substitution of Rb_2O by BaO in the solution gives a Ba^{2+} distribution coefficient in RTP of almost 1, and that increasing the BaO concentration in the solution hardly changes the crystal composition (see table 3.11), we used this fixed BaO concentration to study the variation of the crystallization region of RTP when part of the TiO_2 is substituted by Nb_2O_5 and Yb_2O_3. For this study we chose a basic solution with a composition of Rb_2O – BaO - P_2O_5 - (TiO_2 + Nb_2O_5 + Yb_2O_3) – WO_3 = 43.02 – 0.88 – 23.6 – 22.5 – 10 (mol%).

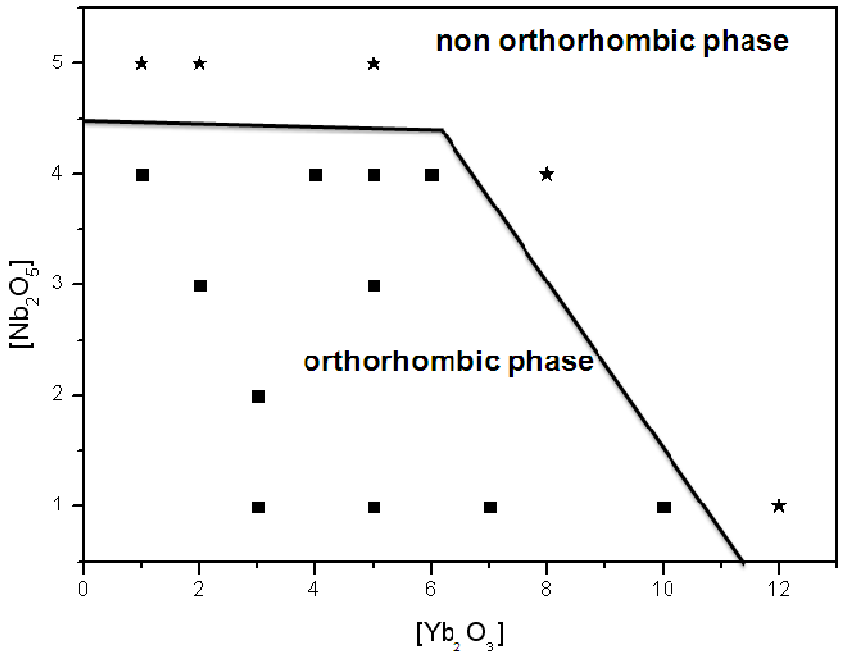

Figure 3.8. Variation of the crystallization region of Ba:RTP with the substitution of TiO_2 by Nb_2O_5 and Yb_2O_3, taking a basic solution with a molar composition of Rb_2O – BaO - P_2O_5 - (TiO_2 + Nb_2O_5 + Yb_2O_3) – WO_3 = 43.02 – 0.88 – 23.6 – 22.5 – 10 (mol%)

As figure 3.8 shows, substituting TiO_2 by Yb_2O_3 in the solution maintains the Ba:RTP orthorhombic phase as the primary crystallization until a substitution of 10 mol %,

while substituting TiO_2 by Nb_2O_5 maintains the Ba:RTP phase until a substitution of 4 mol %.

The substitution used to grow the epitaxial layers was 2 mol % of TiO_2 substituted by Nb_2O_5 and 6 mol % of TiO_2 substituted by Yb_2O_3 in solution, since this combination provides good results in terms of lattice mismatch and distribution coefficients (see Paper I).

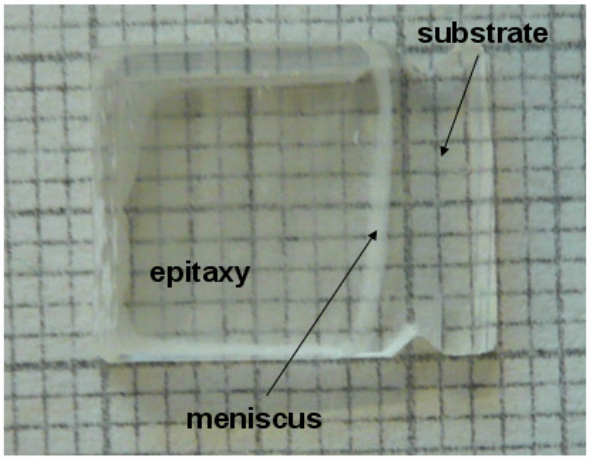

Figure 3.9. As-grown (Ba,Yb,Nb):RTP/RTP (001) epitaxial layer, grown from a solution with composition Rb_2O – BaO - P_2O_5 - TiO_2 - Nb_2O_5 - Yb_2O_3 – WO_3 = 43.02 – 0.88 – 23.6 – 20.7 – 0.45 – 1.35 - 10 (mol %)

As can be seen in figure 3.9 and figure 1 in paper V, the epitaxial layers obtained were transparent and free of both inclusions and cracks. After growth and morphological characterization, they were polished to 10 or 5 μm, depending on the case, in order to obtain PWGs.

3.2.3. (Yb,Nb):$RbTiOPO_4$ and (Ba,Yb,Nb):$RbTiOPO_4$ PWGs on K:$RbTiOPO_4$ (001) substrates

We used a third strategy to obtain planar waveguides suitable for guiding the light in TE and TM polarizations. It consisted of growing Yb^{3+} and Nb^{5+} doped RTP epitaxial layers on RTP doped with K^+ substrates. The crystal growth characteristics of the K:RTP crystals to be used for substrates have been described in section 3.1.2.

The epilayers grown on K^+ doped RTP substrates were obtained from two different solution compositions, both containing 10 mol % of WO_3. The composition of the first solution was: Rb_2O - BaO - P_2O_5 - TiO_2 – Nb_2O_5 – Yb_2O_3 - WO_3 = 43.02 – 0.88 – 23.60

– 20.7 – 0.45 – 1.35 - 10 (mol %). The second solution did not contain BaO and its composition was: Rb_2O - P_2O_5 - TiO_2 – Nb_2O_5 – Yb_2O_3 - WO_3 = 43.90 – 23.60 – 20.7 – 0.45 – 1.35 - 10 (mol %).

The thickness and transparency of the epitaxial layers grown using both solution compositions on K:RTP substrates were similar to those obtained using RTP substrates. However, in a more detailed view, some straight cracks parallel to the ***b*** crystallographic direction appeared in all the epitaxies grown.

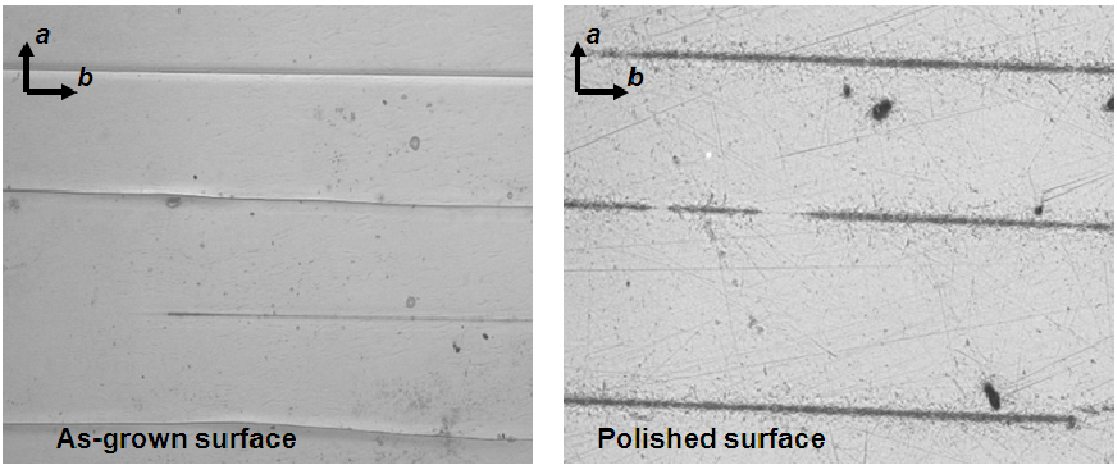

Figure 3.10. Image of the cracks that appeared on the epilayer surface and the same cracks after polishing the epitaxy to a thickness of 10 μm

Figure 3.10 shows the defects in the epitaxial layers grown on K^+ doped RTP substrates. As can be seen in the figure, the defects run throughout the epitaxies disabling them as a base for microstructuration.

3.3. Fabrication of rib waveguides

The aim of integrated photonics (IP) is to fabricate useful devices based on transference of light in the micro world. Integrated photonics uses guided light as a signal and information transfer. As integrated electronics have Cu cables that confine the electrons, IP has rib and channel waveguides to confine the light in two dimensions.

This section presents the results obtained for the fabrication of surface rib waveguides, and describes the procedures used in the fabrication. In this study three techniques have been used to fabricate rib waveguides on (Yb,Nb):RTP/RTP planar waveguides: fs-laser ablation, Ar^+ ion milling and reactive ion etching (RIE).

3.3.1. Rib waveguides by fs-laser ablation

One of the techniques used to fabricate rib waveguides on (Yb,Nb):RTP/RTP planar waveguides is fs-laser ablation. The technique and procedure used to obtain these ribs have been described in detail in section 2.1.4.1. The PWGs used as a basis for fabricating rib waveguides were (Yb,Nb):RTP/RTP epitaxial layers grown by LPE (see section 3.2.1). The epitaxial layers were polished to a thickness of 10 μm before the rib waveguides were made.

As has been explained in section 2.1.4.1, a spatial light modulator was used to obtain seven spots arranged diagonally. For this purpose, a phase map was designed. The multiplexed beam and the phase map can be seen in figure 1 of paper VI.

The rib waveguides were micromachined on the 10 μm-thick PWGs by fs-laser ablation by making two consecutive grooves, with a separation between them of less than 20 μm.

An initial simulation was carried out to obtain information about the waveguide confinement in relation to the rib dimensions and refractive indices. For rib waveguides that were 8 μm deep and 6 to 18 μm wide, the confinement values were higher than 99% in all cases. The rib depth was set at 8 μm, since this value resulted in a good balance in terms of rib wall roughness between fs-laser energy and the spot designed.

Several ribs of different widths were fs-laser micromachined on the PWG surfaces. All the grooves were ablated using the fs-laser parameters described in the experimental techniques chapter.

The main results of the rib waveguides fabricated by the fs-laser ablation technique are reported in paper VI. The end-faces of the sample (PWG and ribs) were polished to show the real shape of the ribs. These were trapezoidal in shape (see figure 2 in paper VI). In fact, the bases of the ribs fabricated were 4 μm wider than their tops. Figure 3.11 shows an ESEM image of the top of the rib waveguides fabricated by fs-laser ablation.

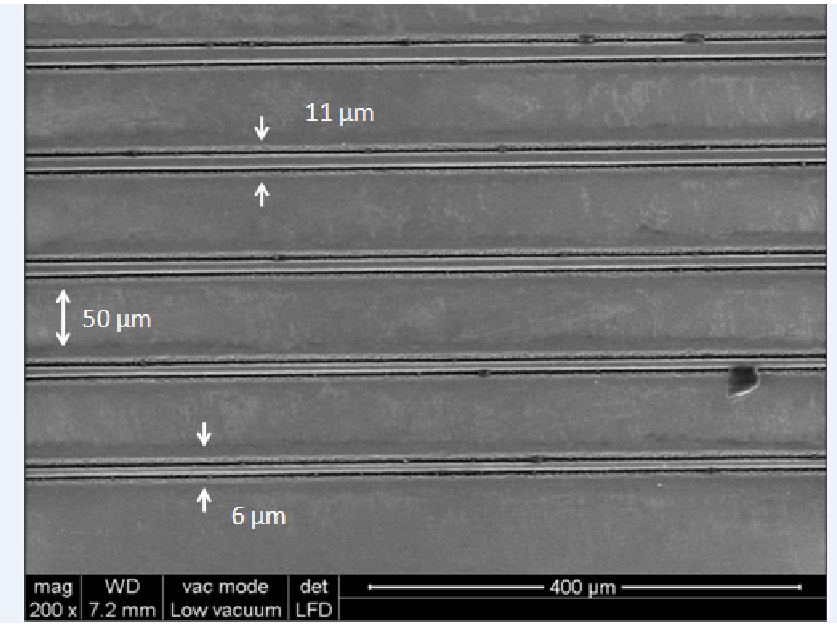

Figure 3.11. ESEM image of rib waveguides fabricated on a (Yb,Nb):RTP/RTP epilayer by fs-laser ablation

3.3.2. Rib waveguides by Ar^+ ion milling

Surface rib waveguides. In this case, we performed some computer simulations to determine a suitable width and depth for the rib waveguides. The PWGs used to obtain surface rib waveguides were 5 µm thick. So, rib waveguides 3 µm deep were simulated on hypothetical (Yb,Nb):RTP/RTP planar waveguides. The refractive indices used in the simulation were measured at 972 nm, since this was the pumping wavelength used to excite the Yb^{3+} in (Yb,Nb):RTP and obtain laser radiation. These values are shown in Table 1 of paper VII.

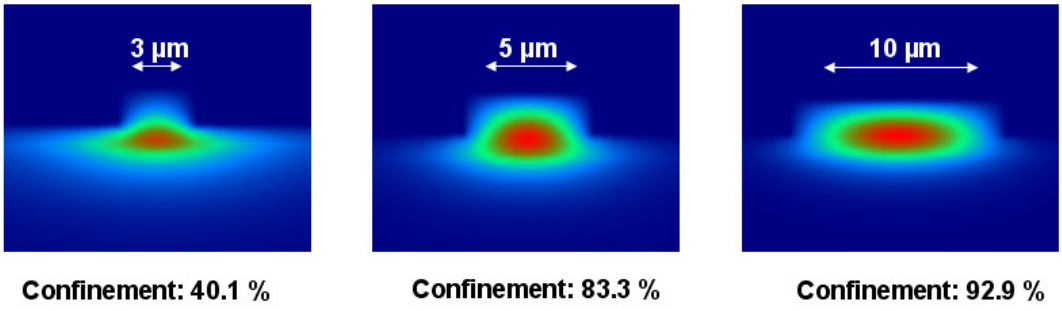

Figure 3.12. Simulation of rib waveguides with different widths

As can be seen in figure 3.12, several rib waveguides were simulated. The depth of the ribs was 3 μm and they were rectangular in shape. The remaining planar waveguide was 2 μm deep. We changed the width of the rib in each simulation in order to obtain a good balance between the confinement and the width of the rib. As can be seen in figure 3.12 the rib that is 3 μm wide has the lowest confinement. On the other hand, the ribs that are 5 and 10 μm wide have qualitatively higher confinement (83.3 % and 92.9 %, respectively). These results show that the rib waveguides can be manufactured on (Yb,Nb):RTP/RTP planar waveguides with high confinements.

The PWGs used to fabricate surface ribs were obtained by LPE, as is explained in sections 3.2.1 - 3.2.3. The composition of the solution used to obtain the epitaxial layers was RbO - P_2O_5 - TiO_2 - Yb_2O_3 - Nb_2O_5 – WO_3 = 43.9 - 23.6 - 20.7 - 1.35 - 0.45 – 10 (mol %). This solution composition has the highest Yb^{3+} atomic concentration of all the solutions used in this study to growth epitaxies (see composition 9 in table 3.8). After the growth of the epitaxial layers, they were polished to a thickness of 5 μm with high optical quality.

In this study, the Ar^+ ion milling technique was applied to make rib waveguides on RTP substrates, for the first time to our knowledge. A 4 μm-thick positive resist (PR) film was spun on an RTP substrate. This procedure is described in chapter 2. The masked sample was held at 45º and rotated at 5 rpm during the process. The substrate, with the PR film pattern, was exposed to an Ar^+ ion beam (accelerated at 500 V with a beam current of 100 mA) for different etching times. In this way, the etch rate could be determined. After these experiments, the etch rate of the resist was estimated to be ~ 1.17 μm/h and that of the RTP ~ 1.15 μm/h. Therefore, for a 3 μm-thick resist layer it would be possible to etch almost ~ 3 μm into the RTP substrate.

The ribs obtained were 2.9 μm deep (see figure 2 in paper VII) and ranged from 3 to 10 μm wide, which is logical taking into account the dimensions of the dark-light mask used (see section 2.1.4.4). Finally, they were 9 mm long.

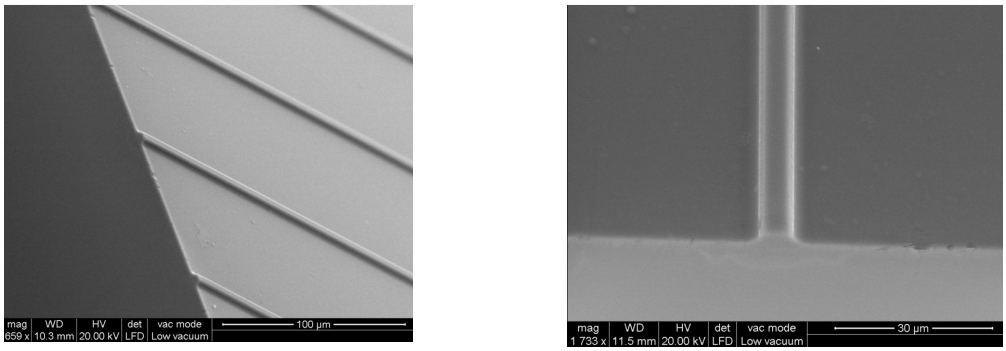

Figure 3.13. General and detailed view of the rib waveguides by ESEM

Figure 3.13 shows the good quality of the channels, the apparent low roughness of the milled surface and the symmetry of the groves. The inset in figure 4 in paper VII shows a cross section of the rib, and it is easy to see the trapezoidal shape. In all cases, these ribs were 4 µm longer at the base than at the top.

Buried rib waveguides. To our knowledge, this study has shown for the first time that it is possible to obtain high quality thin layers of (Yb,Nb):RTP grown by LPE on structured RTP.

The substrates were microstructured by Ar^+ ion milling (see section 2.1.4.2). The nominal width of the groove patterns fabricated on the substrates ranged from 8.6 to 10.0 µm, and the etch depth was 5.1 µm. Figure 3.14 shows a top view of the channels fabricated on an RTP substrate. The inset in the same figure shows a 3D image of two channels.

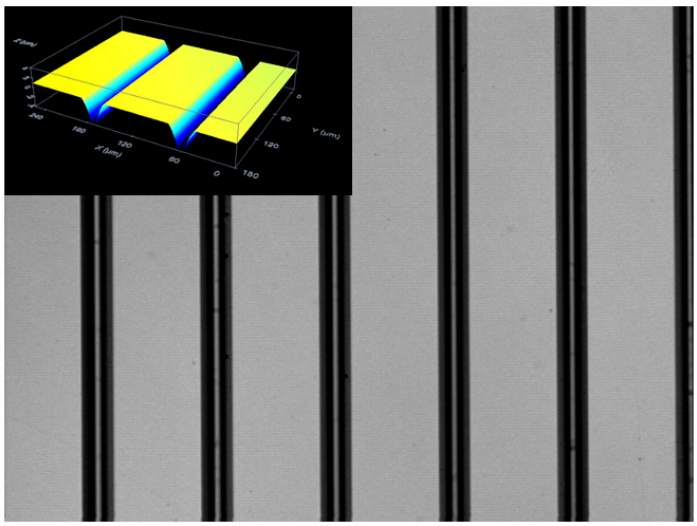

Figure 3.14. Top view of the channels fabricated on a RTP substrate and a 3D image of two channels

A (Yb,Nb):RTP film was grown by LPE over the microstructured surface, filling the grooves and producing buried ribs. The composition of the solution used to grow the epitaxial film was the same as the composition used to grow the surface rib waveguides on a RTP substrate microstructured by Ar^+ ion milling (basic composition 2 in table 3.6). The layer obtained had an average thickness of ~ 40 μm. This film was polished to a thickness of 6 μm to obtain buried rib waveguides. Finally, a RTP cladding was grown over the planar waveguide by LPE. The composition used to grow the cladding was Rb_2O - P_2O_5 - TiO_2 - WO_3 = 44.24 – 18.96 – 16.8 – 20 (mol %), the same as was used to grow the bulk single crystals for substrates.

Figure 3.15 shows a cross section of the ribs after end-face polishing. The ribs, epitaxial film and cladding were free of inclusions and cracks on the μm scale.

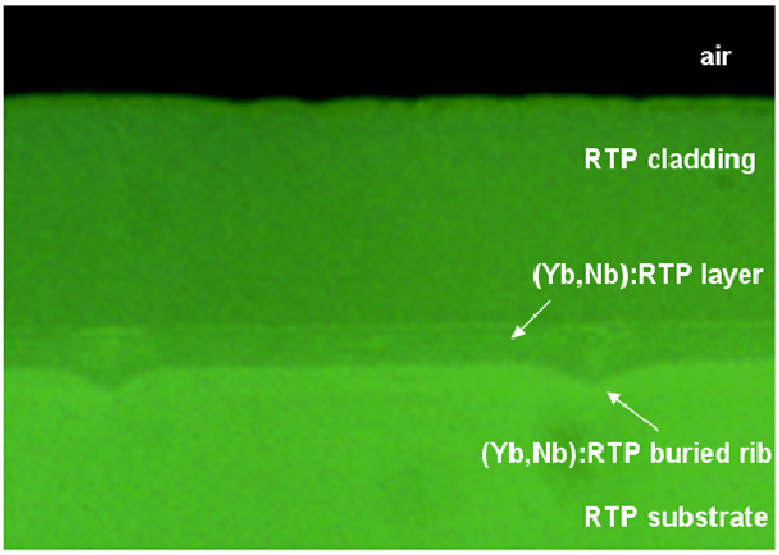

Figure 3.15. Cross section of buried rib waveguides

3.3.3. Rib waveguides by RIE

The planar waveguides used to produce ribs by RIE were fabricated from epitaxial films grown by LPE, as in the previous sections. The composition of the solution used to grow the epitaxial layers was Rb_2O - P_2O_5 - TiO_2 - Yb_2O_3 - Nb_2O_5 - WO_3 = 43.90 - 23.60 - 20.70 - 1.35 - 0.45 - 10 (mol %), the same as was used to grow the films for rib fabrication by ion milling and fs-laser ablation (composition number 2 in table 3.6 with 6 mol% and 2 mol% of TiO_2 substituted by Yb_2O_3 and Nb_2O_5 in solution, respectively).

A preliminary study of the rib waveguides obtained by RIE on RTP substrates was made by varying the power, gas pressure and gas ratio (see paper VIII). The procedure

used was to vary one of these three parameters while the other two parameters remained fixed.

The starting parameters were an RF power of 250 W, a pressure of 50 mTorr, a gas flow rate of 20 sccm and a gas ratio of SF_6:Ar = 90:10. This study shows the effect of these parameters on the etch rate and roughness of the rib waveguide for an etch time of 40 min in all the experiments. Figure 2 of paper VIII shows the result of this study. In summary, the etch rate increases linearly as the power increases and the roughness also increases with the power. The balance between surface roughness and etch rate was good for a power of 250 W. Then, by maintaining the RF power at 250 W and the gas ratio at SF_6:Ar = 90:10 and varying the pressure, it was found that the etch rate decreases with the pressure. A pressure of 50 mTorr gives an etch rate of 8 nm/min and a surface roughness of 1.6 nm. Finally, with a fixed RF power of 250 W and a pressure of 50 mTorr, a study was made of the dependence of the etch rate and roughness on the gas ratio (SF_6:Ar). Results were best for a gas ratio (SF_6:Ar) in the range 50:50 to 70:30, where the etch rate is about 8 nm/min and the surface roughness is less than 1 nm.

(Yb,Nb):RTP/RTP PWGs were microstructured by RIE in two steps: first, the film was etched for 135 minutes by RIE, with a power of 250 W, a gas pressure of 40 mTorr and a gas flow rate of 10 sccm for both SF_6 and Ar. After end-polishing and cleaning, the sample was plasma-ashed in an RIE chamber for 20 minutes with an RIE power of 200 W, a pressure of 50 mTorr and an O_2 flow rate of 10 sccm, which removed any organic impurities present on the substrate.

Figures 3 and 4 of paper VIII show SEM and topographic images of the rib waveguides obtained.

3.4. Channel and planar waveguides by Cs^+ ion exchange

As has been mentioned in the introduction, RTP has many properties that make it interesting for integrated optics. It has high nonlinear optical coefficients, a high damage threshold, and high electro-optical coefficients. It is also a suitable candidate as self frequency doubling (SFD) material, since it can be doped with Yb^{3+} active ions to levels high enough for laser emission [127]. Moreover, periodic poling of RTP has recently been demonstrated by applying a high voltage electric field [100]. Because of all these properties, and those mentioned in the introduction, RTP is an interesting and promising material as a base for integrated optics.

It is interesting to demonstrate that planar waveguides can be created and channel waveguides fabricated by Cs^+ ion exchange.

In an initial stage, we tested the possibilities of Cs^+ ion exchange on RTP to produce PWGs. RTP substrates with areas around 0.7×0.7 cm^2 were used for Cs^+ ion exchange experiments. Diffusions were performed in a $CsNO_3$ melt (for the complete procedure applied in these experiments, see section 2.1.4). Depending on the experiment, the Cs^+ ion exchange took 1, 2, 3 or 5 h. In total, 15 experiments were carried out in which all the experimental conditions were kept the same except the diffusion time. In general, the experiments with a Cs^+ diffusion of 2, 3 and 5 h, generally produced multimodal PWGs. On the other hand, experiments with a diffusion of 1 h mainly produced single-mode PWGs, although some experiments produced no modes at all. For a diffusion time of 3 h or more, the surface of the PWGs generally present some etching region produced by the $CsNO_3$ solution at 698 K.

In the experiments with long diffusion times (more than 3 h), the Cs^+ exchange has a stagnation effect. This may be due to the formation of a Cs^+ diffusion barrier in the substrate when diffusion times are long enough [130]. Thus, we observed an increase in the propagation modes in the waveguide from the beginning of the Cs^+ diffusion to a diffusion time of about 3 h. After that, the number of propagation modes remained constant or even decreased for samples with diffusion times of 5 h or longer.

All the experiments carried out with a diffusion time of 2 h produced multimodal waveguides, and the samples were free of etching. For this reason, the 2 h diffusion experiments were best at producing PWGs and channel waveguides. These multimodal waveguides were free of etching and avoided the scattering losses.

An RTP substrate of 15 x 15 x 2 mm^3 (***a*** x ***b*** x ***c*** crystallographic directions) was polished so that it could be used in the Cs^+ ion exchange process. As can be inferred from these dimensions, the diffusion took place in the ***c*** crystallographic direction. The procedure is described in section 2.1.4. Figure 3.16 shows the Ti dark field mask fabricated directly on the RTP substrate before the Cs^+ ion exchange process. Figure 1 in paper IX shows a more general view of this mask on the substrate. The widths of the channels obtained ranged from 6 to 11 μm with an error of 0.2 μm. The channels were fabricated parallel to the ***b*** crystallographic direction.

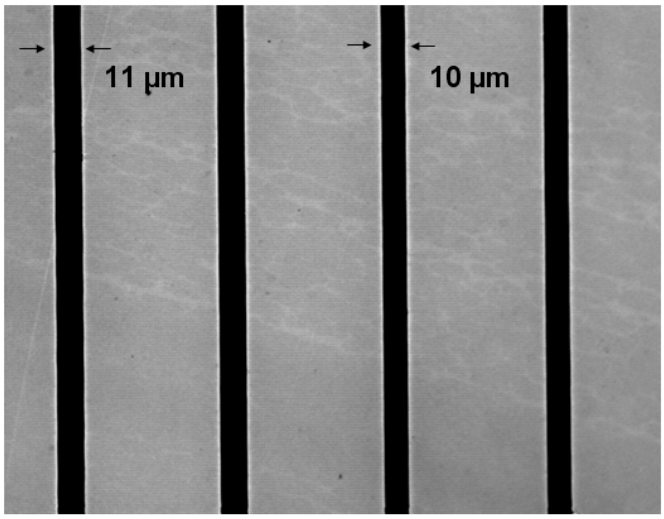

Figure 3.16. Ti dark field mask on a RTP substrate

To obtain samples for characterization, the diffusion was carried out for 2 h using the procedure explained in section 2.1.4.4. The end faces were polished to high optical quality so that the waveguides could be characterised. A transmission image of the channels (see figure 2 in paper IX) shows that the diffusion takes around 20 µm and is straight parallel to the ***c*** crystallographic direction. The dark mode spectra measured from the face without the Ti mask, were used to extrapolate the index profile. In fact, the four TE guided modes fit an exponential function of the form $n(x)=n_{subs}+\Delta n e^{-x/d}$. With a maximum index at the surface of $\Delta n = 0.038$ and a depth of $d = 1.80$ µm.

Chapter 4

Waveguide Characterization

Waveguides must be characterized to know their guiding properties. For instance, a PWG will be determined by its thickness, the refractive indices of the film and the substrate, and the quality of the substrate-layer interface. The number of guiding modes supported by a planar waveguide can be calculated using the layer thickness and the refractive index contrast between the layer and the substrate. In channel waveguides, in addition to the contrast of refractive indices between the layer and the substrate, the geometry and channel dimensions are very important. The loss of the light traveling through the waveguide and the near field pattern give information about the guiding process in the waveguide. In fact, the near field pattern of a waveguide provides experimental proof of the ability of the waveguide to guide.

Thus, in this study, the refractive indices of the substrates and the epitaxial layers have been carefully determined, so that the number of modes supported by the planar waveguides as a function of the thickness can be calculated. The losses in the channel waveguides have been estimated and the near field patterns have been recorded for both, planar and channel waveguides. The second harmonic generation (SHG) process inside

the nonlinear optical (NLO) waveguides has been checked and green light has been obtained from fundamental infrared radiation coupled to the waveguides.

4.1. Basic theoretical concepts of planar waveguides

Planar waveguides are structures that confine light to only one dimension. However, the most common geometry used in integrated photonics is the channel waveguide. In this kind of waveguide light is confined to two dimensions, which allows it to be propagated only along the third one. Obviously, in channel waveguides propagation losses are lower than in planar ones, due to the additional dimension for confinement.

In order to understand the propagation of light inside a waveguide, we need to subject it to mathematical treatment. We pay particular attention to planar waveguides because this treatment is easier than in channel waveguides, and gives a theoretical overview of waveguide behavior.

For simplicity, in this part, a ray optics treatment of planar waveguides, not a wave optics treatment, will be presented. This provides us with the main concepts of a planar waveguide. Subsequently a more extensive and detailed wave treatment will be presented using electromagnetic theory.

A step index planar waveguide consists of a layer of thickness d and refractive index n_{layer} on a substrate with a lower refractive index n_{sub}. The cladding, which is the external boundary, also has a lower refractive index, n_{clad}, than the layer. In summary, $n_{layer} > n_{sub}$ and $n_{layer} > n_{clad}$.

Since the refractive index of the layer is higher than that of the surroundings, if the reflection angle, θ, is higher than the critical angles (in the two interfaces), the light is confined in the waveguide by total internal reflections.

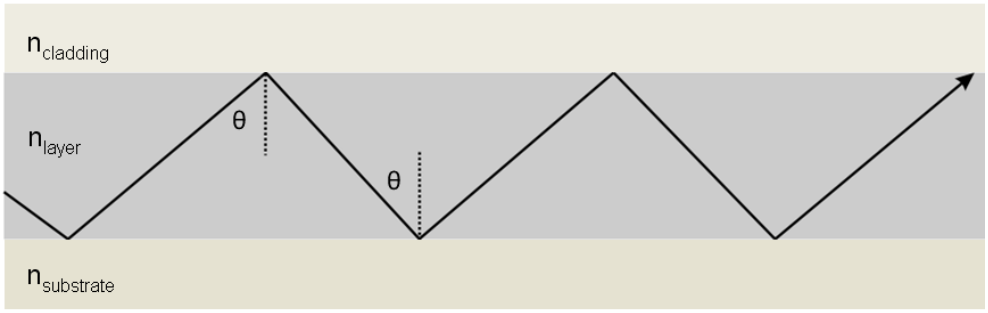

Figure 4.1. Scheme of a ray travelling through the waveguide

We can calculate the critical angles in the layer-substrate and layer-cladding interfaces, $\theta_{crit\,sub} = \sin^{-1}\left(\frac{n_{sub}}{n_{layer}}\right)$ and $\theta_{crit\,clad} = \sin^{-1}\left(\frac{n_{clad}}{n_{layer}}\right)$, from which, for larger incident angles in these interfaces ($\theta > \theta_{crit\ sub}$ and $\theta > \theta_{crit\ clad}$) a total reflection is produced. In this case, the ray of light propagates in a zig-zag pathway through the layer, as can be seen in figure 4.1

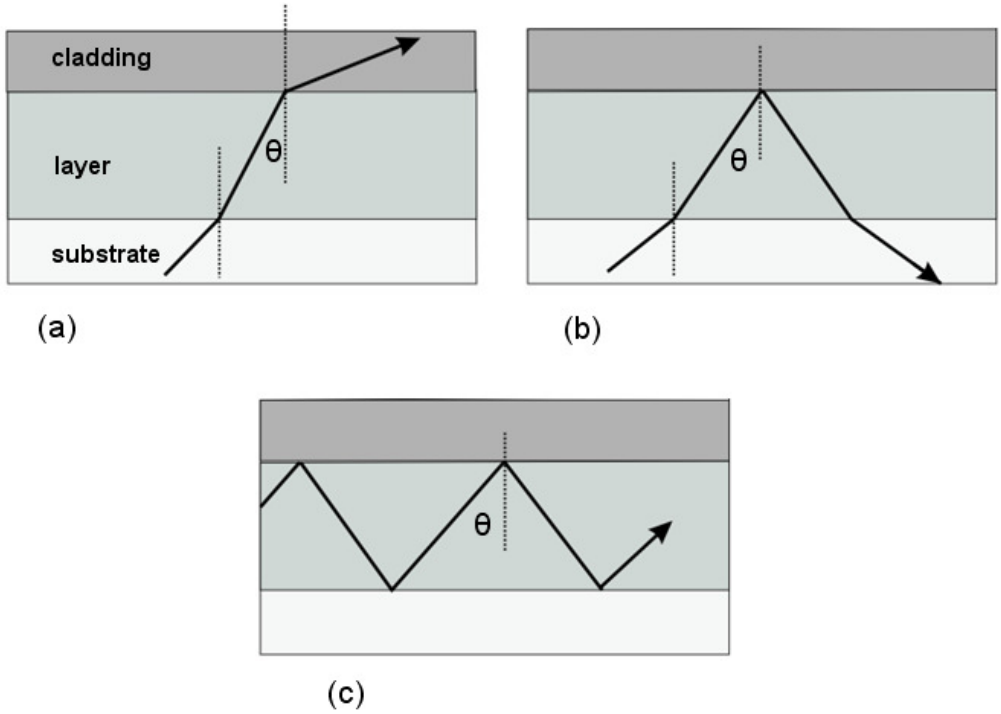

Figure 4.2. Types of mode in a waveguide: (a) radiation mode, (b) substrate mode, and (c) guided mode

If we consider that $n_{layer} > n_{sub} > n_{clad}$, the critical angle at the layer-substrate interface, ($\theta_{crit\ sub}$), is larger than the critical angle at the layer-cladding interface ($\theta_{crit\ clad}$), $\theta_{crit\ sub} > \theta_{crit\ clad}$ and we can distinguish three cases [101], depending on the incident angle of the light:

a) $\theta < \theta_{crit\ clad} < \theta_{crit\ sub}$. In this case the light is not confined and travels through the three regions: substrate, layer and cladding (figure 4.2.a).

b) $\theta_{crit\ clad} < \theta < \theta_{crit\ sub}$. In this case a total reflection at the layer-cladding interface is produced, but the incident angle at the layer-substrate interface is lower than the critical angle and the light penetrates the substrate (figure 4.2.b).

c) $\theta > \theta_{crit\ sub} > \theta_{crit\ clad}$. In this case, total internal reflection of the rays is produced at the two interfaces and the light is confined to the layer (figure 4.2.c). This is the most

interesting case for this thesis, because it is a guided mode which propagates through the waveguide.

In addition to the ray treatment presented, we will now move on to introduce the electromagnetic theory of light, applied to a planar waveguide, which is essential for understanding waveguides. From Maxwell's equations we will obtain the wave equations that govern the behavior of light in planar waveguides for TE and TM propagation modes.

In the study of the propagation of light in a waveguide, we can distinguish two types of propagation modes:

a) TE modes, in which the electric field associated with the mode is transversal.

b) TM modes, in which the electric field is parallel to the propagation plane.

In the first case (figure 4.3), the TE mode, the electric field vector has only component E_y, perpendicular to the incident plane (x-z plane), so $E_x = E_z = 0$.

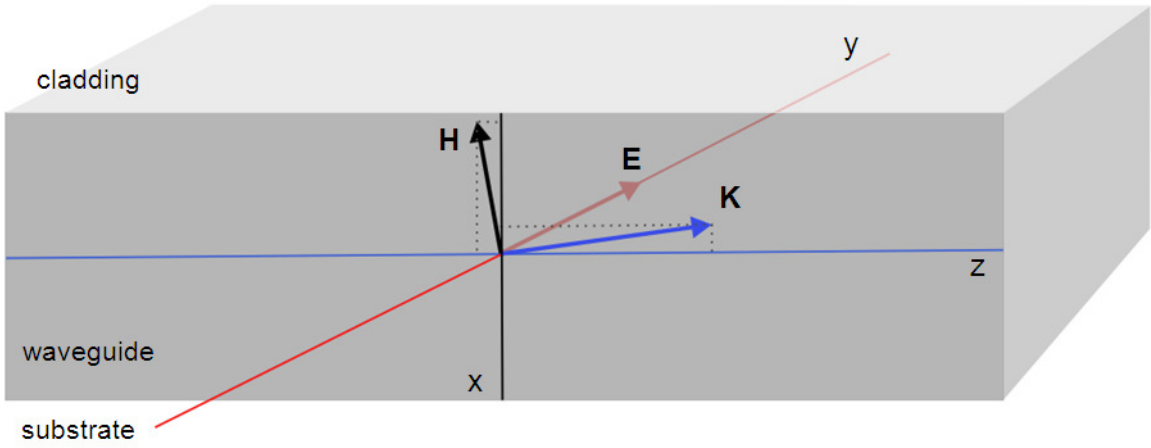

Figure 4.3. TE propagation mode in a planar waveguide

Using Maxwell's equations, and assuming that the light is propagating through a dielectric, non-magnetic and linear material, we can reach the following wave equation [101]:

$$\frac{d^2 E_y(x)}{dx^2} + \left[k^2 n^2(x) - \beta^2\right] E_y(x) = 0 \qquad 4.1$$

where k is the wavenumber and β is the propagation constant of the modes.

In the second case, the TM mode, the electric field vector has only component in the incident plane. Thus, the magnetic field is perpendicular to this plane, as is indicated in figure 4.4:

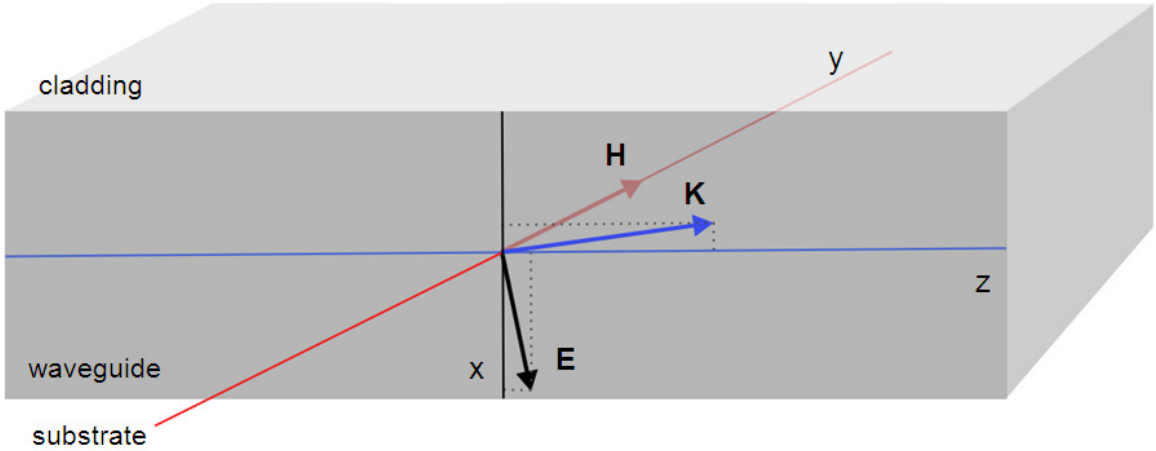

Figure 4.4. TM propagation mode in a planar waveguide

In this case the wave equation is:

$$\frac{d^2 H_y(x)}{dx^2} + \left[k^2 n^2(x) - \beta^2\right] H_y(x) = 0 \qquad 4.2$$

General solution of the waveguide equation for step-index planar waveguides. We will now study the solution of the wave equation for TE polarization. For TM polarization the solution is basically the same, except that the boundary conditions are different. We will examine the mathematical treatment for TE polarization, and for TM polarization will give only the solution with its interpretation.

Starting from wave equation 4.1, characterized by its constant β, we postulate a solution for the E_y (x) component in the form:

$$E_j(x) = A_j e^{i\gamma_j x} + B_j e^{-i\gamma_j x} \qquad 4.3$$

where E_j (x) is the y-component of the electric field in the jth region, which can be the substrate, the layer and the cladding. The parameters A_j and B_j are two complex constants, which will be calculated after imposing the appropriate boundary conditions. Expression (4.3) satisfies equation (4.1) assuming that:

$$\gamma_j = \sqrt{k_j^2 n_j^2 - \beta^2} \qquad 4.4$$

where γ_j is different for each region, characterized by its refractive index n_j (n_{sub}, n_{layer} and n_{clad}).

To discuss the solution in a particular region, we introduce the *effective refractive index* n_{eff}, which represents the refractive index of the mode propagating along the z-axis. This parameter is related to the β of the mode through the formula:

$$\beta \equiv k\, n_{eff} \qquad 4.5$$

The general solution of equation (4.1) given by expression (4.3) can be written in terms of n_{eff} and the refractive indices of different regions, n_j.

In summary, we can say that if the propagation constant $\beta < k\, n_j$ (or $n_{eff} < n_j$) then the parameter γ_j is a real number. Introducing this parameter γ_j into the general solution 4.3, we obtain a sinusoidal function.

On the other hand, if the propagation constant satisfies that $\beta > k\, n_j$ (or $n_{eff} > n_j$), then parameter γ_j is a pure imaginary number, and the general solution 4.3 is an exponential function.

In order to find the guided modes for TE polarization we should take into account each region separately in the step-index planar waveguide. Each one of the three different regions (that is to say, substrate, layer and cladding) has its own refractive index, n_{sub}, n_{layer} and $n_{cladding}$, respectively (figure 4.5).

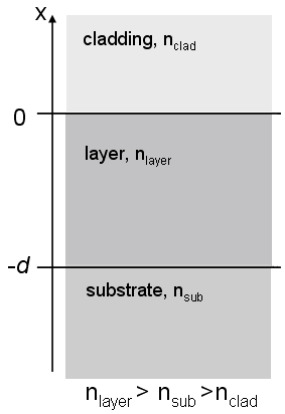

Figure 4.5. Scheme of the distribution of the different regions in a waveguide

The propagation constant β associated with a particular mode must fulfil the condition:

$$k\, n_{sub} < \beta < k\, n_{layer} \qquad 4.6$$

that is

$$n_{sub} < n_{eff} < n_{layer} \tag{4.7}$$

Taking into account the wave equation 4.1 for each of the three regions, we obtain:

$$d^2E_y/dx^2 - \gamma_{clad}^2 E_y = 0 \tag{4.8}$$
$$d^2E_y/dx^2 - \kappa_{layer}^2 E_y = 0 \tag{4.9}$$
$$d^2E_y/dx^2 - \gamma_{sub}^2 E_y = 0 \tag{4.10}$$

where the three parameters γ_{clad}, κ_{layer} and γ_{sub} are given by:

$$\gamma_{clad}^2 = \beta^2 - k^2 n_{clad}^2 \tag{4.11}$$
$$\kappa_{layer}^2 = k^2 n_{layer}^2 - \beta^2 \tag{4.12}$$
$$\gamma_{layer}^2 = \beta^2 - k^2 n_{sub}^2 \tag{4.13}$$

We can obtain the electric field in the cladding, layer and substrate by solving the differential equations 4.8-4.10:

$$E_y(x) = \begin{cases} Ae^{-\gamma_{clad}x} & cladding \\ Be^{i\kappa_{layer}x} + Ce^{-i\kappa_{layer}x} & layer \\ De^{\gamma_{sub}x} & substrate \end{cases} \tag{4.14}$$

Assuming the boundary condition that E_y and dE_y/dx must be continuous at the layer-cladding and layer-substrate interfaces, a set of four equations with five unknown parameters (A, B, C, D and β) are obtained. Thus, the final solution will depend on one of these parameters, in our case, the A parameter.

Using the set of equations to find a general solution, the following equation is obtained:

$$\tan(\kappa_{layer}d) = \frac{\frac{\gamma_{clad}}{\kappa_{layer}} + \frac{\gamma_{sub}}{\kappa_{layer}}}{1 - \left(\frac{\gamma_{clad}}{\kappa_{layer}}\right)\left(\frac{\gamma_{sub}}{\kappa_{layer}}\right)} \tag{4.15}$$

This expression can be regarded as the *dispersion relation* for the asymmetric step-index planar waveguide, and is a transcendental equation that contains the parameters that define the waveguide structure (n_{clad}, n_{layer}, n_{sub}) and the thickness of layer *d*, the working wavelength λ and the propagation constant β of the guided mode. From this

expression one can calculate numerically the propagation constant β. So, according to the tangent function:

$$\tan(\kappa_{layer} d) = \tan(\kappa_{layer} d + m\pi) \qquad m = 0,1,2,\ldots \qquad 4.16$$

This means that, depending on the integer number m, there are several solutions for propagation constant β. This number is called *mode order*.

Now, after propagation constant β has been calculated, the electric field in the three regions can be completely determined:

$$E_y(x) = \begin{cases} Ae^{-\gamma_{clad} x} & cladding \\ A\left(\cos(\kappa_{layer} x) - \dfrac{\gamma_{clad}}{\kappa_{layer}} \sin(\kappa_{layer} x)\right) & layer \\ A\left(\cos(\kappa_{layer} d) + \dfrac{\gamma_{clad}}{\kappa_{layer}} \sin(\kappa_{layer} d)\right) e^{\gamma_{sub}(x+d)} & substrate \end{cases} \qquad 4.17$$

The meaning of the above expression is easy to understand; the electric field decreases exponentially in the cladding and in the substrate, while its dependence is sinusoidal in the layer. This result was expected for the behaviour of a confined mode.

Figure 4.6 shows the graph of the mathematical expression 4.17 for m order 0, 1 and 2. It corresponds to the electric profiles of the first confined modes, supported by a planar waveguide.

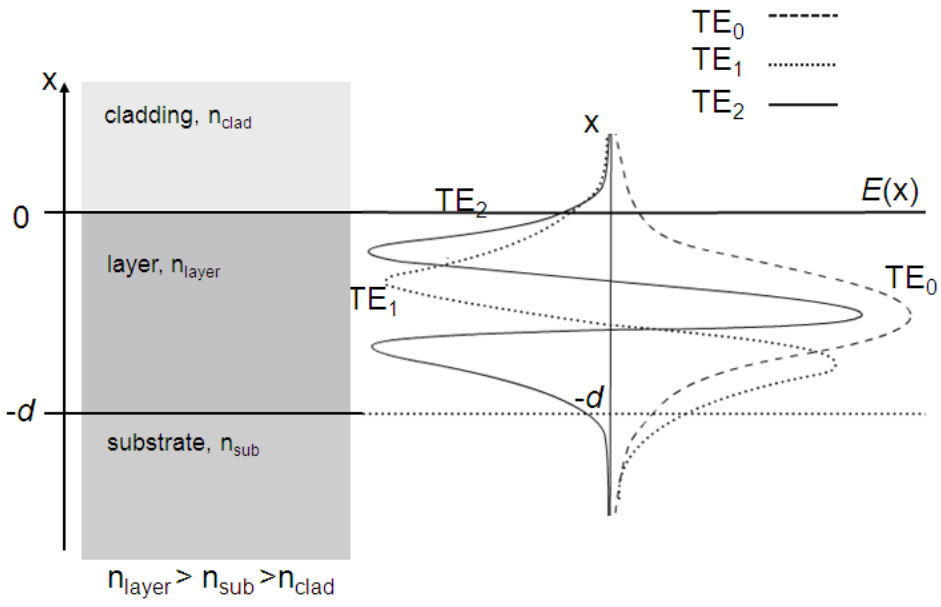

Figure 4.6. TE modes in an asymmetric step-index planar waveguide

4.2. Characterization of the planar waveguides

One important objective of this thesis is to demonstrate the possibility of fabricating channel waveguides on Yb^{3+} doped RTP. So, one of the ways to make these channels in a material is to microstructure previously fabricated PWGs on this material. In this procedure, PWGs need to be fabricated if channel waveguides are to be obtained subsequently. As has been mentioned in the chapter on fabrication, several strategies were used to obtain Yb^{3+} doped RTP planar waveguides, and their characterization will be presented in the following sections.

4.2.1. (Yb,Nb):$RbTiOPO_4$ on $RbTiOPO_4$ (001) substrates

In this study, RTP doped with Yb^{3+} and Nb^{5+} planar waveguides of 5 and 10 μm in thickness have been fabricated on RTP substrates. The fabrication procedure of these PWGs has been extensively described in section 3.2.1.

As was mentioned in the chapter on fabrication, different substitutions of TiO_2 for Yb_2O_3 and Nb_2O_5 have been used. With these substitutions we obtained PWGs with different compositions of Ti^{4+}, Yb^{3+} and Nb^{5+} in the $RbTi_{1-x-y}Yb_xNb_yOPO_4$ stoichiometry. This means that each film has different refractive indices and the PWGs obtained have different guiding properties. The stoichiometric composition of the layers has been presented in table 3.8 of chapter 3. Table 4.1 shows the refractive indices of the epitaxial layers and the substrates for each principal optical direction in several PWGs.

Table 4.1. Refractive indices of the layer and substrate in experiments 4, 6, 8, 9 and 11 of table 3.7.

Exp. No.	Stoichiometric composition of layer/substrate	n_x	n_y	n_z
4	$RbTi_{0.995}Yb_{0.005}OPO_4$	1.7864	1.7981	1.8863
	$RbTiOPO_4$	1.7892	1.8010	1.8882
6	$RbTi_{0.975}Yb_{0.014}Nb_{0.011}OPO_4$	1.7886	1.8019	1.8935
	$RbTiOPO_4$	1.7894	1.8013	1.8889
8	$RbTi_{0.971}Yb_{0.015}Nb_{0.014}OPO_4$	1.7872	1.8018	1.8956

	$RbTiOPO_4$	1.7895	1.8015	1.8898
9	$RbTi_{0.958}Yb_{0.016}Nb_{0.026}OPO_4$	1.7863	1.8016	1.8967
	$RbTiOPO_4$	1.7893	1.8015	1.8897
11	$RbTi_{0.983}Yb_{0.004}Nb_{0.013}OPO_4$	1.7885	1.8016	1.8944
	$RbTiOPO_4$	1.7894	1.8013	1.8884

As an example, Figure 4.7 shows the dark mode spectra for different polarizations of a PWG fabricated in this study. These measurements were recorded at a wavelength of 632.8 nm. The epitaxy used was $RbTi_{0.958}Yb_{0.016}Nb_{0.026}OPO_4/RbTiOPO_4$ which corresponds to experiment 9 in table 3.7. The PWGs fabricated using RTP doped with Nb^{5+} and Yb^{3+} show guided modes in TM polarization only. In fact, the refractive indices of the film were higher than the ones of the substrate only in E//***b*** and E//***c*** polarizations. For E//***a***, the refractive index of the film was lower than the refractive index of the substrate, which means that E//***a*** polarized light can not be guided through the waveguide. Guidance was not possible either in the E//***b*** polarization because of the small contrast of refractive indices, which were one order of magnitude lower than in the case of E//***c*** polarization.

The fact that these PWGs could not guide the light in TE polarization makes them unable to produce guided green light by Type II SHG because, as was explained in the introduction, this nonlinear optical process requires both polarizations, TE and TM, simultaneously.

The near field patterns at 632.8 and 972 nm of all the PWGs fabricated were recorded with a CCD camera. To prove that they could guide the light, papers I and II show some examples of these near field patterns. In fact, all the PWGs were multimodal in TM polarization, and in some cases we were able to separately excite some high order modes. For instance, paper I presents the modes with order m = 0, 1, 2, 3 and 4 at a wavelength of 632.8 nm. On the other hand, as an example, figure 4.8 shows the near field pattern of the TM modes of order 1 and 3 at a wavelength of 972 nm. The PWG used to produce the images shown in figure 4.8 corresponds to experiment 9 in table 3.7.

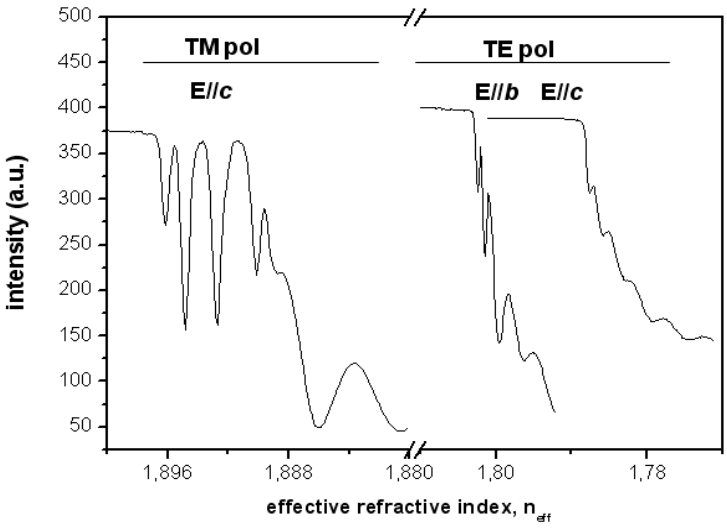

Figure 4.7. Dark mode spectra at 632.8 nm for each polarization

Because of the importance of green light in this study, we checked the guiding possibilities at 532 nm of the PWG fabricated in experiment 8 of table 3.7 and described in Paper I. Figure 4.9 shows the near field pattern of the modes obtained at of 532 nm.

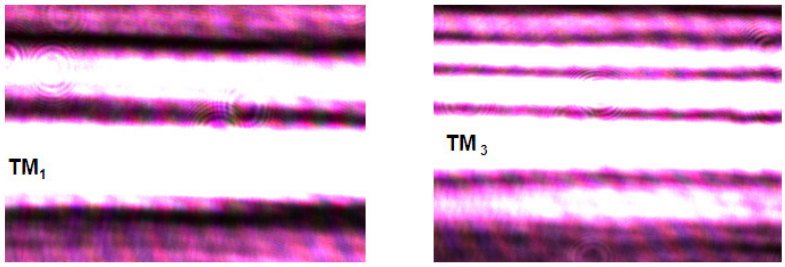

Figure 4.8. Near field pattern of modes TM_1 and TM_3 at 972 nm

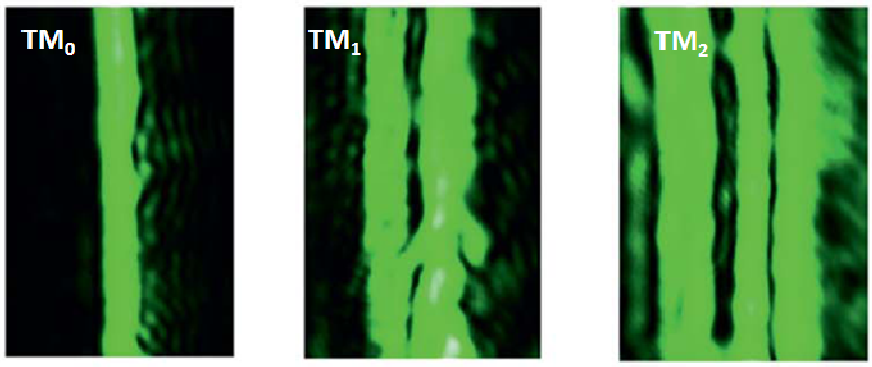

Figure 4.9. Near field pattern of TM_o, TM_1 and TM_2 modes at 532 nm

4.2.2. (Ba, Yb, Nb):$RbTiOPO_4$ on $RbTiOPO_4$ (001) substrates

Unlike the PWGs discussed in the section above, the epitaxial layers grown with Ba^{2+}, and Nb^{5+} and Yb^{3+} as doping elements, produce PWGs with guided modes in TE and TM polarizations. In this case, only one growth composition was used, BaO-Rb_2O-P_2O_5-TiO_2-Nb_2O_5-Yb_2O_3=0.88-43.02-23.61-20.70-0.45-1.35-10.00 (mol %), which was suitable for obtaining PWGs that could guide the light in two polarizations.

Figure 4.10 shows the number of propagation modes which depend on the epitaxial layer thickness, calculated using the refractive indices shown in table 4.2. As can be seen in this figure, a 10 µm thickness waveguide can support two propagation modes for E//***b*** polarization.

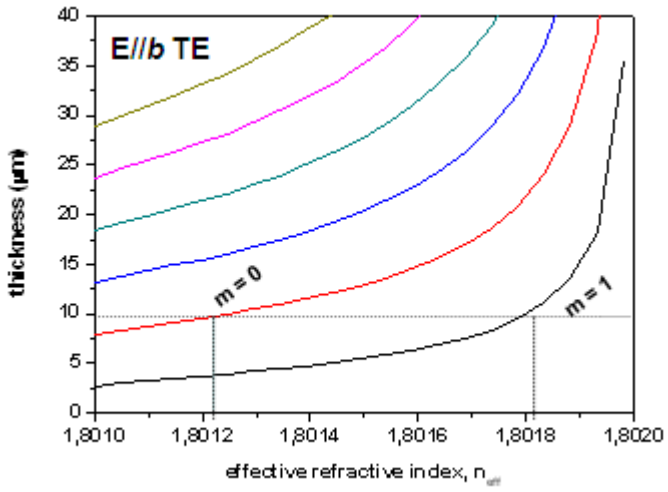

Figure 4.10. Propagation modes as a function of the layer thickness in (Ba,Yb,Nb):$RbTiOPO_4$/$RbTiOPO_4$ (001) PWG in TE (E//***b***) polarization

Table 4.2 shows the refractive indices of the epitaxial layer for several wavelengths and different polarizations, as well as the refractive indices of the RTP substrate at 632.8 nm. These results are also shown in paper IV. This table confirms that the refractive indices of the epitaxial layer are higher than those of the substrate for E//***b*** and E//***c*** polarizations.

Table 4.2. Refractive indices of the (Ba, Yb, Nb):$RbTiOPO_4$ on $RbTiOPO_4$ (001) substrates

Refractive indices of the layer			
Wavelength [nm]	$\mathbf{n_x}$	$\mathbf{n_y}$	$\mathbf{n_z}$
532.0	1.805	1.822	1.921
632.8	1.788	1.802	1.896
770.0	1.776	1.787	1.875
780.4	1.775	1.788	1.873
790.0	1.774	1.786	1.873
820.4	1.772	1.786	1.869
840.9	1.771	1.785	1.867
971.0	1.766	1.779	1.861
980.6	1.765	1.777	1.862
989.2	1.765	1.776	1.861
1526.5	1.755	1.767	1.845
Refractive indices of the substrate			
Wavelength [nm]	$\mathbf{n_x}$	$\mathbf{n_y}$	$\mathbf{n_z}$
632.8	1.789	1.801	1.888

With the values shown in table 4.2 we calculated the Sellmeier coefficients by fitting the chromatic dispersion curves to the equation:

$$n_i^2(\lambda) = A_i + \frac{B_i}{1-\left(\frac{C_i}{\lambda}\right)^p} + \frac{D_i}{1-\left(\frac{E_i}{\lambda}\right)^q} \qquad 4.18$$

The values of the coefficients are shown in table 4.3. The phase-matching curve for type II SHG in (Ba,Yb,Nb):RTP/RTP (001) was also calculated. Both results are reported in paper IV.

Table 4.3. Sellmeier coefficients obtained by fitting the chromatic dispersion curves to the equation 4.18.

	A	B	C(nm)	D	E(nm)	p	q
$\mathbf{n_x}$	2.3718	0.6979	0.2494	1.2900	13.0012	2.0012	1.9412
$\mathbf{n_y}$	2.4081	0.7112	0.2481	0.8041	10.5332	2.0091	1.8981
$\mathbf{n_z}$	2.3412	1.0592	0.2521	0.6771	10.1721	2.0112	1.8001

The dark mode spectra give information about the number of guided modes and also their effective refractive indices. Figure 4.11 presents the real dark mode spectra for each polarization in a PWG of (Ba,Yb,Nb):RTP/RTP with a thickness of 10 μm. As can be concluded from these graphs and from the film and substrate refractive indices, the (Ba,Yb,Nb):RTP/RTP PWG could not support any mode for E//***a*** polarization. But, unlike the (Yb,Nb):RTP/RTP PWG, it does support guided modes in E//***b*** polarization. Figure 4.11 shows the propagation modes in (Ba,Yb,Nb):RTP/RTP PWG , that is to say the dark mode spectra, for these polarizations that enable these PWGs for producing radiation by type II SHG. As can be seen in figure 4.11, in the particular case of E//***b***, there are two propagation modes. Notice that in E//***b*** polarization (TE) spectrum, show one hollow being two propagation modes. This is due to the resolution of the prism coupler equipment.

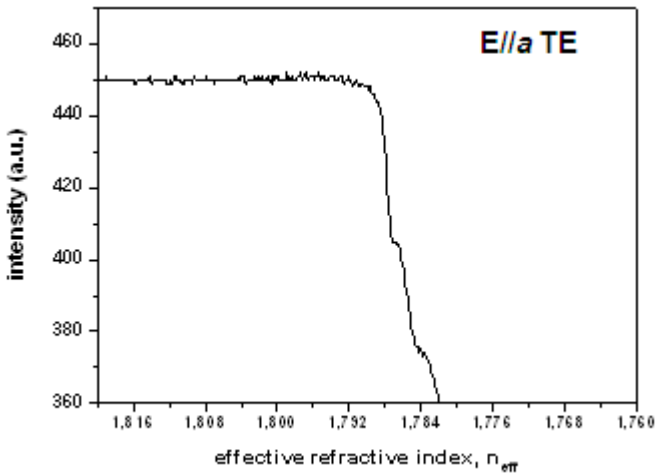

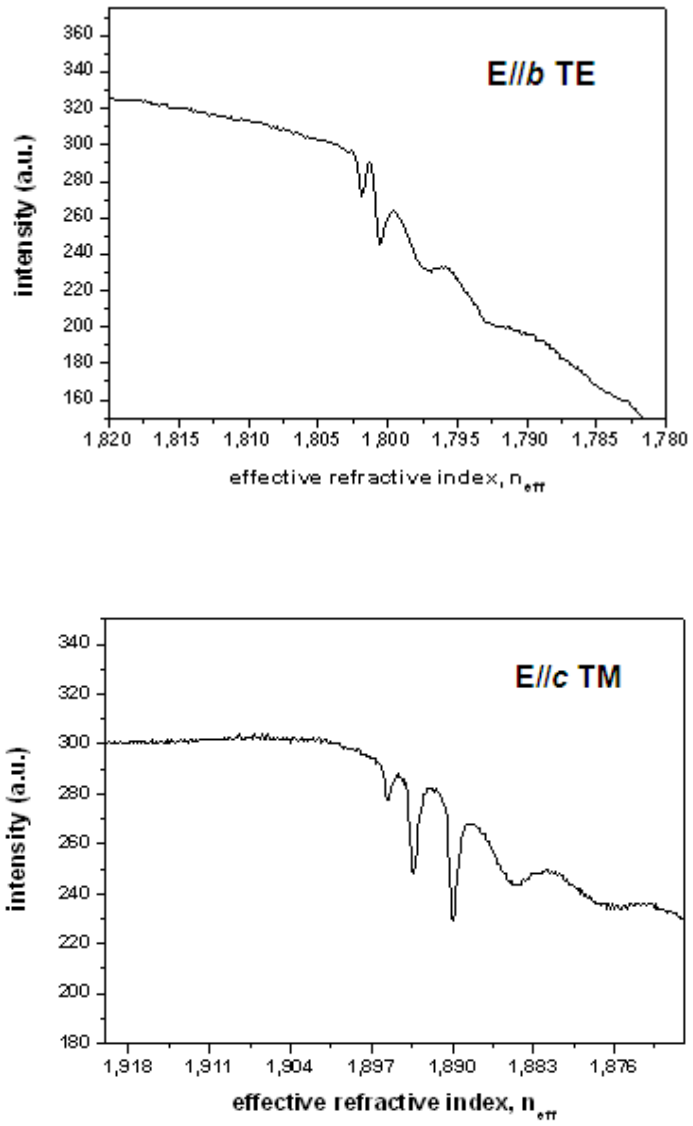

Figure 4.11. Dark mode spectra for different polarizations in (Ba,Yb,Nb):$RbTiOPO_4$/$RbTiOPO_4$ (001) at a wavelength of 632.8 nm

As has been mentioned above, to frequency double of the fundamental radiation in a planar waveguide (PWG) by type II SHG is necessary that radiation in TM and TE polarizations could be guided through the waveguide. In (Ba,Yb,Nb)RTP/RTP planar waveguides this condition is accomplished and thus, type II SHG could be obtained in these waveguides.

Figure 4.12 shows, for the first time to our knowledge, type II SHG planar waveguide conversion in (Ba,Yb,Nb):RTP/RTP with fundamental radiation of 1125 nm and green light generation of 562.5 nm.

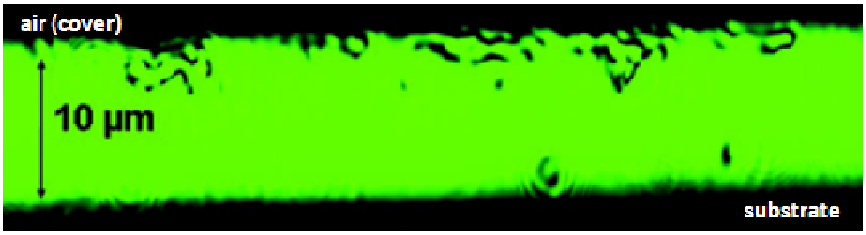

Figure 4.12. Near field pattern of type II SHG

4.3. Characterization of rib and channel waveguides

As has been mentioned previously, an important objective of this thesis was to obtain channel waveguides in Yb^{3+} doped RTP. This was accomplished by microstructuring the PWGs that had been obtained previously. The sections below present the optical characterization of the channel waveguides obtained by fs-laser ablation, Ar^{+} ion milling, reactive ion etching and Cs^{+} ion exchange.

4.3.1. (Yb, Nb):$RbTiOPO_4$ rib waveguides by fs-laser ablation

The optical characterization of the rib waveguides obtained by fs-laser ablation gives us experimental information about the quality of the ribs so that we can know whether this fabrication technique can be applied to RTP crystals.

After manufacturing the rib waveguides, and before optical characterization, the end faces of the samples which were perpendicular to the rib waveguides were polished and studied morphologically. The confocal images (see figure 4.13) reveal a good shape in terms of visual roughness. Moreover, the internal groove wall, which corresponds to the rib wall, is less rough than the external groove. The laser spot used in the fabrication of the ribs was designed taking this into account, since is better for the internal groove wall to be less rough than the external one. The slope of the rib walls is tg α =1/4 (where α is the angle between the vertical and the rib wall), so the ribs were trapezoidal in shape. The rms of the rib walls, estimated from the confocal images, is < 500 nm.

Computer simulations were carried out using the real trapezoidal shape of the ribs. The simulations reveal high theoretical confinement, with confinement factors higher than 90 % in all the cases simulated using different widths and wavelengths of 632.8 and 972 nm.

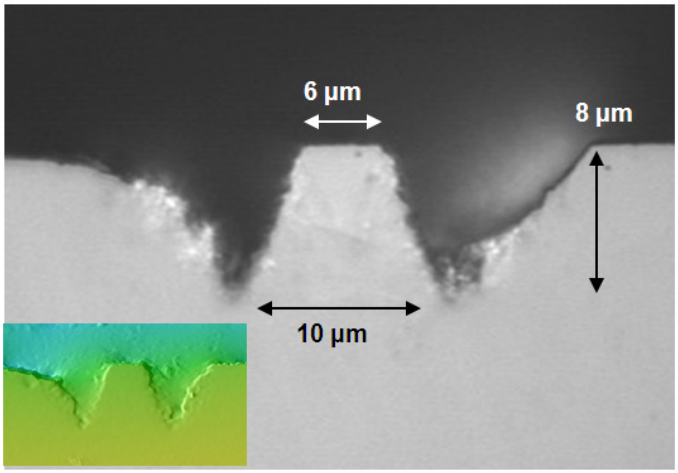

Figure 4.13. Cross section view of a rib 6 µm-width at the top and 10 µm at the bottom. The inset shows the same region imaged with the confocal microscope

Figure 4.14 shows a top view of the ability of the channel to guide the light at a wavelength of 632.8 nm. On the other hand, figure 4.15 shows the near field pattern of the propagation modes at 632.8 nm and 972 nm in a channel fabricated of 13 µm top width fabricated by fs-laser ablation. In both cases, the near field patterns are formed mainly by the fundamental (TM_{00}) mode and give the experimental proof of the ability of these ribs to guide the light. Once the fundamental mode had been excited, a power meter was used to measure the power before the input microscope objective and after the output microscope objective. Then, performing the corrections mentioned in the experimental techniques section, the upper limit of the losses was estimated to be 4.4 dB/cm.

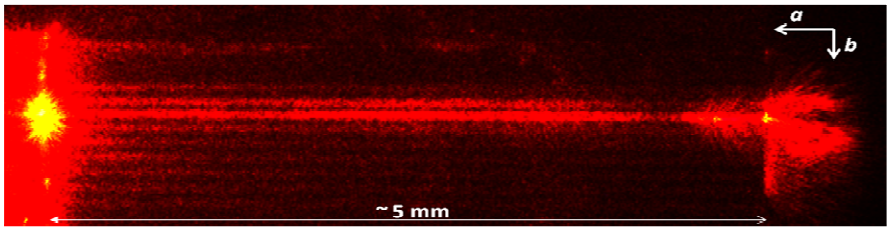

Figure 4.14. Top view of a rib waveguide during the guiding process at 632.8 nm

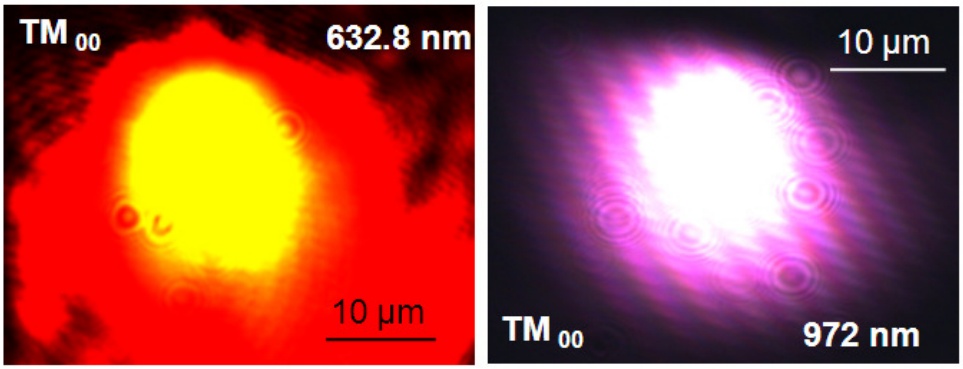

Figure 4.15. CCD picture of the near field pattern of the propagation modes at 632.8 and 972 nm

µ-Raman measurements were used to identify micro scale modifications in the boundaries of the rib waveguides. A set of 64 consecutive Raman spectra were recorded on the surface of the sample at 1 µm step intervals. Figure 4.16 shows two spectra, one taken in the ablated region and the other in the unablated region. As can be observed in this figure, all the peaks that appear in the ablated region, also appear in the spectra measured in the non-ablated region. This indicates that femtosecond irradiation does not induce amorphisation in (Yb,Nb):RTP.

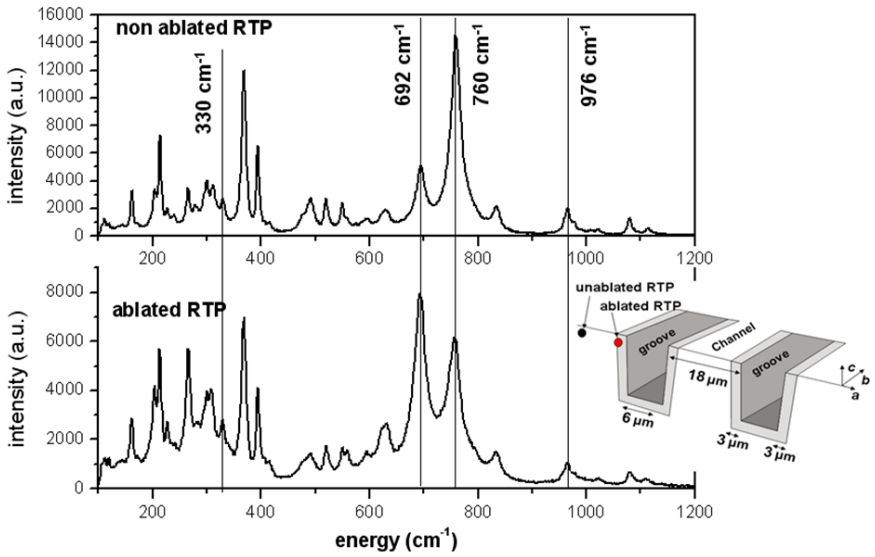

Figure 4.16. Raman spectra of the ablated and unablated RTP zones. Inset: scheme of channel with the points at which Raman spectra were taken marked

We observe significant differences in intensity in two specific peaks, located at ~ 692 cm^{-1} and ~ 760 cm^{-1}. While the peak located at ~ 692 cm^{-1} considerably increases its

intensity in the ablated zone, the intensity of the peak at ~ 760 cm^{-1} considerably decreases in the same zone. One explanation for this may be that, basically, the Raman spectra recorded correspond to those of RTP in a $z(yy)\bar{z}$ polarization configuration. The ~ 760 cm^{-1} signal corresponds to the υ_2 vibration mode of the TiO_6 octahedron, which is the most intense peak for the $z(yy)\bar{z}$ polarization in unablated RTP. The ~ 692 cm^{-1} peak is also related to the υ_2 vibration mode of the TiO_6 octahedron in the same polarized configuration, but its intensity is considerably lower than the one at ~ 760 cm^{-1} also in unablated RTP. This peak may also be related to the υ_1 and υ_3 vibration modes of the TiO_6 octahedron in the $x(yz)\bar{x}$, $y(xx)\bar{y}$ and $y(zz)\bar{y}$ polarization configurations, where this peak is the most intense of these spectra.

From the peak differences mentioned above, we can conclude that the differences in intensity between the ablated and unablated spectra may be due to some orientation changes in the crystal structure in the areas in the proximity of the ablated region, which leads to a mixture of the Raman spectra corresponding to different scattering geometries.

As was expected, the rib waveguides fabricated by fs-laser ablation were used to obtain type II SHG guided green light. Figure 5 in paper VI shows the near field pattern at 568.5 nm produced inside the rib waveguide by exciting the modes at 1137 nm. The modes excited to produce green light, correspond to channel waveguides parallel to the ***a*** crystallographic direction.

4.3.2. (Yb,Nb):$RbTiOPO_4$ rib waveguides by Ar^+ ion milling

The optical characterization explained above was applied to characterize the rib waveguides fabricated by Ar^+ ion milling. This etching technique produces ribs that are much better in terms of roughness and guided light losses than the ribs obtained by fs-laser ablation. As can be seen in the ESEM images, it is evident that the rib walls obtained by Ar^+ ion milling are not merely as rough as the ribs obtained by fs-laser ablation (see figure 4.17 and 4.18). The roughness of the rib is crucial, since the irregularity of the waveguide boundaries introduce dispersion centers that increase the transmittance losses.

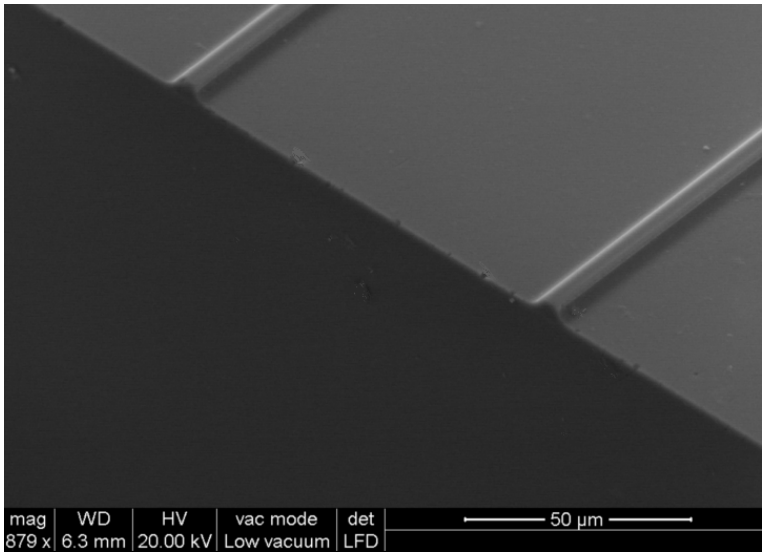

Figure 4.17. General view of two rib waveguides by ESEM

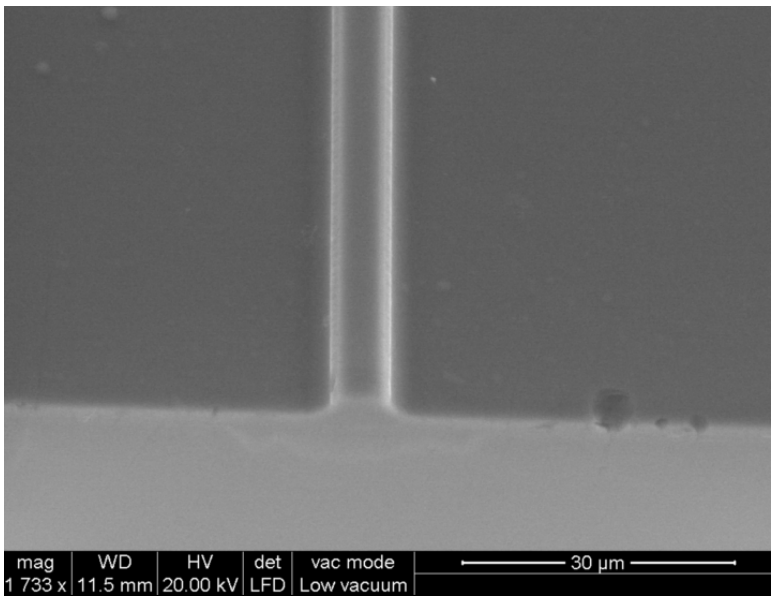

Figure 4.18. Detailed view of the 6 µm nominal width rib waveguide by ESEM

The near field pattern of the modes guided through the rib was recorded with a CCD camera at 972 nm. Figure 5 in paper VII shows the near field pattern of the guided modes in a rib fabricated on a planar waveguide of 5 µm in width. The rib had a top width of 10 µm, a base of 14 µm and a height of 3 µm, over a remaining (Yb,Nb):RTP epitaxial layer of 2 µm high. This figure also shows an inset that has the same pattern but which uses a filter to avoid saturation and provide information about the gaussianity and the asymmetry of the mode.

As an example, Figure 4.19 shows the near field patterns of the guided modes at 972 nm in ribs with a top width of 10 and 3 µm, as can be seen in the figure. In the case of the

rib with a width of 3 µm, part of the energy goes through the PWG. This is in agreement with the simulations carried out using the real parameters of the ribs. In fact, the confinement factor of the rib with a top width of 10 µm was 93.1 %, while for the rib with a top width of 3 µm this factor was 88.5 %, which is still too high.

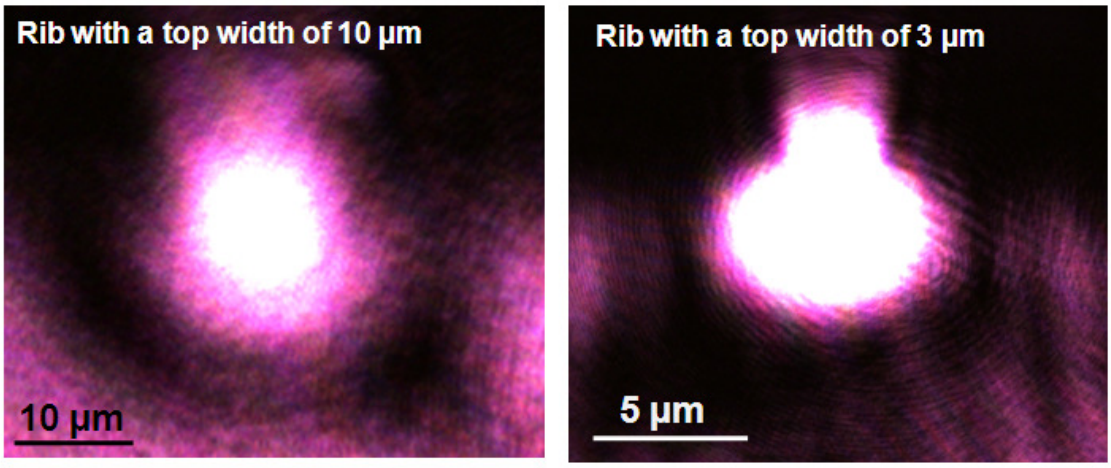

Figure 4.19. Near field pattern of the guided modes in ribs with a top width of 10 µm (left) and 3 µm (right)

The estimated losses were 3 dB/cm. Thus, the Ar^+ ion milling ribs confine and guide the light better than the ribs fabricated by fs-laser ablation. This is logical taking into account the roughness of the top and the walls of the ribs. In fact, this roughness was one order of magnitude higher in the fs-laser ablation ribs than in the ribs fabricated by Ar^+ ion milling.

Figure 4.20 shows the green light obtained in the rib waveguides by type II SHG. The pumping wavelength was at 1140 nm, while the green light recorded by the CCD camera was at 570 nm. As is explained in paper VII, we proved that the green light comes exclusively from the waveguide. To check this we focused the OPO beam in the substrate (that is to say, out of the waveguide) and we obtained a maximum power of type II SHG conversion for an input radiation of 1137 nm. Note that the maximum efficiency in type II SHG process in the rib was for a fundamental radiation of 1140 nm, different than in the substrate, which is logical taking into account the different refractive indices of the rib and the substrate.

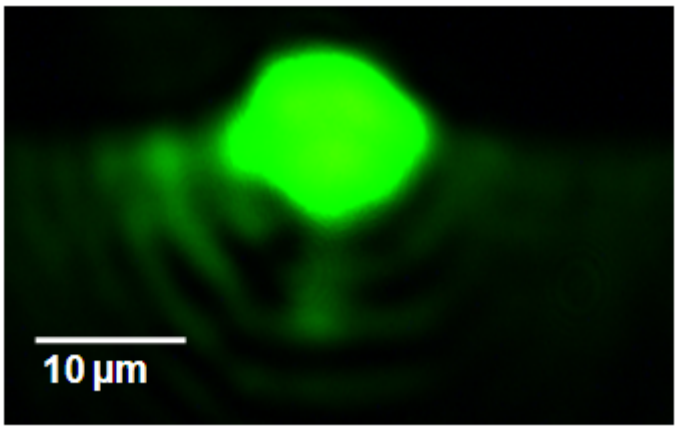

Figure 4.20. Near field pattern of 570 nm green light from Type II SHG of 1140 nm IR light.

4.3.3. (Yb, Nb):$RbTiOPO_4$ rib waveguides by RIE

A non-contact profiler (Zescope by Zemetrics) was used to measure the etch depth of rib waveguides, which turned out to be 1.4 µm, and the etch rate was 10 nm/min. On the other hand, the roughness measured after etching was 8 nm. This value contrasts with the roughness of the surface before etching which was 3 nm. This unexpected value in relation with the results presented above may be due to the longer etch time, as well as the re-deposition of the mask on the un-etched regions. As can be seen in figure 3 in paper VIII for a rib waveguide with a top width of 9.8 µm, the bottom width was 11.2 µm.

Optical characterization was performed at the Optoelectronics Research Centre of the University of Southampton. The guided modes were excited using a fiber-coupled single-mode laser diode from Oclaro with a maximum power of 750 mW and a grating stabilized wavelength of 974 nm. The polarization was controlled by a λ/2 plate. The set-up used in order to align the beam with the rib was similar to that presented in section 2.3. In this case, the input microscope objective was a 16x objective that gave a measured waist radius of 3.2 µm.

Figure 5 in paper VIII shows the near field mode profile for the RIE etched waveguide at a wavelength of 974 nm.

The transmission losses were estimated using a similar procedure as in the case of the ribs fabricated by fs-laser ablation and Ar^+ ion milling and the value was lower than 4 dB/cm for E//***c*** polarization (TM). In this case, in the loss calculations we assumed a launch efficiency value of 50%. The simulated and measured near field patterns of the

guided mode through the rib waveguide in TM polarization are shown in figure 5 in paper VIII.

4.3.4. Planar and channel waveguides by Cs^+ ion exchange on $RbTiOPO_4$

Planar waveguides. As has been explained in the section on the fabrication of PWGs by Cs^+ ion exchange, PWGs with high light confinement were obtained by Cs^+ ion exchange for diffusion times of 2 h.

A sample of RTP with a surface area of 5 x 5 mm^2 was used to produce a PWG by Cs^+ ion exchange for 2 h that was used for optical characterization. After diffusion, the four side faces of the sample were polished to obtain the near field pattern for each polarization. Figure 4.21 shows these results at a wavelength of 632.8 nm.

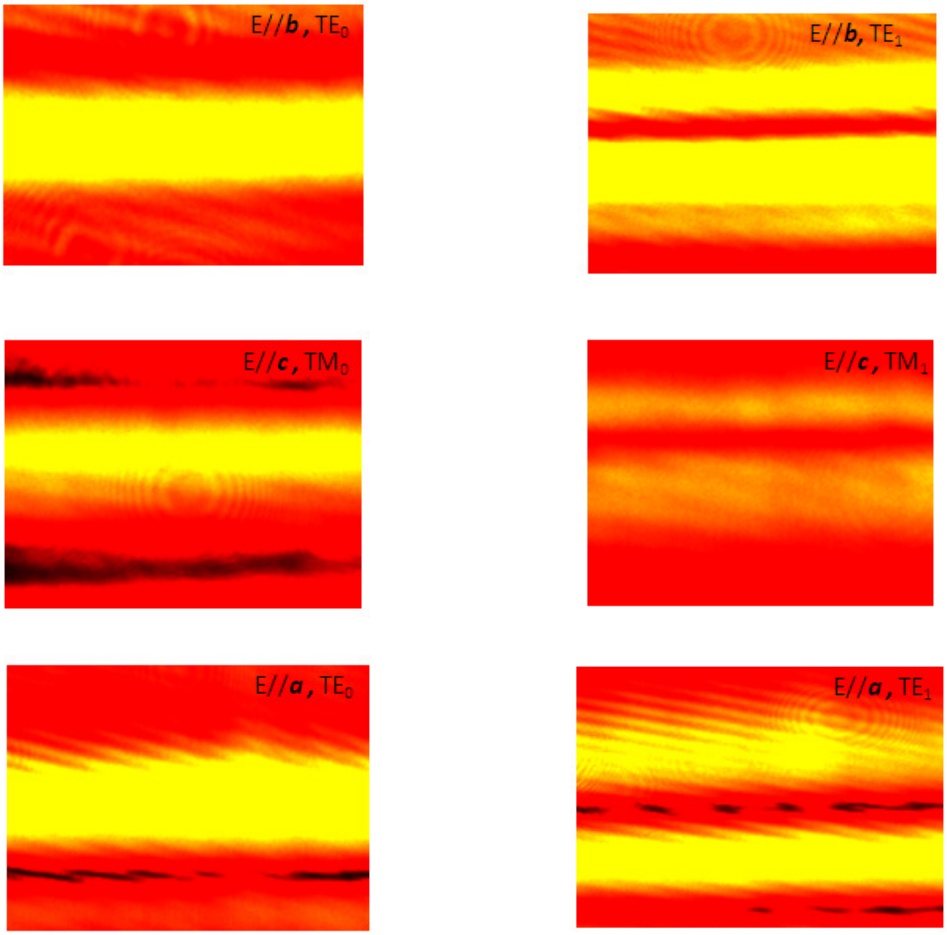

Figure 4.21. Near field pattern of a Cs^+ ion exchange PWG for different polarizations and order modes m = 0 and 1

The same sample was used to obtain type II SHG for both perpendicular propagations; along the ***a*** and ***b*** crystallographic directions. Figures 4.22 and 4.23 show the near field patterns of type II SHG produced for propagation along ***a*** and ***b*** directions, respectively.

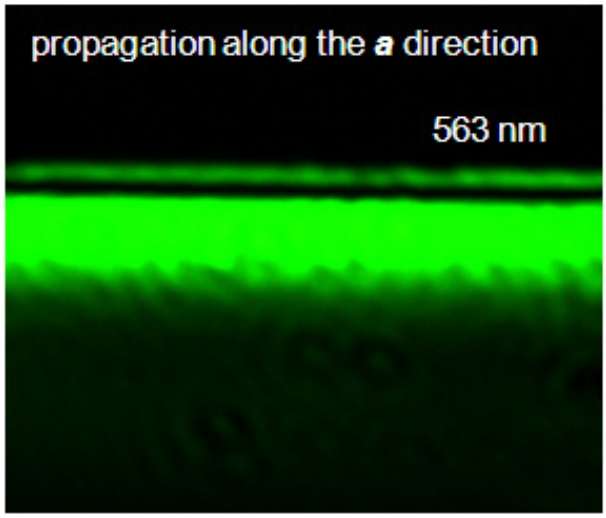

Figure 4.22. Near field pattern of type II SHG conversion of a fundamental radiation of 1126 nm along the ***a*** direction.

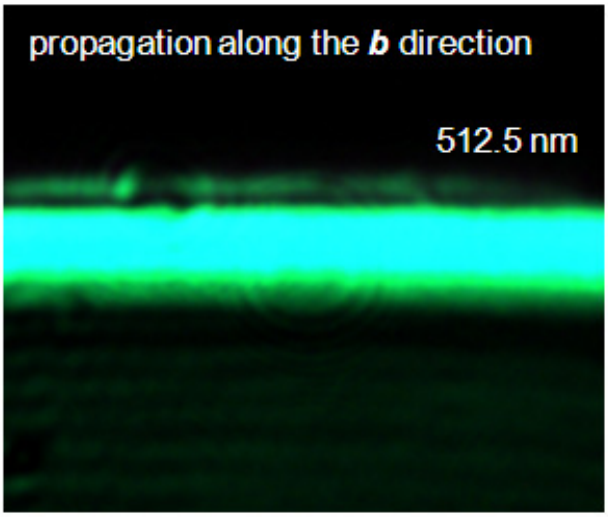

Figure 4.23. Near field pattern of type II SHG conversion of a fundamental radiation of 1025 nm along the ***b*** direction.

All these characterizations prove that planar waveguides can be fabricated by Cs^+ ion exchange in RTP.

Channel waveguides. In this case the characterization was carried out using the same procedure as for the channels obtained by fs-laser ablation and Ar^+ ion milling. So, the near field pattern of the modes was recorded for several channel waveguides. Figure

4.24 shows a top view image of the guided light at a wavelength of 632.8 nm. The channel shown in this figure has a width of 11 µm.

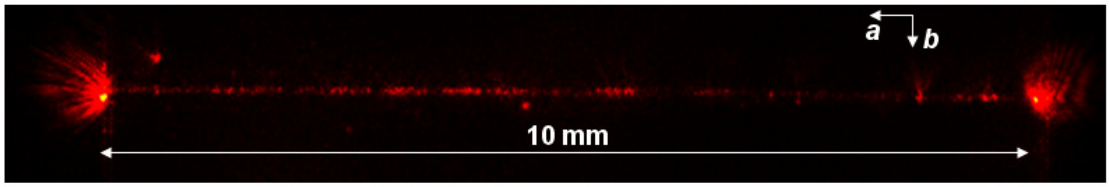

Figure 4.24. Top view of the guided light through the channel waveguide with a top width of 11 µm at 632.8 nm.

In these channels we were able to excite the fundamental mode and other modes separately. As an example, Figure 4.25 presents the near field pattern of the propagation modes with order TM_{00}, TM_{01} and TM_{11} at a wavelength of 972 nm.

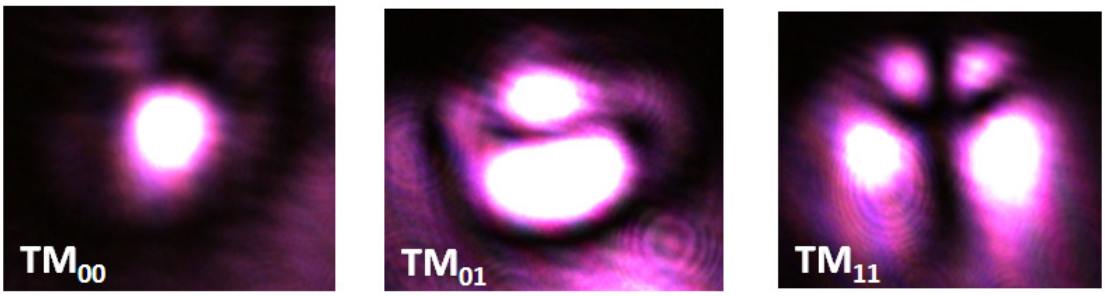

Figure 4.25. CCD images of the dark mode spectra at 972 nm. The exited modes are TM_{00}, TM_{01}, TM_{11}.

In this case, and following the same procedure used up to now, we evaluated the transmittance losses by single-pass transmission measurements. The losses presented for these channels at a wavelength of 972 nm had an upper limit of 3.8 dB/cm.

The Type II SHG process was obtained by exciting the TE and TM channel modes simultaneously. In this case the green light obtained had a wavelength of 566.5 nm, coming from a fundamental wavelength of 1133 nm. To achieve this, a half-plate was placed in front of the input microscope objective. The SHG was produced in several channel waveguides, as can be seen in figure 4.26. This figure shows the SHG produced in two different channels that were 6 µm and 11 µm wide.

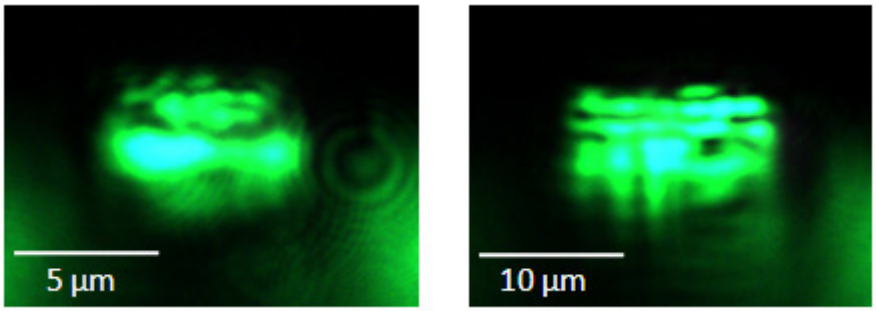

Figure 4.26. Near field patterns at 566.5 nm produced by type II SHG inside channel waveguides

4.4. Preliminary studies of continuous wave (Yb, Nb):$RbTiOPO_4$/ $RbTiOPO_4$ (001) planar waveguide laser

The absorption of Yb^{3+} in the Nb:RTP matrix have been reported by J.J. Carvajal in 2003 [131]. From the three expected peaks, corresponding to the splitting of $^2F_{5/2}$ multiplet, the peaks at 903 and 972 nm were the strongest and the peak at 955 nm was the lowest in all the three polarizations. On the other hand, the emission was also reported [131]. In this case the wavelengths of emission from the excited $^2F_{5/2}$ to the four sublevels of the ground state $^2F_{7/2}$ were 972, 1025, 1051 and 1071 nm. In this Ph D thesis, the emission spectra of the Yb^{3+} were measured in a waveguide, as is reported in paper II.

A planar waveguide fabricated during this study was used to obtain continuous wave laser operation. These experiments were undertaken at the Optoelectronics Research Center of Southampton University (see related publication Rp1).

A planar waveguide 11 µm thick was fabricated from an epitaxial film of Yb^{3+} and Nb^{5+} doped RTP on an RTP substrate. The epitaxial layer was grown using the composition: Rb_2O-P_2O_5-TiO_2-Yb_2O_3-Nb_2O_5 = 40.8-27.2-29.44-1.92-0.64 (mol %). The concentration of Yb^{3+} ions in the film was $2x10^{20}cm^{-3}$. This value is higher than the concentration presented previously in the bulk crystal used for lasing [39]. The guiding characteristics of the PWGs with this composition were studied in the previous section and showed good confinement. Nevertheless these PWG properties were checked before the lasing experiments at a wavelength of 1 µm. The refractive index contrast measured at this wavelength is 0.006 and the waveguide supports three modes in TM polarization (E//***c***).

The pumping radiation for lasing was supplied by a Ti:sapphire laser operating at 900 nm, which corresponds to the absorption peak of Yb in (Yb, Nb):RTP for polarization parallel to the ***c*** crystallographic direction (E//***c***). Thin dielectric mirrors were attached to the polished end faces of the PWG to form the laser cavity, and an HR/HR cavity was obtained. An incident power of 510 mW (absorbed power of 276 mW) was used. An optical chopper was used to chop the pump source and photodiode to monitor the characteristic rise and decay of the fluorescence intensity. The laser operation was proved by a fast and very strong increase in intensity, when the pump power was increased. This strong increase in intensity indicated that the laser threshold had been reached. A threshold absorbed power of 276 mW was observed. Notice that the maximum capability of the Ti:sapphire used (510 mW) corresponds to the threshold of the waveguide laser and therefore measurements of the slope efficiency of the laser were not possible. The calculated gain for total inversion was 0.69 cm^{-1} whereas the measured loss was about 0.16 cm^{-1}, hence the condition of gain>loss is just satisfied.

These experiments are currently ongoing in an attempt to determine the slope efficiency and other laser parameters.

Conclusions

Looking back to the objectives of this study, we conclude that they have largely been accomplished. The main aim was to investigate the possibilities of Yb:RTP waveguides on RTP substrates for photonic applications. Starting from RTP bulk single crystal growth to obtain substrates, we grew (Yb, Nb):RTP/RTP epitaxial layers. These layers were used to fabricate PWGs, which were then characterized. Finally, some of the planar waveguides were microstructured to produce channel waveguides.

RTP bulk single crystals were successfully obtained by the TSSG-SC technique and they were used as a source of planar substrates. The crystals obtained were free of cracks and optical defects, and colorless.

The (Yb,Nb):RTP (001) epitaxial layers grown on RTP substrates by LPE were, in general, free of cracks and defects, which is critical for PWG fabrication. The stoichiometric composition of the epitaxial layer with the highest Yb^{3+} concentration was $RbTi_{0.958}Yb_{0.016}Nb_{0.026}OPO_4$. This means an Yb^{3+} concentration of ~1 x 10^{20} cm^{-3}, which is one order of magnitude above the threshold postulated for lasing. The PWGs obtained from these epitaxial layers, with the corresponding solution composition, give a high refractive index contrast in the ***c*** crystallographic direction. In fact, the PWGs obtained were multimodal in TM polarization. On the other hand, the contrast of refractive indices in the ***b*** crystallographic direction was positive but not enough for guiding. In the ***a*** direction, the contrast was negative, which is not suitable for guiding either.

In an attempt to guide the light in more than one polarization, we grew (Ba,Yb,Nb):RTP (001) epitaxial layers on RTP substrates by LPE. They were generally free of cracks and defects. Despite the low Yb^{3+} concentration, the PWGs obtained from these epitaxial layers guided the light in two polarizations. In fact, the PWGs were multimodal in TM polarization and had a few guided modes in TE_y polarization. In terms of obtaining

Type II Second Harmonic Generation, it was a success. So, we were able to use these PGWs to obtain green SHG radiation with a wavelength of 562 nm.

In addition, the fabrication of PWGs by Cs^+ ion exchange shows that waveguides can be obtained in all the polarizations. In fact, we were able to obtain Type II SHG along the ***a*** and ***b*** polarizations using the PWGs fabricated by this technique. These processes gave radiations of 563 nm along the ***a*** crystallographic direction and 512.5 nm along the ***b*** crystallographic direction.

The Integrated Optics is based on achieving a dominance of the light, such as electronics control the electrons. So, the main characteristic of a potential integrated photonics material is that channel waveguides must be able to be fabricated on it. So, we fabricated channel waveguides on (Yb,Nb):RTP/RTP PWGs using the most important techniques present in the literature. We successfully used fs-laser ablation, Ar^+ ion milling and reactive ion etching (RIE). Channel waveguides were also fabricated on RTP (001) substrates by Cs^+ ion exchange. All the channels obtained in this study have dimensions of around 10 μm in width.

The ribs obtained by fs-laser ablation were trapezoidal in shape and their walls were rougher than those obtained by Ar^+ ion milling and RIE. However, optical characterization reveals good quality light guidance. Green guided light of 568.5 nm from type II SHG was obtained from a source of 1137 nm. On the other hand, the ribs fabricated by Ar^+ ion milling and RIE were also trapezoidal, but they were more top-hat shaped than those obtained by fs-laser ablation. The characterization of the rib waveguides fabricated by Ar^+ ion milling and RIE reveals lower losses than those obtained by fs-laser ablation. Considering that the former are not nearly as rough as the latter, this is quite logical. The type II SHG process was tried out in Ar^+ ion milling ribs at 1140 nm and green light with a wavelength of 570 nm was obtained.

The channels obtained by Cs^+ ion exchange in RTP were graded index waveguides not the step index waveguides obtained by LPE (fs-laser ablation, Ar^+ ion milling and RIE channel waveguides). But the characterization of the Cs^+ ion exchange waveguides reveals a very strong step index in the horizontal direction. This may be why the losses of these channel waveguides were of the same order as those obtained in the waveguides fabricated by Ar^+ ion milling and RIE. In this case, the characterization of type II SHG shows that 1025 nm radiation is converted into guided green light of 512.5 nm.

Finally, preliminary experiments were carried out into laser emission in (Yb,Nb):RTP/RTP channel waveguides fabricated by Ar^+ ion milling. Laser operation was demonstrated by a strong increase in the light intensity with a pumping source of 900 nm. The laser threshold was 276 mW of absorbed power.

References

[1] W.P.Risk, T.R. Gosnell, A.V. Nurmikko, *Compact blue-green lasers.* Cambridge University Press. 2003.

[2] R. W. Boyd, *Nonlinear Optics*, Academic Press, 1992.

[3] P. E. Powers, *Fundamentals of Nonlinear Optics*, CrC Press, 2011.

[4] A. Fragemann, Ph. D. Thesis, Optical Parametric Amplification with Periodically Poled $KTiOPO_4$, Royal Institud of Technology, Stockolm, 2005.

[5] S. Dinakaran, S. Verma, S. Jerome Das, S. Kar, K.S. Bartwal, P.K. Gupta, "Investigations for obtaining enhanced SHG element of KH_2PO_4", *Physica B: Condens. Mater.*, **405**(7), 1809 (2010).

[6] S.P. Meenakshisundaran, S. Parthiban, G. Madhurambal, R. Dhanasekaran, S.C. Mojumdar, "Effect of complexing agent (1,10-phenanthroline) on ADP and KDP crystals", *J. Therm. Anal. Calorim*, **94**(1), 15 (2008).

[7] T.A. Robson, H.J. Ruiz, P.L. Shah, F.K. Tittel, "Efficient second harmonic generation of picosecondslaser pulses", *Appl. Phys. Lett.*, **20**(8), 282 (1972).

[8] H. Tanaka, T. Honma, Y. Benino, T. Fujiwara, T. Komatsu, "YAG laser-induced β-BaB_2O_4 crystalline dot formation in Sm_2O_3-BaO-B_2O_3 glasses", *J. Phys. Chem. Solids*, **64**, 1179 (2003).

[9] D. Li, Z. Ma, R. Haas, A. Schell, J. Simon, R. Diart, P. Shi, P. Hu, P. Loosen, K. Du, "Diode-pumped efficient slab laser with two Nd:YLF crystals and second-harmonic generation by slab LBO", *Opt. Lett*., **32**(10), 1272 (2007).

[10] T.A. Driscoll, H. J. Hoffman, R.E. Stone, P.E. Perkins, "Efficient second-harmonic generation in KTP crystals", *J. Opt. Soc. Am. B*, **3**(5), 683 (1986).

[11] N. E. Yu, S. Kurimura, K. Kitamura, O. Jeon, M. Cha, S. Ashihra, T. Ohta, T. Shimura, K. Kuroda, "fficient second-harmonic generation of ultrafast pulses in periodically poled KNbO3", *Appl. Phys. Lett*., **85**(24), 5839 (2004).

[12] X. Wang, X. Liu, "Second-harmonic generation in α-$LiIO_3$ crystals under the action of a DC field", *Phys. Status Solidi*, **131**(1), k69-k72 (1992).

[13] G.D. Stucky, M.L.F. Philips, T.E. Gier, "The potassium titanyl phosphate structure field: a model for new nonlinear optical materials", *Chem. Mater*., **1**, 492 (1989).

[14.] M.N. Satyanarayan, A. Deepthy, H.L. Bhat, "Potassium titanyl phosphate and its isomorphs: growth, properties, and applications", *Crit. Rev. Solid State*, **24**, 103 (1999).

[15] M.E. Hagerman, K.R. Poeppelmeier, "Review of the structure and processing-defect-property relationships of potassium titanyl phosphate: a strategy for novel thin-film photonic devices", *Chem. Mater*. **7**, 602 (1995).

[16] F.C. Zumnsteg, J.D. Berlein, T.E. Gier, "$K_xRb_{1-x}TiOPO_4$: a nonlinear optical material", *J. Appl. Phys*., **47**, 4980 (1976).

[17] J.C. Jacco, G.M. Loiacono, "Nature of the infrared spectrum in band-edge region of $KTiOPO_4$", *Appl. Phys. Lett*., **58**, 560 (1991).

[18] L. F. Johnson, A.A. Ballman, "Coherent emission from rare earth ions in electro-optic crystals ", *J. Appl. Phys*., **40**, 297 (1969).

[19] T. Y. Fan, A. Cordova-Plaza, M.J.F. Digonnet, R.L. Byer, H.J. Shaw, "Nd:MgO:$LiNbO_3$ spectroscopy and laser devices", *J. Opt. Soc. Am. B*, **3**, 140 (1986).

[20] A. Cordova-Plaza, T.Y. Fan, M.J.F. Digonnet, R.L. Byer, H.J. Shaw, "Nd:MgO:$LiNbO_3$ continuous-wave laser pumped by a laser diode", *Opt. Lett*., **13**, 209(1988).

[21] S. Ishibashi, H. Itoh, T. Kaino, I. Yokohama, K. Kubodera, "New cavity configurations of Nd:MgO:$LiNbO_3$ self-frequency-doubling lasers", *Opt. Commun*., **125**, 177(1996).

[22] K. Zhang, C. Xie, R. Guo, J. Eang, K. Peng, "Laser-diode-pumped cw Nd:MgO:$LiNbO_3$ self-frequency-doubling laser around room temperature ", *Appl. Opt*., **35**, 3200 (1996).

[23] F. Mougel, F. Auge, G. Aka, A. Kahn Harare, D. Vivien, F. Balembois, P Georges, A. Brun, "New green self-frequency-doubling diode-pumped $NdGdCaO(BO_3)_3$", *Appl. Phys. B*, **67**, 533 (1998).

[24] S. Zhang, Z. Cheng, J. Han, G. Zhou, Z. Shao, C. Wang, Y. T. Chow, H. Cheng, "Growth and investigation of efficient self-frequency-doubling $Nd_xGd_{1-x}Ca_4O(BO_3)_3$", *J. Cryst. Growth*, **206**, 197(1999).

[25] C.Q. Wang, Y.T. Chow, W.A. Gambling, S.J. Zhang, Z.X. Cheng, Z.S. Shao, H.C. Chen, "Efficient self-frequency doubling of Nd:GdCOB crystal by type-I phase matching out of its principal planes" , *Opt. Commun*., **174**, 471(2000).

[26] A. Brenier, A. Majchrowski, E. Michalski, T. Lukasievicz, "Evaluation of GdCOB:Nd^{3+} for self-frequency doubling in the optimum phase matching directions", *Opt. Commun*., **217**, 395 (2003).

[27] J.M. Eichenholtz, D.A. Hammons, L. Shaha, Q. Ye,R.E. Peale, M. Richardson, B. Chiai, "Diode-pumped self-frequency doubling in a Nd^{3+}:$YCa_4O(BO_3)_3$", *Appl. Phys. Lett*., **74**, 1954(1999).

[28] Q. Ye, L. Shah, J. Eichenholz, D. Hammons, R. Peale, M. Richardson, A. Chin, B.H.T. Chai, "Investigation of diode-pumped, self-frequency doubled RGB lasers form Nd:YCOB crystals", *Opt. Commun*., **164**, 33(1999).

[29] E. Montoya, J. Campany, L.E. Bausá, T. Kellner, A. Diedning, G. Huber, "Infrared and self-frequency doubed laser action in Yb^{3+}-doped $LiNbO_3$:MgO", *Appl. Phys. Lett*. , **74**, 3113 (1999).

[30] F. Mougel, K. Dardden, G. Aka, A. Kahn-harari, D. Vivien, "Ytterbium-doped $Ca_4GdO(BO_3)_3$: an efficient infrared laser and self-frequency doubling crystal", *J. Opt. Soc. Am. B*, **16**, 164 (1999).

[31] H. Zahng, X. Meng, P. Wang, L. Zhu, X. Liu, Y. Yang, R. Wang, J. Dawes, J. Piper, S. Zhang, L. Sun, "Growth of Yb-doped $Ca_4GdO(BO_3)_3$ crystals and their spectra and laser properties", *J. Cryst. Growth*, **222,** 209 (2001).

[32] P. Wang, P. Dekker, J.M. Dawes, J.A. Piper, Y. Liu, J. Wang, "Efficient continous-wave self-frequency-doubling green diode-pumped Yb:$YAl_3(BO_3)_4$", *Opt. Lett*., **25**(10), 731 (2000).

[33] P. Dekker, J.M. Dawes, J.A. Piper, Y: Liu, J. Wang, "1.1 W CW self-frequency-doubled diode-pumped Yb:$YAl_3(BO_3)_4$", *Opt. Commun*. , **195**, 431 (2001).

[34] P.A. Burns, J.M. Dawes, P. Dekker, J.A. Piper, J. Li, J. Wang, "Coupled-cavity, single-frequency, tunable cw Yb:YAB yellow microchip laser", *Opt. Commun*., **207**, 315 (2002).

[35] P. Dekker, P.A. Burns, J.M. Dawes, J.A. Piper, "Widely tunable yellow-green lasers based on the self-frequency-doubling material Yb:YAB", *J. Opt. Soc. Am. B*, **20**, 706 (2003).

[36] M.J. Lederer, M. Hildebrant, V.Z. Kolev, B. Luther-Davies, B. Taylor, J. Dawes, P. Dekker, J. Piper, H.H. Tan, C. Jagadish, "Passive mode locking of a self-frequency-doubling Yb:$YAl_3(BO_3)_4$ laser", *Opt. Lett*., **27**, 436 (2002).

[37] Z. Zhu, J. Li, A. Brenier, G. Jia, Z. You, X. Lu, B. Wu, C. Tu, "Growth, spectroscopic and laser properties of Yb^{3+}-doped $GdAl_3(BO_3)_4$ crystal: a candidate for infrared laser crystal", *Appl. Phys. B*, **86**, 71 (2007).

[38] I.Parreu, M.C. Pujol, M. Aguiló, F. Díaz, X. Mateos, V. Petrov, "Growth, spectroscopy and laser operation of Yb:$KGd(PO_3)_4$ single crystals", *Opt. Express*., **15**, 2360 (2007).

[39] X. Mateos, V. Petrov, A. Peña, J.J. Carvajal, M. Aguiló, F. Diaz, P.Seconds, B. Boulanger, "Laser operation of Yb^{3+} in acentric $RbTiOPO_4$ codoped with Nb^{5+}", *Opt. Lett*., **32**, 13, 1929 (2007).

[40] C. Becker, T. Oesselke, J. Pandavernes, R. Ricken, K. Rochhausen, G. Schreiber, W. Sochler, H. Suche, R. Wessel, S. Balsamo, I. Montrosset, D. Sciancalepore, "Advanced Ti:Er:$LiNbO_3$ waveguide lasers ", *IEEE J. Selcted Top. Quantum Eletron*. , **6**, 101 (2000).

[41] M. Fujimura, T. Kodama, T. Suhara, H. Nishihara, "Quasi-phase-matched self-frequency-doubling waveguide laser in Nd:$LiNbO_3$", *IEEE Photon. Tech. Lett*., **12**, 1513 (2000).

[42] R.A. Stolzenberger, C.C. Hsu, N. Peyghambarian, J.J. Reid, R. A. Morgan, "Type II sum frequency generation in flux and hydrothermally grown KTP at 1.319 and 1.338 μm", *Photonics Techn. Lett.*, **1** (12), 446 (1989).

[43] R. Solé, V. Nikolov, I. Koseva, P. Peshev, X. Ruiz, C. Zaldo, M.J. Martin, M. Aguiló, F. Díaz, "Conditions and possibilities for rare-earth doping of $KTiOPO_4$ flux-growth single crystals", *Chem. Mater*., **9**, 2745 (1997).

[44] M. Rico, C. Zaldo, J. Massons; F. Díaz, , "Optical absorption of Er^{3+} in $RbTiOPO_4$ and $KTiOPO_4$", *J. Phys.:Condens. Matter*., **10**, 10101 (1998).

[45] R. Solé, X. Ruiz, R. Cabré, Jna. Gavaldà, M. Aguiló, F. Díaz, V. Nikolov, X. Solans, "$KTiOPO_4$ single crystals grown from neodynium modified fluxes", *J. Cryst. Growth*, **167,** 681 (1996).

[46] J.J. Carvajal, V. Nikolov, R. Solé, Jna. Gavaldà, J. Massons, M. Aguiló and F. Díaz, "Crystallization region, crystal growth, and characterization of Rubidium Titanyl Phosphate codoped with Niobium and Lanthanide Ions", *Chem. Mater*., **14**, 3136 (2002).

[47] K. M. Wang, W. Wang, P.J. Ding, W.A. Lanford, Y.G. Liu, "Ion-beam mixing of erbium into potassium titanyl phosphate mega-electron-volt argon beams", *J. Appl. Phys*., **77**, 3581 (1995).

[48] K.M. Wang, F. Lu, M.Q. Meng, B.R. Shi, D.Y. Shen, Y.G. liu, D. Fink, "Depth distribution of rear-earth íons implanted into $KTiOPO_4$ determined by the Rutherford backscattering technique" *Nucl. Instrum. Meth. B*, **145**, 271 (1998).

[49] K.M. Wang, B.R. Shi, N. Cue, Y.Y. Zhu, R.F. Xiao, F. Lu, W. Li, Y.G. Liu, "Waveguide laser film in erbium-doped $KTiOPO_4$ by pulsed laser deposition", *Appl. Phys. Lett*., **73**, 1020 (1998).

[50] J.J. Carvajal, R. Solé, Jna. Gavalda, J. Massons, M. Aguiló, F. Díaz, "Crystal growth of $RbTiOPO_4$:Nb. A new nonlinear host for rare earth doping", *Cryst. Growth & Des*., **1**, 479 (2001).

[51] J.J. Carvajal, R. Solé, Jna. Gavalda, J. Massons, M. Aguiló, F. Díaz, "A new self-doubling material: $RbTiOPO_4$(Nb, Yb) ", *Opt. Mater*., **24**, 425 (2003).

[52] T.H. Maiman, "Stimulated optical radiation in Ruby", *Nature*, **187**, 493 (1960).

[53] B. Ferrand, B. Chambaz, M. Couchaud, "Liquid-phase epitaxy: a versatile technique for the development of miniature optical components in single crystal dielectric media", *Opt. Mat*. **11**, 101 (1999).

[54] R. Chety, E. Millon, A. Boudrioua, J.C. Loulergue, A. Dahoun, J. Perrière, "Growth of $GdCa_4O(BO_3)_3$ thin films by pulsed-laser deposition for nonlinear optical applications", *J. Mater. Chem.*, **11**, 657 (2001).

[55] M.K. Smit, C.J. Van der Laan, G.A. Acket, "Aluminium oxide films for integrated optics", *Thin Solid Films*, **138**, 177 (1986).

[56] E. Daran, D.P. Shepherd, T.B. Huta, C. Serrano, "(1.9 μm) laser Diode arrays", *Electron. Lett*., **35**, 398 (1999).

[57] J.L. Jackel, C.D. Rice, J.J. Veselka, "Proton exchange for high-index waveguides in $LiNbO_3$", *Appl. Phys. Lett*., **41**, 607 (1982).

[58] J.D. Bierlein, H. Vanherzeele, "Potassium titanyl phosphate: propeties and new applications", *J. Opt. Soc. Am*., **6**, 622 (1989).

[59] R.V. Schmidt, I.P. Kaminow, "Metal-diffused optical waveguides in $LiNbO_3$", *Appl. Phys. Lett*., **25**, 458 (1974).

[60] D. Fluck, P. Günter, "Second-harmonic generation in potassium niobate waveguides", *IEEE J. Selected Top. Quantum Electron*., **6**, 122 (2000).

[61] A. Crunteanu, M. Pollnau, G. Jänchen, C. Hibert, P. Hoffmann, R.P. Salathé, R.W. Eason, C. Grivas, D.P. Shepherd, "Ti:sapphire rib channel waveguide fabricated by reactive etching of a planar waveguide", *Appl. Phys. B*, **75**, 15 (2002).

[62] W. Bolaños, J.J. Carvajal, X. Mateos, G.S. Murugan, A. Subramanian, J. S. Wilkinson, E. Cantelar, G. Lifante, M. Aguiló, F. Díaz, "$KY_{0.58}Gd_{0.22}Lu_{0.17}Tm_{0.03}(WO_4)_2$ buried rib waveguide lasers", *Opt. Mater*., **32**(3), 17 (2012).

[63] J. Gottman, D. Wortmann, I. Vasilief, L. Moiseev, D. Ganser, "Manufacturing of $Nd:Gd_3Ga_5O_{12}$ ridge waveguide lasers by pulsed laser deposition and ultrafast laser micromachining", *Appl. Surface Science*, **254**, 1105 (2007).

[64] E. Snitzer, "Optical maser action of Nd^{3+} in a barium crown glass" *Phys. Rev. Lett*., **7**, 444 (1961).

[65] J. I. Mackenzie, "Dielectric solid-state planar waveguide lasers: a review", *IEEE J. Sel. Topics. Quantum Electron*., **13**, 637 (2007).

[66] P.K. Tien, R. Ulrich, R.J. Martin, "Optical second harmonic generation in form of coherent Cerenkov radiation from a thin-film waveguide", *Appl. Phys. Lett*., **17**, 447 (1970).

[67] N. Uesugi, T. Kimura, "Efficient second-harmonic generation in three-dimensional $LiNbO_3$ optical waveguides ", *Appl. Phys. Lett*., **29**, 572 (1976).

[68] D. B. Anderson, J.T. Boyd, "Wideband CO_2 laser second harmonic generation phase matching in GaAs thin-film waveguides ", *Appl. Phys. Lett*., **19**, 266 (1971).

[69] A. Carenco, J. Jerphagnon, A. Perigaud, "Nonlinear optical properties of some m-disubstituted benzene derivatives", *J. Chem. Phys*., **66**, 3806 (1977).

[70] G.I.Stegeman, C.T.Seaton, "Nonlinear integrated optics", *J. Appl. Phys*., **58**, R57 (1985).

[71] N. Uesugi, T. Kimura, "Efficient second-harmonic generation in three-dimensional $LiNbO_3$ optical waveguide" *Appl. Phys. Lett*., **29**, 572 (1976).

[72] W. Sokler, H. Suche, "Second-harmonic generation in Ti-diffused $LiNbO_3$ optical waveguides with 25% conversion efficiency", *Appl. Phys. Lett*., **33**, 518 (1978).

[73] S. Neveu, J.P. Barety, M. DeMicheli, P. Sibillot, D.B. Ostrowsk, M. Papuchon, "High-performance focusing grating coupler fabricated by electron writting" Top. Meet. Integrated Guided Wave Opt., Kisimmee, FL. 1984.

[74] T. Taniuchi, K. Yamamoto, "Second harmonic generation in proton-exchange optical $LiNbO_3$ waveguide", *Proc. SPIE*, **864**, 36 (1988).

[75] G. Tohmon, K. Yamamoto, T. Taniuchi, "Blue light source using guided wave frequency doubler with a diode laser", *Proc. SPIE*, **898**, 70 (1988).

[76] B. Jaskorzynska, G. Arvidsson, F. Laurell, "Periodic structures for phase-matching in second harmonic generation in titanium lithium niobate" *Proc. SPIE*, **651**, 221 (1986).

[77] J. Webjörn, F. Laurell, G. Arvidsson, "Fabrication of periodically domain-inverted channel waveguide in lithium niobate for second harmonic generation", *J. Lightwave Technol.,* **7,** 1597 (1989).

[78] E.J. Lim, M.M. Fejer, R.L. Byer, "Second-harmonic generation of green light in periodically poled planar lithium niobate waveguide", *Electron. Lett*., **25**, 174 (1989).

[79] Y. Ishigame, T. Suhara, H. Nishihara,"$LiNbO_3$ waveguide second-harmonic generation device phase matched with a fan-out domain inverted grating", *Opt. Lett*., **16**, 375 (1991).

[80] F. Armani, D. Delacourt, E. Lallier, M. Papuchon, Q. He, M. DeMicheli, D.B. Ostrowsky, "First order quasiphase matching in $LiNbO_3$", *Electron. Lett*., **28**, 139 (1992).

[81] C. Cao, R. Srivastava, R.V. Ramaswamy, "Efficient quasi-phase matched blue second-harmonic generation in $LiNbO_3$ channel waveguides by a second-harmonic order grating", *Opt. Lett*., **17**, 592 (1992).

[82] C. Cao, B. Rose, R.V. Ramaswamy, R. Srivastava, "Efficient direct diode-laser frequency doubling in quasi-phase-mathced $LiNbO_3$ waveguides", *Opt. Lett*.,**17**, 795 (1992).

[83] M.M. Fejer, M.J. Digonet, R.l. Byer, "Generation of 22 mW of 532 nm radiation by frequency doubling in Ti:MgO:$LiNbO_3$", *Opt. Lett*., **11**, 230 (1986).

[84] N.A. Sanford, J.M. Connors, "Optimization of the Cerenkov sum-frequency generation in proton-exchange Mg:$LiNbO_3$ channel waveguides", *J. Appl. Phys*., **65**, 1429 (1989).

[85] K. Mizzuchi, K. Yamamoto, T. Taniuchi, "Second-harmonic generation of blue Light in a $LiTaO_3$ waveguide", *Appl. Phys. Lett*., **58**, 2732 (1991).

[86] H. Ahlfeldt, J. Webjörn, G. Rvidsson, "Periodic domain inversion and generation of blue light in lithium tantalite waveguides", *IEEE Photon. Tech. Lett*., **3**, 638 (1991).

[87] S. Matsumoto, E.J. Lim, H.M. Hertz, M.M. Fejer, "Quasi-phase-matched second harmonic generation of blue Light in electrically periodically-poled lithium tantalite waveguides", *Electron. Lett*, **27**, 2040 (1991).

[88] K. Mizuuchi, K. Yamamoto, T. Taniuchi, "Fabrication of first-order periodically domain-inverted structure in $LiTaO_3$", *Opt. Lett*., **59**, 1538 (1991).

[89] K. Yamamoto, K. Mizuuchi, "Blue-light generation by frequency doubling of a laser diode in a periodically domain-inverted $LiTaO_3$ waveguide", *IEEE Photon. Tech. Lett*., **4**, 435 (1992).

[90] K. Mizuuchi, K. Yamamoto, "Highly efficient quasi-phase-matched second-harmonic generation using a first-order periodically domain-inverted $LiTaO_3$ waveguide", *Appl. Phys. Lett*., **60**, 1283 (1992).

[91] D. Fluck, B. Binder, M. Küpfer, H. Looser, C. Buchal, P. Günter, "Phase-matched second harmonic blue light generation in ion implanted $KNbO_3$ planar waveguides with 29% conversion efficiency", *Opt. Commun*., **90**, 304 (1992).

[92] D. Fulck, J. Moll, P. Günter, M. Fleuster, C. Buchal, "Blue light generation by frequency doubling CW diode laser radiation in $KNbO_3$ channle waveguides", *Electron. Lett*., **28**, 1092 (1992).

[93] J.D. Berlein, D.B. Laubacher, J.B. Brown, C.J. van de Poel, "Balanced phase matching in segmented $KTiOPO_4$", *Appl. Phys. Lett*., **56**, 1725 (1990).

[94] W.P. Risk, "Fabrication and characterization of planar ion-exchange $KTiOPO_4$ waveguides for frequency doubling", *Appl. Phys. Lett*., **58**, 19 (1991).

[95] C.J. Van der Poel, J.D. Berlein, J.B. Brown, S. Colak, "Efficient type I blue second-harmonic generation in periodically segmented $KTiOPO_4$ wavegudies", *Appl. Phys. Lett*., **57**, 2074 (1990).

[96] L. Zhang, P.J. Chandler, P.D. Townsend, Z.T. Alwahabi, A.J. McCaffery, "Frequency doubling in ion-implnated $KTiOPO_4$ planar waveguides with 25% conversion efficiency", *Electron. Lett.,* **28**, 1478 (1992).

[97] Q. Chen, W.P. Risk, "High efficient quasi-phasematched frequency doubling waveguides in $KTiOPO_4$ fabricated by electric field poling", *Electron. Lett*., **32**, 107 (1996).

[98] M. Jongerius, R.J. Bolt, N.A. Sweep, "Blue second-harmonic generation in waveguides fabricated in undoped and scandium-doped $KTiOPO_4$", *J.Appl. Phys*.,**75**, 3316, (1994).

[99] R.F. Belt, G. Gashurov, Y.S. Liu, "KTP as a harmonic generator for Nd:YAG lasers*", Laser Focus*, October, 110 (1985).

[100] H. Karlsson, F. Laurell, L.K. Cheng, "Periodic poling of $RbTiOPO_4$ for quasi-phase matched blue light generation", Appl. Phys. Lett., **74**, 1519 (1999).

[101] G. Lifante, *Integrated Photonics: fundamentals,* Wiley (2003).

[102] T. Suhara, M. Fujimura, *Waveguide Nonlinear-Optic devices,* Springer (2003).

[103] Yu. S. Oseledchik, A.I. Pisarevsky, A.L. Prosvirnin, V.V. Starshenko, N.V. Svitanko, "Nonlinear optical properties of the flux grown $RbTiOPO_4$ crystal", Opt. Mater., **3**, 237 (1994).

[104] Y. Guillen, B. Ménaert, J.P. Fève, P. Segonds, J. Douady, B. Boulanger, O. Pacaud, "Crystal growth and refined sellmeier equations over the complete transparency range of $RbTiOPO_4$", *Opt. Mater*., **22**, 155 (2003).

[105] L.T. Cheng, L.K. Cheng, J.D. Bierlein, "Linear and nonlinear optical properties of the arsenate isomorphs of KTP", *Proc. SPIE*, **43** , 1863 (1993).

[106] J.J Carvajal, PhD. Thesis, *Growth and characterization of $RbTiOPO_4$. A new self-frequency doubling crystal*, Departament de Química i Inorgànica, Universitat Rovira i Virgili, Tarragona, Spain (2005).

[107] A. Peña, PhD. Thesis, *Ytterbium and erbium doped $RbTi_{1-x}M_xOPO_4$ (M=Nb or Ta) crystals. New laser and nonlinear bifunctional materials*, Departament de Química Física i Inorgànica, Universitat Rovira i Virgili, Tarragona, Spain (2007).

[108] L.K. Cheng, J.D. Bierlein, A. A. Ballman, "Crystal growth $KTiOPO_4$ isomorphs from tungstates and molybdate fluxes", *J. Cryst. Growth*, **110**, 697 (1991).

[109] D. Elwell, H.J. Scheel, *Crystal growth from high temperature solutions*, Academic Press, 1975.

[110] J. Gottman, G. Schlaghecken, R. Wagner, E.W. Kreutz, "Fabrication of erbium-doped planar waveguides by pulsed-laser deposition and laser micromachining for Optoelectronics Device Fabrication", *Proc SPIE*., 4941,148 (Edited by Ostenddorf, 2003).

[111] J. Lancok, M. Jelinek, "Study of fabrication of channel waveguide in Ti:Sapphire layers", *Laser Physics*, **8**, 303 (1998).

[112] C.N. Borca, Y.E. Romanyuk, "Optical channel waveguide in $KY(WO_4)_2$:Yb^{3+}" *Quantum electronics and laser science conference* (CLEO), 2006.

[113] C.H. Jeong, D.W. Kim, "Sapphire etching with BC13/HBr/Ar plasma", *Surf. Coat. Tech*., **171**, 280 (2002).

[114] D.W. Kim, C. H. Jeong, "High rate sapphire etching using BC13-based inductively coupled plasma", *J. Korean Phys. Soc*., **42**, S795 (2003).

[115] H. Jeong, D. W. Kim, "A study of sapphire etching characteristics using BC13 based inductively coupled plasmas", *Jpn. J. Appl. Phys*., **41**, 6206 (2002).

[116] D. J. Kang, I. S. Kim, "Inductively coupled plasma reactive ion etching of sapphire using C_2F_5- and NF_3- based gas mixtures", *Mat. Sci. Semicon. Proc*., **11**, 16 (2008).

[117] B.D. Cullity, *Elements of X-Ray Diffraction*, second edition, Addison-Westley Pu. Co, Inc. (1978).

[118] J. Rodríguez-Carvajal. *Short reference guide for the computer program FULLPROF*, Laboratoire Léon Brillouin, CEA-CNRS, Gif sur Yvette, 1998.

[119] R.A. Young. *The Rietveld method, International Union of Crystallography*, monographs on crystallography 5, Oxford University Press, Oxford, 1995.

[120] P.K. Tien, R. Ulrich, "Theory of Prism-Film Coupler and Thin-Film Light Guides", *J. Opt. Soc. Am*. A, **60** (10), 1325 (1970).

[121] Y. Okamura, S. Yoshinaka, S Yamamoto, "Measuring mode propagation losses of integrated optical waveguides: a simple method", *Appl. Opt*. **22**, 3892 (1983).

[122] P.A. Thomas, S.C. Mayo, B.E. Watts, "Crystal structures of $RbTiOAsO_4$, $KTiO(P_{0.56}As_{0.42})O_4$, $RbTiOPO_4$, and $(Rb_{0.465}K_{0.535})TiOPO_4$, analysis of pseudosymmetry in crystals of the $KTiOPO_4$", *Acta. Crystallogr.*, **B48**, 401 (1192).

[123] V.I. Voronkova, V.K. Yanovskii, "Morphology of crystals of $KTiOPO_4$", *Sov. Phys. Crystallogr*., **31**, 123 (1986).

[124] N.I. Povlova, V.M. Garmash, G.B. Sil'nitskaya, N.P. Stekol'shchikova, V.A. Gerken, "Morphologies of $KTiOPO_4$ single crystals", *Sov. Phys. Crystallogr*., **31**, 87 (1986).

[125] J.J. Carvajal, R. Solé, J. Gavaldà, J. Massons, F. Díaz, M. Aguiló, "Phase transitions in $RbTiOPO_4$ doped with Niobium", *Chem. Mater*., **15**, 2730 (2003).

[126] J.J. Carvajal, V. Nikolov, R.Solé, Jna. Gavaldà, J. Massons, M. Rico, C. Zaldo, M. Aguiló and F. Díaz, "Enhancement of the erbium concentration in $RbTiOPO_4$ by codoping with niobium", *Chem. Mater.* , **12**, 3172 (2000).

[127] K. Iliev, P. Peshev, V. Nikolov, I. Koseva, "Physicochemical properties of high- temperature solutions of the K_2O-P_2O_5-TiO_2-WO_3 system, suitable for the growth of $KTiOPO_4$ (KTP) single-crystals", *J. Cryst. Growth*, **100** (1-2), 225 (1990).

[128] N. Yamada, Y. Yamamoto, "Refractive index profiles of $KTiOPO_4$ Ion-exchange waveguides and effect of barium ion", *Jpn. J. Appl. Phys*., **33**, 6572 (1994).

[129] A. Aznar, O. Silvestre, M.C. Pujol, R. M. Solé, M. Aguiló, F. Díaz, "Liquid-phase epitaxy crystal growth of monoclinic $KLu_{1-x}Yb_x(WO4)_2/KLu(WO_4)_2$", *Cryst. Growth & Des*., **6**, 1781 (2006).

[130] K. Daneshvar, E. A. Giess, D. Kang, J. R. Williams, D. Dawes, "Rb ion-exchange profile in potassium titanyl phosphate (KTP)", *Opt. Mater*., **12**, 453 (1999).

[131] J.J. Carvajal, R. Solé, Jna. Gavaldà, J. Massons, P. Segonds, B. Boulanger, A. Brenier, G. Boulon, J. Zaccaro, M. Aguiló, F. Díaz, "Spectroscopic and second harmonic generation properties of a new crystal: Yb-doped $RbTiOPO_4$", *Opt. Mater*., **26**, 313 (2004).

Paper I

Crystal growth and characterization of $RbTi_{1-x-y}Yb_xOPO_4/RbTiOPO_4$ (001) non-linear optical layers

J. Cugat, R.M. Solé, J.J. Carvajal, M. C. Pujol, X. Mateos, F. Díaz, M. Aguiló,

CrystlEngComm, **13**, 2015 (2011).

CrystEngComm

Dynamic Article Links

Cite this: *CrystEngComm*, 2011, **13**, 2015

www.rsc.org/crystengcomm

PAPER

Crystal growth and characterization of $RbTi_{1-x-y}Yb_xNb_yOPO_4/RbTiOPO_4$ (001) non-linear optical epitaxial layers†

Jaume Cugat, Rosa Maria Solé, Joan J. Carvajal, Maria Cinta Pujol, Xavier Mateos, Francesc Díaz and Magdalena Aguiló*

Received 15th September 2010, Accepted 26th November 2010
DOI: 10.1039/c0ce00647e

In this paper we report the growth of $RbTi_{1-x-y}Yb_xNb_yOPO_4/RbTiOPO_4$ epitaxial layers by the liquid phase epitaxy method and discuss their structural and optical characterization. The layers were grown on (001) oriented substrates because this plane contains the phase-matching direction for Yb^{3+} type-II second-harmonic generation. In $RbTi_{0.971}Yb_{0.015}Nb_{0.014}OPO_4/RbTiOPO_4$ epitaxial layers we obtained enough contrast of refractive indices ($\Delta n_z = 0.007$ at 632.8 nm) to guide the light in TM polarization. The maximum Yb^{3+} concentration obtained in these layers was 1.43×10^{20} atoms per cm^3, which may be suitable for laser action. The lattice mismatch between the epitaxial layers and the substrates was low enough to obtain high quality epitaxial layers. Confinement of the light at 532 and 632.8 nm was demonstrated and there was good agreement between theoretical calculations, dark-mode spectra and modes of propagation.

1. Introduction

$RbTiOPO_4$ (RTP) belongs to the $KTiOPO_4$ (KTP) family of non-linear optical crystals. At room temperature, the crystal symmetry of RTP is orthorhombic and belongs to the non-centrosymmetric space group $Pna2_1$, with lattice parameters $a =$ 12.974(2) Å, $b = 6.494(3)$ Å and $c = 10.564(6)$ Å.[1] RTP crystals are positive biaxial crystals, with $n_x < n_y < n_z$ ($n_a < n_b < n_c$) and point symmetry *mm*2. Because of their non-centrosymmetry and non-linearity, they can be used for frequency doubling of lasers that emit in the IR spectral range.[2] In the non-linear optical process, the (001) plane is especially interesting because it contains the Yb^{3+} type-II phase-matching direction and the ferroelectric vector is parallel to the [001] direction. This enables domains that are useful for Quasi Phase Matching (QPM) processes to be obtained. Moreover, RTP can be doped with active ions to obtain self-frequency doubling (SFD) materials, which are useful for compact and efficient laser sources in the visible range. Moreover, all these properties can be converged in waveguides for integrated photonics. A waveguide structure to confine the interacting optical waves enables compact and efficient devices to be constructed.[3] Thin-film optical waveguides also offer interesting possibilities for non-linear optics since the intrinsic confinement of the electromagnetic field in at least one dimension to distances of the order of the radiation wavelength leads to high power densities.[4]

Ytterbium is interesting because of its emission at a wavelength of around 1 μm and its simple energy level scheme consisting of only two energy levels: the ground state $^2F_{7/2}$ and the excited state $^2F_{5/2}$. The Yb^{3+} ion has several advantages, including its broad absorption and emission bandwidth, low quantum defect and long lifetime. It also has no absorption losses at the second-harmonic generation (SHG) frequency, which makes it particularly relevant for SFD.[5]

In an earlier study we investigated the RE^{3+} doping of KTP.[6] The RE^{3+} distribution coefficients obtained were very low (typically about 10^{-3}). RTP has a higher Yb^{3+} distribution coefficient than KTP but it is still too low for laser operation. It has recently been shown that the distribution coefficient of Yb^{3+} in RTP can be increased by co-doping with Nb^{5+} (ref. 5) and lasing in RTP co-doped with Nb^{5+} and Yb^{3+} has been demonstrated.[7] Growing Yb,Nb:RTP single crystals with high optical quality presents several difficulties, mainly associated with the low growth rate, the crystal morphology (plate shape) and the tendency for cracks to appear.[8] To increase the optical absorption of Yb^{3+} in RTP by increasing the optical path, and guiding the light, we grew epitaxial composites of Yb:RTP/RTP (001) by the Liquid Phase Epitaxy (LPE) method. However, due to the low Yb^{3+} distribution coefficients in RTP, the refractive indices contrast between the epilayers and the substrate was too low for optical waveguiding. To increase the distribution coefficient of Yb^{3+} in RTP and increase the optical absorption in the crystals and the contrast of refractive

Física i Cristal·lografia de Materials i Nanomaterials (FiCMA-FiCNA), Universitat Rovira i Virgili (URV), Campus Sescelades, C/Marcel·lí Domingo s/n E-43007, Tarragona, Spain. E-mail: magdalena.aguilo@urv.cat

† Electronic supplementary information (ESI) available: Experimental details of single crystal growth for substrates. See DOI: 10.1039/c0ce00647e

indices for guiding the light, we grew Yb:Nb:RTP/RTP epitaxial films.

Here we describe the crystal growth characteristics of bulk crystals for substrates and report suitable conditions for obtaining Yb:RTP/RTP and Yb:Nb:RTP/RTP epitaxial layers. We characterize the epitaxial layers by measuring the refractive indices, ion concentration, lattice parameters, *etc.* Finally, we study the light-guiding properties at 632.8 and 532 nm.

2. Experimental section

2.1. Liquid-Phase Epitaxial (LPE) growth

Liquid-phase epitaxy experiments were carried out in a special vertical furnace built with better isolation and a larger tubular core than the furnace used for bulk single crystal growth. We obtained a wide zone of uniform temperature so that the temperature gradient in the solution was practically zero. The crucible used was cylindrical, 30 mm in diameter and 40 mm in height, and filled with about 80 g of solution. The reagents used were the same as in the growth of substrates (Rb_2CO_3 (99%), $NH_4H_2PO_4$ (99%), TiO_2 (99.9%) and WO_3 (99.9%)), and Yb_2O_3 (99.9%) and Nb_2O_5 (99.9%) were used for substitution. To obtain a highly confined light waveguide, we used several solution compositions in order to obtain a suitable contrast of refractive indices. Mainly we used three different oxide relations between Rb_2O–P_2O_5–(TiO_2 + Nb_2O_5 + Yb_2O_3)–WO_3. In experiments 1–8 in Table 2, we used solutions with composition Rb_2O–P_2O_5–(TiO_2 − Nb_2O_5 + Yb_2O_3)–WO_3 = 40.80–27.20–32.00–0.00 (mol%) and different levels of substitution of TiO_2 by Yb_2O_3 and Nb_2O_5, taking into account the results of varying the crystallization region of RTP by substituting TiO_2 with Nb_2O_5 and Yb_2O_3.[9] To reduce the viscosity of the growth solution, as in the solution used to obtain the substrates, we used WO_3-containing solutions. In experiments 9 and 10, we used solutions with 10 mol% of WO_3. In this case, we did a trade-off between the presence of W^{6+} in the layer and solution viscosity because incorporating W^{6+} into the crystals could hinder future applications. Taking into account the crystallization region of RTP in solutions containing 10 mol% WO_3, we chose a solution composition located in the central zone of the RTP crystallization region. The composition used was Rb_2O–P_2O_5–(TiO_2 + Nb_2O_5 + Yb_2O_3)–WO_3 = 43.90–23.6–22.50–10.00 (mol%). In experiment 11, we used a solution containing 20 mol% WO_3, with composition Rb_2O–P_2O_5–(TiO_2 + Nb_2O_5 + Yb_2O_3)–WO_3 = 43.82–22.58–13.60–20.00 (mol%), which has already been used by our group to successfully grow single crystals.[10] After homogenization of the solution, its saturation temperature was accurately determined with a (001)-oriented RTP seed. We also studied the kinetics of the growth/dissolution processes because this is important in deciding the experimental conditions for growing the LPE single-crystal layers. In all experiments we used the same type of substrate, (001) plates with polished faces to grow layers along the (001) plane. The plate substrates were prepared by cutting 1.5 mm thick slices from single crystals with a diamond saw and polishing the slices with alumina powder. The (001) or *a*–*b* plane is interesting because it contains the type-II non-critical phase matching direction for the ytterbium laser emission wavelength range (from 985 to 1118 nm). The substrates were cut with the edges parallel to the *a* and *b* crystallographic directions. Before they were placed in the furnace, the substrates were carefully and consecutively cleaned in the following solutions: 1 : 1 HNO_3 : H_2O (in volume), distilled water, acetone and ethanol (5 minutes in each case). They were then slowly introduced into the furnace to prevent thermal stresses and held above the surface of the solution for about 1 h to achieve thermal equilibrium with the solution. The substrates were then dipped into the solution and kept at a temperature 1 K above the saturation temperature for 5 minutes to dissolve the outer part of the crystal. To begin epitaxial growth, the temperature of the solution was then decreased to 2–10 K below the saturation temperature and growth was allowed to progress for several hours.

Finally, the crystal was removed from the solution and kept a few millimetres above the surface of the solution while the furnace was cooled to room temperature at 15 K h^{-1} to avoid thermal stresses between the substrate and the epitaxial layer that could lead to cracks. The epitaxial layers were observed using an optical microscope, a Sensofar PLμ 2300 interferometric microscope, and finally an atomic force microscope (AFM). With these devices we observed the morphologies of the epitaxial layers. We also profiled the layers, obtaining the thickness along several directions of the epitaxial layer.

To study how the thickness of the layer changes as a function of the growth time (velocity of growth), in experiment 3 the substrate was initially dipped 10 mm into the solution and then pulled out in steps of 2 mm for known time intervals. In the final step, the substrate was completely removed from the solution.

The chemical composition of the $RbTi_{1-x-y}Yb_xNb_yOPO_4$ single crystals and that of the epitaxial layers obtained by LPE were determined by electron probe microanalysis (EPMA) in a Cameca SX-50 microprobe analyzer. The electron beam was generated with an intensity of 15 nA and an accelerating voltage of 20 KV. The X-rays produced by the samples were detected and characterized by a wavelength-dispersive spectrometer (WDS). The X-ray pattern of the sample was compared with that of standard samples containing known concentrations of the elements to be analyzed. $RbTiOPO_4$ was used as a standard for determining Rb, Ti and P. Nb metal was used to determine the Nb concentration and YbF_3 was used for Yb measurements. All samples were prepared in the same way: first, a small piece of crystal was placed in a cylindrical container, where a polyester resin was added with a catalyst. After the resin had solidified, the surface containing the crystal was polished with a 1 μm diamond powder.

2.2. X-Ray powder diffraction

To measure the unit cell parameters, small single crystals of Yb:Nb:RTP were grown on a Pt wire immersed in the solution. The saturation temperature was determined by decreasing the solution temperature at intervals of 10 K every 30 minutes until the crystals appeared. The temperature of the solution was then maintained for several hours to grow the crystals. The lattice parameters of these crystals with different compositions were determined at room temperature by X-ray powder diffraction (XRD). The data were collected with a Siemens D5000 X-ray powder diffractometer with the Bragg–Brentano parafocusing

geometry and a θ–θ configuration. Cu K_α radiation was used in these experiments and the 2θ range was from 10 to 70°, with a step scan (ss) of 0.02° and a scan time (st) of 16 s. The crystal cell parameters were calculated from the diffraction data using the FULLPROF program[11] and the Rietveld method.[12] These results were used to calculate the lattice mismatch between the epitaxial layer and the substrate, which is of great interest for optimizing the quality of the epilayer/substrate interface.

2.3. Planar waveguide fabrication and characterization techniques

We used the epitaxies grown in the previous steps to fabricate planar waveguides. The first step in the fabrication was to remove the epilayer grown on one of the faces of the substrate. The remaining epilayer was then polished with alumina powder to obtain a 50 μm thick highly transparent layer to be used for measuring the refractive indices. We were then able to calculate the number of propagation modes as a function of the thickness of the epitaxy. After polishing the sample, we measured the refractive indices of the epitaxy and substrate using the total internal-reflecting-angle law, coupling the light by a prism using a Metricon prism coupler.

Visualization of the propagation modes in the epitaxial layer requires calculation of the proper thickness to obtain a small number of modes. Using the refractive indices, we applied the equation of dispersion for a wave propagating along the guide:[13]

$$\frac{2\pi d}{\lambda}\left(n^2 - n_{\text{eff}}^2\right)^{1/2} = m\pi + \phi_{n_a} + \phi_{n_s},$$

where m is the mode number, d is the thickness of the epilayer, λ is the wavelength of the light in vacuum and n_a and n_s are the air and substrate refractive indices, respectively, while n is the refractive index of the guiding layer. In our case, $n = n_z$, n_{eff} is the effective refractive index of the propagation mode in the epilayer, and

$$\phi_{n_j} = arctg\left[\left(\frac{n}{n_j}\right)^{2\rho}\left(\frac{n_{\text{eff}}^2 - n_j^2}{n^2 - n_{\text{eff}}^2}\right)\right]^{\frac{1}{2}},$$

where $j = a$, s and

$$\rho = \begin{cases} 0 \text{ for TE polarization} \\ 1 \text{ for TM polarization} \end{cases}.$$

We were then able to determine the number of allowed modes for a given thickness of the epitaxial layer.

After checking the calculations, the samples were polished until the thickness required to obtain a few propagation modes. The prism coupler system was used to record the dark-mode spectrum at 632.8 nm using a He–Ne laser beam as the light source with TM polarization. The same experiments were carried out using a 532 nm laser beam to record the dark-mode spectrum with TM polarization. Finally, we used a CCD camera to visualize the different guided modes that the waveguide can support by coupling the light of the He–Ne laser emitting at 632.8 nm and the frequency doubled Nd:YAG laser emitting at 532 nm at the input and output ends of the waveguide with microscope objectives (40× and 60×, respectively).

3. Results and discussion

3.1. Single-crystal growth for substrates and liquid phase epitaxial (LPE) growth

RTP crystals, to be cut for substrates, were grown in a tubular furnace as described in the Experimental section. Table 1 shows the crystal growth conditions, dimensions and weights of several single crystals that were cut for substrates. The crystals obtained were generally colorless, transparent and free of inclusions and cracks. Their dimensions were 14.0–9.2, 15.1–26.0 and 11.1–21.9 mm in the a, b and c crystallographic directions, respectively, and their weights ranged from 5.71 g to 13.94 g. In several experiments we pulled the crystals (see Table 1) to obtain a larger dimension along the c crystallographic direction in the single crystals. From each single crystal we were therefore able to cut more substrates. Moreover, as observed in Table 1, by pulling the crystal, the average growth velocity increases. The crystals were then cut in plates of dimensions 4.2–10.3, 12–19.3 and 1 mm along the a, b and c crystallographic directions, respectively, to be used for substrates. All the substrates were cut perpendicular to the c crystallographic direction or (001) face to obtain the a–b plane. This plane is interesting because it contains the non-critical phase matching (PM) type-II SHG direction. Moreover, the a–b plane is perpendicular to the ferroelectric vectors of the domains, which makes it possible to produce a periodic inversion of them and realize Quasi Phase Matching. The plates were polished to optical quality to obtain surfaces with 50–80 nm of roughness and 8–20 m of curvature, otherwise the defects could propagate from the interface to the epitaxial film. Fig. 1 shows a photograph of an as-grown crystal to be cut for substrates.

Table 1 Growth conditions, dimensions and weight of some crystals grown for substrates

Experiment number	Cooling interval/K	Total pulling/mm	Crystal dimensions $a \times b \times c$/mm	Crystal weight/g
1	20	0	14.0 × 26.0 × 11.1	7.99
2	20	0	14.9 × 15.1 × 15.9	5.71
3	27	4	17.3 × 18.7 × 20.4	9.37
4	28	5.5	17.9 × 20.0 × 21.5	12.32
5	30	6.5	19.2 × 21.1 × 21.9	13.94

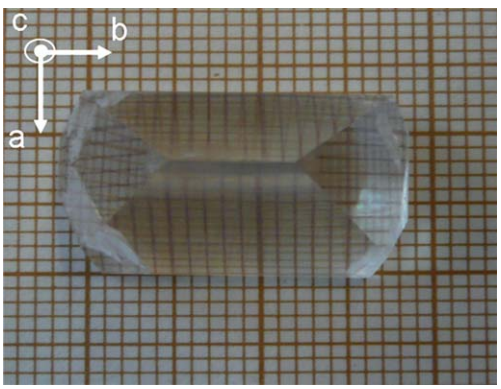

Fig. 1 Photograph of an as-grown single crystal, to be cut for substrates.

Table 2 Conditions of epitaxial growth. Solution composition, size of the substrates, $\Delta T = T_s - T_g$ (T_s = saturation temperature, T_g = growth temperature) and growth time

Experiment number	Solution composition Rb_2O–P_2O_5–TiO_2–Yb_2O_3–Nb_2O_5–WO_3/mol%	Substrate dimensions $a \times b \times c$/mm	$\Delta T = T_s - T_g$/K	Growth time/h
1	40.8–27.2–30.08–1.92–0–0	6.7 × 16.9 × 1.0	2	3
2	40.8–27.2–30.08–1.92–0–0	6.5 × 12.0 × 1.0	2	6
3	40.8–27.2–30.08–1.92–0–0	6.9 × 19.3 × 1.0	2	0.30–1–2.30–4–15
4	40.8–27.2–30.4–0.64–0.96–0	4.2 × 18.5 × 1.0	2	16
5	40.8–27.2–29.76–1.92–0.32–0	6.5 × 18.5 × 1.0	2	5
6	40.8–27.2–29.76–1.92–0.32–0	9.6 × 13.6 × 1.0	2	5
7	40.8–27.2–29.44–1.92–0.64–0	10.3 × 18.2 × 1.0	2	6
8	40.8–27.2–29.44–1.92–0.64–0	6.2 × 16.1 × 1.0	2	6
9	43.9–23.6–20.70–1.35–0.45–10	10.24 × 18.14 × 1.0	9	7
10	43.9–23.6–20.70–1.35–0.45–10	10.15 × 12.58 × 1.0	10	6
11	43.82–22.58–12.92–0.27–0.41–20	8.6 × 16.2 × 1.0	7	3

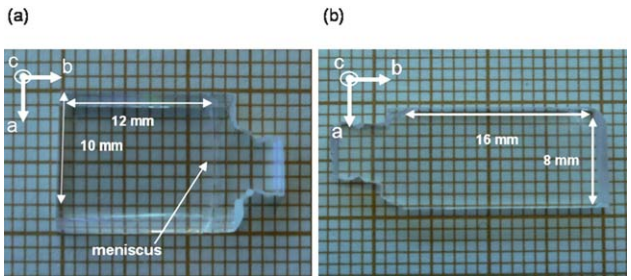

Fig. 2 (a) Photograph of the as-grown epitaxy obtained in experiment 11 (Table 2). (b) Photograph of the epitaxy grown in experiment 9 (Table 2) after a polishing process.

Table 1 summarizes the dimensions and weights of some of the crystals grown for this purpose.

The epitaxial layers were grown by liquid phase epitaxy (LPE) from self-flux solutions and WO_3-containing solutions. This method was successfully used earlier in the KTP family.[14] Table 2 summarizes the LPE experiments conducted using (001) substrate plates. We grew epitaxial layers as large as 16 mm, which, unlike with bulk crystals, have a very large optical path. The solution composition, substrate dimensions, $\Delta T = T_s - T_g$ (where T_s is the saturation temperature and T_g is the growth temperature) and growth time are shown in Table 2. Generally, the epitaxial layers were grown with high crystalline quality. The epitaxial layers grown in experiments 1–3 (see Table 2) have low concentrations of Yb^{3+} and, therefore, low contrasts of refractive indices, which make the guided modes of the light extremely difficult. Therefore, we grew RTP epitaxial layers doped with Yb^{3+} and Nb^{5+} (see experiments 4–11), bearing in mind that Nb^{5+} improves the distribution coefficient of Yb^{3+} and increases the contrast of the refractive indices. These composites, as we will see in the Waveguide characterization section, guided the light in TM polarization. Moreover, we grew epitaxial layers from WO_3-containing solutions because the solutions containing W^{6+} are less viscous than self-flux solutions and allow for easier growth. Moreover, the poor incorporation of W^{6+} in the crystal structure is in competition with Nb^{5+}, which helps to produce better charge compensation. Finally, the incorporation of W^{6+} into the crystal structure slightly increases the refractive index contrast along the c crystallographic direction, which allows for better confinement in TM polarization. Experiments 9–11 were done in WO_3-containing solutions. Fig. 2(a) shows the as-grown epitaxial layer obtained in experiment 11 (see Table 2) and Fig. 2(b) shows the epilayer grown in experiment 9 (see Table 2) after it was polished down to a thickness of 10 μm.

The morphologies of the as-grown epitaxial layers were observed by optical microscope, confocal microscope and atomic force microscope, depending on the scale of observation. The surfaces of the epilayers grown from self-flux solutions were generally smoother than those of the epilayers grown from WO_3-containing solutions. Fig. 3 shows a confocal image of the epilayer grown in experiment 9, and a detail of a 100 × 100 μm² region obtained by AFM. There is also a profile of the 75–125 nm high macrosteps generated by screw dislocations. The reason why morphologies such as screw dislocations and macrosteps were obtained at the surface of the epilayers grown from WO_3-containing solutions while the epilayers grown from self-flux solutions were generally smoother could be the lower viscosity of

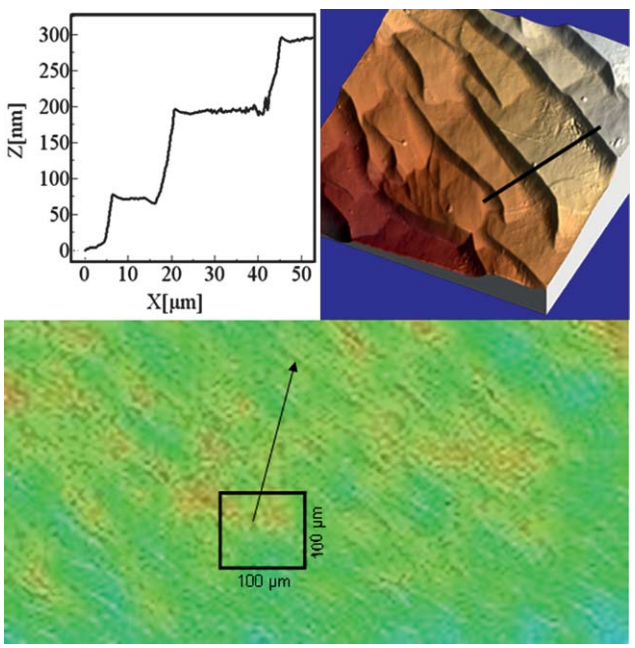

Fig. 3 Confocal image of the epilayer grown in experiment 9. Detail of a 100 × 100 μm² region obtained by AFM and profile of the macrosteps observed in the AFM image.

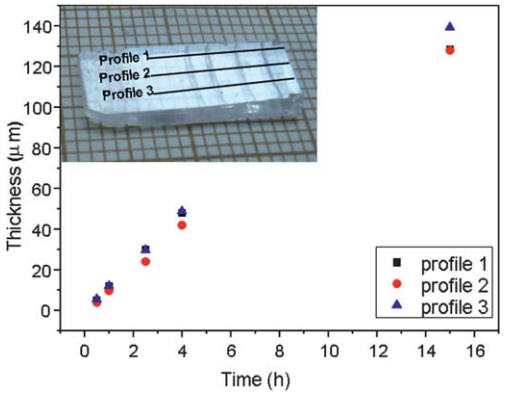

Fig. 4 Thickness of the epitaxial layer against the time of growth. The inset shows the location on the crystal of the three profiles used to take the measurements.

the WO_3-containing solutions, which permits a higher rate of growth.

In experiment 3, we studied the dependence of layer thickness on growth time by keeping all the other growth conditions constant. As we explained in the Experimental section, the substrate was initially dipped 10 mm into the solution and pulled out in 2 mm steps at the time intervals given in Table 2. The thickness of the epitaxial layer grown on the different parts of the substrate (corresponding to different growth times) was measured with the confocal microscope. Similar measurements were taken at both sides of the central region of the crystal to check there was no important dispersion between the growth thicknesses of different crystal zones for the same growth time. The results are shown in Fig. 4, the inset of which shows the location of the three profiles along which the measurements were taken. Here a linear behavior is observed between the epitaxial thickness and the growth time, at least up to 5 hours of growth, with a slope of 8.3 μm h^{-1}.

The composition of the epitaxial layers was measured by EPMA (see Table 3). From these results we calculated the coefficients of distribution of Yb^{3+} and Nb^{5+}, according to $K_{Yb} = \frac{\{[Yb]/([Yb]+[Nb]+[Ti])\}_{crystal}}{\{[Yb]/([Yb]+[Nb]+[Ti])\}_{solution}}$ for Yb^{3+} and $K_{Nb} = \frac{\{[Nb]/([Nb]+[Yb]+[Ti])\}_{crystal}}{\{[Nb]/([Nb]+[Yb]+[Ti])\}_{solution}}$ for Nb^{5+}, where [Yb], [Nb] and [Ti] are the Yb^{3+}, Nb^{5+} and Ti^{4+} concentrations in at%. W^{6+} concentration is not included in the chemical formula of the epitaxial layers in Table 3 because its distribution coefficient for substituting Ti in RTP is very low (in the order of 0.002).[15]

Table 3 shows the composition of the epitaxial layers grown from different solution compositions and the Yb^{3+} and Nb^{5+} distribution coefficients. We can see that in the epitaxial layers grown in experiments 6, 8 and 9 (the numbers of the experiments are the same as those in Table 2), the Yb^{3+} concentration is of the same order, around 10^{20} atoms per cm^3 which may be enough for laser demonstration.[5] On the other hand, the epilayers grown in experiments 1 and 11 contain Yb^{3+} concentrations of the order of 10^{19} atoms per cm^3. This concentration of active ions may not be enough for efficient lasing, though this would need to be checked. The lower Yb^{3+} concentration in sample 1 is due to the absence of Nb^{5+} in the solution since it has already been shown that the presence of Nb^{5+} in the solution helps to increase the Yb^{3+} distribution coefficient in the crystal.[7] Moreover, the epilayer obtained in experiment 11 has a lower Yb^{3+} concentration than other epitaxial layers because in the solution the presence of Yb_2O_3 is much lower (approximately three times). From experiments 1, 6 and 8 we can see that the presence of Nb^{5+} increases the distribution coefficient of Yb^{3+}. In experiment 9, there is an increase of K_{Nb} and also, though to a lesser extent, of K_{Yb}, perhaps because of the change in the solution composition.

The composition homogeneity of the epitaxial layers was analyzed by EPMA on the polished epilayer grown in experiment 8. Results show a homogeneity of Yb^{3+} and Nb^{5+} distribution along the epitaxy (see Fig. 5, which plots the concentration of the doping ions (Yb^{3+} + Nb^{5+}) against the distance to the epitaxial surface). In this figure we can also see the sharp compositional change in the interface, which indicates that there is practically no diffusion of the doping ions from the layer to the substrate. This is interesting for the light confinement in the waveguides.

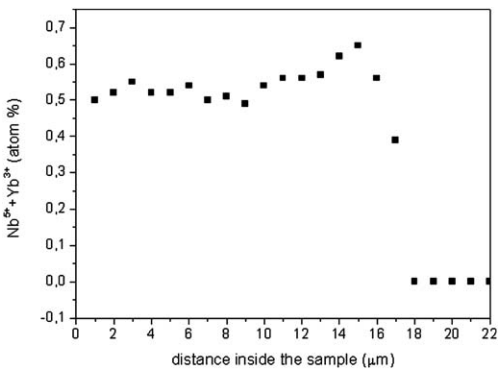

Fig. 5 Concentration of the doping ions (Yb^{3+} + Nb^{5+}) against distance to the epitaxial surface.

Table 3 Composition of the epitaxial layers grown from different solution composition and distribution coefficients of the doping ions

Exp. num.	$\frac{[Yb_2O_3]}{[TiO_2]+[Yb_2O_3]+[Nb_2O_5]} \times 100$ (mol%)	$\frac{[Nb_2O_5]}{[TiO_2]+[Yb_2O_3]+[Nb_2O_5]} \times 100$ (mol%)	Epilayer stoichiometry	K_{Yb}	K_{Nb}
1	6	0	$RbTi_{0.995}Yb_{0.005}OPO_4$	0.04	—
6	6	1	$RbTi_{0.975}Yb_{0.014}Nb_{0.011}OPO_4$	0.125	0.590
8	6	2	$RbTi_{0.971}Yb_{0.015}Nb_{0.014}OPO_4$	0.135	0.378
9	6	2	$RbTi_{0.958}Yb_{0.016}Nb_{0.026}OPO_4$	0.140	0.658
11	2	3	$RbTi_{0.983}Yb_{0.004}Nb_{0.013}OPO_4$	0.106	0.226

Table 4 Unit cell parameters of $RbTi_{1-x-y}Yb_xNb_yOPO_4$

Exp. num.	Stoichiometric formula	*a*/Å	*b*/Å	*c*/Å
Subs.	$RbTiOPO_4$	12.9650(5)	6.5007(3)	10.5576(4)
1	$RbTi_{0.995}Yb_{0.005}OPO_4$	12.9664(6)	6.5012(3)	10.5611(5)
6	$RbTi_{0.975}Yb_{0.014}Nb_{0.011}OPO_4$	12.9831(8)	6.5116(4)	10.5711(6)
8	$RbTi_{0.971}Yb_{0.015}Nb_{0.014}OPO_4$	12.9933(2)	6.5150(6)	10.5852(8)

Table 5 Lattice mismatch between $RbTi_{1-x-y}Nb_yYb_xOPO_4$ and RTP (001) substrate. The unit cell parameters of the substrate used in these calculations correspond to RTP grown from a solution containing 20% WO_3

Epitaxial layer	Substrate/epilayer lattice mismatch (001)
$RbTi_{0.995}Yb_{0.005}OPO_4$	0.05
$RbTi_{0.975}Yb_{0.014}Nb_{0.011}OPO_4$	0.342
$RbTi_{0.971}Yb_{0.015}Nb_{0.014}OPO_4$	0.473

3.2. X-Ray powder diffraction

Table 4 gives the unit cell parameters of RTP and Yb:Nb:RTP obtained from the X-ray powder diffraction data discussed in the Experimental section. We can see that the presence of Yb^{3+} and Nb^{5+} in the crystal structure leads to an increase in the lattice parameters. An explanation for the expansion of the unit cell is that Nb^{5+} and Yb^{3+} have larger ionic radii than Ti^{4+}, which causes the crystal unit cell to expand.[16]

The lattice mismatch between the layer and the substrate is important for the quality of the layer/substrate interface. High mismatches produce stress at the interface, which favors the formation of cracks that can propagate through the layer.[17] Taking into account the difference in the unit cell parameters between $RbTi_{1-x-y}Yb_xNb_yOPO_4$ and $RbTiOPO_4$ for different levels of substitution of Ti^{4+} by Yb^{3+} and Nb^{5+}, we calculate the lattice mismatch from the expression

$$f_{(hkl)} = 100(S_{(hkl)}\,(\text{layer}) - S_{(hkl)}\,(\text{substrate}))/S_{(hkl)}\,(\text{substrate}),$$

where $S_{(hkl)}$ (layer) and $S_{(hkl)}$ (substrate) are the areas obtained from the (*hkl*) periodicity vectors of the layer and the substrate, respectively. Table 5 gives the lattice mismatches on the (001) plane for the different substitutions studied. We can see that the substitution of Ti^{4+} by Yb^{3+} and Nb^{5+} increases the lattice mismatch. These lattice mismatches are relatively low compared to those we obtained for other materials.[18]

Table 6 Refractive indices of the samples corresponding to the experiments 4, 6, 8, 9 and 11, in Table 2

Exp. num.	Sample	Composition	n_x	n_y	n_z
4	Layer	$RbTi_{0.995}Yb_{0.005}OPO_4$	1.7864	1.7981	1.8863
	Substrate	$RbTiOPO_4$	1.7892	1.8010	1.8882
6	Layer	$RbTi_{0.975}Yb_{0.014}Nb_{0.011}OPO_4$	1.7886	1.8019	1.8935
	Substrate	$RbTiOPO_4$	1.7894	1.8013	1.8889
8	Layer	$RbTi_{0.971}Yb_{0.015}Nb_{0.014}OPO_4$	1.7872	1.8018	1.8956
	Substrate	$RbTiOPO_4$	1.7895	1.8015	1.8898
9	Layer	$RbTi_{0.958}Yb_{0.016}Nb_{0.026}OPO_4$	1.7863	1.8016	1.8967
	Substrate	$RbTiOPO_4$	1.7893	1.8015	1.8897
11	Layer	$RbTi_{0.983}Yb_{0.004}Nb_{0.013}OPO_4$	1.7885	1.8016	1.8944
	Substrate	$RbTiOPO_4$	1.7894	1.8013	1.8884

3.3. Waveguide characterization

The epitaxial composites were characterized following the steps outlined in the Experimental section. The thin films were polished to a thickness of around 50 μm in order to ensure that the modes were not lost and the refractive indices could be determined. From the refractive indices we calculated the proper thickness for supporting a few propagation modes. The refractive indices of several layers and substrates measured with the Metricon prism coupler equipment are shown in Table 6 (note that we use the same experiment numbers as in Tables 2–4). We can see that in the epitaxial layers that contain neither Nb^{5+} nor W^{6+} substitution produces a negative contrast of refractive indices between the layer and the substrate ($n_{layer} - n_{substrate}$). This means that the epitaxial layer cannot guide the light and we can conclude that Yb^{3+} substitution in RTP decreases the refractive indices. The results in Table 6 show that n_z is the index most affected by the presence of Nb^{5+}: it increases when Nb^{5+}

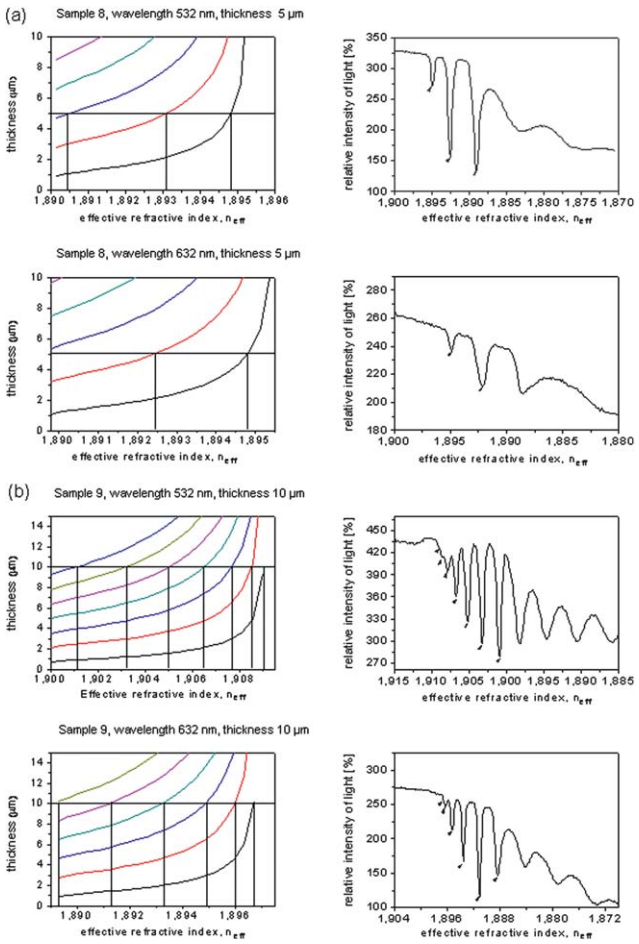

Fig. 6 Number of propagation modes *versus* the epitaxial thickness (left hand side) and dark-mode spectrum (right hand side). Calculations and experiments were done first at 532 nm and finally at 632.8 nm. (a) Sample 8, with 5 μm of thickness. (b) Sample 9, with 10 μm of thickness.

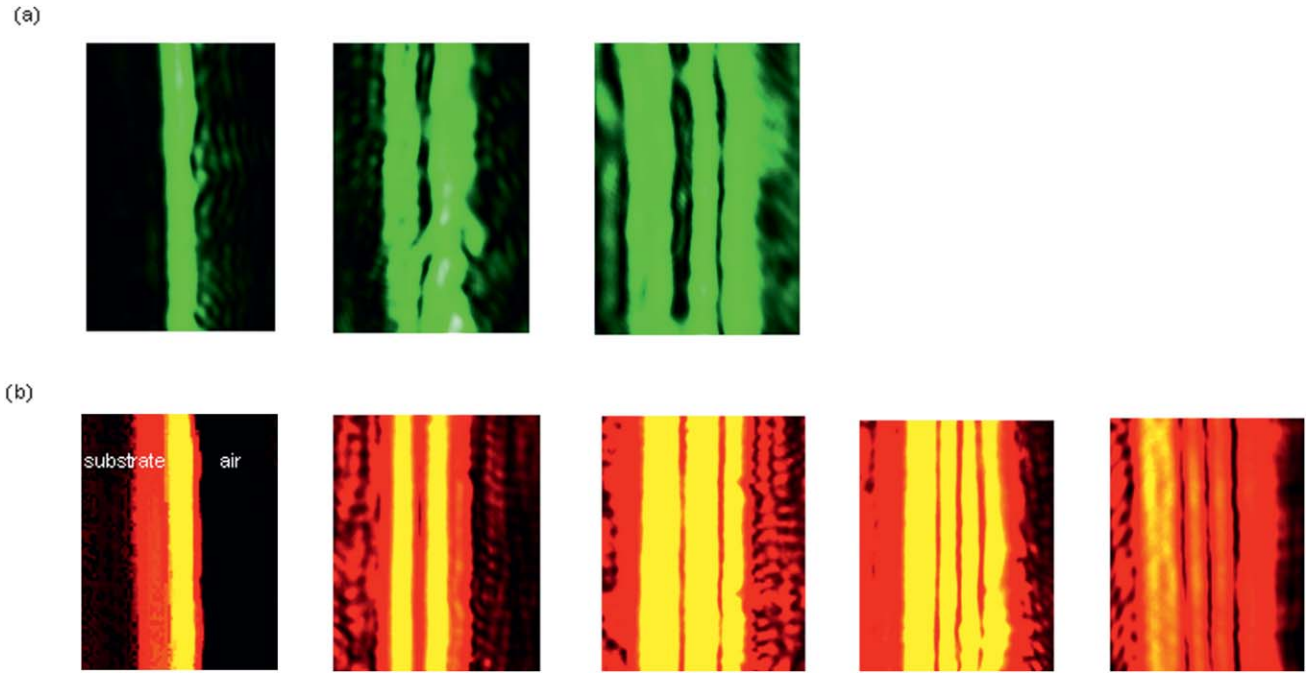

Fig. 7 CCD pictures of: (a) propagation modes of the order of $m = 0$, 1 and 2 in sample 8, with 5 μm of thickness at 532 nm. (b) Propagation modes of the order of $m = 0$, 1, 2, 3 and 4 in sample 9, with 10 μm of thickness at 632.8 nm.

increases. On the other hand, n_y increases very slowly as Nb^{5+} increases. Finally, n_x decreases in all cases when Nb^{5+} is incorporated into the crystal. These results show that the epitaxial layers are only able to guide the light in the TM polarization, which implies that the electric field vector is parallel to the *c* crystallographic direction. This is an important step for obtaining quasi-phase-matched periodically poled waveguides.

To demonstrate the light guiding in the epitaxial layers, we calculated the thickness needed to support a few propagation modes. Calculations were made using the expressions in the Experimental section and agreement between the theory and the experimental results using our waveguides was studied. To do so, we polished the epilayers obtained in experiments 8 and 9 until they reached a thickness of 10 and 5 μm, respectively. On the left hand side of Fig. 6(a) and (b) are the results of the thickness calculations against the effective refractive index. On the right hand side of this figure is the dark-mode spectrum done with the Metricon prism coupler equipment, in which the sharp grooves are due to the propagating modes of the light. In Fig. 6(a) for experiment 8, we can see 3 propagation modes at 532 nm and 2 propagation modes at 632.8 nm. This is logical because the confinement of the light is higher for low wavelengths. Fig. 6(b), on the other hand, which corresponds to the epilayer obtained in experiment 9, shows 7 propagation modes at 532 nm and 6 propagation modes at 632.8 nm. Note the high degree of agreement between the theoretical and the experimental results.

Fig. 7(a) shows the guided modes of order $m = 0$, 1 and 2 propagated along the epitaxial layer grown in experiment 8 and polished to a 10 μm thickness. These modes were obtained using 532 nm light. These results agree well with the theoretical calculations (left hand side of Fig. 6(a)) and the dark mode spectrum for the same sample (right hand side of Fig. 6(a)). Fig. 7(b) shows the guided modes of order $m = 0$, 1, 2, 3 and 4 propagated along the epilayer grown in experiment 9 and polished to a thickness of 5 μm. In this case the wavelength of the light was 632.8 nm. Excitation of the guided mode of order 5 had some difficulties caused by the limitation of the movement steps of the support of the sample. We therefore tried to excite this mode of propagation and began to excite the mode of order 4. The lesser difference in the refractive indices along the *c* crystallographic direction between the epilayer and the substrate than between the epilayer and the air causes a shift in the energy density profile in the epitaxy–substrate interface due to the lower confinement of light than on the epitaxy–air boundary. This phenomenon can be seen in the propagation mode of order 0 in Fig. 7(b). These results confirmed experimentally that the waveguides obtained in this study confine the light successfully and that there is good agreement between the theoretical calculations (left hand side of Fig. 6(b)), the dark mode spectrum (right hand side of Fig. 6(b)) and our experimental results.

4. Conclusions

We have reported the growth of $RbTi_{1-x-y}Yb_xNb_yOPO_4$/$RbTiOPO_4$ (001) epitaxial layers and the efficient guiding possibilities. We achieved a maximum concentration of Yb^{3+} in the epilayers of 1.43×10^{20} atoms per cm^3. The maximum distribution coefficient of Nb^{5+} was 0.658. This allows a contrast of refractive indices between the epitaxial layer and the substrate that is high enough for optical waveguiding in TM polarization and to maintain an optimum Yb^{3+} concentration. After calculating the thickness of the epilayer needed to guide a few propagation modes, we showed that 532 and 632.8 nm light can be efficiently guided along these epitaxial layers. Photographs of several propagation modes are shown. In conclusion, these novel Yb:Nb:RTP/RTP (001) epitaxial composites are promising

materials for integrated photonics and laser applications such as self-frequency doubling (SFD) waveguides and second-harmonic generation (SHG) waveguide lasers.

Acknowledgements

This work was supported by the Spanish Government under projects MAT2008-06729-C02-02/NAN, MAT2008-04046-E/MAT, TEC2010-21574-C02-02, PI09/90527, HF2008-0045, DE2009-0002 and by the Catalan Authority under project 2009SGR235. J. Cugat thanks the Spanish Government for the FPI fellowship BES-2009-024190. J. J. Carvajal is supported by the Spanish Ministry of Education and Science and the European Social Fund under the Ramon y Cajal programs RYC2006-858.

References

1 P. A. Thomas, S. C. Mayo and B. E. Watts, *Acta Crystallogr., Sect. B: Struct. Sci.*, 1992, **48**, 401.
2 C. Zumsteg, C. J. Bierlein and T. E. Gier, *J. Appl. Phys.*, 1976, **47**, 4980.
3 S. Suhara and M. Fujimura, *Waveguides and Nonlinear-Optic Devices*, Springer, Photonics, 2003.
4 G. I. Stegeman and C. T. Seaton, *J. Appl. Phys.*, 1985, **58**, R57.
5 X. Mateos, V. Petrov, A. Peña, J. J. Carvajal, M. Aguiló, F. Díaz, P. Segonds and B. Boulanger, *Opt. Lett.*, 2007, **32**, 1929.
6 (*a*) R. Solé, V. Nikolov, I. Koseva, P. Peshev, X. Ruiz, C. Zaldo, M. J. Martín, M. Aguiló and F. Díaz, *Chem. Mater.*, 1997, **9**, 2745; (*b*) C. Zaldo, M. Rico, F. Díaz and J. J. Carvajal, *Opt. Mater. (Amsterdam)*, 1999, **13**, 175.
7 J. J. Carvajal, R. Solé, Jna. Gavaldà, J. Massons, P. Segonds, B. Boulanger, A. Brenier, G. Boulon, J. Zaccaro, M. Aguiló and F. Díaz, *Opt. Mater. (Amsterdam)*, 2004, **26**, 313.
8 J. J. Carvajal, R. Solé, Jna. Gavaldà, J. Massons, M. Aguiló and F. Díaz, *Cryst. Growth Des.*, 2001, **1**(6), 479.
9 J. J. Carvajal, V. Nikolov, R. Solé, Jna. Gavaldà, J. Massons, M. Aguiló and F. Díaz, *Chem. Mater.*, 2002, **14**, 3136.
10 A. Peña, J. J. Carvajal, M. C. Pujol, X. Mateos, M. Aguiló, F. Díaz, V. Petrov, P. Segonds and B. Boulanger, *Opt. Express*, 2007, **15**, 14580.
11 J. Rodriguez-Carvajal, *Short Reference Guide of the Program FULLPROF*, Laboratoire Leon Brilloin, 1998.
12 R. A. Young, *The Rietveld Method*, Oxford Science Publication, International Union of Crystallography, 1995.
13 (*a*) P. K. Tien, R. Ulrich and R. J. Martin, *Appl. Phys. Lett.*, 1969, **14**, 291; (*b*) A. Boudrioua, P. Moretti, J. C. Loulergue and K. Polgar, *Opt. Mater. (Amsterdam)*, 2000, **14**, 31.
14 (*a*) C. Dubs, J. P. Ruske, E. Werner, A. Tünnermann, Ch. Schimidt and G. Bruchlos, *Opt. Mater. (Amsterdam)*, 2001, **17**, 477; (*b*) R. Solé, V. Nikolov, A. Vilalta, J. J. Carvajal, J. Massons, Jna. Gavaldà, M. Aguiló and F. Díaz, *J. Mater. Res.*, 2002, **17**(3), 563.
15 R. Solé, V. Nikolov, I. Koseva, P. Peshev, X. Ruiz, C. Zaldo, M. J. Martín, M. Aguiló and F. Díaz, *Chem. Mater.*, 1997, **9**, 2745.
16 R. D. Shannon, *Acta Crystallogr., Sect. A: Cryst. Phys., Diffr., Theor. Gen. Crystallogr.*, 1976, **32**, 751.
17 R. Solé, V. Nikolov, A. Vilalta, J. J. Carvajal, J. Massons, Jna. Gavaldà, M. Aguiló and F. Díaz, *J. Cryst. Growth*, 2002, **237**, 602.
18 A. Aznar, O. Silvestre, M. C. Pujol, R. Solé, M. Aguiló and F. Díaz, *Cryst. Growth Des.*, 2006, **6**, 1781.

Paper II

Waveguiding demonstration on Yb:Nb:$RbTiOPO_4$/$RbTiOPO_4$ (001) epitaxies grown by LPE

J. Cugat, R. Solé, M.C. Pujol, J.J. Carvajal, X. Mateos, F. Díaz, M. Aguiló,

Optical Materials, **32**, 1648 (2010).

Optical Materials 32 (2010) 1648–1651

Contents lists available at ScienceDirect

Optical Materials

journal homepage: www.elsevier.com/locate/optmat

Waveguiding demonstration on Yb:Nb:$RbTiOPO_4$/$RbTiOPO_4$(0 0 1) epitaxies grown by LPE

J. Cugat, R. Solé, M.C. Pujol, J.J. Carvajal, X. Mateos, F. Díaz, M. Aguiló *

Física i Cristal·lografia de Materials i Nanomaterials (FiCMA-FiCNA), Universitat Rovira i Virgili (URV), Campus Sescelades, C/Marcel·lí Domingo s/n, E-43007 Tarragona, Spain

ARTICLE INFO

Article history:
Received 23 December 2009
Accepted 16 April 2010
Available online 26 May 2010

Keywords:
Liquid phase epitaxy
Waveguide
$RbTiOPO_4$

ABSTRACT

The present paper shows epitaxial layers grown by liquid phase epitaxy of $RbTiOPO_4$ doped with Yb^{3+} on substrates of RTP. The layers were grown on (0 0 1) plane, which contains the phase matching direction for type-II second harmonic generation for the Yb^{3+} emission wavelength range. The layer guides polarized light parallel to *c* crystallographic direction. A 10 m-thickness epitaxial layer guides five modes which had been observed by dark-mode spectrum. The measured losses were about 0.7 dB/cm.

1. Introduction

$RbTiOPO_4$ (RTP) belongs to the $KTiOPO_4$ (KTP) family of nonlinear optical crystals which crystallize in the orthorhombic system, with the non-centrosymmetric space group $Pna2_1$. Both, KTP and RTP are of interest due to its excellent nonlinear and thermomechanical properties [1]. Due to its non-centrosymmetry, these materials can be used for frequency doubling of lasers emitting in the IR spectral range.

The doping of RTP and KTP with laser active ions, like lanthanides, is interesting for obtaining self-frequency doubling (SFD) materials, offering the possibility to obtain compact and efficient laser sources in the visible. Among all the lanthanide ions, Yb^{3+} is of great interest due to its emission at around a wavelength of 1 μm, having a very simple energy level scheme, consisting of only two energy levels: the ground state $^2F_{7/2}$ and the excited state $^2F_{5/2}$. The Yb^{3+} ion is characterized by: low quantum defect, broad absorption bandwidth, broad emission bandwidth, which allows a wide tunability and generation of ultrashort lasers pulses, high lifetime, and finally it is especially relevant for SFD, avoiding absorption losses at the second harmonic generation (SHG) [2].

The maximum doping levels of Yb^{3+} previously achieved in KTP bulk crystals were not enough for laser operation. The distribution coefficient of Yb^{3+} in RTP is slightly higher than in KTP but not enough for lasing [3].

Recently, it has been successfully demonstrated the laser action in RTP codoped with Nb^{5+} and Yb^{3+} and the effective non-linearity was presented too [4]. But the crystal growth of Yb:Nb:RTP bulk single crystal shows some difficulties. The self-flux solution has a high viscosity and the homogenization of the flux take a lot of time. The crystals obtained show low quality, especially because cracks appear due to the stress produced by the difference between the ionic radius of the active ion and Ti cation constituent of the crystal structure. In order to avoid the crystal growth difficulties in the present work we grew epitaxial layer of RTP doped with Yb^{3+} and Nb^{5+} (Yb:Nb:RTP) on RTP substrates by liquid phase epitaxy (LPE) method.

Moreover, the fabrication of planar waveguide structures based on this nonlinear material, could lead to new applications for this material in integrated optical devices; due to its improvement in conversion efficiency (high optical power densities over long interaction optical path length) for nonlinear applications and also enable to use low power continuous wave pump lasers.

In this paper we will describe the growth of Yb:Nb:RTP epitaxial layers on undoped isostructural substrates by LPE method. We characterized the epilayers; measuring their refractive indices and studying the propagation modes and losses. Finally, we evaluate the fluorescence of the active ion in this new epitaxial nonlinear optics composite.

2. Epitaxial layer growth

We grew epitaxial layers of $RbTi_{1-x-y}Yb_xNb_yOPO_4$ on (0 0 1) $RbTiOPO_4$ substrates. The non-active substrates were prepared by cutting plates perpendicular to the crystallographic directions from RTP single crystals. The *a*–*b* plane is interesting because contains the non-critical phase matching (PM) type-II SHG directions for ytterbium laser emission wavelength range (from 985 to

* Corresponding author. Tel.: +34 977559520; fax: +34 977559563.
E-mail address: magdalena.aguilo@urv.cat (M. Aguiló).

0925-3467/$ - see front matter © 2010 Elsevier B.V. All rights reserved.
doi:10.1016/j.optmat.2010.04.027

1118 nm). So, mainly the substrates were cut parallel to the (0 0 1) plane with the edges parallel to the *a* and *b* crystallographic direction.

The epitaxial layers were grown by the liquid phase epitaxy (LPE) method from self-flux solutions and fluxes containing 20 mol% of WO_3. As starting chemicals Rb_2CO_3 (99%), $NH_4H_2PO_4$ (99%), TiO_2 (99.9%), WO_3 (99.9%) were used. The procedure was similar to that already reported by our group in relation with LPE growth of several epitaxial layers [5–7].

The solution compositions were Rb_2O–P_2O_5–TiO_2–Yb_2O_3–Nb_2O_5 = 40.8–27.2–29.76–1.92–0.32 (% molar composition), in the case of self-flux solutions and Rb_2O–P_2O_5–TiO_2–Yb_2O_3–Nb_2O_5–WO_3 = 43.82–22.58–12.92–0.27–0.41–20 (% molar composition) for WO_3 containing solutions. Both compositions located inside the RTP crystallization region [8]. The supersaturation of the solution was produced by decreasing its temperature by 2 and 6 K below the saturation temperature, which is around 1195 and 1133 K, respectively. In all the LPE experiments, a rotation of 60 rpm was applied. The chemical composition of the epitaxies was determined by electron probe microanalysis (EPMA) and resulted $RbTi_{0.971}Yb_{0.015}Nb_{0.014}OPO_4$ and $RbTi_{0.977}Yb_{0.004}Nb_{0.013}W_{0.006}OPO_4$. The thickness of the as-grown epitaxial layers was around 100 μm, measured by optical microscope profilometer, taking into account substrate surface as a reference.

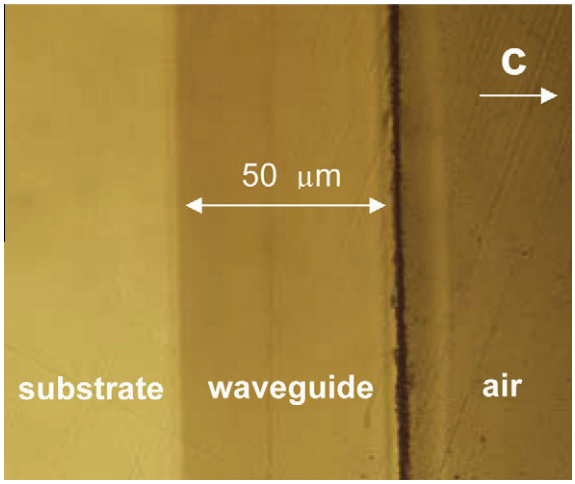

Fig. 1. Optical microscope photograph of lateral view of $RbTi_{0.971}Yb_{0.015}Nb_{0.014}OPO_4$/$RbTiOPO_4$(0 0 1) epitaxy.

3. Modal characterization

After growing the epitaxies, they were polished to obtain optical flatness for characterization. The thickness of the epilayers after polishing was 50 μm, as it can be seen in Fig. 1. RTP crystals are positive biaxial crystals, with $n_x < n_y < n_z$ ($n_a < n_b < n_c$), point symmetry *mm*2. The incorporation of the Nb^{5+} ions in RTP structure increases the refractive index of the layer as compared to the undoped RTP substrate generating waveguide effect. The refractive indices of epitaxy as well as the ones of the substrate were measured using the total internal reflection angle law coupling the light by a prism (Metricon prism coupler equipment). Table 1 shows the refractive indices measured for *x*, *y* and *z* optical directions of the epilayer in transverse electric (TE) and transverse magnetic (TM) polarization. The substrate/epilayer contrast of refractive indices with light polarized in *z* direction, $\Delta n_z \approx 0.005$, was large enough for guiding the light in TM polarization. In RTP, this polarization means that the electric field of the light is parallel to *c* crystallographic direction. As can be observed in Table 1, the samples containing W^{6+} show a smaller increase of the effective refractive index.

The visualization of the propagating modes requires the calculation of the convenient thickness to reduce their number. Using the refractive indices measured before and the equation of dispersion for a wave propagating along the guide [9,10]:

$$\frac{2\pi d}{\lambda}\left(n^2 - n_{eff}^2\right)^{\frac{1}{2}} = m\pi + \phi_{n_a} + \phi_{n_s}$$

where *m* is the mode number, *d* the thickness of the epilayer, λ the wavelength of the light in vacuum and n_a and n_s are the air and the substrate refractive indices, respectively, while *n* is the refractive index of the guiding layer, in our case $n = n_z$, and n_{eff} is the effective refractive index of the propagation mode in the epilayer and

$$\phi_{n_j} = arctg\left[\left(\frac{n}{n_j}\right)^{2\rho}\left(\frac{n_{eff}^2 - n_j^2}{n^2 - n_{eff}^2}\right)\right]^{\frac{1}{2}}$$

where $j = a, s$, and

$$\rho = \begin{cases} 1 & \text{for TM} \\ 0 & \text{for TE} \end{cases}$$

Fig. 2 shows the calculated number of modes by the above expressions, the five propagating modes related with a 10 μm-thickness and their corresponding effective refractive indices.

To check these calculations, the sample was polished until 10 μm-thickness and a prism coupler system was used for recording the dark-mode spectrum at 632.8 nm, using He–Ne laser beam

Table 1
Effective refractive indices calculated from the dark-mode spectrum.

Layer composition	Direction	Polarization	Substrate refractive indices	Layer refractive index	Contrast refractive indices Δn	Mode order	Effective refractive indices
$RbTi_{0.971}Yb_{0.015}Nb_{0.014}OPO_4$	n_x	TE	1.7895	1.7872	0.0023	–	–
	n_y	TE	1.8015	1.8018	0.0004	–	–
	n_z	TM	1.8898	1.8956	0.0058	0	1.8952
						1	1.8946
						2	1.8937
						3	1.8922
						4	1.8900
$RbTi_{0.977}Yb_{0.004}Nb_{0.013}W_{0.006}OPO_4$	n_x	TE	1.7894	1.7885	0.0009	–	–
	n_y	TE	1.8013	1.8016	0.0003	–	–
	n_z	TM	1.8884	1.8943	0.0059	0	1.8938
						1	1.8932
						2	1.8921
						3	1.8907
						4	1.8885

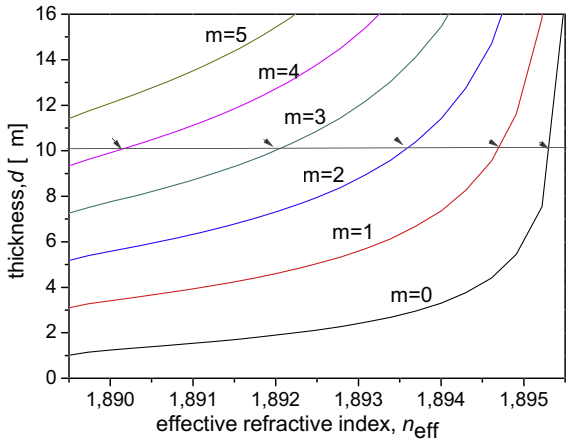

Fig. 2. Epitaxial thickness, d, versus the effective refractive index, n_{eff}, for $n_s = 1.8898$, $n_z = 1.8956$ at 632.8 nm wavelength, for $RbTi_{0.971}Yb_{0.015}Nb_{0.014}OPO_4$/$RbTiOPO_4$(0 0 1) epitaxy.

as light source with TM polarization. In Fig. 3, we can observe five sharp dips; each dip corresponds to a real propagation mode, in good agreement with the previous calculations. Their sharpness indicates a good confinement of the optical wave. Table 1 resumes the order of the modes in TM polarization with their corresponding effective refractive indices. They are larger than the refractive index of the substrates.

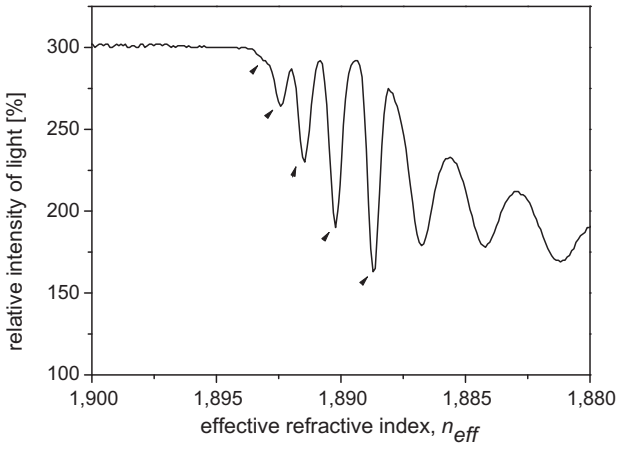

Fig. 3. TM-dark-mode spectrum for a 10 μm-thickness $RbTi_{0.971}Yb_{0.015}Nb_{0.014}OPO_4$/$RbTiOPO_4$(0 0 1) epitaxy at 632.8 nm wavelength.

The refractive index contrast assures guiding, so a crack-free epitaxial layer was tested as a planar waveguide. The sample was polished in both end-faces, and also, the surface epitaxial layer. To visualize the TM modes of the $RbTi_{0.971}Yb_{0.015}Nb_{0.014}OPO_4$/RTP(0 0 1) waveguide we recorded the near field pattern by a CCD camera, using a He–Ne laser beam, coupled into, and out from the waveguide using two microscope objectives. The propagation direction along the waveguide was parallel to the b crystallographic direction. As an example, Fig. 4, shows the results obtained by exciting different modes.

The propagation loss is of importance for evaluating the quality of the waveguides; these losses are related to different factors such as: surface and interface roughness, internal scattering. To measure approximately the propagation losses we coupled a He–Ne laser beam into the waveguide exciting the TM_0 mode and recorded the intensity of the scattered light with a CCD camera. The measured light intensity measured is related with the propagation distance following the next equation [11]:

$$10\log I(x) = 10\log I_0 - \alpha x$$

where I_0 is the initial power, $I(x)$ is the transmitted power through the waveguide at the distance x, and α represents the attenuation of a guiding mode. The waveguide losses are evaluated assuming than the scattered light intensity is proportional to the total light intensity inside the waveguide. The loss is measured to be about 0.7 ± 0.3 dB/cm, this is a low value, demonstrating that we have a good quality waveguide.

4. Ytterbium fluorescence in waveguide

Ytterbium spectroscopy in Nb:RTP host has been already studied deeply in Refs. [12–14]. In this host Yb^{3+} can be located in two different sites, with point symmetry C_1, substituting the Ti[1], and Ti[2] cations. It has been reported that Nb^{5+} cation is expected to substitute the Ti[1], forcing the Yb^{3+} to occupy the Ti[2] site. On the other hand in Yb:RTP it has been observed that the Yb^{3+} can occupy both Ti sites. So the Nb/Ti ratio in the chemical composition of the host will govern the localization of active Yb^{3+} ion in this material [14].

Ti–sapphire laser can be used for selectively exciting of Yb^{3+}, in the wavelength range from 875 to 960 nm [15]. Fig. 5 shows the unpolarized spectra in the range from 930 to 1100 nm from an Yb:Nb:RTP epitaxial layer grown in WO_3 containing solutions ($RbTi_{0.977}Yb_{0.004}Nb_{0.013}W_{0.006}OPO_4$) and from an Yb:Nb:RTP bulk crystal ($RbTi_{0.956}Yb_{0.011}Nb_{0.031}W_{0.002}OPO_4$). These emission spectra were obtained by pumping at 902 nm, at room temperature. As can be seen in the figure the epitaxial layer luminescence practically maintains the shape and position of the emission peaks found in the bulk crystal. The presence of the Nb^{5+} in the epitaxial layer

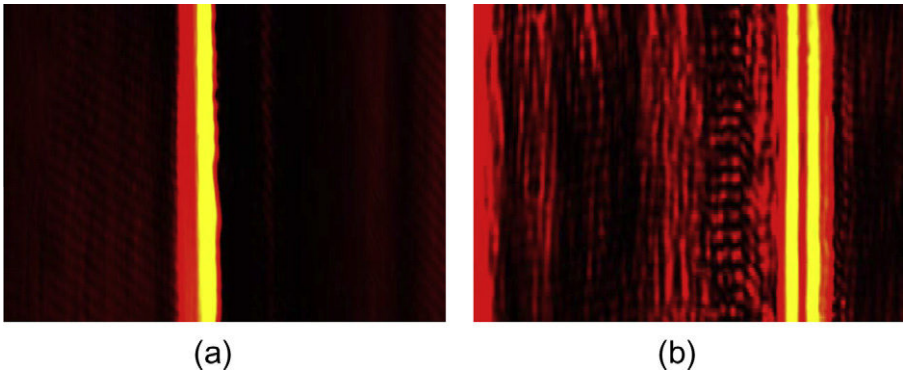

Fig. 4. Near field pattern of 10 μm-thickness $RbTi_{0.971}Yb_{0.015}Nb_{0.014}OPO_4$/$RbTiOPO_4$(0 0 1) waveguide, (a) $m = 0$ mode, (b) $m = 1$ mode.

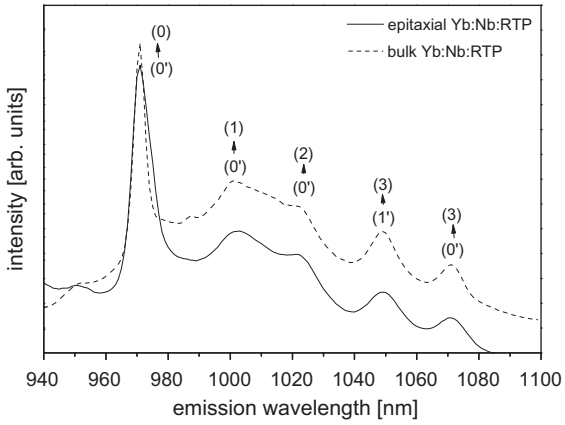

Fig. 5. Photoluminescence emission of Yb^{3+} in $RbTi_{0.977}Yb_{0.004}Nb_{0.013}W_{0.006}OPO_4$/$RbTiOPO_4$(0 0 1) epitaxy, at room temperature.

and the similarity in the peaks positions points out to state that Yb^{3+} has to be mostly located in the Ti[2] site. Other small discrepancies observed in the luminescence spectra of the epitaxial layer and the bulk crystal such as different ratio of the peak intensities and some broadening can be related to the existent stress in the epitaxial layer due to non-null lattice mismatch. The luminescence of the Yb:Nb:RTP waveguide shows that the waveguide practically keeps the luminescence properties found in the bulk crystal, demonstrating that this kind of waveguides could be used for active integrated waveguide devices.

5. Conclusions

We reported the efficient guiding possibilities of the Yb:Nb:RTP layers grown on non-active RTP(0 0 1) substrates by liquid phase epitaxy method. The refractive index and modal characterization reveals a relative high index contrast allowing the existence of five excited modes in TM polarization in 10 μm thickness layer. Low losses, 0.7 ± 0.3 dB/cm, were evaluated in the TM_{00} (polarization parallel to *c* crystallographic direction and propagation along *b* direction) guided mode by a CCD camera. Their fluorescence spectra showed no major differences with the bulk, showing that Yb^{3+} environment is nearly identical in the epitaxial layer and bulk material. These novel Yb:Nb:RTP/RTP(0 0 1) epitaxial composites appear as very promising materials for various components of laser applications such as self-frequency doubling waveguide lasers or second harmonic generation waveguide laser.

Acknowledgments

This work was supported by the Spanish Government under Projects MAT2008-06729-C02-02/NAN and PI09/90527 and the Catalan Authority under Project 2009SGR235. The authors are grateful to the Serveis Cientifico-Tècnics of the University of Barcelona for EPMA measurements. J. Cugat thanks the Spanish Government for the funds provided through the fellowship FPI. J.J. Carvajal and M.C. Pujol are supported by the Education and Science Ministry of Spain and European Social Fund under the Ramon y Cajal program, RYC2006-858 and RYC2004-1453, respectively.

References

[1] C. Zumsteg, J.D. Bierlein, T.E. Gier, J. Appl. Phys. 47 (1976) 4980.
[2] X. Mateos, V. Petrov, A. Peña, J.J. Carvajal, M. Aguiló, F. Díaz, P. Segonds, B. Boulanger, Opt. Lett. 32 (2007) 1929.
[3] R. Solé, V. Nikolov, I. Koseva, P. Peshev, X. Ruiz, C. Zaldo, M.J. Martín, M. Aguiló, F. Díaz, Chem. Mater. 9 (1997) 2745.
[4] J.J. Carvajal, R. Solé, Jna. Gavaldà, J. Massons, P. Segonds, B. Boulanger, A. Brenier, G. Boulon, J. Zaccaro, M. Aguiló, F. Díaz, Opt. Mater. 26 (2004) 313.
[5] R. Solé, V. Nikolov, A. Vilalta, J.J. Carvajal, J. Massons, Jna. Gavaldà, M. Aguiló, F. Díaz, J. Cryst. Growth 237 (2002) 602.
[6] A. Aznar, O. Silvestre, M.C. Pujol, R. Solé, M. Aguiló, F. Díaz, Cryst. Growth Des. 6 (2008) 1781.
[7] W. Bolaños, J.J. Carvajal, M.C. Pujol, X. Mateos, G. Lifante, M. Aguiló, F. Díaz, Cryst. Growth Des. 9 (2009) 3525.
[8] J.J. Carvajal, V. Nikolov, R. Solé, Jna. Gavaldà, J. Massons, M. Aguiló, F. Díaz, Chem. Mater. 14 (2002) 3136.
[9] P.K. Tien, R. Ulrich, J. Opt. Soc. Am. 60 (1970) 1325.
[10] A. Boudrioua, P. Moretti, J.C. Loulergue, K. Polgar, Opt. Mater. 14 (2000) 31.
[11] C. Jia, X. Wang, K. Wang, Y. Jiang, L. Wang, Appl. Phys. B 91 (2009) 139.
[12] A. Peña, J.J. Carvajal, M.C. Pujol, X. Mateos, M. Aguiló, F. Díaz, V. Petrov, P. Segonds, B. Boulanger, Opt. Express 15 (2007) 14581.
[13] J.J. Carvajal, V. Nikolov, R. Solé, Jna. Gavaldà, J. Massons, M. Aguiló, F. Díaz, Chem. Mater. 14 (2002) 3136.
[14] J.J. Carvajal, G. Ciatto, A. Peña, M.C. Pujol, Jna. Gavaldà, F. Díaz, M. Aguiló, Appl. Phys. Lett. 94 (2009) 061908.
[15] R. Brinkman, W. Sohler, H. Suche, Electron. Lett. 27 (1991) 415.

Paper III

Green light waveguide demonstration on Yb:Nb:$RbTiOPO_4$/$RbTiOPO_4$ epitaxial layers

J. Cugat, R.M. Solé, J.J. Carvajal, M. C. Pujol, X. Mateos, M. Aguiló, F. Díaz,

Physics Procedia, **8**, 136 (2010).

Available online at www.sciencedirect.com
ScienceDirect
Physics Procedia 8 (2010) 136–141
Physics Procedia
www.elsevier.com/locate/procedia

VI Encuentro Franco-Español de Química y Física del Estado Sólido
VI^{ème} Rencontre Franco-Espagnole sur la Chimie et la Physique de l'État Solide

Green light waveguide demonstration on Yb:Nb:RbTiOPO$_4$/RbTiOPO$_4$ epitaxial layers

Jaume Cugat, Rosa Maria Solé, Joan J. Carvajal, Maria Cinta Pujol, Xavier Mateos, Magdalena Aguiló* and Francesc Díaz

Física i Cristal·lografia de Materials i Nanomaterials (FiCMA-FiCNA), Universitat Rovira i Virgili (URV), Campus Sescelades, c/Marcel·lí Domingo s/n, 43007 Tarragona, Spain

Abstract
In this paper epitaxial layers of RbTiOPO$_4$ doped with Yb^{3+} on substrates of RbTiOPO$_4$ have been grown by Liquid Phase epitaxy on the (001) plane, which contains the phase matching direction for Type II Second Harmonic Generation for the Yb^{3+} emission wavelength range. These layers can guide polarized light parallel to the ***c*** crystallographic direction. A 5 μm-thickness epitaxial layer can guide 3 propagation modes as it has been observed by the dark-mode spectrum. The sample was polished in both end-faces to visualize the TM modes of the waveguides. The near field pattern was recorded by a CCD camera, using a green diode laser at a wavelength of 532 nm, coupled into, and out from the waveguide using two microscope objectives. The demonstration of good guiding at a wavelength of 532 nm in Yb:Nb:RbTiOPO$_4$ waveguides is one of the important steps to obtain Self Frequency Doubling laser waveguides.

Kewywords: single crystal growth; epitaxial growth, dielectric waveguides, optical waveguides, planar waveguide lasers.

1. Introduction

The efficiency of nonlinear-optical interactions in planar dielectric waveguides can be enhanced by a combination of long interaction length and tight beam confinement usually not produced in bulk crystals [1, 2]. There has been a recent increase in compact short-wavelength light sources with the objective to obtain output powers in the mW range based on diode lasers for applications in integrated optics [3, 4].

The crystals of the KTiOPO$_4$ (KTP) family have large nonlinear-optical susceptibilities and are sufficiently birefringent to phase match a variety of interactions in the visible and near infrared spectral ranges [5]. RbTiOPO$_4$ (RTP) belongs to this family of nonlinear-optical crystals and at room temperature, the crystal symmetry of RTP is orthorhombic, and also belongs to the non-centrosymmetric space group *Pna*2$_1$. RTP crystals are positive biaxial

* Corresponding author. Tel.: +34- 977-559-520; Fax: +34-977-559-563
Email address: magdalena.aguilo@urv.cat

1875-3892 © 2010 Published by Elsevier Ltd.
doi:10.1016/j.phpro.2010.10.024

crystals, with $n_x < n_y < n_z$, ($n_a < n_b < n_c$) and point symmetry mm2. Due to their non-centrosymmetry and nonlinearity, they can be used for frequency doubling of lasers that emit in the IR spectral range [6].

The doping of the RTP epitaxial layers with laser active ions is interesting for obtaining self-frequency doubling (SFD) materials, offering the possibility to obtain compact and efficient laser sources in the visible. The Yb^{3+} lanthanide ion is of great interest due to its emission at around 1 μm, having a very simple energy level scheme, consisting of only two energy levels: the ground state $^2F_{7/2}$ and the excited state $^2F_{5/2}$. The Yb^{3+} ion has also some interesting properties like its low quantum defect, broad absorption bandwidth, broad emission bandwidth and high lifetime.

RTP can incorporate a higher Yb^{3+} concentration than KTP but it is still too low for laser operation. It has recently been shown that the concentration of Yb^{3+} in RTP can be increased by codoping with Nb^{5+} [7]. Lasing of RTP co-doped with Nb^{5+} and Yb^{3+} has been demonstrated [8]. The growth of Yb:Nb:RTP single crystals presents some difficulties mainly associated with the low growth rate, the crystal morphology (plate shape) and the tendency for cracks to appear [9].

To increase the optical paths as well as taking into account the advantages of guiding light, we grew epitaxial composites of Yb:Nb:RTP / RTP (001) by the Liquid Phase Epitaxy (LPE) method. The epitaxial layers were grown on the (001) crystallographic plane because this plane contains the phase matching direction and when the light is propagating through this direction in the appropriate wavelength the Second Harmonic Generation can occur.

In this paper we describe the main characteristics of the epitaxial layer growth, as well as the ion concentration measured by Electron Probe Microanalysis (EPMA) and the calculations of the lattice mismatches form the cell parameters refined by X-ray diffraction. In this work we describe the waveguide characterization: refraction indices measurements, dark-mode spectrum and calculations of the theoretical thickness required by the sample for obtaining a determined number of propagation modes. With the aim to obtain epitaxial layers useful for Self Frequency Doubling (SFD) of the fundamental radiation of Yb^{3+} at 1060 nm, as well as useful for Integrated Photonics (IP) in the visible range, we need to study the guiding properties of these epitaxial layers at about 530 nm, since this wavelength is half of 1060 nm, so we will show the main results in this direction.

2. Experimental

$RbTi_{1-x-y}Yb_xNb_yOPO_4$ epitaxial layers were grown on (001) RTP substrates. Single crystals were grown for substrates using the Top Seeded Solution Growth (TSSG) method. The solution used to obtain single crystals contained WO_3 because it helps to low the viscosity of the growth solution. Rb_2CO_3 (99%), $NH_4H_2PO_4$ (99%), TiO_2 (99.9%) and WO_3 (99.9%) were used as starting chemicals. The composition used was Rb_2O-P_2O_5-TiO_2-WO_3 = 44.24-18.96-16.8-20 (mol %), which has already been shown by our group [10] to be optimum.

The substrates were prepared by cutting single crystals in slices perpendicular to the ***c*** crystallographic direction before they were used. This plane is important because it contains the non-critical phase matching (PM) type-II SHG direction.

The epitaxial layers were grown by the LPE method in a special tubular furnace [11, 12, 13], build with better isolation and longer tubular core than the furnaces used for single-crystal growth. In this way we obtained a wide zone of uniform temperature so that the temperature gradient in solution was practically zero. The LPE experiments were carried out from self-flux solutions and fluxes containing 20 mol % of WO_3. The solution compositions were Rb_2O-P_2O_5-TiO_2-Yb_2O_3-Nb_2O_5 = 40.8-27.2-29.76-1.92-0.32 (mol %), in the case of self-flux solutions and Rb_2O-P_2O_5-TiO_2-Yb_2O_3-Nb_2O_5-WO_3 = 43.82-22.58-12.92-0.27-0.41-20 (mol %) for WO_3 containing solutions. Both compositions were chosen from the RTP crystallization region determined previously [10]. The supersaturation of the solution was produced by decreasing its temperature by 2 and 6 K below the saturation temperature of the solution. In both cases, a substrate rotation of 60 rpm was applied.

With the aim to investigate the lattice parameters and calculate the lattice mismatch [12], some small $RbTi_{1-x-y}Yb_xNb_yOPO$ single crystals were obtained on a platinum disk, 1.5 cm in diameter, rotating at 60 rpm by slow cooling of the solutions with the same composition than those used for LPE experiments. When nucleation was observed on the platinum disk, a cooling program of 0.5 – 1 K/h for 10-25 K was applied to grow the crystals.

The chemical composition of the samples was determined by EPMA with a CAMECA SX 50 equipment. The measurements were performed at 15 nA of beam current and 20 kV of acceleration voltage. The X-ray pattern of the sample was compared with that of standard samples, which contains known concentrations of the elements to be analyzed. RTP was used as a standard for the determination of Rb, Ti and P. Nb metal was used for determining the Nb concentration and YbF_3 for Yb measurements. In the measurements an integration time of 10 s for oxygen, rubidium, titanium and phosphorus, and for 30 s for measuring ytterbium was applied.

The lattice parameters of the epitaxial layers and crystals used for substrates were determined by X- ray powder diffraction using a Bruker- AXS D8-Discover diffractometer. Cu K_α radiation was used for these measurements. The data were collected in the 2θ range from 5 to 70º, with a step scan of 0.02º and a scan time of 16 s.

The refractive indices of the crystals and the epitaxial layers were measured at a wavelength of 532 nm by the prism-film coupling technique using a METRICON 2010 system. The TE light polarization allowed the n_x and n_y refractive indices measurements while the TM light polarization was used to determine the n_z refractive index. We also used the prism-film coupling system to observe the TM guided modes, supported by our waveguides and recording the dark-mode spectrum.

3. Results and discussion

To grow bulk single crystals for substrates the crucible was placed into the furnace in a region where the axial temperature gradient in the solution was 1.3 $K{\cdot}cm^{-1}$ at the first centimeter and 0.8 $K{\cdot}cm^{-1}$ at the next 1.5 cm, being the bottom hotter than the surface of the solution. The RTP bulk single crystals obtained were generally colorless, transparent and free of inclusions and cracks. Their maximum dimensions were 9.2, 26.0 and 21.9 mm along the ***a, b*** and ***c*** crystallographic directions, respectively. The crystals were then cut in plates of dimensions 4.2-10.3, 12-19.3 and 1.5 mm along the ***a, b*** and ***c*** crystallographic directions, respectively, to be used for substrates. All the substrates were cut perpendicular to the ***c*** crystallographic direction to obtain the ***a-b*** plane which is interesting for obtaining birrefringent phase matching. The plates were polished to optical quality in order to avoid defects into the epitaxial growth which could generate scattering centers.

Generally, the epitaxial layers were grown with high crystalline quality and they were as large as 16 mm. The chemical composition of these epitaxies, determined by EPMA, is $RbTi_{0.971}Yb_{0.015}Nb_{0.014}OPO_4$ and $RbTi_{0.977}Yb_{0.004}Nb_{0.013}W_{0.006}OPO_4$. The Yb^{3+} concentration of the first sample is around 10^{20} $atoms{\cdot}cm^3$ which may be enough for laser demonstration [8]. The second one is around 10^{19} $atoms{\cdot}cm^3$, this concentration of active ions may not be enough for efficient lasing, though this would need to be checked.

The small single crystals of $RbTi_{0.971}Yb_{0.015}Nb_{0.014}OPO_4$ and $RbTiOPO_4$ were used to determine the unit cell parameters from the X-ray powder diffraction data. The results are shown in table 1. We can see that the presence of Yb^{3+} and Nb^{5+} in the crystal structure leads to an increase in the lattice parameters. An explanation for the expansion of the unit cell is that Yb^{3+} and Nb^{5+} have larger ionic radii than Ti^{4+} [14]. The lattice mismatch between the layer and the substrate is important for the quality of the layer/substrate interface. High mismatches produce stress at the interface and favors the formation of defects. Taking into account the difference in the unit cell parameters between $RbTi_{0.971}Yb_{0.015}Nb_{0.014}OPO_4$ and $RbTiOPO_4$, we calculate the lattice mismatch from the expression

$$f_{(hkl)} = 100 \times (S_{hkl}(layer) - S(substrate)) / S_{hkl}(substrate)$$

where S_{hkl} (layer) and S_{hkl} (substrate) are the areas obtained from the (hkl) periodicity vectors of the layer and the substrate, respectively. According this formula the lattice mismatch is 0.473 which is relatively low compared to those we obtained for other materials [12].

Table 1. Unit cell parameters

Stoichiometric Formula	**a (Å)**	**b (Å)**	**c (Å)**
$RbTiOPO_4$	12.9650(5)	6.5007(3)	10.5576(4)
$RbTi_{0.971}Yb_{0.015}Nb_{0.011}OPO_4$	12.9933(2)	6.5150(6)	10.5852(8)

The refractive indices of the epitaxy as well as those of the substrate were measured using the total internal reflection law coupling the light with a prism (Metricon prism coupler equipment) for a wavelength of 532 nm. Table 2 shows the refractive indices measured for x, y and z optical directions of the epilayer in transverse electric (TE) and transverse magnetic (TM) polarization. The substrate/epilayer contrast of refractive indices with light polarization in z direction was $\Delta n_z \sim 0.006$ for both samples. This contrast was large enough for guiding the light in TM polarization.

Table 2. Refractive indices of the epitaxial layers and the substrates

Sample	**Stoichiometric Formula**	$\mathbf{n_x}$	$\mathbf{n_y}$	$\mathbf{n_z}$
Layer	$RbTi_{0.971}Yb_{0.015}Nb_{0.011}OPO_4$	1.7872	1.8018	1.8956
Substrate	$RbTiOPO_4$	1.7895	1.8015	1.8898
Layer	$RbTi_{0.977}Yb_{0.004}Nb_{0.013}W_{0.006}OPO_4$	1.7885	1.8016	1.8944
Substrate	$RbTiOPO_4$	1.7894	1.8013	1.8884

We calculated theoretically the thickness required to the sample to obtain 3 propagation modes, with TM polarization, and oscillating along the ***c*** crystallographic direction. The epitaxial thickness, *d,* versus the effective index, n_{eff}, calculations are shown in Figure 1 (left). As can be seen in the figure, an epitaxial layer with 5 µm of thickness can support 3 propagation modes. So, the sample was polished to a thickness 5 µm, and then the TM dark-mode spectrum was realized recorded. The TM dark-mode spectrum is shown in Figure 1 (right), where we can see the propagation modes of order 0, 1 and 2.

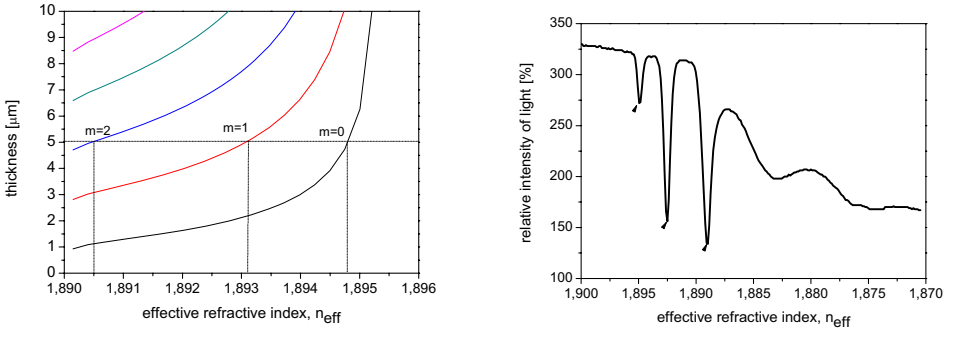

Figure 1. (Left) Epitaxial thickness versus the effective refractive index, n_{eff}, for $n_s = 1.889$ and and $n_z = 1.895$ at a wavelength of 532 nm, where n_s, n_z and n_{eff} are substrate, epitaxial layer and effective refractive indices along the ***c*** crystallographic direction, respectively. (Right) TM dark-mode spectrum of a 5 µm thickness Yb:Nb:RTP epitaxial film using the Metricon prism coupling system.

The sample was polished in both end-faces to visualize the TM modes of the $RbTi_{0.971}Yb_{0.015}Nb_{0.014}OPO_4$ / RTP (001) waveguides. We recorded the near field pattern by a CCD camera, using a green diode laser at a wavelength of 532 nm, coupled into, and out from the waveguide using two microscope objectives. The propagation direction along the waveguide was parallel to the ***b*** crystallographic direction.

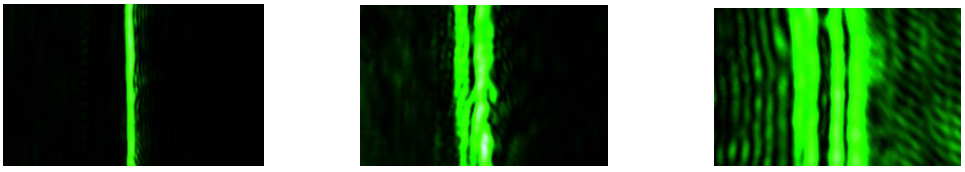

TM_{00} TM_{01} TM_{02}

Figure 2. Propagation modes order 0, 1 and 2 obtained with coupling light of 532 nm at the input and output ends of the waveguide with microscope objectives (40x and 60x, respectively).

Since the contrast of refractive indices in the epitaxial layer grown from WO_3 containing solutions was practically the same than in samples grown from self-flux solutions, both samples shows 3 propagation modes in 5 μm of epitaxial layer at 532 nm as it was expected.

4. Conclusions

We have successfully grown active epitaxial layers of RTP doped with Nb^{5+} and Yb^{3+} with high refractive index contrast on RTP substrates. The chemical composition of the epitaxial composites was $RbTi_{0.971}Yb_{0.015}Nb_{0.014}OPO_4$ and $RbTi_{0.977}Yb_{0.004}Nb_{0.013}W_{0.006}OPO_4$ for self-flux and WO_3 flux, respectively. The dark-mode spectrum at a wavelength of 532 nm was obtained successfully showing 3 propagation modes. The propagation modes were also observed by end-face coupling the laser at 532 nm. We believe that $RbTi_{0.971}Yb_{0.015}Nb_{0.014}OPO_4$/RTP epitaxial layer has active ion concentration high enough to allow efficient waveguide laser generation.

Acknowledgments

This work was supported by the Spanish Government under projects MAT2008-06729-C02-02/NAN, MAT2008-04046-E/MAT, TEC2010-21574-C02-02, PI09/90527, HF2008-0045, DE2009-0002 and the Catalan Authority under project 2009SGR235. J. Cugat thanks the Spanish Government for the FPI fellowship BES-2009-024190. J. J. Carvajal is supported by the Education and Science Ministry of Spain and European Social Fund under the Ramon y Cajal programs RYC2006 – 85

5. References

[1] P. K. Tien, *Light waves in thin films and integrated optics* Applied Optics 10, 2395 (1971).
[2] M. M. Fejer, M. J. F. Digonnet, R. L. Byer, *Generation of 22 mW of 523-nm radiation by frequency doubling in Ti:MgO:LiNbO$_3$ waveguides* Opticls Letters 11(4), 230 (1986).
[3] F. Laurell, J. B. Brown, J. D. Bierlein, *Sum-frequency seneration in segmented KTP waveguides* Applied Physics Letters 60 (9), 1064 (1992)
[4] G. I. Stegeman, C. T. Seaton , *Nonlinear integrated optics* Journal of Applied Physcs 58 (12), R57 (1985)
[5] J. D. Bierlein, H. Vanherzeele, *Potassium titanyl phosphate: properties and new applications* Journal of the Optical Society of America 6(4), 622 (1989).
[6] F. C. Zumsteg, J. D. Bierlein, T. E. Gier , *$K_xRb_{1-x}TiOPO_4$: A new nonlinear optical material* Journal of Applied Physics 47, 4980 (1976).

[7] J.J. Carvajal, R. Solé, Jna. Gavaldà, J. Massons, P. Seconds, B. Boulanger, A. Brenier, G. Boulon, J. Zaccaro, M. Aguiló, F. Díaz, *Spectroscopic and second harmonic generation properties of a new crystal: Yb-doped $RbTiOPO_4$* Optical Materials 26, 313 (2004).

[8] X. Mateos, V. Petrov, A. Peña, J. J. Carvajal, M. Aguiló, F. Díaz, P. Segonds, B. Boulanger, *Laser operation of Yb^{3+} in the acentric $RbTiOPO_4$ codoped with Nb^{5+}* Optics Letters 32 (13), 1929 (2007).

[9] J.J. Carvajal, R. Solé, Jna. Gavaldà, J. Massons, F. Díaz, M. Aguiló *A new Self-doubling Material: $RbTiOPO_4$(Nb,Ln)* Optical Materials, 24, 425 (2003).

[10] J.J. Carvajal, V. Nikolov, R Solé, Jna. Gavaldà, J. Massons, M. Rico, C. Zaldo, M. Aguiló, F. Díaz, *Enhancement of the erbium concentration in $RbTiOPO_4$ by codoping with niobium* Chemistry Materials, 12 (10), 3171 (2000)

[11] R. Solé, V Nikolov, A. Vilalta, J.J. Carvajal, J. Massons, Jna. Gavaldà, M. Aguiló, F. Díaz, *Liquid phase epitaxy of $KTiOPO_4$ on $KTi_{1-x}Ge_xOPO_4$* Journal of Crystal Growth. 237, 602 (2002).

[12] A. Aznar, O. Silvestre, M.C. Pujol, R. Solé, M. Aguiló, F. Díaz, Crytsal Growth & Design, *Liquid-phase epitaxy crystal growth of monoclinic $KLu_{1-x}Yb_x(WO_4)_2/KLu(WO_4)_2$*, 6, 1781 (2006).

[13] W. Bolaños, J.J. Carvajal, M.C. Pujol, X. Mateos, G. Lifante, M. Aguiló, F. Díaz, Crystal Growth & Desing *Epitaxial growth of lattice matched $KY_{1-x-y}Gd_xLu_y(WO_4)_2$ thin films on $KY(WO_4)_2$ substrates for waveguiding appliction*, 9, 3525 (2009).

[14] R. D. Shannon, *Revised effective ionic radii and systematic studies of interatomic distances in halides and chalcogenides*, Acta Crystallographica A32, 751 (1976).

Paper IV

Efficient Type II phase-matching second-harmonic generation in

Ba:Yb:Nb:$RbTiOPO_4$/$RbTiOPO_4$ waveguides

J. Cugat, R. Solé, J.J. Carvajal, X. Mateos, M.C. Pujol, J. Massons, F. Díaz, M. Aguiló,

Optics Letters, **36**(10), 1881 (2011).

Efficient Type II phase-matching second-harmonic generation in $Ba:Yb:Nb:RbTiOPO_4/RbTiOPO_4$ waveguides

J. Cugat, R. Solé,* J. J. Carvajal, X. Mateos, M. C. Pujol, J. Massons, F. Díaz, and M. Aguiló

Física i Cristal·lografia de Materials i Nanomaterials (FiCMA-FiCNA) and Centre de Recerca en Enginyeria de Materials i Micro i Nanosistemes (EMaS), Universitat Rovira i Virgili (URV), Campus Sescelades, C/Marcel·lí Domingo s/n E-43007 Tarragona, Spain

**Corresponding author: rosam.sole@urv.cat*

Received January 28, 2011; revised March 31, 2011; accepted March 31, 2011; posted March 31, 2011 (Doc. ID 141932); published May 13, 2011

Efficient Type II phase-matching second-harmonic generation of a 1125 nm fundamental beam has been obtained using $Ba:Yb:Nb:RbTiOPO_4/RbTiOPO_4$ waveguides grown by liquid phase epitaxy. The refractive indices of the epitaxial layer have been measured at different wavelengths, and the Sellmeier coefficients of the chromatic dispersion curves have been obtained. The phase-matching curve shows that the Ba^{2+} doping in $RbTiOPO_4$ contributes to increase the phase-matching range until 900 nm. The measured effective refractive indices of the propagation modes agree well with the theoretical calculations.

OCIS codes: 190.0190, 310.0310, 230.0230.

Rubidium titanyl phosphate, $RbTiOPO_4$ (RTP), is a nonlinear optical crystal that belongs to the $KTiOPO_4$ (KTP) family. It crystallizes in the orthorhombic space group $Pna2_1$ [1]. This biaxial crystal has high nonlinear optical and electro-optical coefficients, which make it particularly useful for frequency doubling IR laser radiation to obtain visible laser radiation [2]. More importantly, RTP presents a high surface damage threshold (9.0×10^6 MW/m^2) and a large temperature matching bandwidth (50 K/cm), which make this material especially suitable for high power laser applications [3]. The incorporation of laser active ions, such as lanthanide (Ln^{3+}) ions, into the RTP structure is interesting for obtaining both emission and frequency doubling (self-frequency doubling) in the same crystal. By codoping with Nb^{5+}, the Ln^{3+} concentration in these crystals has been demonstrated to be high enough for laser emission [4].

Of all the lanthanide ions, Yb^{3+} is of particular interest for emission at $\sim 1\,\mu$m and because it has a simple energy level scheme of only two energy levels, high absorption and emission cross sections, a low quantum defect, an absence of excited state absorption, and a long lifetime.

Thus, epitaxial layers of Yb:Nb:RTP/RTP are interesting for fabricating compact and efficient laser sources in the IR and visible spectral regions by combining the emission (with large optical paths) and second-harmonic generation (SHG) processes with the waveguide structure that could be used in guided high power lasers. In a previous study, we probed the guiding of 532 and 632.8 nm laser radiation with TM polarization through $RbTi_{1-x-y}Yb_xNb_yOPO_4/RbTiOPO_4$ epitaxial layers, but the refractive index step along the y principal optical direction between the epilayer and the substrate was not large enough to allow guiding of the light in the TE polarization [5].

The aim of this study is to obtain RTP epitaxial layers doped with Yb^{3+} and a contrast of refractive indices between the epilayer and the substrate high enough to allow the confinement of light in the TM and TE polarizations. According to the literature, introducing Ba^{2+} ions into the KTP structure increases the refractive indices of the crystal [6]. Thus, we investigated the effect of Ba^{2+} in epitaxial layers of Yb:Nb:RTP/RTP grown by liquid phase epitaxy (LPE). We measured the refractive indices of the substrate and the epilayer to predict theoretically the number of modes in the TE and TM polarizations that could be guided depending on the thickness of the epilayer. We found that the measured effective refractive indices of the modes agreed well with our calculations. Finally, we studied the second-harmonic radiation generated by Type II birefringent phase-matching (PM) that was guided in these structures.

We used solutions containing WO_3 to grow $Rb_{1-x}Ba_xTi_{1-y-z}Yb_yNb_zOPO_4$ epitaxial layers by the LPE method. The solution composition was $BaO–Rb_2O–P_2O_5–TiO_2–Nb_2O_5–Yb_2O_3–WO_3 = 0.88–43.02–23.61–20.70–0.45–1.35–10.00$ (mol. %) and its weight was about 80 g. The thermal gradients in the solution were practically zero.

After the solution had been homogenized, we accurately determined its saturation temperature (T_s) and also studied the kinetics of the growth/dissolution at temperatures slightly above/below of the T_s ($T_s = 1135$ K). The substrates were 1.5 mm thick plates parallel to the (001) plane and were cut from RTP single crystals and polished down to an rms of 50–60 nm [7]. The (001) plane is of particular interest because it contains the direction of the Type II birefringent PM ($\sim 1\,\mu$m), which includes the Yb^{3+} wavelength emission. The substrates, previously cleaned [8], were slowly introduced into the furnace to avoid thermal stresses and heated for about 1 h slightly above the solution surface. After that, they were dipped into the solution at a temperature of 1 K above the T_s to dissolve their surface slightly for 5 min. The next step was to decrease the temperature of the solution by 8 K below T_s to grow the epilayer for 5 h. During the whole process, the substrate was rotated at 60 rpm. Finally, the substrate and the epilayer were removed from the solution and kept at a few millimeters above the surface of the solution, while the furnace was slowly cooled (15 K/h) to room temperature to avoid thermal stresses.

0146-9592/11/101881-03$15.00/0

Table 1. Refractive Indices of the Ba:Yb:Nb:RTP/RTP Waveguide

Refractive Indices of the Epilayer			
Wavelength (nm)	n_x	n_y	n_z
532.0	1.805	1.822	1.921
632.8	1.788	1.802	1.896
770.0	1.776	1.787	1.875
780.4	1.775	1.788	1.873
790.0	1.774	1.786	1.873
820.4	1.772	1.786	1.869
840.9	1.771	1.785	1.867
971.0	1.766	1.779	1.861
980.6	1.765	1.777	1.862
989.2	1.765	1.776	1.861
1526.5	1.755	1.767	1.845
Refractive Indices of the Substrate			
632.8	1.789	1.801	1.888

The grown epitaxial layers show good optical quality and the average growth rate was 8.3 μm/h. The epilayer used for optical characterization had a thickness of 52 μm.

The chemical composition of the epitaxial layers, determined by electron probe microanalysis (EPMA), was $RbTi_{0.973}Yb_{0.009}Nb_{0.018}OPO_4$. The Ba^{2+} concentration in the epitaxial layer was lower than the detection limit of this ion by EPMA. However, this ion was present in the epitaxial layers, since their refractive indices changed, as described below. The low level of Ba^{2+} incorporation in the RTP structure could be explained by the different ionic charge of the Ba^{2+} and Rb^{+} ions and the different ionic radii of these two ions [9].

The refractive indices of the epitaxial layers and the substrates, as a function of the wavelength, were measured by the total internal reflection angle law. The light was coupled with a prism (Metricon prism coupler) using several laser sources. To optimize the coupling process, the epilayer was polished down to a thickness of 50 μm. The refractive indices obtained for the $RbTi_{0.973}Yb_{0.009}Nb_{0.018}OPO_4$ epitaxial layer with Ba^{2+} traces and those of the substrate at 632.8 nm are summarized in Table 1. The refractive indices of the epilayer are higher than those of the substrate along the y and z directions, indicating that this layer could support TM and TE propagation modes.

From these refractive indices, we calculated the Sellmeier dispersion curves for these epilayers according to the expressions [10]

$$n_i^2(\lambda) = A_i + \frac{B_i}{1 - \left(\frac{C_i}{\lambda}\right)^p} + \frac{D_i}{1 - \left(\frac{E_i}{\lambda}\right)^q}, \qquad (1)$$

where $i = x$, y, and z.

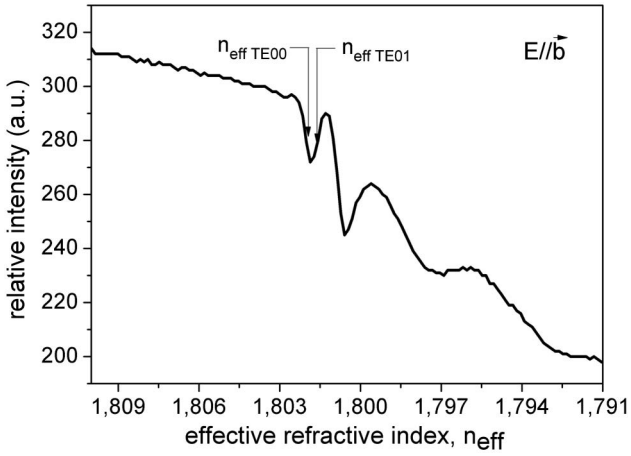

Fig. 1. Dark mode spectrum with TE polarization in a 10 μm Ba:Yb:Nb:RTP/RTP epitaxial layer at 632.8 nm.

The Sellmeier coefficients obtained are listed in Table 2. According to Type II SHG, TM and TE fundamental IR modes should propagate into the layer and TE second-harmonic modes should be generated. The PM condition for SHG is: $1/2[n_{TE}(\lambda_{pm}) + n_{TM}(\lambda_{pm})] - n_{TE}(\lambda_{pm}/2) = 0$, where $n_{TE}(\lambda_{pm})$ and $n_{TM}(\lambda_{pm})$ are the effective refractive indices for the TE and TM propagation modes at the phase-matching wavelength (λ_{pm}), respectively, and $n_{TE}(\lambda_{pm}/2)$ is the effective refractive index for the TE guided mode at the second-harmonic wavelength ($\lambda_{pm}/2$) [11].

To check PM conditions, and demonstrate the propagation of the TM and TE modes in the waveguide, we polished the epitaxial layer down to 10 μm thickness. Figure 1 shows the dark mode spectrum in the TE polarization (electric field of the incident light parallel to the b crystallographic direction) obtained by the prism–film coupling technique, where only one propagation mode is observed. If the electric field of the incident light is parallel to the c crystallographic direction (TM polarization), we could observe five propagation modes into the 10 μm thickness epilayer. It is interesting to have only one TE propagation mode and a reduced number of TM propagation modes into the epilayer to have a better coupling among them and obtain a more efficient SHG process [12].

The Type II PM curves in the a–b plane were obtained from the Sellmeier equations calculated for these epilayers, together with the phase-matching condition and taking into account the Fresnel equation for biaxial crystals. The expression obtained was

$$\frac{2}{\sqrt{\frac{\cos^2(\varphi)}{n_y^2(2\omega)} + \frac{\sin^2(\varphi)}{n_x^2(2\omega)}}} = n_z(\omega) + \frac{1}{\sqrt{\frac{\cos^2(\varphi)}{n_y^2(\omega)} + \frac{\sin^2(\varphi)}{n_x^2(\omega)}}}, \qquad (2)$$

where φ is the angle of light propagation into the waveguide in the a–b plane, and n_x, n_y, and n_z are the

Table 2. Sellmeier Coefficients Obtained by Fitting the Chromatic Dispersion Curves to Eq. (1)

	A	B	C (nm)	D	E (nm)	p	q
n_x	2.3718	0.6979	0.2494	1.2900	13.0012	2.0012	1.9412
n_y	2.4081	0.7112	0.2481	0.8041	10.5332	2.0091	1.8981
n_z	2.3412	1.0592	0.2521	0.6771	10.1721	2.0112	1.8001

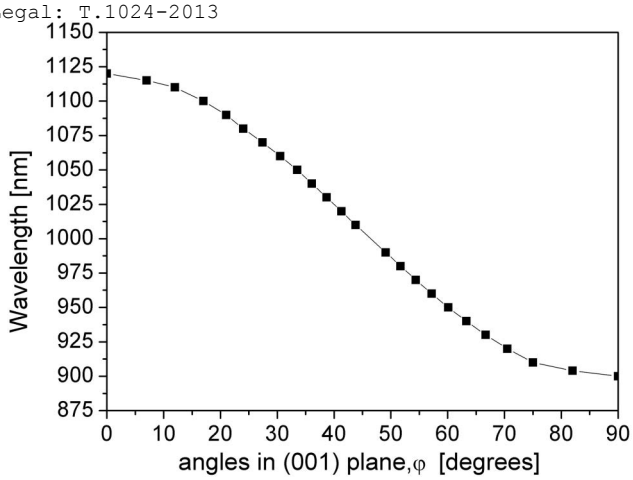

Fig. 2. Calculated phase-matching curve for Type II SHG in the Ba:Yb:Nb:RTP/RTP epitaxial layer.

refractive indices with the electric field parallel to the a, b, and c crystallographic directions, respectively. Figure 2 shows the phase-matching curve for Type II PM SHG calculated from these equations. From this figure we can observe that the range of wavelengths for which Type II PM can be obtained in these samples is larger than in undoped RTP [10] and the SHG wavelengths extend toward the blue region.

To investigate the single-pass Type II PM SHG, we polished the faces perpendicular to the a crystallographic direction. We used a tunable OPO source to obtain radiation with the wavelength required to obtain maximum efficiency of SHG for propagation along the crystallographic a direction. This light was coupled into the waveguide using a microscope objective. The waveguide length was 1.1 cm. An achromatic half-wave plate was placed between the laser source and the sample at an angle of 22.5° to ensure Type II SHG. The guided green light obtained by SHG was observed with a CCD camera and is shown in Fig. 3, which also shows the wavelength spectrum in the inset. The most efficient SHG was obtained for a fundamental wavelength of the IR light coupled to the epilayer of 1125 nm, with 0.008 mJ per pulse (10 ns per pulse), a little above the theoretical value but close to it, whereas the second-harmonic radiation generated was in the green region (562.5 nm) (see inset in Fig. 3). After filtering the output radiation with an IR filter, we measured the second-harmonic power with a power-meter. The efficiency of Type II PM SHG, calculated using the expression $\eta = P_{2\omega}/P_{\omega}$, was 0.69.

To summarize, we have shown a highly efficient method of obtaining Type II PM SHG on Ba:Yb:Nb:RTP/RTP waveguides. When the epitaxial layer was codoped with Ba^{2+}, we obtained TM and TE polarization modes confined in the waveguide, which is essential for Type II PM SHG interactions. The PM curve calculated from the Sellmeier equations obtained for these epilayers showed that the wavelengths that can be doubled ranged from 900 to 1125 nm, a range that includes the Yb^{3+} emission in these materials. We could confirm experimentally the

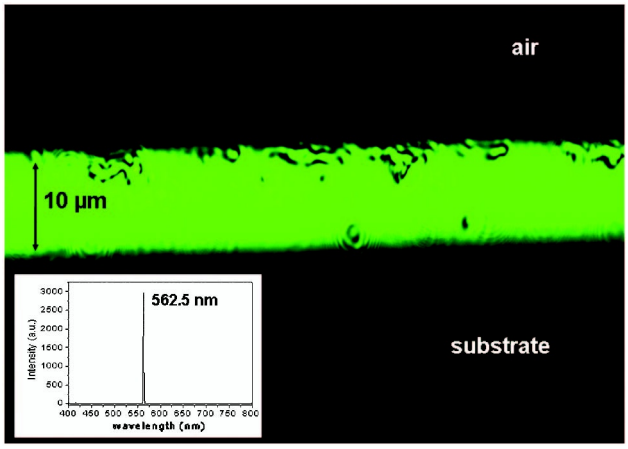

Fig. 3. Type II SHG in a Ba:Yb:Nb:RTP/RTP epitaxial layer with the fundamental radiation of 1125 nm and second-harmonic radiation of 562.5 nm. Inset, wavelength spectrum with maximum at 562.5 nm.

upper limit of this curve, indicating that self-frequency doubling could be obtained in these epilayers in the future.

This work was supported by the Spanish Government under projects MAT2008-06729-C02-02/NAN, TEC2010-21574-C02-02, PI09/90527, HF2008-0045, and DE2009-0002 and by the Catalan Authority under project 2009 SGR235. J. Cugat thanks the Spanish Government for fellowship BES-2009-024190. J. J. Carvajal is supported by the Spanish Ministry of Education and Science and the European Social Fund under the Ramon y Cajal programs RYC2006—858.

References

1. P. A. Thomas, S. C. Mayo, and B. E. Watts, Acta Crystallogr. B **48**, 401 (1992).
2. C. Zumsteg, C. J. Bierlein, and T. E. Gier, J. Appl. Phys. **47**, 4980 (1976).
3. Y. S. Oseledchik, S. P. Belokrys, V. V. Osadchuk, A. L. Prosvirnin, A. F. Selevich, V. V. Starshenko, and K. V. Kuzemchenko, J. Cryst. Growth **125**, 639 (1992).
4. X. Mateos, V. Petrov, A. Peña, J. J. Carvajal, M. Aguiló, F. Díaz, P. Segonds, and B. Boulanger, Opt. Lett. **32**, 1929 (2007).
5. J. Cugat, R. Solé, M. C. Pujol, J. J. Carvajal, X. Mateos, F. Díaz, and M. Aguiló, Opt. Mater. **32**, 1648 (2010).
6. N. Yamada and Y. Yamamoto, Jpn. J. Appl. Phys. **33**, 6572 (1994).
7. J. Cugat, R. Solé, J. J. Carvajal, M. C. Pujol, X. Mateos, F. Díaz, and M. Aguiló, CrystEngComm **13**, 2015 (2011). .
8. R. Solé, V. Nikolov, A. Vilalta, J. J. Carvajal, J. Massons, Jna. Gavaldà, M. Aguiló, and F. Díaz, J. Mater. Res. **17**, 563 (2002).
9. R. D. Shannon, Acta Crystallogr. A **32**, 751 (1976).
10. Y. Guillen, B. Ménaert, J. P. Fève, P. Segonds, J. Douady, B. Boulanger, and O. Pacaud, Opt. Mater. **22**, 155 (2003).
11. W. P. Risk, T. R. Gosnell, and A. V. Nurmikko, *Compact Blue-Green Lasers* (Cambridge U. Press, 2003).
12. W. P. Risk, S. D. Lau, R. Fontana, L. Lane, and Ch. Nadier, Appl. Phys. Lett. **63**, 1301 (1993).

Paper V

Efficient second harmonic generation green light in RTP planar waveguide

J. Cugat, R.M. Solé, M.C. Pujol, J.J. Carvajal, X. Mateos, F. Díaz, M. Aguiló,

Physics Status Solidi C, 8(9), 2946 (2010).

Early View publication on wileyonlinelibrary.com
(issue and page numbers not yet assigned;
citable using Digital Object Identifier – **DOI**)

Phys. Status Solidi C, 1–4 (2011) / **DOI** 10.1002/pssc.201084095

physica status solidi c
www.pss-c.com
current topics in solid state physics

Efficient second harmonic generation green light in RTP planar waveguides

Jaume Cugat, Rosa Maria Solé, Maria Cinta Pujol, Joan Josep Carvajal, Xavier Mateos, Francesc Díaz, and Magdalena Aguiló*

Física i Cristallografia de Materials i Nanomaterials (FiCMA-FiCNA), University Rovira i Virgili (URV), Campus Sescelades, C/Marcel lí Domingo s/n, 43007 Tarragona, Spain

Received 3 October 2010, accepted 4 February 2011
Published online 26 May 2011

Keywords liquid phase epitaxy, second harmonic generation, waveguide, guiding simulation

* Corresponding author: e-mail magdalena.aguilo@urv.cat

In this paper, epitaxial layers of $Rb_{1-x}Ba_xTi_{1-y-z}Yb_yNb_zOPO_4$ have been successfully grown on (001) oriented $RbTiOPO_4$ substrates. Although the Ba^{2+} contents in these layers was very low, the contrasts in refractive indices between the epitaxial layer and the substrate were high enough to allow the propagation of one TE and three TM modes, at the wavelength of 632.8 nm, using a 5 μm thickness epilayer. These light propagation modes were first simulated, using the refractive indices of the layer and the substrate measured previously. The TE and TM dark-mode spectra obtained experimentally, using the prism coupler method and a He-Ne laser beam, agree well with the simulation results. Finally, type II Second Harmonic Generation experiments were carried out with pumping at 1130 nm and obtaining green light at 565 nm. The experimental efficiency in the Second Harmonic Generation experiments was of 69 %/mWcm^2.

1 Introduction

Rubidium titanyl phosphate, $RbTiOPO_4$ (RTP), is an orthorhombic biaxial nonlinear optical crystal which has high nonlinear optical and electrooptical coefficients [1]. Belongs to the non-centrosymmetric space group $Pna2_1$. Due to these properties, this crystal is very interesting for frequency doubling (Second Harmonic Generation, SHG) of the fundamental radiation at around 1 μm in the infrared spectral region. The doping of RTP with laser active ions as Ln^{3+} (lanthanides) ions is accompanied by a low concentration of the doping ion. This concentration can be increased by codoping with Nb^{5+} [2]. Among the Ln^{3+} ions, Yb^{3+} has special interest due to its emission at around 1 μm and its simple energy level scheme, with only two energy levels: the fundamental $^2F_{7/2}$ and an excited state $^2F_{5/2}$. Other interesting properties of Yb^{3+} are their broad absorption and emission bandwidths, low quantum defect, long lifetime and absence of excited state absorption. Laser action of Yb:Nb:RTP single crystal has already been demonstrated [3]. Epitaxial layers have some advantages over single crystals as their higher heat removal efficiency and the waveguide structure [4]. If the epitaxial layers of a nonlinear optical material contain Yb^{3+} ions in a concentration level high enough high for lasing, the self-doubling process can occur in the crystal and it is possible to guide the light along the waveguide when the contrast in refractive indices between the epilayer and the substrate is suitable. In this way, it is possible to obtain efficient and compact laser sources in the visible region.

In a previous work, we have shown that Yb:Nb:RTP/RTP epilayers can guide the light at 532 and 632.8 nm only in TM polarization, but not in TE polarization [5]. This is due to the small contrast of refractive indices between the epilayer and the substrate. The incorporation of Ba^{2+} ions in the $KTiOPO_4$ (KTP) structure produces an increasing of the refractive indices [6] which can be enough to guide the light both in TM and TE polarizations.

In this work, we grow Ba:Yb:Nb:RTP epitaxial layers on RTP substrates with the aim to obtain enough contrast of refractive indices between the epilayer and the substrate to guide the light in TM and TE polarizations. The contrast of refractive indices between the epilayer and the substrate is measured and the dark-mode spectrum obtained.

2 Experimental details

2.1 Liquid phase epitaxy (LPE) The $Rb_{1-x}Ba_xTi_{1-y-z}Yb_yNb_zOPO_4$ epitaxial layers on (001) oriented RTP substrates were grown by the Liquid Phase Epitaxial (LPE) method. The substrates were obtained by cutting and polishing slices parallel to the (001) plane, from a RTP single crystal obtained as it is explained in Ref. [5]. Figure 1 shows a RTP single crystal, a scheme of the cutting process and an as-grown epitaxy. The epitaxial growth was carried out in a vertical furnace with a wide zone where the temperature differences were practically null. Figure 2 shows a scheme of this furnace. The solvent used contained WO_3 and an excess of Rb_2O and P_2O_5. The WO_3 has been introduced in the solution to decrease its viscosity and thus favors the crystal growth [6].

The chemicals used were BaO, Rb_2CO_3, $NH_4H_2PO_4$, TiO_2, Yb_2O_3, Nb_2O_5 and WO_3. The basical solution composition was Rb_2O/P_2O_5 = 65/35 (molar ratio), (Rb_2O + P_2O_5)/TiO_2 = 75/25 (molar ratio), and 10 mol % of WO_3. The substitution was carried out by replacing 2 mol % of Rb_2O by BaO, 2 mol % of TiO_2 by Nb_2O_5 and 6 mol % of TiO_2 by Yb_2O_3. The solution weighted about 80 g and was prepared in a Pt cylindrical crucible, 30 mm in diameter. The saturation temperature of the solution was determined accurately by measuring the growth/dissolution rates, depending on the temperature, of an RTP seed in contact with the surface of the solution and rotating at 40 rpm. Information about the rates of growth/dissolution at temperatures slightly lower/higher than the saturation temperature was also obtained.

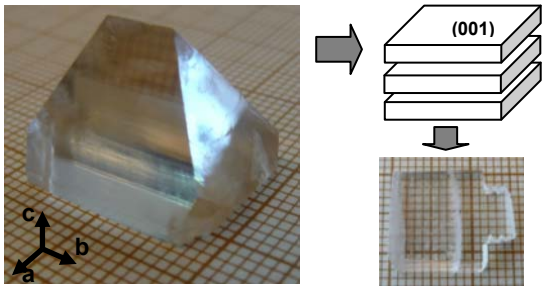

Figure 1 As-grown RTP single crystal, scheme of the cutting process and as-grown epitaxy.

The substrates, with typical dimensions 10.2 mm, 18.1 mm and 1.5 mm along the ***a***, ***b*** and ***c*** crystallographic directions, respectively, were cleaned as it is detailed in Ref. [5]. After that, they were slowly introduced in the furnace to avoid thermal stresses and hold for 1 h above the solution surface. The substrate was introduced into the solution and maintained at 1 K above the saturation temperature for 5 min to dissolve the outer part of it. After that, the temperature of the solution was decreased to 8 K below the saturation temperature and the epilayer grew for 5 h. During all the process the substrate rotated at 40 rpm.

The composition of the epitaxial layer was measured by Electron Probe Microanalysis (EPMA) using a CAMECA SX 50 equipment. The standard used to measure Rb, Ti and P was an RTP single crystal, while the standards used to measure Nb and Yb were Nb metal and YbF_3, respectively.

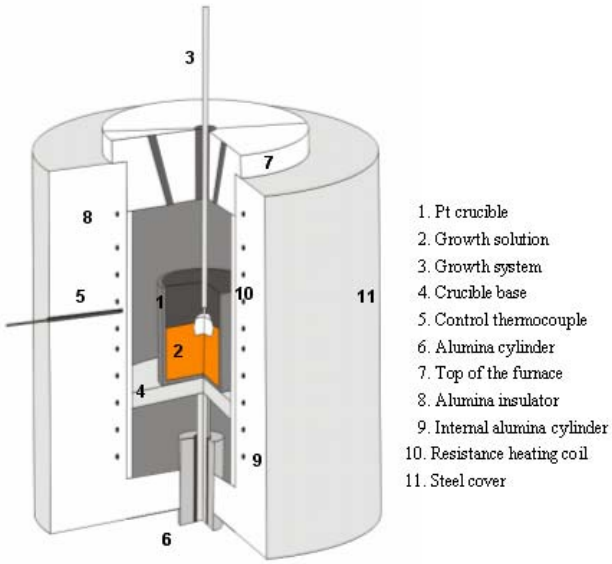

Figure 2 Scheme of the furnace used for LPE growth.

2.2 Optical characterization After growing the epitaxies, they were polished to obtain flat samples for characterization. The prism coupler system was used to record the refractive indices as well as the dark-mode spectrum at 632.8 nm using a He-Ne laser beam as the light source. The TM polarization was used for determining the refractive index along the ***c*** crystallographic direction (n_z) and the TM-dark-mode spectrum. On the other hand, TE polarization was used for determining the refractive indices along ***a*** and ***b*** crystallographic directions (n_x and n_y, respectively) and also the TE-dark-mode spectrum.

The effective index method was used to simulation the propagation modes. This simulation was carried out with OlympIO software [7], using the refractive indices of the epitaxial layer and the substrate measured previously with the prism coupler system at 632.8 nm. We simulated a 5 µm thickness planar waveguide at 632 nm for TM and TE polarizations. After making the simulations we polished the epitaxial layer until 5µm for to obtain the TM and TE-dark-mode spectrum.

In order to investigate the single pass type-II SHG, light from a longitudinal-mode pulsed OPO laser was coupled into the waveguide using microscope objectives. To ensure type-II SHG, an achromatic half-plate was set to

22.5º and placed between the laser source and the sample. In this way the TM and TE modes were excited simultaneously. An approximate efficiency was measured by putting a filter which cut the visible after the waveguide and using the formula [9]:

$$\eta = \frac{(p_{2\omega} / p_{\omega})}{p_{\omega} L^2}$$

where $p_{2\omega}$ is the second harmonic power, p_{ω} is the fundamental power and L is the waveguide length.

3 Results and discussion

3.1 Liquid Phase Epitaxy (LPE) The epitaxial layers obtained were generally transparent and colourless. The average growth rate of these epitaxial layers was about 8 µm/h. The crystal composition, obtained by EPMA, was $RbTi_{0.973}Yb_{0.009}Nb_{0.018}OPO_4$. The Ba^{2+} concentration in the epilayer was lower than the detection limit of EPMA. This low concentration can be due to the different ionic radii of Rb^+ and Ba^{2+} [10]. In any case, the presence of Ba^{2+} ions in the crystals, even at the level of traces, can be significant for changing the refractive indices and allow the waveguiding with two different polarizations.
After growing the epitaxial layer, this was polished until 50 µm thickness for measuring the refractive indices of this material. The refractive indices are shown in Table 1.

Table 1 Refractive indices of the Ba:Yb:Nb:$RbTiOPO_4$/ $RbTiOPO_4$ at a wavelength of 632.8 nm.

Material	n_x	n_y	n_z
Epitaxial layer	1.788	1.802	1.896
Substrate	1.789	1.801	1.888

Table 1 shows that the light polarized along the ***y*** and ***z*** optical directions can be guided through the epilayer due to the positive refractive indices contrast. Otherwise the light polarized along the ***x*** optical direction cannot be guided through the epilayer due to the negative refractive index contrast.

The simulations have been carried out using the refractive indices shown in Table 1, measured on a 5 µm thickness epitaxial layer, at wavelength of 632 nm. The results were one TE mode (light polarization along the ***y*** direction) and three TM modes (light polarization along the ***z*** direction). Figures 3 and 4 show the simulation pictures of TE_{00} and TM_{02} propagation modes, respectively.

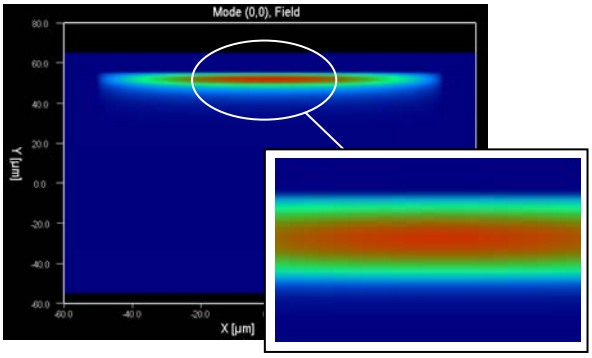

Figure 3 Simulation picture of the TE_{00} of the Ba:Yb:Nb:$RbTiOPO_4$ / $RbTiOPO_4$.

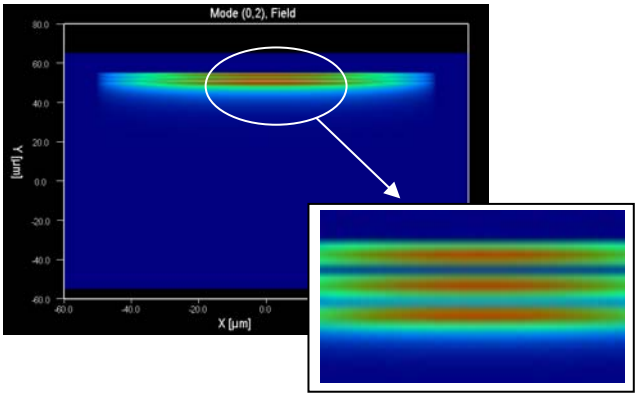

Figure 4 Simulation picture of the TM_{02} of the Ba:Yb:Nb:$RbTiOPO_4$ / $RbTiOPO_4$.

Figure 5 shows the TE-dark-mode spectrum of the epitaxial layer studied. According to the simulation, it contains the TE_{00} mode and its effective refractive index is 1.8026. On the other hand, Fig. 6 shows the TM-dark-mode spectrum of the same sample. There are three propagation modes with effective refraction indices: $n_{eff}(TM_{00})$=1.896, $n_{eff}(TM_{01})$=1.893 and finally $n_{eff}(TM_{02})$=1.890. The agreement between the experimental and simulation values is as low as 0.1 %.

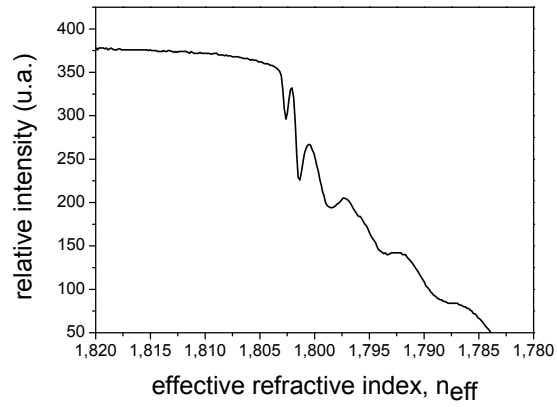

Figure 5 TE-dark-mode spectrum of the Ba:Yb:Nb:$RbTiOPO_4$/$RbTiOPO_4$.

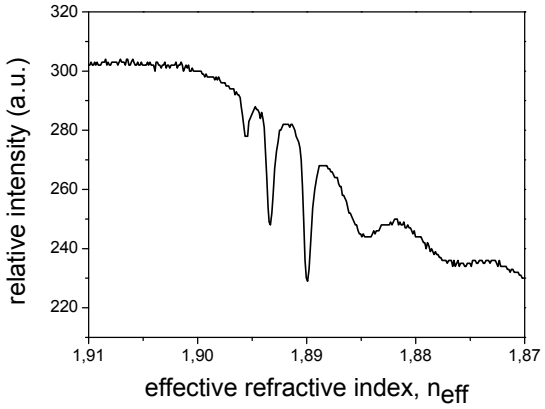

Figure 6 TM-dark-mode spectrum of the Ba:Yb:Nb:$RbTiOPO_4$/$RbTiOPO_4$.

The end faces of the waveguide were polished in order to end-couple efficiently the laser light. We polished the (100) end-faces for light propagation along the ***a*** crystallographic direction, since in this waveguide the TE and TM polarizations only could be stimulated simultaneous in this configuration.

Type II Second Harmonic Generation experiments were carried out with the tunable OPO as a waveguide pump, we could prove the efficient conversion of the pump at 1130 nm obtaining green light at 565 nm with 69 %/mWcm^2 of efficiency.

4 Conclusions

We reported the efficient guiding possibilities of the Ba:Yb:Nb:RTP layers grown on non-active RTP (001) substrates by the Liquid Phase Epitaxial method. The refractive indices measurements reveal a relative high refractive indices contrast. In fact, the modal simulation as well as the TE and TM dark-mode spectra reveals the existence of one and three propagation modes for TE and TM polarizations, respectively, at a wavelength of 632.8 nm. On the other hand the Type II Second Harmonic Generation experiments in the waveguide show an efficiency of 69 %/mWcm^2, showing that these composites are able to converse the fundamental infrared emission of Yb^{3+} with high efficiency.

Acknowledgements This work was supported by the Spanish Government under projects MAT2008-06729-C02-02/NAN, MAT2008-04046-E/MAT, TEC2010-21574-C02-02, PI09/90527, HF2008-0045, DE2009-0002 and the Catalan Authority under project 2009SGR235. J. Cugat thanks the Spanish Government for the FPI fellowship BES-2009-024190. J. J. Carvajal is supported by the Education and Science Ministry of Spain and European Social Fund under the Ramon y Cajal programs RYC2006–85

References

[1] Y. Guillien, B. Menaert, J. P. Feve, P. Segonds, J. Douady, B. Boulanger, and O. Pacaud. Opt. Mater. **22**, 155 (2003).
[2] J. J. Carvajal, R. Solé, Jna. Gavaldà, J. Massons, P. Seconds, B. Boulanger, A. Brenier, G. Boulon, J. Zaccaro, M. Aguiló, and F. Díaz, Opt. Mater. **26**, 313 (2004).
[3] X. Mateos, V. Petrov, A. Peña, J. J. Carvajal, M. Aguiló, F. Díaz, P. Segonds, and B. Boulanger, Opt. Lett. **32**(13), 1929 (2007).
[4] G. I. Stegeman and C. T. Seaton, J. Appl. Phys. **58**, R57 (1985).
[5] J. Cugat, R. Solé, J. J. Carvajal, M. C. Pujol, X. Mateos, F. Díaz, and M. Aguiló, Cryst. Eng. Commun. (2010) (submitted).
[6] J. J. Carvajal, V. Nikolov, R. Solé, Jna. Gavaldà, J. Massons, M. Rico, C. Zaldo, M. Aguiló, and F. Díaz, Chem. Mater. **12**, 3171 (2000).
[7] Olympios, integrated optics software versión 5.2, Netherlands (2004).
[8] N. Yamada and Y. Yamamoto, Jpn. J. Appl. Phys. **33**, 6572 (1994).
[9] M. J. Jongerius, R. J. Bolt, and N. A. Sweep, J. Appl. Phys. **75**(7), 3316 (1994).
[10] R. D. Shannon, Acta Cryst. **A3**, 751 (1976).

Paper VI

Fs-laser microstructuring of ribs on active (Yb,Nb):RTP/RTP planar waveguides

J. Cugat , A. Ruiz de la Cruz, R. Solé , A. Ferrer, J.J. Carvajal, X. Mateos, J. Massons , J. Solís, G. Lifante, F. Díaz, M. Aguiló,

Journal of lightwave technology, **31**(3), 385 (2013).

Femtosecond-Laser Microstructuring of Ribs on Active (Yb,Nb):RTP/RTP Planar Waveguides

J. Cugat, A. Ruiz de la Cruz, R. Solé, A. Ferrer, J. J. Carvajal, X. Mateos, J. Massons, J. Solís, G. Lifante, F. Díaz, and M. Aguiló

***Abstract*—We have produced rib waveguides by femtosecond-laser structuring of active (Yb,Nb):$RbTiOPO_4$/$RbTiOPO_4$ epitaxial layers. The ribs were produced by the approximation scanning technique combined with beam multiplexing. The so-obtained waveguides are trapezoidal in shape and show propagation losses with an upper bound of $\sim$4 dB/cm. A simulation of the rib waveguides with real geometry parameters reveals high levels of light confinement at 632 and 972 nm. The near-field patterns of the fundamental modes have been obtained by exciting the waveguides at wavelengths of 632 and 972 nm. Micro-Raman spectroscopy study reveals that the damage to the crystalline structure in the rib boundaries, showing no amorphization traces, is around 3 μm in length and depth, which is significantly shorter than the total width of the ribs.**

***Index Terms*—Femtosecond-laser microstructuring, nonlinear optical crystals, waveguides.**

I. Introduction

$RbTiOPO_4$ (RTP) belongs to the $KTiOPO_4$ (KTP) family of nonlinear optical crystals. It crystallizes in the orthorhombic space group $Pna2_1$ [1]. Because of its non-linear optical properties, RTP can be used for frequency doubling the light emitted by Yb and Nd lasers with a wavelength close to 1 μm [2]. RTP can also be doped with active ions to obtain a self-frequency doubling (SFD) material, which can be useful for compact and efficient laser sources in the visible range. KTP family of non-linear optical crystals has large electro-optical coefficients and low dielectric constants making them attractive for such electro-optical applications as modulators and Q switches [3]. These interesting properties make RTP a good candidate as a base material for integrated photonics.

Among other possible active ions, Yb^{3+} was chosen for this study because it has several advantages. Its ionic radius is much closer to the radius of Ti^{4+} than the ionic radius of the other Ln^{3+} ions, which produces a higher distribution coefficient of Yb^{3+} in the crystals of the KTP family [4]. The emission wavelength of Yb^{3+} is similar to that of Nd^{3+} in the region close to 1 μm, but its energy scheme is simpler. It has only two energy levels: the ground state $^2F_{7/2}$ and the exited state $^2F_{5/2}$. This prevents some effects that reduce the laser efficiency, for instance, excited-state absorption, cross-relaxation, and upconversion. On the other hand, the similarity between the pumping and the laser wavelength means that there is a small quantum defect that reduces the thermal loading of the crystals during laser operation [5]. Yb^{3+} also has no absorption losses at the second harmonic generation (SHG) frequency, which makes it particularly suitable for SFD [6].

The maximum doping levels of Yb^{3+} previously achieved in KTP bulk crystals are not enough for laser operation. The distribution coefficient of Yb^{3+} in single-doped RTP is slightly higher than in KTP but not enough for lasing [4]. The codoping of RTP with Yb^{3+} and Nb^{5+} significantly increases the distribution coefficient of Yb^{3+} in RTP [7]. Thus, the content of Yb^{3+} in RTP was high enough to successfully obtain laser emission in these crystals [8].

In order to avoid the difficulties of growing bulk (Yb,Nb):RTP crystals, which are often of low quality [9], and to increase the optical path, (Yb,Nb):RTP planar waveguides were grown on RTP substrates by the liquid phase epitaxy (LPE) method [10]. In these samples efficient type II SHG has already been reported [11].

For the fabrication of nonlinear optical waveguides, ion-incorporation techniques such as ion implantation [12] and ion diffusion have been applied [3]. Other techniques such as LPE [10], molecular beam epitaxy [13], chemical vapor deposition, and pulsed laser deposition [14] have also been widely used to obtain optical waveguides. Subsequent structuring methods such as ion milling [15] reactive ion etching, [16], and laser structuring, [17] are also available.

Microstructuring the surface by femtosecond-laser (fs-laser) ablation could be a good technique for the commercial fabrication of optical waveguides in the field of integrated photonics. The main advantage it has over other techniques is that it enables rapid prototyping with a relatively cheaper production cost that does not require to be carried out in a clean room.

Manuscript received September 04, 2012; revised November 22, 2012; accepted November 23, 2012. Date of publication November 29, 2012; date of current version December 31, 2012. This work was supported by the Spanish Government under Projects TEC2010-21574-C02-02, TEC2011-22422, MAT2011-29255-C02-02, PI09/90527, and the Catalan Authority under Project 2009SGR235. This work was also supported in part by the European Commission under the Seventh Framework Programme under Project FP7-SPACE-2010-1-GA-263044. The work of J. Cugat was supported by the Spanish Government under the FPI fellowship BES-2009-024190.

J. Cugat, R. Solé, J. J. Carvajal, X. Mateos, J. Massons, F. Díaz, and M. Aguiló are with Física i Cristal.logafía de Materials i Nanomaterials, Universitat Rovira i Virgili, 43007 Tarragona, Spain (e-mail: jaume.cugat@urv.cat; rosam.sole@urv.cat; joanjosep.carvajal@urv.cat; xavier.mateos@urv.cat; jaume.masons@urv.cat; magdalena.aguilo@urv.cat).

A. Ruiz de la Cruz and J. Solís, are with Laser Processing Group, Instituto de Óptica, 28006 Madrid, Spain (e-mail: alejandro@io.cfmac.csic.es; j.solis@io.cfmac.csic.es).

A. Ferrer was with the Laser Processing Group, Instituto de Óptica, 28006 Madrid, Spain. He is now with the Ultrafast Dynamics Group, Institute for Quantum Electronics, ETH Zurich, CH-8093 Zurich, Switzerland (e-mail: a.ferrer@io.cfmac.csic.es).

G. Lifante is with Departamento de Física de Materiales C-IV, Universidad Autónoma de Madrid, 28049 Madrid, Spain (e-mail: gines.lifante@uam.es).

Color versions of one or more of the figures in this paper are available online at http://ieeexplore.ieee.org.

Digital Object Identifier 10.1109/JLT.2012.2230615

In this paper, we show that low-loss rib waveguides can be produced by fs-laser structuring on (Yb,Nb):RTP epitaxial layers grown by LPE. The microstructures were generated by fs-laser ablation. A morphological, optical, and Raman spectroscopy characterization of the ribs is presented.

II. Rib Waveguide Fabrication

A. Structure Performance Simulations

In order to determine what the best geometry is for the ribs in terms of light confinement, the performance of the devised structures at 632 and 972 nm were simulated using the MG finite difference (Real) method at 632 and 972 nm from the OlympIOs software package.

The initial structure considered is an epitaxial layer (Yb, Nb):RTP with thickness of 10 μm on bulk RTP (see Section II-B). Since the ribs are produced by sculpting two parallel trenches on the sample surface by laser surface structuring, the initial simulations considered ribs of different widths and heights using the previously determined values of the corresponding refractive indexes of the epilayer and the substrate.

The real refractive indexes of the waveguide and the substrate in TM polarization were 1.8967 for the layer and 1.8897 for the substrate at 632 nm [9]. Similar measurements were made in TM polarization at 972 nm and the values obtained for the refractive indexes were 1.8632 for the layer and 1.8573 for the substrate, measured in this study.

The rib structures considered in the initial simulation were 8 μm height and 6–18 μm wide (with 2 μm steps). The depth was chosen to be 8 μm, because the initial tests of fs-laser structuring on RTP substrates showed this value to provide a good compromise in terms of crystal damage and groove shape. The confinement area for simulation was designed taking into account the rib boundary that extended down to the planar waveguide–substrate interface. The simulation enables to estimate approximately the percentage of energy confined within this region (confinement). Although part of the mode propagates through the planar region, the simulation reveals a high level of confinement. The estimated confinement values depended on rib dimensions and were in all the cases above 99.0 % at both 632 and 972 nm. The experimentally determined losses were analyzed by simulating the power attenuation in the waveguides using the beam propagation method.

B. Growth by LPE

We grew epitaxial layers of (Yb,Nb):RTP on (001) RTP substrates. Plates perpendicular to the *c* crystallographic direction and cut from RTP single crystals were used as substrates. The *ab* plane is interesting because it contains the type II noncritical phase matching SHG directions for the range between 985 and 1118 nm. This range contains the Yb^{3+} laser emission at 1060 nm.

The epitaxial layers were grown by the LPE method from WO_3-containing solutions. Rb_2CO_3 (99%), $NH_4H_2PO_4$ (99%), TiO_2 (99.9%), Yb_2O_3 (99.9%), Nb_2O_5 (99.9%), and WO_3 (99.9%) were used as starting chemicals. The procedure was similar to that already reported Solé and coworkers for the LPE growth of several epitaxial layers [18], [19]. The solution composition was Rb_2O-P_2O_5-TiO_2-Yb_2O_3-Nb_2O_5-WO_3 = 43.90-23.60-20.70-1.35-0.45-10 (mol%). To start the growth process, the solution was supersaturated by decreasing its temperature by 2 K below the saturation temperature, which was around 1153 K. In all the LPE experiments, a rotation of 60 r/min was applied. The epitaxial layers grown showed good optical quality and the average growth rate was 8.3 μm/h. The chemical composition of the epitaxies was determined by electron probe microanalysis and the result was $RbTi_{0.958}Yb_{0.016}Nb_{0.026}OPO_4$. The thickness of the as-grown epitaxial layers measured by interferometric microscopy and using the substrate surface as a reference was around 50 μm. After growth, the epitaxial layer was polished up to 10 μm in thickness.

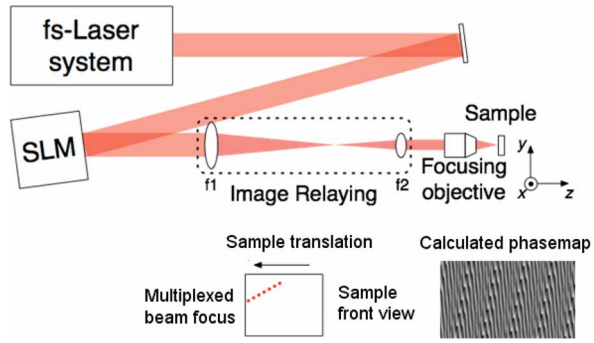

Fig. 1. Experimental setup used to inscribe the surface channels for the fabrication of waveguides. The focused beam is multiplexed into seven spots, which makes it possible to perform the approximation scanning technique in a single scan.

C. Femtosecond-Laser Setup and Experimental Conditions

In order to produce the rib structures, sets of two parallel ablated channels were micromachined on the sample surface using the fs-laser irradiation setup sketched in Fig. 1. We used a pulsed fs-laser amplification system (Tsunami and Spitfire from Spectra-Physics), working at a 1 KHz repetition rate and a pulse duration of $\tau_p \approx 120$ fs. The output pulse energy was $E = 1$ mJ and the central wavelength $\lambda = 799$ nm. We also used a spatial light modulator (SLM, Hamamatsu X8267) to control the beam wavefront before focusing on the surface of the sample. This allowed us to design the intensity profile of the focused beam. An image relaying system with magnification $M = 0.4$ (f1 = 50 cm and f2 = 20 cm) transferred the beam at the SLM surface to the back-focal position of the focusing microscope objective (Mitutoyo M Plan Apo NIR 20X NA = 0.4). The sample was placed on a three-axis motorized stage. During processing, the sample was translated at a speed of v = 100 μm/s.

In order to improve the quality of the micromachined channels, we used the *approximation scanning* technique [20]. It consists of performing several irradiation scans, each one slightly displaced from the previous one in the direction perpendicular to the channels. This produces steeper channel walls than when a single irradiation scan is used. It also helps minimizing the redeposition of debris in the walls of the channel and reduce surface roughness.

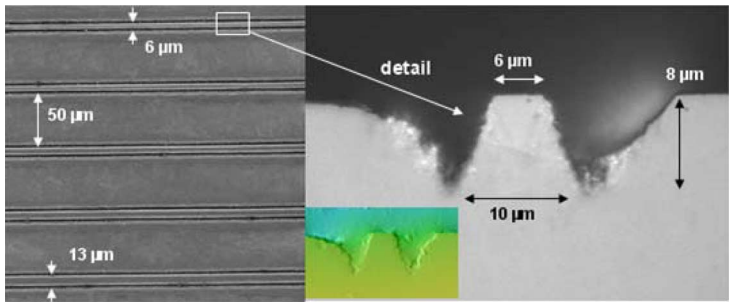

Fig. 2. (Left) General view of the rib waveguides produced obtained with an ESEM. (Right) Cross-sectional view of a rib with 6 μm width at the top and 10 μm at the bottom. The inset shows the same region imaged with an optical confocal microscope.

Our approach uses an SLM to multiplex the irradiation beam at the material surface, creating seven spots. The spots are arranged diagonally (see Fig. 1), such that each spot rewrites the channel written by the previous one, but with a slight lateral displacement just as the approximation scanning does. Thus, a multiplexed beam requires only a single scan to inscribe a channel in the sample, while a nonmultiplexed beam requires several scans. In order to multiplex the beam, the wavefront of the irradiation was tailored using the phase-only SLM in order to obtain a predesigned intensity distribution at the focus of the lens. The corresponding phase map is shown in Fig. 1. It was generated using a weighted Gerchberg–Saxton algorithm, which helps to equalize the peak intensities of the multiplexed spots in the designed intensity distribution [21].

During the channel structuring process, the value of the local maximum fluence of each multiplexed spot (2.1 μm full-width at half-maximum) at the surface was 4.1 J/cm^2 (per pulse). For the scanning speed used, a multiplexed spot receives in average of 21 pulses. For reference, the single-shot/single-spot ablation threshold of the sample is 1.1 J/cm^2. It is worth noting at this point that the sample shows a negligible linear absorption at the irradiation wavelength, and therefore, surface ablation is the consequence of multiphoton and avalanche ionization processes associated to the high peak power of fs-laser pulses [22].

III. Rib Waveguide Characterization

A. Environmental Scanning Electron Microscopy and Confocal Morphological Characterization

Fig. 2 shows an environmental scanning electron microscopy (ESEM) image of the ribs made on the planar waveguides, obtained using a Quanta 200 microscope. After polishing the end face of the sample, which is perpendicular to the ribs, images of some channels were obtained both with the ESEM and a confocal microscope, as can be seen in the detail of Fig. 2 (right). These images reveal that, in terms of visual roughness, the rib had a good shape. In this figure, it can be seen that the internal groove wall, that is to say, the rib wall, shows clearly less roughness than the external groove wall. The rms roughness of the rib walls is $\sim$500 nm, an encouraging result if it is taken into account that this value is $\sim$50% of the wavelength of interest (around 1 μm). This confirms that the use of *approximation scanning* combined with the beam multiplexing is beneficial for the performance of the laser written structures.

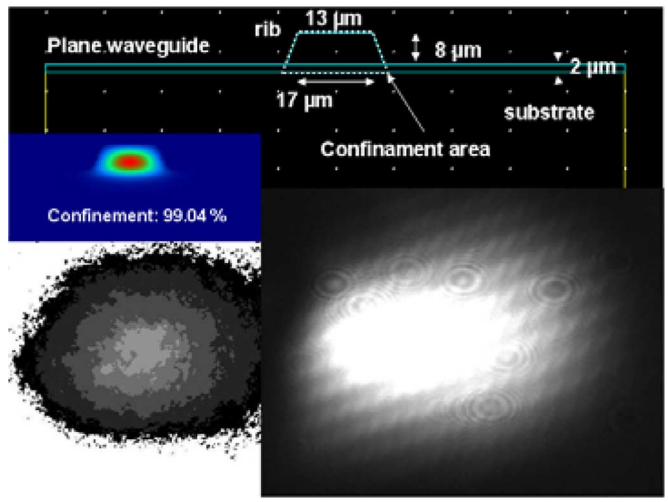

Fig. 3. CCD picture of the near field pattern of the mode obtained at 972 nm and intensity profile. Geometry of the rib used for simulation and confinement obtained by simulation.

Still, the shape of the rib was not rectangular but trapezoidal. The produced grooves were $\sim$8 μm deep. At the top, the dimensions of the channels produced were 6, 7, 8, 9, 13, 14, 15, and 18 μm. The rib walls show a slope $\mathrm{tg}(\alpha) \sim 0.25(\sim 14^\circ)$. This makes, as can be seen in Fig. 2, that the bases of the ribs are about 4 μm wider than their tops while the structures are symmetrical in all the cases. The observed trapezoidal shape does not imply though a big problem in terms of confinement, as shown by the simulations with real parameters.

B. Near-Field Pattern and Propagation Losses

As shown in Fig. 2, the walls of the ribs obtained by fs-laser structuring are not vertical. It was thus advisable to perform a simulation with real parameters. The simulations were carried out with the same software that was used in the preliminary simulation. As above mentioned, the ribs obtained are trapezoidal in shape. They were 6–18 μm at the top, and 10–22 μm at the base and they were all symmetrical. The simulation again reveals a high confinement. The confinement values provided by numerical simulations ranged between 99.75% and 99.80% at 632 nm and between 98.37% and 99.04% at 972 nm. So, theoretically the confinement is high even for the rib with the lowest cross section area.

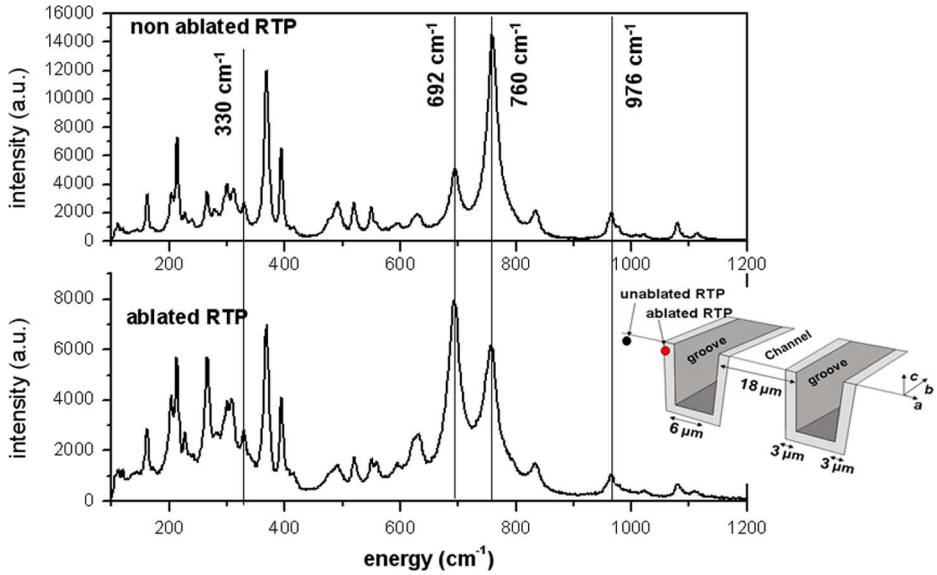

Fig. 4. Raman spectra of the ablated and unablated RTP zones. Inset: scheme of a channel with the indications of the points where the Raman spectra were taken.

The rib waveguide modes were excited at 632 and 972 nm in order to test the performance of the laser-written structures. All the channels were excited successfully but the 13 μm channel (width at the top) was used for characterization. As an example, Fig. 3 shows the near field pattern of this channel at a wavelength of 972 nm. A high optical density filter was used to record the mode's profile with a CCD camera. The propagation losses of the rib waveguide with a top width of the 6 μm were estimated at 972 nm by coupling a laser beam to the waveguide with a 10 $\times$ objective microscope. The fundamental waveguide mode was excited using an *xyz* translation stage in order to prevent the multi modal dispersion. The light transmitted by the waveguide was then collected using a 50$\times$ objective microscope. The power of the laser beam was measured before the input objective microscope and after the output one. The optical losses of these rib waveguides were evaluated by single pass transmission measurements. The expression used in dB/cm was $\text{Loss} = (10/d)\log(P_{\text{out}}/P_{\text{in}})$, where d is the length of the channel waveguides. Some corrections had to be made to both powers (P_{out} and P_{in}). The estimation of the propagation losses has to consider though some corrections to the values of P_{out} and P_{in} like the transmission losses of the microscope objectives, the Fresnel losses at the waveguide interfaces, the losses associated to the mismatch between the laser field distribution at the focal plane of the lens and the mode of the waveguide (calculated through the corresponding overlapping integral [23]). Since we have not corrected the losses associated to the effect of the different numerical apertures of the waveguide and the input microscope objective and the losses associated to the absorption of the beam by the small amount of Yb present in the waveguide, the estimated value of the propagation loss have to be considered as an exaggerated upper bound. The upper limit obtained is 4.4 dB/cm which compares well with recent values obtained by fs-laser structuring of Nd:GGG [24]. In this respect, it is worth noting that BPM simulations of the propagation loss of this waveguide using a roughness with a rms value of 500 nm provide values in the order of 7 dB/cm which indicate that the "visual" estimation of roughness above indicated should be overestimated. The roughness was modeled via a seventh order autoregressive estimator calculated using the measured roughness function $f(z)$. In our case, this function indicates that the underlying statistics are exponential and the corresponding autocorrelation function gives a standard deviation of $\sigma = 0.21$ μm and a correlation length of $Lc = 0.78$ μm.

C. Micro-Raman Scattering

One of the techniques used to investigate the induced microscale modifications in the crystalline material is micro-Raman (μ-Raman) measurement [25]. Micro-Raman scattering measurements were made using a micro-Raman Reinshaw Confocal InVia spectrometer equipped with a Leica 2500 confocal microscope and a CCD camera as the detector. With this equipment, 64 consecutive Raman spectra were recorded on the surface of the sample, at 1 μm intervals. The excitation wavelength for these measurements was 514 nm. The Raman signal was collected using a pinhole and focusing every time on the desired region.

As can be seen in Fig. 4, the Raman spectrum for these materials is very complex: it has more than 30 peaks corresponding to A_1, A_2, B_1, and B_2 symmetry representations [25]. We observed that all the peaks in the unablated area are also present in the ablated area, indicating that femtosecond irradiation does not induce amorphisation of (Yb,Nb):RTP, at least in the spatial resolution we used.

In general, we observed that the intensity of the peaks in the ablated area of the sample is less than the intensity of the peaks for the unablated area. The intensity of the Raman peaks is a function of the change in polarization of the molecule during a vibration. Thus, a significant decrease in intensity of the bands indicates a constraint on the vibrational degrees of freedom of the molecule [26]. This constraint on the vibrational degrees of freedom of the molecule is due to the introduction of defects and changes in the crystallographic structure of the material.

Basically, the Raman spectra recorded correspond to those of RTP in a $z(yy)\bar{z}$ polarization configuration [27]. However, we observed significant differences in the intensity of the peaks located at $\sim$692 and $\sim$760 cm^{-1} for the spectra recorded in the ablated and unablated areas, respectively. While the first peak increases its intensity considerably in the ablated zone, the intensity of the peak at 760 cm^{-1} decreases considerably in the same zone. The $\sim$760 cm^{-1} signal corresponds to the ν_2 vibration mode of the TiO_6 octahedron, and it is the most intense peak for the polarized $z(yy)\bar{z}$ Raman spectrum of RTP. The $\sim$692 cm^{-1} signal is also related to the ν_2 vibration mode of the TiO_6 octahedron in the same polarized configuration, but its intensity is considerably lower than the one at 760 cm^{-1}. However, it may also be related to ν_1 and ν_3 vibration modes of the TiO_6 octahedron in the $x(yz)\bar{x}$, $y(xx)\bar{y}$, and $y(zz)\bar{y}$ polarization configurations, where it corresponds to the most intense peak of these spectra. Thus, the difference in intensity of these peaks in the ablated region spectrum compared with the nonablated region spectrum might be due to some orientational changes in the crystal structure in the areas in the proximity of the ablated region, which leads to a mixture of Raman spectra corresponding to different scattering geometries [28]. Thus, ultrafast laser ablation clearly induces a permanent local micrometric stress in (Yb,Nb):RTP, as has been reported for such others materials as Nd:MgO:$LiNbO_3$ [28] or Si wafers [29]. This permanent induced stress may be due to the shock waves produced after the absorption of the femtosecond pulse.

Apart from the different intensity observed for these two peaks in the ablated and unablated regions, which is the most evident change in the Raman spectra, the intensity of other peaks also changes. For instance, the intensity of the peak at 976 cm^{-1} is also reduced in the ablated areas. This peak corresponds to the ν_1 vibration of PO_4 tetrahedra [27] indicating that not only are modes related to the TiO_6 group affected by the constraint on their vibrational degrees of freedom, but modes related to PO_4 tetrahedra also are. In fact, the peaks related to Rb-O polar vibration [27] appearing at around 330 cm^{-1} are also affected by the decrease in intensity depending on the polarization analyzed in the spectra, indicating that the whole structure of (Yb,Nb):RTP crystal is affected by the permanent induced stress generated by ultrafast laser ablation.

By comparing the Raman scattering spectra recorded in an area far from the microstructured channel with spectra recorded from ablated grooves and close boundaries, we obtained some information about the dimensions of the affected area during the ablation process. In fact, we found that after ablation, the stressed area up to the groove wall was 3 μm long, as the inset of Fig. 4 shows.

Regarding the depth of the laser affected region, it is worth noting that given the laser repetition rate used for structuring, and the thermal properties of the material ($D = 0.015$ cm^2·s^{-1}), no heat accumulation effects are expected for consecutive pulses [30] during the structuring process. A crude estimation of the heat diffusion length ($L = 2\sqrt{Dt}$) during the absorption of a single pulse leads to a value of $\sim$0.8 nm, much shorter than thickness of the stressed regions. Still, even when a large proportion of the energy of the incoming pulses is expected to be carried with the ablating plasma [31], the material remaining underneath the ablating region is heated by the plasma over much longer time scales and may eventually melt. Ben-Yakar *et al.* [32] provide an expression to estimate the maximum expected thickness of the induced molten using the threshold fluence for ablation and different thermo-optical parameters of the material. Such an estimate leads in our case to a value of $\sim$420 nm for the initial molten layer and a maximum propagated molten layer depth always below than 1 μm. The extension of the stressed region (also not amorphized) seems to be thus more related to the effect of the produced shock waves than to the plasma induced heating of the layer underneath the ablating region.

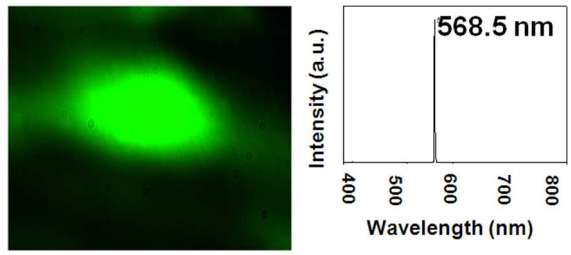

Fig. 5. CCD image of 568.5 nm green light from type II SHG of 1137 nm IR light and the spectra recorded at the end of waveguide.

D. Second Harmonic Generation

A tunable OPO was used to generate radiation with the wavelength required to obtain efficient SHG. The maximum SHG efficiency was obtained pumping with a fundamental beam of 1137 nm of wavelength. The modes excited to produce the green light correspond to a channel waveguide parallel to the $\boldsymbol{a}$ crystallographic direction. They were excited using a microscope objective with the same guiding setup indicated above; an achromatic half-wave plate was placed between the laser source and the sample in order to ensure type II SHG. In fact, the green light generation by type II regime requires guided photons with perpendicular polarizations simultaneously. The guided green light obtained by SHG was recorded with a CCD camera and can be seen in Fig. 5 together with the spectra recorded at the end of the waveguide.

IV. Conclusion

We have produced by fs-laser structuring rib waveguides in (Yb,Nb):RTP/RTP active layers using a combination of approximation scanning and beam multiplexing. The sides of the rib waveguides show a roughness of the order of 500 nm, leading to propagation losses with an upper bound of $\sim$4 dB/cm. This value is lower or comparable to propagation losses before reported with fs-laser structuring in other studies. The approximation used (approximation scanning plus beam multiplexing) has the additional advantage of allowing to produce structures with easily controllable shape in a single scan by controlling the transverse separation of the writing laser spots in the surface.

Taking into account the refractive indexes of the epitaxy and the substrate, as well as the designed geometries, a previous simulation revealed that the confinement can be high. After fs-laser ablation, the simulation with real geometry parameters revealed

that high confinements were still obtained. The near-field pattern of the fundamental mode was observed at 632 and 972 nm, which showed that the guiding was of good quality. Raman spectroscopy reveal some damage to the crystalline structure boundaries in the rib waveguides. This damage was most probably produced by the fs-laser pulses. It is though remarkable that amorphization is not observed. The Raman study showed that the damage boundary region was around 3 μm in length, which is shorter than the total width of the ribs. However, this boundary damage could increase the confinement by increasing the refractive indexes in this zone.

REFERENCES

[1] P. A. Thomas, S. C. Mayo, and B. E. Watts, "Crystal structures of $RbTiOAsO_4$, $KTiO(P_{0.58},As_{0.42})O_4$, $RbTiOPO_4$ and $(Rb_{0.465},K_{0.535})TiOPO_4$, and analysis of pseudosymmetry in crystals of the $KTiOPO_4$ family," *Acta Crystallogr., Sect. B: Struct. Sci.*, vol. B48, pp. 401–407, 1992.

[2] Y. Guillen, B. Ménaert, J. P. Fève, P. Segonds, J. Douady, B. Boulanger, and O. Pacaud, "Crystal growth and refined Sellmeier equations over the complete transparency range of $RbTiOPO_4$," *Opt. Mater.*, vol. 22, pp. 155–162, 2003.

[3] M. N. Satyanarayan, A. Deepthy, and H. L. Bhat, "Potassium titanyl phosphate and its isomorphs: Growth, properties, and application," *Crit. Rev. Solid State Mater. Sci.*, vol. 24, no. 2, pp. 103–191, 1999.

[4] R. Solé, V. Nikolov, I. Koseva, P. Peshev, X. Ruiz, C. Zaldo, M. J. Martín, M. Aguiló, and F. Díaz, "Conditions and possibilities for rare-earth doping of $KTiOPO_4$ flux-grown single crystals," *Chem. Mater.*, vol. 9, pp. 2745–2749, 1997.

[5] A. Peña, J. J. Carvajal, J. Massons, J. Gavaldà, F. Díaz, and M. Aguiló, "Yb:Ta:$RbTiOPO_4$, a new strategy to further increase the lanthanide concentration in crystals of the $KTiOPO_4$ family," *Chem. Mater.*, vol. 19, pp. 4069–4076, 2007.

[6] X. Mateos, V. Petrov, A. Peña, J. J. Carvajal, M. Aguiló, F. Díaz, P. Segonds, and B. Boulanger, "Laser operation of Yb^{3+} in the acentric $RbTiOPO_4$ codoped with Nb^{5+}," *Opt. Express*, vol. 32, pp. 1929–1931, 2007.

[7] J. J. Carvajal, R. Solé, J. Gavaldà, J. Massons, M. Aguiló, and F. Díaz, "Crystal growth of $RbTiOPO_4$:Nb: A new nonlinear optical host for rare earth doping," *Cryst. Growth Des.*, vol. 1, no. 6, pp. 479–484, 2001.

[8] X. Mateos, V. Petrov, A. Peña, J. J. Carvajal, M. Aguiló, F. Díaz, P. Seconds, and B. Boulanger, "Laser operation of Yb^{3+} in the acentric $RbTiOPO_4$ codoped with Nb^{5+}," *Opt. Lett.*, vol. 32, no. 13, pp. 1929–1931, 2007.

[9] J. Cugat, R. Solé, M. C. Pujol, J. J. Carvajal, X. Mateos, F. Díaz, and M. Aguiló, "Waveguiding demonstration on Yb:Nb:$RbTiOPO_4$/$RbTiOPO_4$ (001) epitaxies grown by LPE," *Opt. Mater.*,, vol. 32, pp. 1648–1651, 2010.

[10] J. Cugat, R. Solé, J. J. Carvajal, M. C. Pujol, X. Mateos, F. Díaz, and M. Aguiló, "Crystal growth and characterization of $RbTi_{1-x-y}Yb_xNb_yOPO_4$/$RbTiOPO_4$ (001) non-linear optical epitaxial layers," *CrystEngComm.*, vol. 13, pp. 2015–2022, 2011.

[11] J. Cugat, R. Solé, J. J. Carvajal, X. Mateos, M. C. Pujol, J. Massons, F. Díaz, and M. Aguiló, "Efficient type II phase-matching second-harmonic generation in Ba:Yb:Nb:$RbTiOPO_4$/$RbTiOPO_4$ waveguides," *Opt. Lett.*, vol. 36, no. 10, pp. 1881–1883, 2011.

[12] L. Zhang, P. J. Chandler, P. D. Townsnd, and P. A. Thomas, "Helium ion-implanted optical waveguide in $KTiOPO_4$," *Electron. Lett.*, vol. 28, pp. 650–652, 1992.

[13] C. Grivas and W. Eason, "Dielectric binary oxide films as waveguide laser media: A review," *J. Phys.: Condens. Matter.*, vol. 20, pp. 264011–264014, 2008.

[14] K. Wang, B. Shi, N. Cue, Y. Zhu, R. Xiao, F. Lu, W. Li, and Y. Liu, "Waveguide laser film in erbium-doped $KTiOPO_4$ by pulsed laser deposition," *Appl. Phys. Lett.*, vol. 73, no. 8, pp. 1020–1022, 1998.

[15] W. Bolaños, J. J. Carvajal, X. Mateos, G. S. Murugan, A. Z. Subramanian, J. S. Wilkinson, E. Cantelar, D. Jaque, G. Lifante, M. Aguiló, and F. Díaz, "Mirrorless buried waveguide laser in monoclinic double tungstates fabricated by a novel combination of ion milling and liquid phase epitaxy," *Opt. Express*, vol. 18, pp. 26937–26945, 2010.

[16] F. Laurell, J. Webjörn, G. Arvidsson, and J. Holmberg, "Wet etching of proton-exchanged lithium niobate a novel processing technique," *J. Lightw. Technol.*, vol. 10, no. 11, pp. 1606–1609, 1992.

[17] J. Gottmann, D. Wortmann, I. Vasilief, L. Moiseev, and D. Ganser, "Manufacturing of Nd:$Gd_3Ga_5O_{12}$ ridge waveguide lasers by pulsed laser deposition and ultrafast laser micromachining," *Appl. Surf. Sci.*, vol. 254, pp. 1105–1110, 2007.

[18] R. Solé, V. Nikolov, A. Vilalta, J. J. Carvajal, J. Massons, J. Gavaldà, M. Aguiló, and F. Díaz, "Liquid phase epitaxy of $KTiOPO_4$ on $KTi_{1-x}Ge_xOPO_4$ substrates," *J. Cryst. Growth*, vol. 237, pp. 602–607, 2002.

[19] A. Aznar, O. Silvestre, M. C. Pujol, R. Solé, M. Aguiló, and F. Díaz, "Liquid-phase epitaxy crystal growth of monoclinic $KLu_{1-x}Yb_x(WO_4)_2$/$KLu(WO_4)_2$ layers," *Cryst. Growth Des.*, vol. 6, pp. 1781–1787, 2008.

[20] J. Gottmann, G. Schlaghecken, R. Wagner, and E. W. Kreutz, "Fabrication of erbium-doped planar waveguides by pulsed-laser deposition and laser micromachining," in *Conf. Laser Micromachin. Optoelectron. Device Fabricat. Proc SPIE 4941*, 2003, pp. 148–156, Edited by Ostendorf.

[21] R. D. Leonardo, F. Ianni, and G. Ruocco, "Computer generation of optimal holograms for optical trap arrays," *Opt. Express*, vol. 15, no. 4, pp. 1913–1922, 2007.

[22] B. C. Stuart, M. D. Feit, S. Herman, A. Rubenchik, B. Shore, and M. Perry, "Nanosecond-to-femtosecond laser-induced breakdown in dielectrics," *Phys. Rev.*, vol. B53, pp. 1749–1761, 1996.

[23] A. K. Mairaj, P. Hua, H. N. Rutt, and D. W. Hewak, "Fabrication and characterization of continuous wave direct UV ($\lambda = 244$ nm) written channel waveguides in chalcogenide (Ga:La:S) glass," *J. Light. Tech.*, vol. 20, pp. 1578–1584, 2002.

[24] Y. Jia, N. Dong, F. Chen, J. R. V. D. Aldana, and S. Zhou, "Ridge waveguide lasers in Nd:GGG crystals produced by swift carbon ion irradiation and femptosecond laser ablation," *Opt. Exp.*, vol. 20, pp. 9763–9768, 2012.

[25] G. E. Kugel, F. Bréhat, B. Wyncke, M. D. Fontana, G. Marnier, C. Carabatos-Nedelec, and J. Mangin, "The vibrational spectrum of a $KTiOPO_4$ single crystals studied by Raman and infrared reflectivity spectroscopy," *J. Phys. C: Solid State Phys.*, vol. 21, pp. 5565–5568, 1988.

[26] C. D. Deshpande, A. P. Malshe, E. A. Stach, V. Radmilovic, D. Alexander, D. Doerr, and D. Hirt, "Investigation of femtosecond laser assisted nano and microscale modifications in lithium niobate," *J. Appl. Phys.*, vol. 97, pp. 74316–74325, 2005.

[27] J. J. Carvajal, P. Segonds, A. Peña, J. Zaccaro, B. Boulanger, F. Díaz, and M. Aguiló, "Structural and optical properties of $RbTiOPO_4$:Nb crystals," *J. Phys.: Condens. Matter.*, vol. 19, pp. 116214–116317, 2007.

[28] A. Rodenas, J. A. Sanz García, D. Jaque, G. A. Torchia, C. Mendez, I. Arias, L. Roso, and F. Agulló-Rueda, "Optical investigation of femptosecond laser induced microstress in neodynium doped lithium niobate crystals," *J. Appl. Phys.*, vol. 100, pp. 033521–033529, 2006.

[29] M. S. Amer, M. A. El-Ashry, L. R. Dosser, K. E. Hix, J. F. Maguire, and B. Irwin, "Femptosecond versus nanosecond laser machining: Comparison of induced stresses and structural changes in silicon wafers," *Appl. Surf. Sci.*, vol. 162, pp. 162–167, 2005.

[30] S. M. Eaton, H. Zhang, P. R. Herman, F. Yoshino, L. Shah, J. Bovatsek, and A. Arai, "Heat accumulation effects in femtosecond laser-written waveguides with variable repetition rate," *Opt. Express*, vol. 13, pp. 4708–16, 2005.

[31] T. Y. Choi and C. P. Grigoropoulos, "Plasma and ablation dynamics in ultrafast laser processing of crystalline silicon," *J. Appl. Phys.*, vol. 92, pp. 4918–4925, 2002.

[32] A. Ben-Yakar, A. Harkin, J. Ashmore, R. L. Byer, and H. A. Stone, "Thermal and fluid processes of a thin melt zone during femtosecond laser ablation of glass: the formation of rims by single laser pulses," *J. Phys. D: Appl. Phys.*, vol. 40, pp. 1447–1459, 2007.

Author biographies not included by author request due to space constraints.

Paper VII

J. Cugat, A. Choudhary, R. Solé, J.J. Carvajal, J. Massons, D.P. Shepherd, F. Díaz, M. Aguiló,

Ar^+ ion milling rib waveguides on nonlinear optical (Yb,Nb):RTP/RTP epitaxial layers

Applied Materials & Interfaces, (to be submitted).

Ar^+ ion milling rib waveguides on nonlinear optical (Yb,Nb):RTP/RTP epitaxial layers

Jaume Cugat[1], Amol Choudhary[2], Rosa Maria Solé[1]*, Joan J. Carvajal[1], Jaume Massons[1], David P. Shepherd[2], Francesc Díaz[1] and Magdalena Aguiló[1]

[1] Física i Cristal·lografia de Materials i Nanomaterials (FiCMA-FiCNA) and EMaS, Universitat Rovira i Virgili (URV), Marcel·lí Domingo s/n, Tarragona E-43007, Spain

[2]Optoelectronics Research Centre (ORC), University of Southampton, Southampton SO171BJ, UK

**Corresponding author:* E-mail: rosam.sole@urv.cat

Abstract. In this paper we present the fabrication and characterization of rib waveguides made on (Yb,Nb):$RbTiOPO_4$/$RbTiOPO_4$ epitaxial layers. Liquid phase epitaxy (LPE) technique was used to grow planar thin films followed by Ar^+ ion milling for surface rib fabrication. Here, we report the detailed fabrication procedure and characterization of the ribs. The study reveals good confinement and that type II second harmonic generation inside the rib was obtained, showing the generation of green light at 570 nm.

1. INTRODUCTION

The $RbTiOPO_4$ (RTP) is a nonlinear optical crystal that belongs to the $KTiOPO_4$ (KTP) family and crystallizes in the orthorhombic space group $Pna2_1$ [1)]. The crystals of this family have been extensively used for frequency doubling infra-red (IR) laser radiation close to 1 μm, such as Yb^{3+} and Nd^{3+} laser emissions [2, 3)]. RTP has similar nonlinear optical coefficients to KTP [4)], but unlike KTP, it can be doped with Yb^{3+} ions to high enough concentration to allow efficient laser action [5-7)]. Therefore, by combining the emission of Yb^{3+} with the nonlinear optical properties of the crystal, it is possible to obtain a self-frequency doubling material. RTP has other interesting properties, such as a high laser damage threshold, about 2 times larger than that of KTP [8,9)], large electro-optical coefficients, low dielectric constants [10)], high chemical stability and low photorefractive damage susceptibility [11)]. Owing to all these interesting properties, RTP is a promising candidate as a platform material for integrated photonics.

Yb^{3+} has many advantages in comparison to other rare-earth ions. Its ionic radius is much closer to the radius of Ti^{4+} than the radius of other Ln^{3+} ions, which may be the cause of the higher distribution coefficient of Yb^{3+} in relation to other Ln^{3+} ions in the crystals of the KTP family [5)]. Moreover, the Yb^{3+} ion has a simpler energy scheme than Nd^{3+} with a similar

emission range in the IR region. The Yb^{3+} energy scheme consists of only two energy levels: the ground state $^2F_{7/2}$ and the exited state $^2F_{5/2}$. This is important since it avoids many effects which can lead to a reduction of the laser efficiency, such as excited-state absorption, cross-relaxation and up-conversion. The quantum defect, which leads to the thermal loading of the crystal during the laser operation, is very small in Yb^{3+} due to the similarity between the pumping and the laser wavelengths [12]. Moreover, the Yb^{3+} ion has no absorption losses at the second-harmonic generation frequency [7], which makes it interesting for self-frequency doubling.

Previously, (Yb,Nb):RTP planar waveguides were successfully fabricated on RTP substrates by the liquid phase epitaxy (LPE) method [13], and efficient type II second harmonic generation (SHG) was obtained [14]. In this paper, we have used Ar^+ ion milling [15] to microstructure the surface of the epitaxial layers and obtain rib waveguides.

2. EXPERIMENTAL SECTION

In order to know the suitable width and depth of the channels, we have carried out a computer simulation, using the Multy Grid Finite Difference (Real) method at 972 nm, with commercially available software (OlympIOs). This wavelength is considered better than others because, in previous works, it was used to pump (Yb,Nb):RTP to receive laser action [7]. The refractive indices of the epitaxial layer and the substrate used in the simulation were measured experimentally using the dark modes method and the light was coupled to the sample with a prism (Metricon prism coupler equipment) with a Ti:sapphire laser as a source at 972 nm. Table I shows the refractive index values obtained. In this work, only TM values were used corresponding to the n_z polarization. We simulated the ribs produced on a hypothetical planar waveguide with a thickness of 5 μm. The ribs were 3, 5 and 10 μm in width and 3 μm in depth. The confinement factor of the ribs, defined as the fraction of the mode intensity within the cross section of the rib area, was 40.0 % for ribs of 3 μm in width, 83.3 % for ribs of 5 μm in width, and finally 92.9 % for ribs of 10 μm in width.

With aim to obtain planar waveguides with a thickness of 5 μm, we grew epitaxial layers of (Yb,Nb):RTP on (001) oriented RTP substrates. The planar substrates, which were 1.5-mm-thick, with faces perpendicular to the ***c*** crystallographic direction, were cut from bulk RTP single crystals. The ***a-b*** plane is interesting because it contains the non-critical phase matching (PM) type II SHG directions for the range of 985 to 1118 nm, moreover the Yb^{+3} laser emission at 1060 nm is in this range. To grow the epitaxial layers we used the LPE method from WO_3-containing solutions. Rb_2CO_3 (99%), $NH_4H_2PO_4$ (99%), TiO_2 (99.9%), Yb_2O_3

(99.9%), Nb_2O_5 (99.9%) and WO_3 (99.9%) were used as starting chemicals. The fabrication procedure has been previously reported [16-18]. The solution composition was Rb_2O-P_2O_5-TiO_2-Yb_2O_3-Nb_2O_5-WO_3 = 43.9-23.6-20.7-1.35-0.45-10 (mol %). The saturation temperature of the solution was around 1153 K, and the growth process started by producing supersaturation by cooling the solution 2 K below the saturation temperature. During the growth process a rotation of 60 rpm was applied. The chemical composition of the epitaxial layers was determined by electron probe microanalysis (EPMA) with a final result of $RbTi_{0.958}Yb_{0.016}Nb_{0.026}OPO_4$. The thickness of the as-grown epitaxial layers, measured by an interferometric microscope was around 50 µm.

The epitaxial layer was reduced to a layer of 5 µm in thickness and polished, since with this dimensions and according with the previous simulations, a 5 µm thickness planar waveguide can support a few propagation modes.

The substrate was included in glue on a glass slide in order to remove any edge effects for the following photolithographic process. A 4-µm-thick layer of S1828 resist was spin-coated onto the sample before masking and development. A dark field mask was used with waveguide widths from 2 µm to 10 µm, with a separation of 100 µm between them. The dark field mask channels were carefully aligned along the ***a*** crystallographic direction of the substrate in order to produce ribs on it parallel to this direction. As can be seen in table I, the refractive index contrast between the doped layer and the undoped substrate is positive for the ***b*** and ***c*** polarizations and negative for the ***a*** polarization. Thus, guiding is possible in TM and TE regimes along ***a*** direction, but only in TM along ***b*** direction. The etching process was carried out in an Oxford Plasma Technology Ionfab 300 Plus system. The masked sample was held at 45º and rotated at 5 rpm during the process. An Ar^+ ion beam was accelerated at 500 V with a beam current of 100 mA. This beam etched the sample for 2 hours and 20 minutes to etch 3-µm-high ribs in the film. The resist was then removed by acetone and plasma ashing. Figure 1 shows a schematic view of the complete process of rib waveguide fabrication.

3. RESULTS AND DISCUSSION

A Sensofar PLµ 2300 optical confocal microscope was used to check the quality of the ribs. With this microscope we measured the top widths of the ribs and found them to range from 3 µm to 10 µm, in agreement with the values of the mask used. The profile of the ribs was studied using a non-contact profiler (Zescope by Zemetrics). Figure 2 shows a 3D image of a rib waveguide, demonstrating the good quality of the side-walls.

The rms roughness was measured to be 50 nm on the top and the wall of the side-walls of the ribs. The depth milled was 2.9 μm as can be seen from the inset of Figure 2. It is important to note that the shape of the rib is not rectangular (see Figure 2), but is trapezoidal. This fact is important since it affects the waveguide properties. The end-faces of the waveguides were then polished with the sample sandwiched between two glass blocks to protect the edges. After polishing the end faces we were able to measure the width of the rib base and it was found to be 4 μm larger than the width at the top, indicating that the slope of the rib walls was 34 degrees off vertical. Figure 3 is a general view of the ribs in a top view regime using the Environmental Scanning Electron Microscope (ESEM). In a more detailed view, Figure 4 shows a rib of 9 μm in width and the good quality of the rib walls is qualitatively confirmed. The length of ribs after end-faces polishing process was 6 mm.

As the microscopy characterization reveals, the rib walls obtained by Ar^+ ion milling were not vertical. Therefore, a simulation using the real parameters was carried out in order to check the degree of expected optical confinement. The dimensions of the ribs simulated were between 3 and 10 μm at the top and between 7 and 14 μm at the base, all of them with symmetrical trapezoidal shape. The simulation shows values of the confinement factor of 88.5 % and 93.1 % for ribs of 3 μm and 10 μm in width, respectively. So, it reveals a theoretical high confinement, even for the ribs with lower cross section area.

In order to estimate the transmission losses of the channel waveguides, a 10x objective microscope was used to couple the 972 nm laser beam into the rib waveguide. Using a x-y-z translation stage, the fundamental mode was excited. It is important to obtain the best coupling between the laser pump and the waveguide mode and to excite the fundamental mode instead of high order modes in order to avoid multimodal excitation. Finally a 50x microscope objective was used to collect the transmitted light. To estimate the transmission losses, the beam power was measured before the input microscope objective, as well as, after the output microscope objective. The expression applied to estimate the transmission losses was the corresponding to the single pass transmission method, $Loss=(-10/d)*\log(P_{out}/P_{in})$, where P_{out} is the power at the end of the channel waveguide, P_{in} is the power launched into the channel waveguide and *d* is the waveguide length. Fresnel losses, the transmission of the microscope objectives, the Yb^{3+} absorption and the launch efficiency were taken into account in order to calculate P_{in} and P_{out} from the measured values. By applying these corrections and using the expression mentioned above, we estimated an upper limit of the transmission losses of 3 dB/cm.

The near field pattern was measured in order to understand the energy distribution of the propagation modes for the pump wavelength. The experimental set up was the same as that used for the loss measurement, except that in this case a CCD camera was put behind the output objective microscope to observe the image of the output facet of the rib waveguides. A Ti:Sapphire laser at 972 nm was coupled into the waveguide, and the modes in TM polarization were observed. Figure 5 shows the near field pattern of the rib of 10 μm in top-width. This figure shows the good agreement between the expected profile of the TM fundamental mode of simulation and the real profile, but the camera response is saturated. A high optical density filter was used to record a non-saturated profile of the mode as is shown in the inset of Figure 5. As it was expected, the mode is asymmetric, with near-Gaussian profiles with $1/e^2$ beam radii of ~8.5 μm and ~3.5 μm in the ***b*** and ***c*** directions respectively.

The Second Harmonic Generation (SHG) inside the rib waveguide was checked using a pulsed laser from an optical parametric oscillator (OPO) (Vibrant HE 355 II + UV model from Opotech company) coupled to the rib waveguides by a microscope objective. The OPO was tuned to obtain maximum efficiency of SHG for propagation along the ***a*** crystallographic direction. An achromatic half-wave plate was placed between the laser source and the sample at an angle of 22.5º to ensure in this way that the TM and TE modes were excited simultaneously, which is required for type II SHG. The guided green light, obtained exclusively inside the channels, was collected with a CCD camera and it is showed in Figure 6. This figure shows the 570 nm green light obtained from type II SHG in a rib of 10 μm top-width. The fundamental wavelength was 1140 nm. In order to check that the 570 nm light was coming exclusively from the rib waveguide we focused the OPO beam through the substrate, obtaining non guided light, and then we tuned the laser obtaining a maximum of frequency conversion at 1137 nm. Note that this value is different than that obtained inside the rib, which is logical taking into account that the effective refractive indices of the rib are different than the refractive indices of the bulk, and in addition the chemical composition of the bulk and the epitaxy are different.

4. CONCLUSIONS

We can conclude that we have reported for the first time microstructured rib waveguides on (Yb,Nb):RTP/RTP active planar waveguides. An initial simulation revealed that rectangular ribs with 10 μm width have optical confinement as high as 92.9 %. Experimentally, after microstructuring planar waveguides, we found that the shape of the ribs was trapezoidal, and the simulations with real parameters showed confinements of 93.1 % for ribs with a 10 μm

top-width. A single pass transmission measurement was used to estimate the losses of the rib waveguides, showing losses of 3 dB/cm. Type II second harmonic generation was demonstrated by exciting both, TE and TM modes simultaneously at a wavelength of 1140 nm, obtaining 570 nm green light.

ACKNOWLEDGMENTS

This work was supported by the Spanish Government under projects TEC2010-21574-C02-02, MAT2011-29255-C02-02, and the Catalan Authority under project 2009SGR235. This work has been partially funded by the European Commission under the Seventh Framework Programme, under project Cleanspace, FP7-SPACE-2010-1–GA-263044. This work was also supported by the U.K. EPSRC under project EP/H035745/1. J. Cugat thanks the Spanish Government for the FPI fellowship BES-2009-024190. A.Choudhary acknowledges N.Sessions and D.Sager for technical support in the ORC cleanrooms.

REFERENCES

[1] P.A. Thomas, S.C. Mayo, B.E. Watts, Acta Crystallogr. Sect. B: Struct. Sci. **48** (1992) 401.

[2] R.F. Belt, G. Gashurov, Y.S. Liu, Laser Focus **21** (1985) 110.

[3] C. Bibeau, R.J. Beach, S.C. Mitchell, M.A. Emanuel, J. Skidmore, C.A. Ebbers, S.B. Sutton, K.S. Jancaitis, IEEE J. Quantum Electron. **34** (1998) 2010.

[4] C. Zumsteg, J.D. Bierlein, T.E. Gier, J. Appl. Phys. **47** (1976) 4980.

[5] R. Solé, V. Nikolov, I. Koseva, P. Peshev, X. Ruiz, C. Zaldo, M.J. Martín, M. Aguiló, F. Díaz, Chem. Mater. **9** (1997) 2745.

[6] J.J. Carvajal, R. Solé, Jna. Gavaldà, J. Massons, M. Aguiló, F. Díaz, Cryst. Growth & Des. **1** (2001) 479.

[7] X. Mateos, V. Petrov, A. Peña, J.J. Carvajal, M. Aguiló, F. Díaz, P. Segonds, B. Boulanger, Opt. Lett. **32** (2007) 1929.

[8] Y.S. Oseledchik, A.I. Pisarevsky, A.L. Prosvirnin, V.V. Starshenko, N.V. Svitanko, Opt. Mater. **3** (1994) 237.

[9] Y. Guillen, B. Ménaert, J.P. Feve, P. Segonds, J. Douady, B. Boulanger, O.Pacaud, Opt. Mater. **22** (2003) 155.

[10] M.N. Satyanarayan, A. Deepthy, H.L. Bhat, Critical Reviews in Solid State and Material Science **24** (1999) 103.

[11] T. Suhara; M. Fujimura, Waveguide Nonlinear-Optic Devices (Springer, 2003).

[12] A. Peña, J.J. Carvajal, J. Massons, Jna. Gavaldà. F. Díaz, M. Aguiló, Chem. Mater. **19** (2007) 4069.

[13] J. Cugat, R. Solé, J.J. Carvajal, M.C. Pujol, X. Mateos, F. Díaz, M. Aguiló, CrystEngComm. **13** (2011) 2015.

[14] J. Cugat, R. Solé. J.J: Carvajal, X. Mateos, M.C. Pujol, J. Massons, F. Díaz, M. Aguiló, Opt. Lett. **36** (2011) 1881.

[15] W. Bolaños, J.J. Carvajal, X. Mateos, G. S. Murugan, A.Z. Subramanian, J.S. Wilkinson, E. Cantelar, D. Jaque, G. Lifante, M. Aguiló, F. Díaz, Opt. Express **18** (2010) 26937.

[16] R. Solé, V. Nikolov, A. Vilalta, J.J. Carvajal, J. Massons, Jna. Gavaldà, M. Aguiló, F. Díaz, J. Cryst. Growth **237** (2002) 602.

[17] A. Aznar, O. Silvestre, M.C. Pujol, R. Solé, M. Aguiló, F. Díaz, Cryst. Growth & Des. **6** (2008) 1781.

[18] W. Bolaños, J.J. Carvajal, M.C. Pujol, X. Mateos, G. Lifante, M. Aguiló, F. Díaz, Cryst. Growth & Des. **9** (2009) 3525.

FIGURE CAPTIONS

Figure 1. Schematic diagram of the surface rib waveguide fabrication.

Figure 2. 3D image taken by a non-contact profiler of a rib waveguide with a nominal width of 10 μm and its profile in inset.

Figure 3. General top view of the rib waveguides by Environmental Scanning Electron Microscope (ESEM).

Figure 4. Detailed view of the 9 μm nominal width rib waveguide by ESEM, with cross section view in inset.

Figure 5. Near Field Pattern (NFP) of the fundamental mode at 972 nm of the 10 μm top width rib with the respective simulation. As well as the distribution of energy.

Figure 6. CCD image of 570 nm green light from type II SHG of 1140 nm IR light, parallel to the ***a*** crystallographic direction.

Table:

Table I. Refractive index values at a wavelength of 972 nm and contrast of refractive indices between film and substrate.

	n_x (E//***a***)	n_y(E//***b***)	n_z (E//***c***)
substrate	1.7675	1.7774	1.8573
film	1.7649	1.7778	1.8631
$\Delta n(n_{film}-n_{sub})$	-0.0026	0.0004	0.0058

Figures:

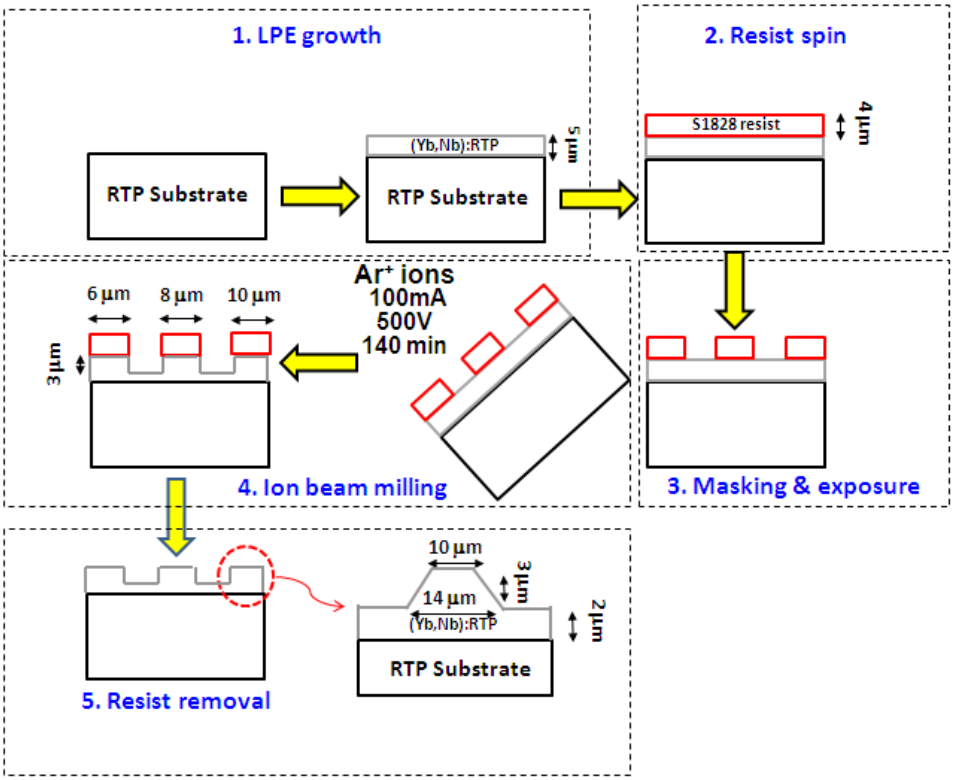

Figure 1

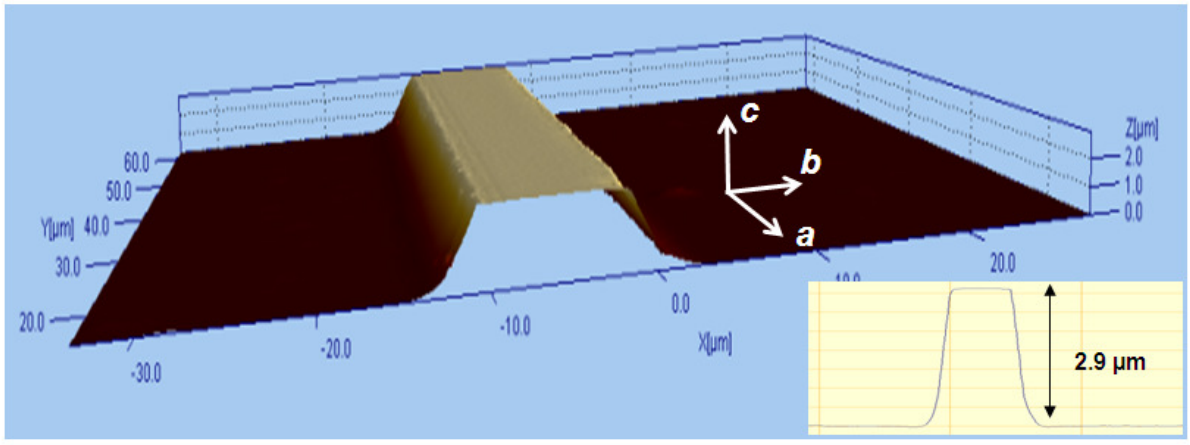

Figure 2

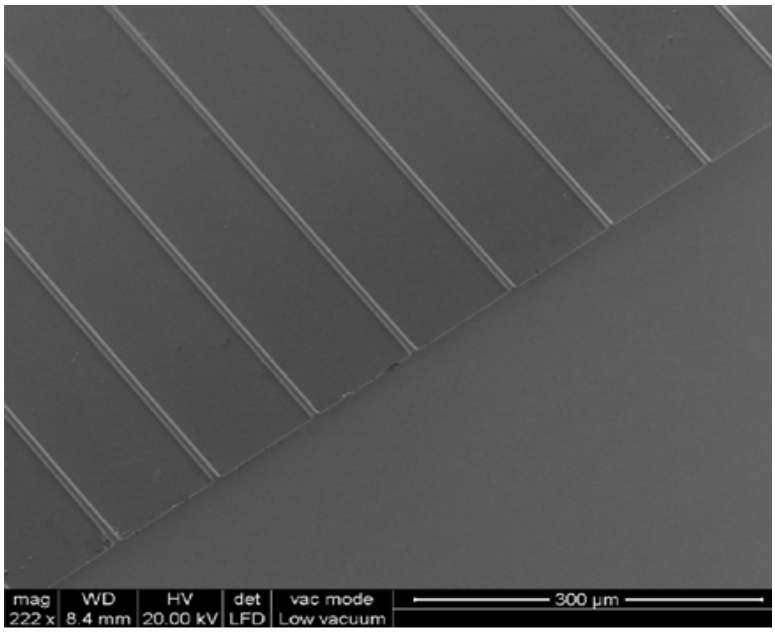

Figure 3

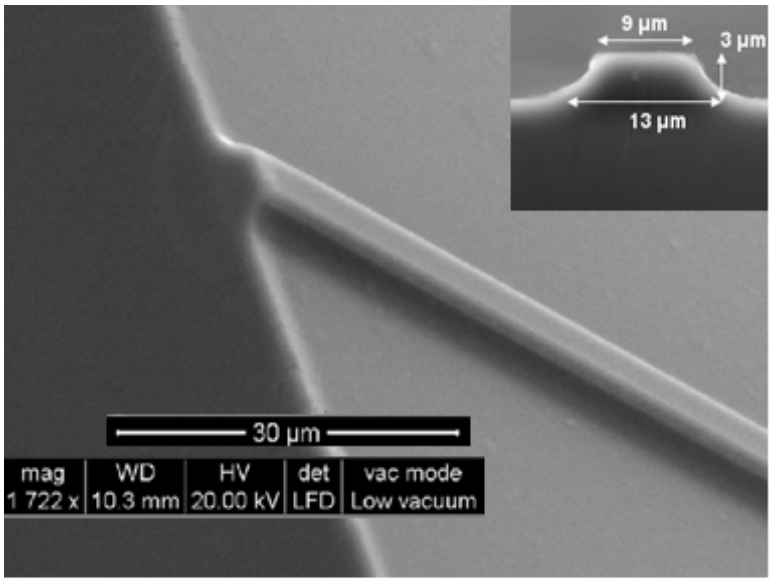

Figure 4

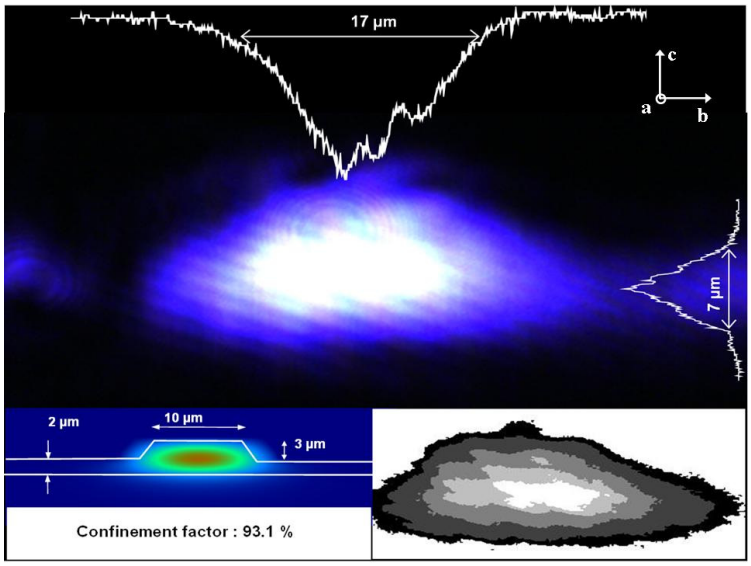

Figure 5

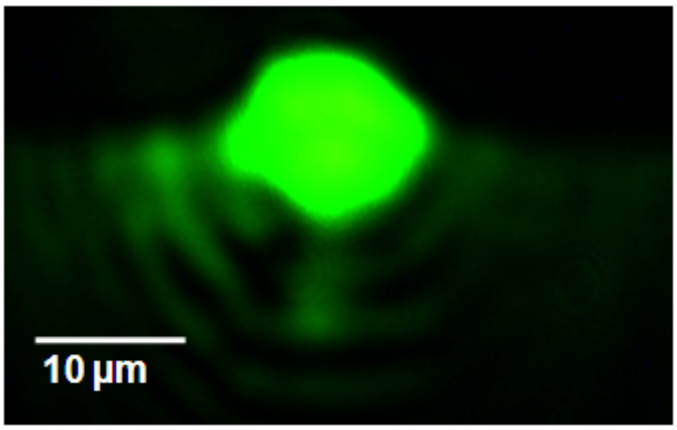

Figure 6

Paper VIII

A. Choudhary, J. Cugat, K. Pradeesh, R. Solé, F. Díaz, M. Aguiló, H.M.H. Chong, D.P. Shepherd,

Single-mode rib waveguides in (Yb, Nb):$RbTiOPO_4$ by reactive ion etching

Journal of Physics D: Applied Physics, **46**, 145108 (2013).

IOP PUBLISHING JOURNAL OF PHYSICS D: APPLIED PHYSICS

J. Phys. D: Appl. Phys. **46** (2013) 145108 (6pp) doi:10.1088/0022-3727/46/14/145108

Single-mode rib waveguides in (Yb,Nb) : $RbTiOPO_4$ by reactive ion etching

A Choudhary[1], J Cugat[2], K Pradeesh[1], R Solé[2], F Díaz[2], M Aguiló[2], H M H Chong[3] and D P Shepherd[1]

[1] Optoelectronics Research Centre, University of Southampton, Southampton, SO171BJ, UK
[2] Física i Cristal·lografia de Materials i Nanomaterials, Universitat Rovira i Virgili, Tarragona 43007, Spain
[3] School of Electronics and Computer Science, University of Southampton, Southampton, SO171BJ, UK

E-mail: ac12g10@orc.soton.ac.uk

Received 25 September 2012, in final form 22 January 2013
Published 14 March 2013
Online at stacks.iop.org/JPhysD/46/145108

Abstract
We present the fabrication of single-mode rib waveguides in (Yb,Nb) : $RbTiOPO_4$ ((Yb,Nb) : RTP) by reactive ion etching (RIE) with a combination of SF_6 and Ar gases. The influence of the gas pressure, RF power and gas ratio on the etch rate and surface quality was studied to optimize the etching of RTP. Optimized parameters were used to fabricate rib waveguides in a (Yb,Nb) : RTP film, grown by liquid phase epitaxy, with an etch rate of 10 nm min^{-1}. Channel waveguide propagation was demonstrated for the first time in an RIE etched (Yb,Nb) : RTP rib structure.

(Some figures may appear in colour only in the online journal)

1. Introduction

Ytterbium (Yb^{3+}) doped gain media are useful materials for the realization of efficient power-scalable lasers [1]. They operate near the 1 μm spectral regime and have the advantages of a broad absorption band making them suitable for high-power diode pumping, low thermal load due to a small quantum defect and negligible losses due to parasitic processes such as up-conversion and excited state absorption. Recently, laser operation has been demonstrated in Yb^{3+}-doped $RbTiOPO_4$ (RTP) crystals [2]. RTP belongs to the $KTiOPO_4$ (KTP) class of orthorhombic crystals and is therefore of interest for nonlinear applications. However, in comparison with KTP, RTP can be doped with rare earth elements to a higher level and so is also of interest as a laser host. When doped with Yb^{3+}, RTP has a very broad emission bandwidth [3] making it a good candidate for the generation of ultrashort pulses, with pulses as short as 155 fs being demonstrated to date [4].

(Yb,Nb) : RTP gain media can be grown in a waveguide geometry by liquid phase epitaxy (LPE) [5] and planar waveguides with losses lower than 1 dB cm^{-1} have been demonstrated. Fabrication of channel waveguides based on this thin-film growth technology is motivated by noting recent work on ion-exchanged glass waveguides [6], showing that Yb^{3+}-doped channel waveguides are of interest as compact ultrafast sources with multi-GHz repetition rates, and consequently have potential application in areas such as optical sampling [7], metrology [8] and biological imaging [9]. The non-linear properties of the RTP crystal could also be utilized for fabricating compact self-frequency-doubled [3, 10] integrated waveguide sources, which would have enhanced performance in a low-loss channel waveguide geometry.

Structuring of RTP has been demonstrated using femtosecond laser ablation [11] and wet chemical etching [12]. Reactive ion etching (RIE) is a commonly used method for etching materials in the semiconductor industry [13]; however, there is a lack of literature on the plasma-based micromachining of RTP and to date there have not been any demonstrations of channel waveguide structures in RTP. In addition to the fabrication of waveguides, RIE of RTP could also be used to fabricate other optical devices, such as gratings [11] and antiresonant reflecting optical waveguides (ARROWs) [14].

Chlorine-rich gases have been extensively used for etching materials by RIE, but chlorine-based plasma is toxic and can be damaging to the chamber. Fluorine-based gases are more environmental friendly and RIE of other interesting candidates for ultrafast waveguide lasers, such as sapphire [15] and KYW [16], have both given promising results with fluorine-rich chemistry. In this paper we explore the RIE of RTP in a fluorine-rich environment with the view of fabricating channel (Yb,Nb) : RTP waveguide lasers. We have performed an extensive study of the etching characteristics of RTP by RIE with SF_6 and Ar gases by varying the RF power, gas pressure and gas ratio. On correlating the etch rates and surface roughness of the etched regions with different conditions we reached the optimum conditions for etching RTP. The optimum parameters were used to fabricate channel waveguides in a LPE-grown (Yb,Nb) : RTP film with an etch rate of 10 nm min^{-1}. The channels had a measured surface roughness of 8 nm and a side-wall angle of 63°. Single-mode propagation was demonstrated in these channels with mode radii of 7.9 μm by 4.3 μm.

2. Growth of single crystals for substrates and LPE growth of films

The RTP crystals used as substrates for the etching experiments were grown in a tubular furnace [17] using the top-seeded solution growth method (TSSG) and super-saturation of the solution was obtained by slow cooling [18]. We used an RTP seed parallel to the *c* crystallographic direction, since this orientation is one of the best to grow high-quality RTP crystals and from these crystals it is possible to obtain substrates with suitable dimensions in the ***ab*** plane. In fact, this plane has interest for non-critical phase matching type-II second harmonic generation (SHG) [3] for fundamental radiation around 1 μm, which is close to the emission wavelength of Yb^{3+}. Moreover, the ***ab*** plane is perpendicular to the orientation of the ferroelectric domains, which makes it possible to obtain a periodic domain inversion, producing quasi-phase matching [19]. All the substrates were cut perpendicular to the *c*-crystallographic axis and polished.

LPE growth of a (Yb,Nb) : RTP thin film was carried out in a furnace where a zone of uniform temperature suitable for epitaxial growth was obtained. The composition of the solution used for epitaxial growth was Rb_2O–P_2O_5–(TiO_2 + Nb_2O_5 + Yb_2O_3)–WO_3 with concentration of 43.90 mol%–23.6 mol%–22.50 mol%–10.00 mol%, respectively. TiO_2 was partially substituted by Nb_2O_5 and Yb_2O_3 up to concentrations of 2 mol% and 6 mol%, respectively, with Nb_2O_5 co-doping allowing higher concentrations of Yb^{3+} to be obtained [20]. After the homogenization of the solution, the saturation temperature was measured to be 1135 K. Following which, the substrates were slowly introduced into the furnace to avoid possible cracks due to thermal stress. The substrates were then dipped into the solution and kept at 1 K above the saturation temperature for 5 min to dissolve the outer part of the crystal. To begin the epitaxial growth, the temperature of the solution was decreased to 9 K below the saturation temperature in order to create super-saturation in the solution, which is the driving force behind the crystal growth. The substrates were stirred at 60 rpm and maintained under these conditions for 6 h. The obtained epitaxial layers were morphologically studied using a Sensofar PLμ 2300 interferometric microscope in order to check if they were free of defects and to measure the film thickness, which was initially 70 μm and then polished to a uniform thickness of 6 μm. The dimensions of the substrate were 12 mm × 8 mm × 2 mm.

The composition of the epitaxial layer was determined by electron probe micro-analysis with a wavelength dispersive spectrometer (EPMA-WDS), using a Cameca SX-50 microprobe analyser. This equipment works in a similar way to a scanning electron microscope, but collects the characteristic x-rays of the elements to be analysed and identifies the elements by recording the WDS spectra. The concentration of Yb^{3+} in the epitaxial layer was found to be 0.33 at%, which corresponds to an Yb^{3+} concentration of 2×10^{20} cm^{-3}. The refractive index contrast in TM polarization ($E \parallel c$-axis) was measured to be 4×10^{-3} at a wavelength of 972 nm (from a Ti : sapphire laser) by m-line measurements. The crystalline quality of the epitaxial layer was studied by x-ray diffraction measurements. The peaks recorded for the substrate and the epitaxial layer corresponding to the (0 0 4) reflection are sharp and narrow, indicating that the film has high crystalline quality comparable to that of the substrate.

3. Optimization of the RIE of RTP

The etching of RTP by RIE was optimized to reduce the RMS surface roughness in order to fabricate low-loss waveguides. A 300 nm layer of Cr was deposited by e-beam evaporation after which a 1.3 μm layer of S1813 resist was photolithography patterned to give waveguide features of widths ranging from 1 to 10 μm. The Cr layer was then wet etched and the resist was removed by solvent cleaning. The hard-masked RTP substrates were then etched in an RIE chamber with SF_6 and Ar gases where the pattern of the Cr was transferred on the RTP substrate, following which the Cr mask was chemically removed (the stages involved are shown in figure 1). RIE was carried out in an OPT Plasmalab 80 plus RIE system (Oxford Instruments) with an RF frequency of 13.56 MHz.

The RF power, the gas pressure and the gas ratio were the three parameters which were varied during RIE. An RF power of 250 W, a pressure of 50 mTorr , a total gas flow rate of 20 sccm and a gas ratio of 90 : 10::SF_6 : Ar were chosen as starting parameters. The temperature was kept fixed at 20 °C for all the experiments. There is a lack of literature on the dry etching of RTP, but halides are known to form volatile compounds with KTP [21] and hence the etching described here was carried out in a fluorine-rich environment. SF_6 was selected because this gas provides more free fluorine radicals [22] when compared with the other available fluoride gas, CHF_3. In contrast, Ar is an inert gas and is predominantly used to bombard the surface and hence make the etching process more physical. A 90% SF_6 gas mixture was used initially in order to have a predominantly chemical process. These parameters were then varied systematically to study their effect on etch rate and surface roughness. The measured substrate

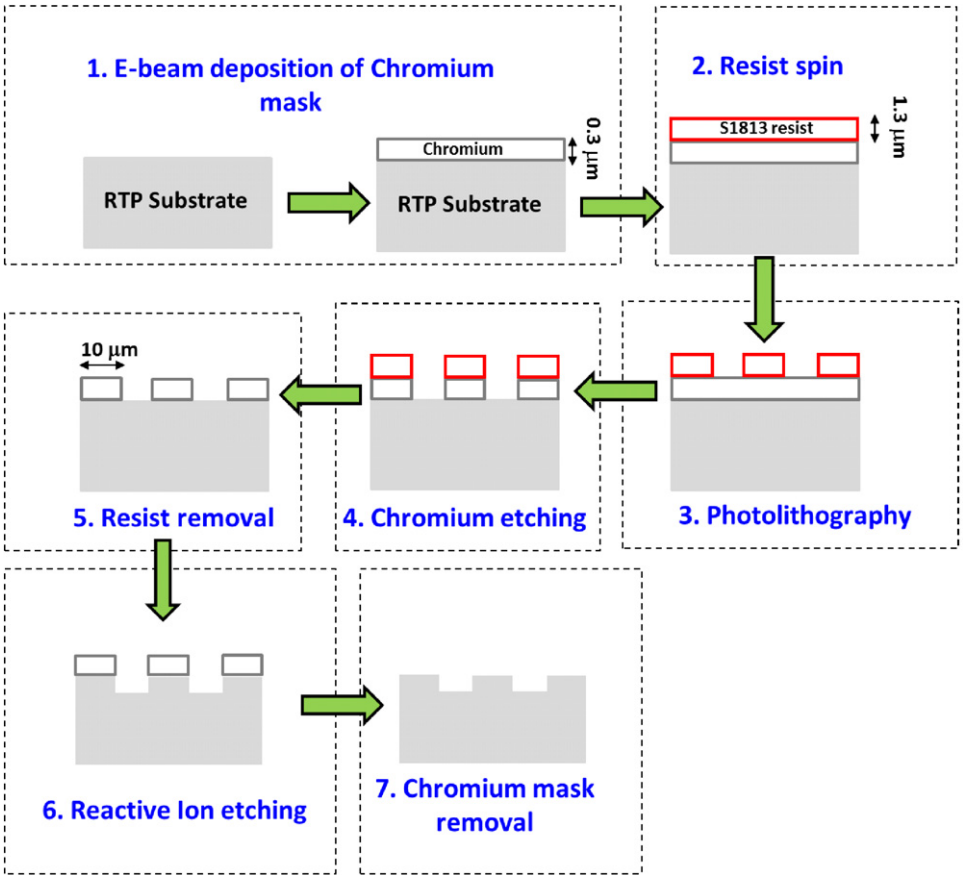

Figure 1. Different steps involved in the RIE of RTP.

RMS surface roughness before etching varied from 2 nm up to 5 nm from sample to sample; hence the change in the RMS surface roughness (after etching-before etching) is presented in figure 2.

Keeping all the other parameters fixed and an etch time of 40 min, the RF power was varied and the results obtained for etch rates of RTP and Cr, as well as the RMS surface roughness of RTP are presented in figure 2(*a*). As expected, the etch rate increases linearly with power, and an etch rate as high as 13 nm min^{-1} is obtained for an RF power of 350 W. The surface roughness also increases with the power and a surface roughness of 3.4 nm is obtained for 350 W RF power. The power was not increased beyond 350 W as the value of surface roughness becomes very high beyond this point.

A good balance was achieved between surface roughness and etch rate for a power of 250 W and hence the power was fixed at 250 W and the SF_6 : Ar ratio was fixed to 90 : 10 for the next set of experiments. The chamber pressure was then varied and the results obtained for etch rates and surface roughness are presented in figure 2(*b*). The etch rate decreased with pressure. This is because of the increase in scattering with pressure and hence a decrease in the mean free path for the radicals [23] and a loss of kinetic energy. It was found that a pressure of 50 mTorr resulted in an etch rate of 8 nm min^{-1} and a surface roughness of 1.6 nm. Thus, this pressure was fixed for the study of etch rate and surface quality dependence on the gas ratio.

The results obtained for etch rates and surface roughness against gas ratio are presented in figure 2(*c*). At low SF_6 concentrations, the etch rate is very high (16 nm min^{-1}) and so is the surface roughness (3.4 nm). This is a predominantly physical process and a lot of the material is sputtered by the Ar^+ ions. At very high SF_6 concentrations, the etch rate decreases, but the surface roughness also increases slightly. The optimum operation point for gas ratio (SF_6 : Ar) is in the range 50 : 50 to 70 : 30, where the etch rate is about 8 nm min^{-1} and the surface roughness is less than 1 nm.

The selectivity (ratio of etch rates of RTP to chromium) was found to be greater than 5 for almost all conditions. This allows the use of thin Cr masks for deep etching of RTP.

4. Channel waveguides in (Yb,Nb) : RTP

The (Yb,Nb) : RTP thin-film described in section 2 was etched for 135 min with RIE power of 250 W, gas pressure of 40 mTorr and gas flow rates of 10 sccm for both SF_6 and Ar. The pressure was reduced to 40 mTorr from 50 mTorr to increase the etch rate without compromising the surface roughness. This sample was then end-polished to a length of 7.5 mm, cleaned in an ultrasonic bath with acetone, isopropanol and DI water, blow-dried with N_2, and finally dehydrated in an oven at 90 °C for 10 min. The mask was chemically removed, after which the sample was plasma-ashed in an RIE chamber for 20 min with RIE power of 200 W, pressure of 50 mTorr and O_2 flow rate of

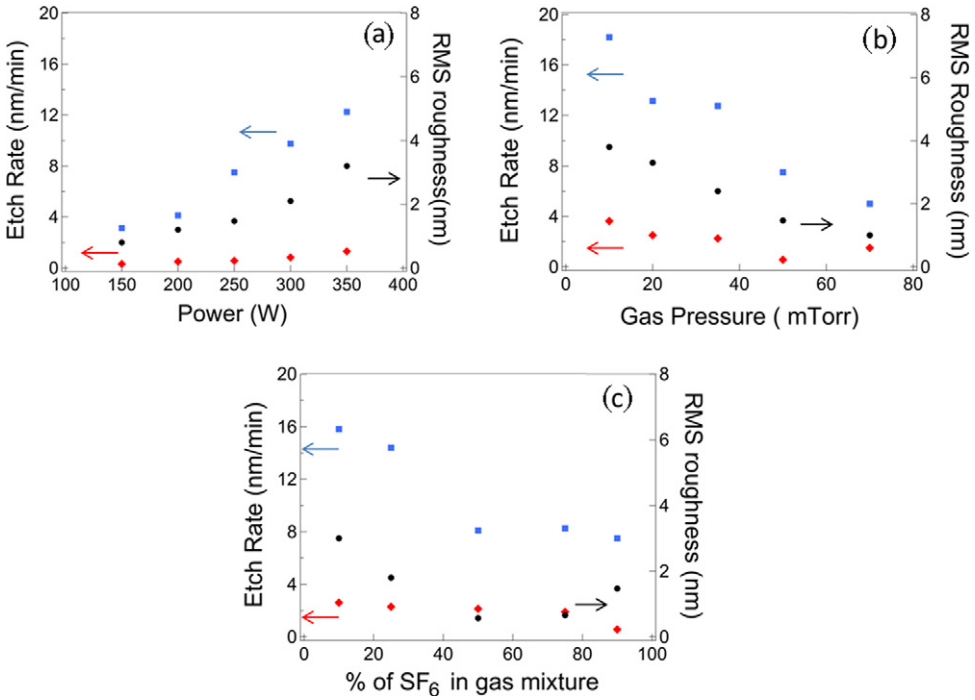

Figure 2. Effect of changing different RIE parameters on the etch rate and surface roughness. (*a*) RIE power, (*b*) gas pressure, (*c*) percentage of SF_6 in gas mixture. Blue: etch rate of RTP, red: etch rate of Cr, black: RMS surface roughness of the etched surface.

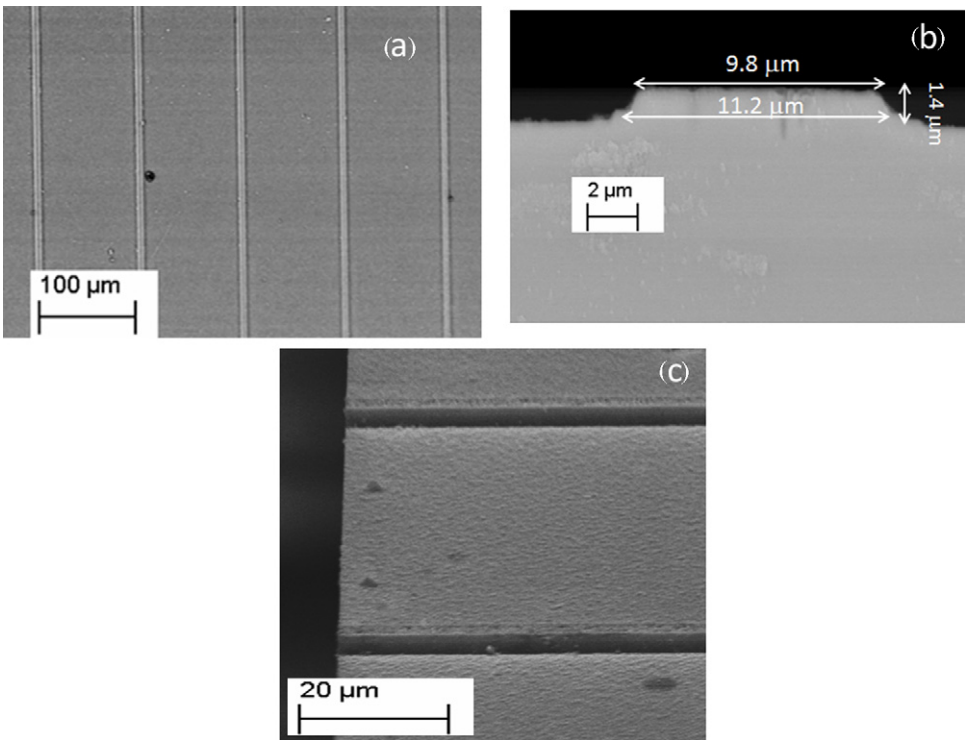

Figure 3. SEM images of the (Yb,Nb):RTP samples etched with RIE power of 250 W, $SF_6 = 10$ sccm, Ar = 10 sccm and pressure = 40 mTorr. (*a*) Top view, (*b*) cross-section of waveguide with top width of 9.8 μm. (*c*) SEM image taken by tilting the sample by 70° to show the side-wall quality.

10 sccm, which removed any organic impurities present on the substrate. The etch depth was measured to be 1.4 ± 0.1 μm, giving an etch rate of 10 nm min^{-1}. This etch depth was chosen to support a fundamental mode near 1 μm. The surface roughness of the film before etching was 3 ± 0.5 nm, and after etching it was measured to be 8 ± 0.5 nm. The fact that it is slightly higher when compared with the expected values from figure 2 could be due to the longer etch time for this process combined with re-deposition of the mask on the un-etched regions. Figure 3 shows the SEM images of the etched sample. For a waveguide with a top width of 9.8 μm, the width at the bottom was 11.2 μm giving a sidewall angle of 63°.

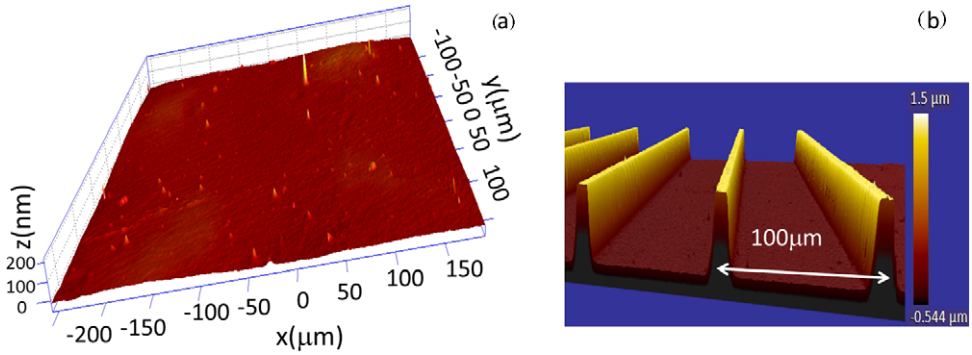

Figure 4. Surface topography of an etched planar region (*a*) and a region with etched ribs (*b*) measured by non-contact profiler (Zescope by Zemetrics).

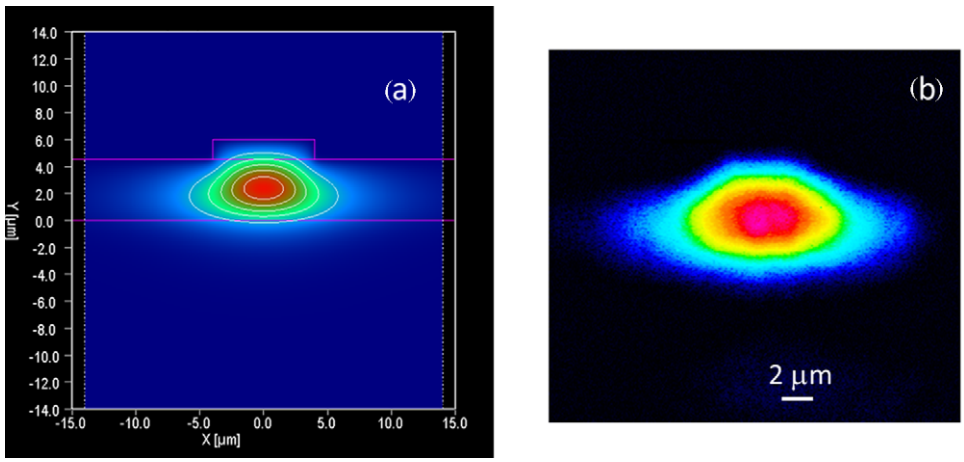

Figure 5. (*a*) Simulation of the mode profile in an 8 μm wide (Yb,Nb) : RTP rib waveguide at a wavelength of 0.98 μm. (*b*) Measured near-field mode profile for the RIE etched waveguide.

The surface topography of the planar region and the ribs measured by a non-contact profiler (Zescope by Zemetrics) is shown in figure 4. It can be seen from figure 4(*a*) that the surface quality, barring a few spikes (possibly due to the re-deposition of the mask), is very good.

Optical characterization was carried out by end-fire coupling a fibre-coupled single-mode laser diode from 3S photonics with a maximum power of 750 mW and a grating stabilized wavelength of 980.6 nm. The collimated pump was passed through a $\lambda/2$ plate to control the polarization. This was coupled into the waveguide by a 16× objective giving a measured waist radius of 3.2 μm. The output from the waveguide was collected by a 6× objective and imaged on a camera to measure the mode profile or was incident on a power meter for transmission measurements. The losses were estimated by comparing the transmitted light from the channel waveguide with the incident light and accounting for Fresnel reflections, transmission of the objectives, etc.

Transmission was measured at various powers and losses were estimated to be $<3.5\,\mathrm{dB\,cm^{-1}}$ for the $E \parallel c$ crystallographic axis (TM). This calculation assumes 50% launch efficiency due to the imperfect match between the launch mode size and shape compared with the propagation mode but it may be considerably worse and hence the losses may be significantly lower.

On rotating the polarization, the losses increased to $>10\,\mathrm{dB\,cm^{-1}}$ for TE polarization. This is consistent with the fact that the index contrast is very low for this polarization. It should be noted that in this configuration, the spectroscopy of (Yb,Nb) : RTP means that TM is the preferred polarization for lasing [2]. The loss for the TE polarization has to be further reduced before these waveguides can be used for self-frequency doubling applications. The waveguide structure is designed to be single mode at 981 nm and the simulated and measured TM profile is shown in figure 5. The $1/e^2$ mode radii were measured to be 7.9 μm and 4.3 μm in the x and y directions, respectively. This is in good correlation with the simulated values of 7.6 μm and 3.4 μm along the x and y directions, respectively (simulated by a commercially available software OlympIOs).

5. Conclusions

Optimization of the reactive ion etching of RTP was systematically carried out by varying the process parameters: RIE power, SF_6 and Ar gas ratios and gas pressure. This led to optimized parameters; RIE power of 250 W, gas pressure of 40 mTorr, 50 : 50 gas ratio and total gas flow rate of 20 sccm. These parameters were used to fabricate single-mode rib waveguides in (Yb,Nb) : $RbTiOPO_4$ for the

first time to our knowledge. Single-mode waveguides with mode radii of 7.9 μm $\times$ 4.3 μm were realized with losses estimated to be $<$3.5 dB cm^{-1} by transmission measurements. Such waveguides could have promising applications in the development of compact ultrafast lasers.

Acknowledgments

This work was supported by EPSRC under project EP/H035745/1 and by the Spanish Government under projects TEC2010-21574-C02-02, MAT2011-29255-C02-02, PI09/90527 and by the Catalan government under project 2009SGR235. J Cugat thanks the Spanish Government for the FPI fellowship BES-2009-024190. The authors would also like to thank Neil Sessions and Dave Sager for their advice and technical support in the integrated photonics cleanroom at the Optoelectronics Research Centre (ORC). Useful discussions with Dr Senthil Ganapathy are acknowledged as well.

References

[1] Krupke W F 2000 *IEEE J. Sel. Top. Quantum Electron.* **6** 1287–96
[2] Mateos X, Petrov V, Peña A, Carvajal J J, Aguiló M, Díaz F, Segonds P and Boulanger B 2007 *Opt. Lett.* **32** 1929–31
[3] Carvajal J J *et al* 2004 *Opt. Mater.* **26** 313–7
[4] Carvajal J J *et al* 2010 *Opt. Express* **18** 7228–42
[5] Cugat J, Solé R, Pujol M C, Carvajal J J, Mateos X, Díaz F and Aguiló M 2010 *Opt. Mater.* **32** 1648–51
[6] Choudhary A, Lagatsky A A, Pradeesh K, Sibbett W, Brown C T A and Shepherd D P 2012 *Opt. Lett.* **37** 4416–8
[7] Janke C, Först M, Nagel M, Kurz H and Bartels A 2005 *Opt. Lett.* **30** 1405–7
[8] Bartels A, Gebs R, Kirchner M and Diddams S 2007 *Opt. Lett.* **32** 2553–5
[9] Chu S, Liu T, Sun C, Lin C and Tsai H 2003 *Opt. Express* **11** 933–8
[10] Cugat J, Solé R, Carvajal J J, Mateos X, Pujol M, Massons J, Díaz F and Aguiló M 2011 *Opt. Lett.* **36** 1881–3
[11] Kumar G R *et al* 2011 *Opt. Mater.* **34** 207–14
[12] Carvajal J J, Woensdregt C F, Solé R, Díaz F and Aguiló M 2006 *Cryst. Growth Des.* **6** 2667–73
[13] Jansen H, Gardeniers H, de Boer M, Elwenspoek M and Fluitman J 1996 *J. Micromech. Microeng.* **6** 14–28
[14] Gehler J, Karthe W, Wachter C, Brauer A, Rasch A and Rottschalk M 1997 *IEEE Photon. Technol. Lett.* **9** 470–2
[15] Kang D-J, Kim I-S, Moon J-H and Lee B-T 2008 *Mater. Sci. Semicond. Process.* **11** 16–19
[16] Borca C N, Romanyuk Y E, Gardillou F, Pollnau M, Bernal M P and Morettiin P 2006 *Conf. on Lasers Electro-Optics (Long Beach, CA)* CMFF3
[17] Cugat J, Solé R, Carvajal J J, Pujol M C, Mateos X, Díaz F and Aguiló M 2011 *Cryst. Eng. Commun* **13** 2015–22
[18] Elwell D and Scheel H J 1975 *Crystal Growth from High-Teperatures Solutions* (New York: Academic)
[19] Fragemann A, Pasiskevicius V, Nordborg J, Hellström J, Karlsson H and Laurell F 2003 *Appl. Phys. Lett.* **83** 3090–2
[20] Carvajal J J, Nikolov V, Solé R, Gavaldà J, Massons J, Aguiló M and Díaz F 2002 *Chem. Mater.* **14** 3136–42
[21] Köhler M 1999 *Etching in Microsystem Technology* (Weinheim: Wiley-VCH Verlag GmbH) p 270
[22] Legtenberg R, Jansen H, de Boer M and Elwenspoek M 1995 *J. Electrochem. Soc.* **142** 2020–8
[23] Choi H J and Lee B T 2003 *J. Electron. Mater.* **32** 1–4

Paper IX

J. Cugat, R. Solé, J.J. Carvajal, X. Mateos, J. Massons, G. Lifante, F. Díaz, M. Aguiló,

Channel waveguides on $RbTiOPO_4$ by Cs^+ ion exchange

Optics Letters, **38**(3), 323 (2013).

Channel waveguides on $RbTiOPO_4$ by Cs^+ ion exchange

J. Cugat,[1] R. Solé,[1,*] J. J. Carvajal,[1] X. Mateos,[1] J. Massons,[1] G. Lifante,[2] F. Díaz,[1] and M. Aguiló[1]

[1]*Física i Cristal·lografia de Materials i Nanomaterials (FiCMA-FiCNA) and EMaS, Universitat Rovira i Virgili (URV), Campus Sescelades, C/Marcel·lí Domingo s/n, Tarragona 43007, Spain*

[2]*Departamento de Física de Materiales C-IV, Universidad Autónoma de Madrid, Madrid 28049, Spain*

**Corresponding author: rosam.sole@urv.cat*

Received September 19, 2012; revised December 5, 2012; accepted December 14, 2012; posted December 20, 2012 (Doc. ID 176542); published January 28, 2013

In this Letter we report Cs^+ ion exchange channel waveguides on $RbTiOPO_4$ (RTP) for what we believe is the first time. A Ti channel mask was fabricated on an RTP substrate by conventional photolithography. The ion exchange process was carried out in a $CsNO_3$ melt, and the channels produced ranged from 6 to 11 μm in width. The near-field pattern of the modes was recorded, and type II second harmonic generation in waveguide regime was obtained, producing 512.5 nm green light. The optical characterization shows optical losses of 3.8 dB/cm. © 2013 Optical Society of America

OCIS codes: 190.0190, 130.0130.

$KTiOPO_4$ (KTP) and its isostructural $RbTiOPO_4$ (RTP) are well-known for their high nonlinear optical coefficients. They crystallize in the noncentrosymmetric orthorhombic space group $Pna2_1$ [1]. The crystals of this family have been widely used for frequency conversion devices, especially for the second harmonic generation (SHG) of the Nd^{3+} and Yb^{3+} emissions [2]. RTP has similar nonlinear optical coefficients to KTP [3], a higher laser-damage threshold (~2 times larger than the one of KTP) [4, 5], a wide range of wavelength and angular acceptance for frequency doubling, high chemical stability, and low photorefractive damage susceptibility [6]. Moreover, RTP has a higher damage threshold than $LiNbO_3$, which, despite this disadvantage, is widely used for integrated optics (IO) [7,8]. For all these properties, RTP is particularly useful for short wavelength generation [3,9]. RTP also has large electro-optical coefficients and low dielectric constants, which gives chances for various electro-optical applications, such as modulators and *Q* switches. Moreover, RTP is a suitable candidate as self-frequency doubling material in waveguide regime, since it can be doped with Yb^{3+} active ions [10] to levels high enough to produce laser radiation [11].

Although type II phase-matching SHG has been widely used in the crystals of the KTP family to obtain visible radiation, the quasi-phase-matching interaction in this kind of ferroelectric crystals has gained interest due to the possibility of using the largest nonlinear optical coefficient in the frequency conversion process to increase the frequency doubling efficiency. Recently, periodic poling of RTP has been demonstrated by applying a high voltage electric field at room temperature [12].

Numerous advantages over other optical technologies make IO interesting. In general, the IO devices interface efficiently with optical fibers and can reduce the cost in complex circuits by eliminating the need of separate and individual packaging of each circuit element. They also offer lower power consumption, improved reliability, smaller size, and weight [13].

Taking into account the abovementioned properties of RTP, this crystal becomes an interesting and promising material as a base for IO; hereby, it is interesting to demonstrate the fabrication of waveguides in RTP. There are two main kinds of waveguides: graded index and step index waveguides. In the literature, different methods of fabrication of graded index waveguides, such as ion exchange [14,15], proton exchange [16], and ion implantation [17], have been successfully used on KTP. Literature related to waveguides with graded index in RTP is scarce. The ion implantation method involves a high-energy process that can produce damage in the crystal. Thus, in this work, we have fabricated RTP channel waveguides by Cs^+ ion exchange. We used this ion because Cs^+ diffusion in RTP produces an increase of the refractive indices and its ionic radius is not far from the Rb^+ one. To our knowledge, RTP waveguides fabricated by Cs^+ ion exchange have not been demonstrated.

The diffusion channels were made on a plate-shaped RTP substrate. The orientation of the substrate was perpendicular to the ***c*** crystallographic direction. The substrates were cut from RTP bulk crystals grown by top seeded solution growth [10]. The plates used as substrates in this study had dimensions of 12, 15, and 1.5 mm along the ***a***, ***b***, and ***c*** directions, respectively.

The width of the channels ranged from 5 to 10 μm, with steps of 1 μm, and is separated by 100 μm.

For the fabrication of the light mask, first a 100 nm Ti film was sputtered on a glass substrate. Then, a layer of photoresist AZ 1505 from Microchemicals was spin-coated on the Ti-glass. A laser lithography system was used to selectively expose the resist to UV light for channel pattern fabrication. After developing the exposed part, the channel pattern was transferred to the Ti mask film by etching with $H_2O_2:NH_4OH$ in 2:1 molar ratio.

In order to transfer to the Ti sputtered substrate the same channel pattern already made on the Ti-glass, we used the process detailed above related to Ti-glass mask fabrication, but the UV-exposure was made by conventional photolithography, using a MG 1410 mask aligner. In this procedure, the Ti-glass mask, previously fabricated, was used. As a result, a thin film of Ti with channels shape openings of width 6 to 11 μm ± 0.2 μm were obtained on the substrates. These channels were fabricated parallel to the ***b*** crystallographic direction. Figure 1 shows the pattern of Ti-channels on the RTP substrate.

To produce the Cs^+ diffusion, the sample with the Ti pattern was horizontally immersed in a crucible containing 25 g of $CsNO_3$ at 425°C. The sample, previously

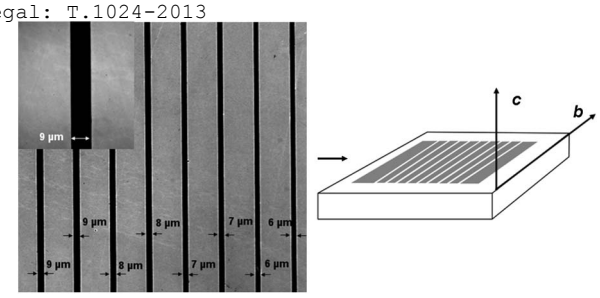

Fig. 1. Ti channels pattern on an RTP substrate and scheme of the position of the mask in relation with the substrate.

heated to obtain thermal equilibrium with the melt, was dipped at about 6 mm below the melt surface to avoid the usual instabilities at the melt surface. The sample was maintained in the melt for 2 h and rotated at 40 rpm in order to obtain a good homogeneity in the liquid phase. Finally, it was slowly removed from the solution.

After that, the faces perpendicular to the channels were end-polished, and waveguides of 7.3 mm along the ***b*** crystallographic direction were obtained. Both faces were polished by sandwiching the sample between two glass blocks to minimize the edge-bend effect. Preliminary information about the diffusion was obtained by optical microscope. The equipment used was an Olympus BH-2 microscope. Figure 2 shows the Cs^+ ion exchange in RTP. As can be seen in this figure, the Cs^+ diffusion is straight parallel to the ***c*** crystallographic direction. This was expected since in the RTP structure the conductivity along the ***c*** direction is significantly higher than along the other directions due to the existence of the Rb channels [15]. A small mistake of around 4° was made in the cutting process of the substrates (see Fig. 2), but its influence in the results was not substantial.

The index profile of the diffused waveguide was determined by measuring the dark mode spectra at 632.8 nm. The four TE guided modes fit to an exponential function of the form $n(x) = n_{\text{subs}} + \Delta n e^{-x/d}$, with a maximum index at the surface of $\Delta n = 0.038$ and a depth of $d = 1.80$ μm.

To characterize the channel waveguides, the near-field pattern of the guided modes must be obtained. A 50 × microscope objective was used to couple the light into the 11 μm channel and a CCD camera was used to record the modes after the output microscope objective. The waveguide modes were excited by a He–Ne laser at a wavelength of 632.8 nm, as well as a Ti:Sapphire at 972 nm. All the experiments were performed in TM polarization.

The excitation of the guided modes separately was difficult, since the spot size of the beam after the input microscope objective (~20 μm) was larger than the area of the channel. We were still able to obtain the near-field patterns of the TM_{00}, TM_{11} and TM_{11} modes, as can be seen in Fig. 3. In this case, the near-field patterns of the TM_{01} and TM_{11} modes show a vertical asymmetry, since the lower lobules are expanded in front of the upper lobules. This could be due to the vertical refractive index gradient. We finally estimate the FWHM of the fundamental mode at 632.8 nm, being 9.7 μm for the horizontal profile and 7.5 μm for the vertical one.

With the aim to check the SHG inside the channel waveguides, a pulsed laser beam (pulse length 7 ns and repetition rate 10 Hz) from an OPO, model Vibrant HE 355 II+UV from Opotech, was coupled into it. The average power at the input was 3.5 mW. The same guiding setup as in the above sections was used. In this case, an achromatic half-wave plate was placed between the laser source and the sample at an angle of 22.5° to ensure the type II SHG. The guided green light obtained from the channels (average output power 0.2 mW) was collected with the CCD camera, and the image obtained is shown in Fig. 4. This figure shows the type II SHG obtained in the 11 μm wide channel by pumping at a wavelength of 1025 nm.

To estimate the transmission losses of the channel waveguides, a 50 × objective microscope was used to couple the 972 nm laser beam from a Ti:sapphire laser into the 11 μm channel waveguide. We use this wavelength because it is near 1 μm and is the pumping wavelength for Yb^{3+} laser emission. The fundamental mode was exited in the channel using a x–y–z mobile stage. A 50 × microscope objective was used to collect the transmitted light. In order to estimate the transmission losses, the beam power was measured before the input microscope objective (spot size ~20 μm in diameter), as well as after the output microscope objective. The expression applied to estimate the transmission losses was the corresponding to the single pass transmission method and is $\text{loss} = (10/d)\log(P_{\text{out}}/P_{\text{in}})$, where P_{out} is the power measured after the output microscope

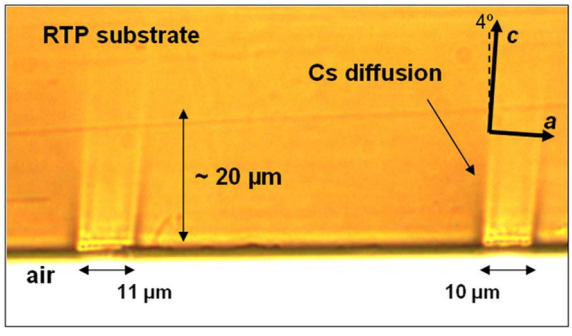

Fig. 2. (Color online) Transmission microscope image of a polished end face of the sample where the profile of the diffusion can be observed.

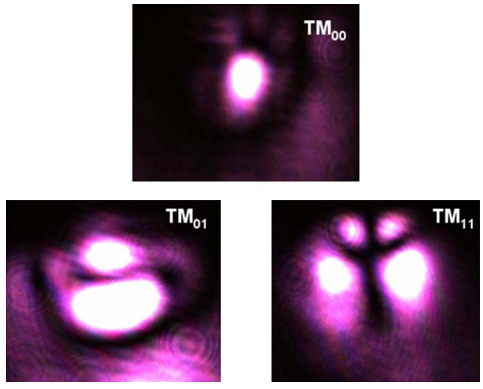

Fig. 3. (Color online) CCD images of the excited modes at 972 nm. The modes correspond to the TM_{00}, TM_{01} and TM_{11} mode orders.

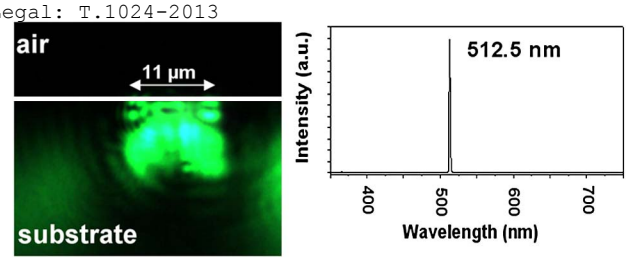

Fig. 4. (Color online) Type II SHG in an 11 μm channel width. The fundamental radiation was at 1025 nm and the second harmonic radiation was at 512.5 nm.

objective, P_{in} is the power measured before the input microscope objective, and d is the waveguide length. The input and output powers were corrected in order to reach a good accuracy. In fact, the Fresnel losses, transmission of the microscopes, and the launch efficiency were taken into account. By applying these corrections and using the expression mentioned above, we estimated an upper limit of the transmission losses of 3.8 dB/cm.

In summary, Cs^+ ion exchange channel waveguides on RTP were reported for the first time to our knowledge. The Cs^+ diffusion obtained was straight along the ***c*** crystallographic direction. This is an important result since it produces a high index contrast perpendicular to the ***c*** crystallographic direction, improving the guidance quality. The type II SHG radiation was demonstrated by coupling an IR light beam of 1025 nm to the waveguide. So, a green light radiation was recorded in a CCD camera.

This work was supported by the Spanish Government under projects TEC2010-21574-C02-02, MAT2011-29255-C02-02, PI09/90527, and the Catalan Authority under project 2009SGR235. This work has been partially funded by the European Commission under the Seventh Framework Programme, under project Cleanspace, FP7-SPACE-2010-1-GA-263044. J. Cugat thanks the Spanish Government for the FPI fellowship BES-2009-02419.

References

1. P. A. Thomas, S. C. Mayo, and B. E. Watts, Acta Crystallogr. Sect. B **48**, 401 (1992).
2. R. F. Belt, G. Gashurov, and Y. S. Liu, Laser Focus **21**, 110 (1985).
3. M. N. Satyanarayan, A. Deepthy, and H. L. Bhat, Crit. Rev. Solid State Mater. Sci. **24**, 103 (1999).
4. Yu. S. Oseledchik, A. I. Pisarevsky, A. L. Prosvirnin, V. V. Starshenko, and N. V. Svitanko, Opt. Mater. **3**, 237 (1994).
5. Y. Guillen, B. Ménaert, J. P. Fève, P. Segonds, J. Douady, B. Boulanger, and O. Pacaud, Opt. Mater. **22**, 155 (2003).
6. J. D. Bierlein, D. B. Laubacher, J. B. Brown, and C. J. van der Poel, Appl. Phys. Lett. **56**, 1725 (1990).
7. G. Lifante, *Integrated Photonics: Fundamentals* (Wiley, 2003).
8. T. Suhara and M. Fujimura, *Waveguide Nonlinear-Optic Devices* (Springer, 2003).
9. F. Laurell, L. K. Cheng, and J. D. Berlein, *Compact Blue-Green Lasers* (OSA, 1994).
10. J. Cugat, R. Solé, J. J. Carvajal, M. C. Pujol, X. Mateos, F. Díaz, and M. Aguiló, CrystEngComm **13**, 2015 (2011).
11. X. Mateos, V. Petrov, A. Peña, J. J. Carvajal, M. Aguiló, F. Díaz, P. Segonds, and B. Boulanger, Opt. Lett. **32**, 1929 (2007).
12. H. Karlsson, F. Laurell, and L. K. Cheng, Appl. Phys. Lett. **74**, 1519 (1999).
13. T. L. Koch, F. J. Leonberger, and P. G. Suchoski, *Handbook of Optics*, *Integrated Optics* (McGraw-Hill, 1995).
14. J. D. Bierlein, A. Ferretti, L. H. Brixner, and W. Y. Hsu, Appl. Phys. Lett. **50**, 1216 (1987).
15. J. Bierlein and H. Vanherzeele, J. Opt Soc. Am. B **6**, 622 (1989).
16. M. G. Roelofs, A. Ferretti, and J. D. Bierlein, J. Appl. Phys. **73**, 3608 (1993).
17. L. Zhang, P. J. Chandler, P. D. Townsend, Z. T. Alwahai, and A. J. McCaffery, Electron. Lett. **28**, 1478 (1992).